The Dissertation Committee for Seong-Hoon Kee Certifies that this is the approved version of the following dissertation:

EVALUATION OF CRACK DEPTH IN CONCRETE USING NON-CONTACT SURFACE WAVE TRANSMISSION MEASUREMENT

Committee:

Jinying Zhu, Supervisor

James O. Jirsa

Oguzhan Bayrak

Kevin J. Folliard

Kenneth H. Stokoe II

Clark R. Wilson

EVALUATION OF CRACK DEPTH IN CONCRETE USING NON-CONTACT SURFACE WAVE TRANSMISSION MEASUREMENT

by

Seong-Hoon Kee, B.S., M.S.

Dissertation

Presented to the Faculty of the Graduate School of

The University of Texas at Austin

in Partial Fulfillment

of the Requirements

for the Degree of

Doctor of Philosophy

The University of Texas at Austin

May, 2011

To

my wife and family

Acknowledgements

EVALUATION OF CRACK DEPTH IN CONCRETE USING NON-CONTACT SURFACE WAVE TRANSMISSION MEASUREMENT

Seong-Hoon Kee, PH.D.

The University of Texas at Austin, 2011

Supervisor: Jinying Zhu

The purpose of this study is to develop a non-contact air-coupled NDT method to identify and characterize surface-breaking cracks in concrete structures using surface wave transmission measurements. It has been found that the surface wave transmission (SWT) across a surface-breaking crack is related to the crack depth. However, inconsistence was noticed in surface wave transmission measurements. In this dissertation, the author first summarized limitations of the current SWT method for application to concrete structures, which include inconsistent sensor coupling, near-field effect of sensors, effects of crack width, external loading effect on surface wave transmission coefficient, and lack of a repeatable source.

In this dissertation, the author attempts to find solutions to the aforementioned problems. First, non-contact air-coupled sensors were applied to the SWT method to reduce experimental errors caused by inconsistent coupling condition of conventional contact sensors. Air-coupled sensing enables reliable and consistent results, and significantly improves test-speed. Results from laboratory and field tests demonstrate effectiveness of air-coupled sensors. Second, appropriate sensor-to-source configurations

are proposed to reduce undesirable effects: *(i) the near-field effect of sensors around a crack*, and *(ii) contribution of multiple modes in a plate-like structure with a finite thickness*. Near-scattering of surface waves interacting with a surface-breaking crack was investigated using numerical simulations (finite element method) and experimental studies over a wide range of the normalized crack depth (h/λ: crack depth normalized by wavelength of surface waves) and the normalized frequency-thickness ratio ($f\text{-}H/C_R$: frequency-thick normalized by Rayleigh wave speed). Third, effects of external loadings on transmission coefficient of surface waves in concrete were investigated through a series of experimental studies. In the research, variation of the transmission coefficient is presented as a function of crack mouth opening displacement (CMOD). This provides a guideline on minimum CMOD to which the SWT method can be reasonably applied. In addition, the author experimentally demonstrates that using low-cost piezoceramic sensors is effective in generating consistent stress waves in concrete. Finally, the author demonstrates that the air-coupled SWT method developed in this study is effective for in-situ estimates of a surface-breaking crack in large concrete structures.

Table of Contents

ix

List of Tables

List of Figures

xxiv

xxvi

xxviii

xxix

xxx

PART I INTRODUCTION

Chapter 1   General Introduction

1.1   BACKGROUND OF THE RESEARCH

Concrete structures in civil infrastructure systems are susceptible to deterioration from various sources. Many concrete structures contain defects and internal voids of varying severity that are threatening the safety of structures and public users. Recently, the American Society of Civil Engineers (ASCE) reported that existing infrastructure systems including concrete structures are substantially outdated and nearly failing [1]. The average grade of America's infrastructure is "D". It is estimated that $ 2.2 trillion over five-year investment is needed to improve the situation.

Infrastructure management agencies in the United States have realized the current situation and dedicated a considerable portion of their construction budget to restoration, rehabilitation, and maintenance of old and damaged concrete structures as opposed to new construction. To maximize working efficiency with limited sources, the management actions are generally prioritized based on evaluating current condition of civil infrastructure systems. In this sense, the infrastructure management agencies require planned field inspection, which is primarily relying on visual examinations and some destructive tests (e.g., core extractions). However, visual examinations can only provide superficial information, and the results strongly depend on the experience of the inspectors. Moreover, visual inspections are only effective when deterioration appears on concrete surface. In contrast, destructive tests such as core extraction may provide detailed information of the concrete. However, they are labor-intensive and time-consuming to cover large civil infrastructure systems. Currently, many researchers are seeking reasonable solutions by developing reliable and consistent non-destructive test (NDT) method. Successful NDT methods can be used to determine optimum timing of inspections and rehabilitations to minimize total cost in maintenance, which will help to accomplish more sustainable and resilient civil infrastructure in the United States.

2

1.2   EVALUATION OF SURFACE-BREAKING CRACKS IN CONCRETE

Deterioration of reinforced concrete structures is generally manifested as surface-breaking cracks in concrete. The appearance of cracks in concrete members may not necessarily imply structural failure. However, it causes many serviceability and durability problems, e.g., stiffness degradation, corrosion of the reinforcement bars, and infiltration of moisture and/or deleterious ingredients. These effects cause further deterioration and lead to early malfunction of concrete structures.

Characterizing surface-breaking cracks will provide useful information to evaluate current health condition and remaining life of concrete structures, and help infrastructure agencies make appropriate rehabilitation decisions. Although crack width and density can be directly measured on the concrete surface, crack depth measurement in concrete has always been a challenging task. The currently available NDT methods are divided into two categories according to the principle of the methods: the time-of-flight diffraction (TOFD) and surface wave transmission (SWT) methods. In the TOFD method, two sensors are located at the either side of a surface-breaking crack [2-4]. Ultrasonic waves are sent from one sensor on one side of the crack, and received by the other sensor on the opposite side of the crack. The depth can be calculated from the measured travel time of ultrasonic waves. The accuracy of TOFD results depends on determination of arrival time of the diffracted waves by a tip of a surface-breaking crack. Some researchers [5, 6] have noticed that the TOFD method may not always provide reasonable crack depth estimation in field applications. Infiltration of dust/water in the cracks, and shape of crack tips may affect accurate arrival time determination of diffracted waves.

The SWT method is based on measurements of surface wave transmissions across a surface-breaking crack. Previous studies have demonstrated that the SWT method is effective for estimating crack depth in metals and concrete. Fundamental background of the SWT method is summarized in Chapter 2. In the SWT method, two sensors are

located on the either side of the crack according to the self-calibrating (SC) procedure [7-9]. The SC procedure is effective in reducing the experimental variability caused by inconsistent source input and receiver coupling. The transmission coefficient of surface waves is defined as spectral amplitude ratio between the transmitted surface waves (R_{tr}) and the incident surface waves (R_i) in the frequency domain. The depth of a surface-breaking crack can be estimated from the pre-established relation between transmission coefficient and crack depth. However, there are several limitations to obtain consistent and reliable results from concrete structures using the SWT method.

1.3   MEASUREMENT OF STRESS WAVES USING AIR-COUPLED SENSORS

Good coupling between ultrasonic transducers and concrete surface is required to obtain reliable measurement of surface wave transmission coefficients. Inconsistent coupling condition of conventional contact sensors (e.g., accelerometers) makes it difficult to obtain reliable, consistent, and rapid transmission measurements. Temporary sensor mounting methods, such as wax, adhesive and magnetic mounts, will induce a low resonant frequency, which significantly affects experimental measurements if the center frequency of input signal is close to resonance frequency of sensors. On the other hand, permanent mounting cannot meet the requirement of rapid NDT test. In addition, rough surface on concrete in field structures poses difficulties in obtaining good coupling between contact sensors and concrete.

Using non-contact sensors (i.e., laser vibrometers and air-coupled sensors) is a possible solution of the coupling issue in ultrasonic tests. A laser vibrometer, however, has difficulties in measuring stress waves on rough concrete surface. In contrast, air-coupled sensors have been successfully used by previous researchers to measure leaky surface waves, and Lamb waves [10-15]. Compared to contact sensors, the air-coupled sensors have the following benefits:

- The non-contact sensing technique eliminates sensor coupling problems, and thus gives more consistent measurement results; and
- The non-contact features enable rapid scanning of large civil engineering structures.

1.4   OBJECTIVES AND SCOPE OF THE RESEARCH

The purpose of this research is to develop an air-coupled NDT method for evaluating the depth of a surface-breaking crack in concrete structures using the SWT method. There are several unanswered questions in order to apply the method to concrete structures in-situ. In this research, the author attempts to find solutions to the following problems that limit application of the SWT method:

- Appropriate sensor-receiver configuration to minimize the near-field effect of sensors and contribution of multiple modes of lamb waves in thin plates
- Effects of distributed surface-breaking cracks
- Effects of multiple cracks on transmission measurements
- Effects of crack width (i.e., crack mouth opening displacement: CMOD), and external loadings on transmission coefficient of surface waves in concrete
- Inconsistent coupling problems caused by contact sensors
- Lack of a consistent source for generating stress waves in concrete
- Lack of available data from field applications

As a result, the author proposed the '**Air-coupled SWT**' measurement model to evaluate the depth of surface-breaking crack in concrete (see **Figure 1-1**). The air-coupled SWT method contains: (i) appropriate source-receiver configurations; (ii) reliable transmission function to quantitatively estimate the depth of surface-breaking

crack; (iii) appropriate types of sources and receivers and (iv) data acquisition systems for rapid in-situ inspection which can be controlled by a computer program developed by the author.

Finally, the air-coupled SWT method developed in this study is applied to evaluating surface-breaking cracks in in-situ concrete structures for the verification purposes.
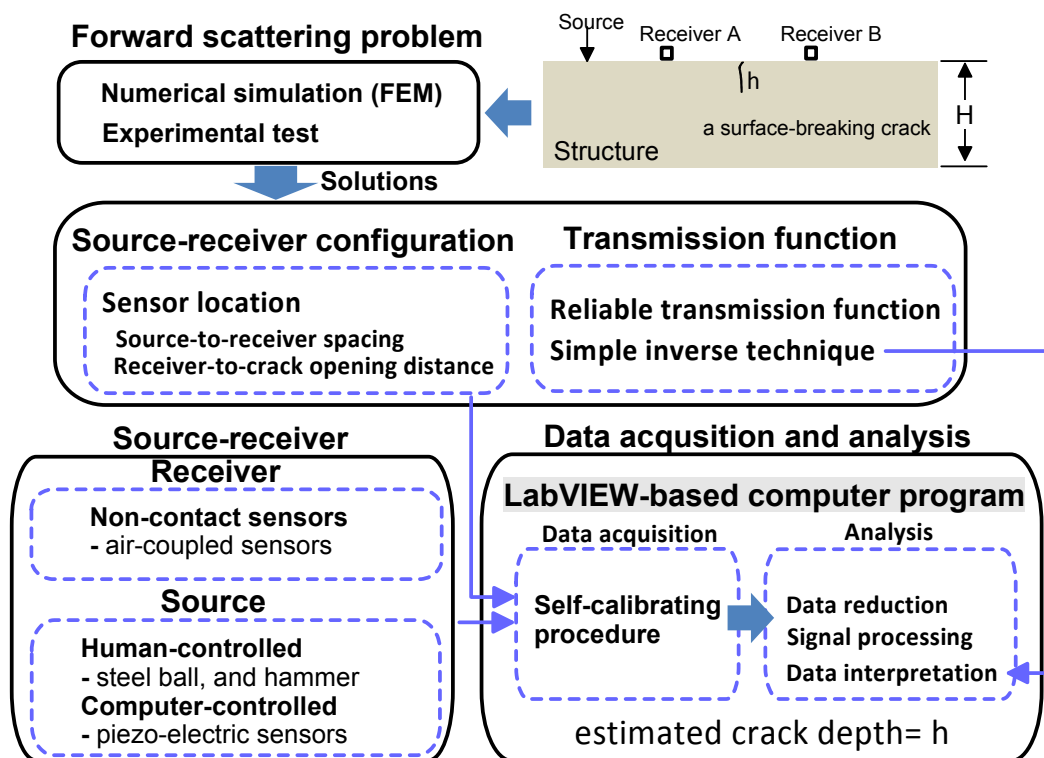
Figure 1-1: A measurement model for the air-coupled SWT method

1.5   OUTLINE OF THE RESEARCH

The results of this research are described in the five parts of this dissertation as shown in **Figure 1-2**.

- Introduction (Chapters 1 - 2)

6

- Theoretical studies (Chapters 3-5)
- Application to concrete (Chapters 6-10)
- Field application (Chapter 11)
- Conclusions (Chapters 12)

PART I: Introduction	• General background (Chapter 1) • Literature review of the SWT method (Chapter 2)
PART II: Theoretical study	• Near field effect of sensors (Chapter 3) • Surface wave transmission across distributed cracks (Chapter 4) • Contribution of multiple modes of lamb waves (Chapter 5)
PART III: **Application to concrete** **(Lab test)**	• Air-coupled sensing for concrete NDT (Chapter 6) • SWT method to concrete (Chapter 7) • Application to thin concrete plates (Chapter 8) • SWT method across a partially closed crack (Chapter 9) • Developing consistent source and receiver (Chapter 10)
PART IV: **Field application**	• Evaluation of ASR/DEF Damage in in-situ concrete structrues (Chapter 11)
PART V: **Conclusions**	• Summary, conclusions and recommendations (Chapter 12)

Figure 1-2: Structure of the dissertation.

The first part of this research provides a general background of the remainder of the dissertation. Theoretical backgrounds and literature reviews on the SWT method are described in Chapter 2.

In the second part of the research, emphases are placed on further developing the SWT method through theoretical studies. In Chapter 3, near-field scattering of surface waves interacting with a surface-breaking crack (near field effects of sensors) is investigated in the useful frequency range of the SWT method. Furthermore, effects of distributed surface-breaking cracks on surface wave transmission measurements are described in Chapter 5, and then, effects of multiple-modes of Lamb waves on transmission coefficient surface waves are explored in Chapter 6.

The SWT method is applied to concrete in the third part of the research. Chapter 6 provides a fundamental basis of air-coupled sensing technique for concrete NDT. The air-coupled sensing technique is applied to thick and thin concrete plates in Chapter 7 and Chapter 8, respectively. Furthermore, effects of various interfacial conditions of cracks on transmission coefficients of surface waves are investigated in Chapter 9. In addition, preliminary results on developing consistent source and receiver for measuring stress waves in concrete are summarized in Chapter 10.

In the fourth part of the research, the air-coupled SWT method is applied to in-situ testing of concrete structures. In Chapter 11, the air-coupled SWT method is used to evaluate surface-breaking cracks in prestressed concrete beams affected by different degrees of Alkali-Silica Reaction and Delayed Ettringite Formation (ASR/DEF). Large test areas in concrete specimens are investigated through rapid acoustic scanning. In this chapter, 2D image technique is also developed to efficiently show the results from large test areas.

In the last part of the research, recommendations for future works and conclusions of this study are summarized in Chapter 12.

Chapter 2   Background and Literature Review

2.1   INTRODUCTION

Surface waves are mechanical waves propagating along the surface of solid materials with both longitudinal and transverse motion. Most energy of surface waves is confined near the free surface of a solid body with frequency-dependent penetration depth. The lower frequency components have deeper penetration. A single surface-breaking crack normal to the free surface causes scattering of surface waves at the crack, and attenuates incident surface waves by diffraction, reflection, transmission, and mode conversion. Previous researchers have demonstrated that transmission coefficient of surface waves across a surface-breaking crack is a good ultrasonic parameter for crack depth estimation in metals. An NDT method based on surface wave transmission measurement (SWT method) has been verified effective to evaluate the depth of a surface-breaking crack in concrete. However, there are still some difficulties that prevent consistent and reliable surface wave transmission from concrete structures. One possible reason is related to the near-field effect of sensors and the contribution of multiple modes of lamb waves in surface wave transmission measurements. Another critical issue is the inconsistent sensor coupling condition when temporary mounting method is used.

This chapter provides fundamental background information for the following chapters of this dissertation. The author first reviews the limitations of the current SWT method through literature review. Chapter 2.2 and 2.3 review fundamental properties of surface waves and Chapter 2.4 further reviews scattering theory of surface waves by a surface-breaking crack in solid. Furthermore, backgrounds of the SWT method are organized in Chapter 2.5.

9

2.2 PROPERTIES OF SURFACE WAVES

Surface waves (or Rayleigh waves) were widely investigated in various fields of science and engineering after Rayleigh theoretically demonstrated existence of surface waves in 1885 [16]. Since the 1940's, surface waves in the ultrasonic range have been extensively used for near-surface or sub-surface defect evaluation, and material characterization of the sub-surface area of test samples. The theoretical background of surface waves and their applications to NDT were well documented by Viktorov [17].

Surface waves are essentially a guided wave composed of coupled longitudinal and shear waves that propagate along the surface of a solid. In semi-infinite media surface waves are non-dispersive, i.e., the wave velocity does not change with frequency. The particle motion on the surface is elliptical in nature and retrograde with respect to the direction of propagation (i.e., it is counter clockwise for a wave travelling to the right). **Figure 2-1** shows the ratio of in-plane to out-of-plane displacement of surface waves (U_x/U_z) with respect to the ratio of the depth to the surface wavelength λ_R. The horizontal component of the displacement is smaller than the vertical component at the surface (e.g., U_x/U_z is around 0.6). The in-plane displacement decreases quickly with depth and reaches zero at a depth of about 0.2 λ_R, where the phase inverts.

Figure 2-2 shows the displacement components at different depth in the solid for Poisson's ratio of v=0.25 and 0.34. The displacements have been normalized with respect to the free surface displacement in the vertical direction U_{z0}. The depth has been normalized with respect to the surface wavelength λ_R. U_z (z) of surface waves exponentially decays with the distance from the free surface boundary. The penetration depth of surface wave is usually defined as λ_R. At $z= \lambda_R$ and $z= 2\lambda_R$, U_z decreases to 20% and 1.5% of U_{z0}. Therefore lower frequency components have deeper penetration depth. This property of surface waves is particularly useful for evaluating surface-breaking cracks in solids.
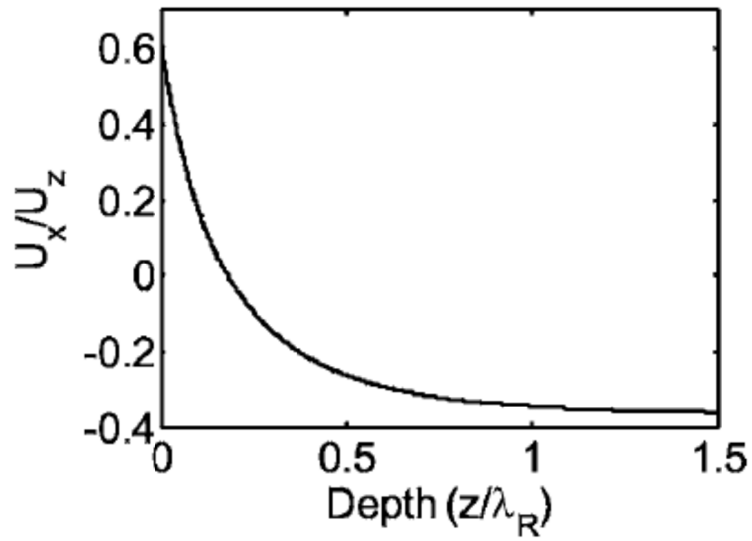
Figure 2-1: Ratio of in-plane displacement component to out-of-plane component of continuous surface wave with respect to the ratio of depth z to λ_R (after Viktorov [17]).
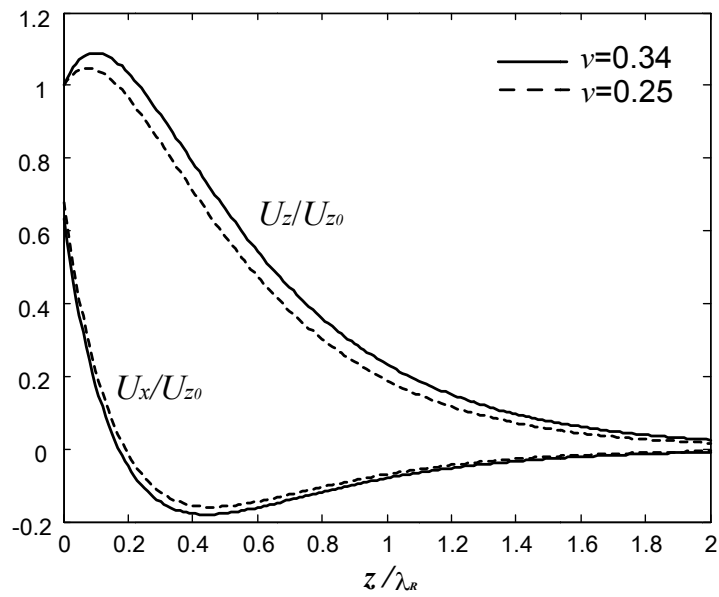
Figure 2-2: Normalized displacement component of surface waves (U_z/U_{z0}, and U_x/U_{z0}) with respect to the ratio of depth z to λ_R, where $U_{z0} = U_z$ (z=0) (after Viktorov [17]).

2.3   IMPACT-INDUCED SURFACE WAVES

In civil engineering, an impulse hammer or a point impactor has been widely used as an effective source for surface wave generation. The response of surface waves resulting from a transient point loading on a half space surface was first studied by Lamb in 1904 [18], and has been of great practical interest to NDE researchers. Since then this class of problems has been called Lamb's problem. **Figure 2-3** shows the normalized vertical displacement calculated by the closed-form solution given by Pekeris [19]. It can be seen that very large amplitude occurs near the R-wave arrival time. Therefore, R waves are easily generated in a solid by a transient point source, and more readily measured than P and S-waves due to the large amplitude. In addition to the large amplitude, R-waves have other advantages over P- and S-waves. For waves generated by a point source, R-waves attenuate with distance on the order of $r^{-1/2}$ along the free surface, while P- and S-waves attenuate on the order of r^{-2}. **Figure 2-4** illustrates the particle motion of Rayleigh waves in comparison to P- and S-waves. At the distance of 2.5
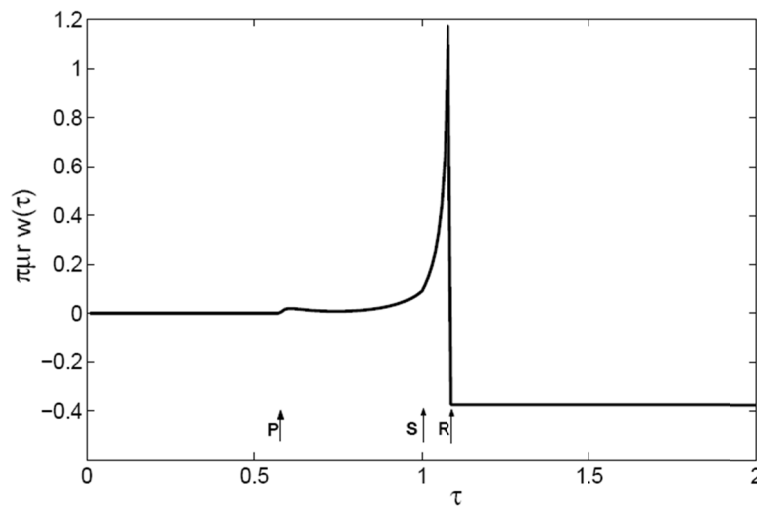
Figure 2-3: Vertical displacement at the free surface of an elastic half space resulting from a unit step load at a point. Arrival of P-,S-and R- waves are denoted (after Pekeris [19]).

12
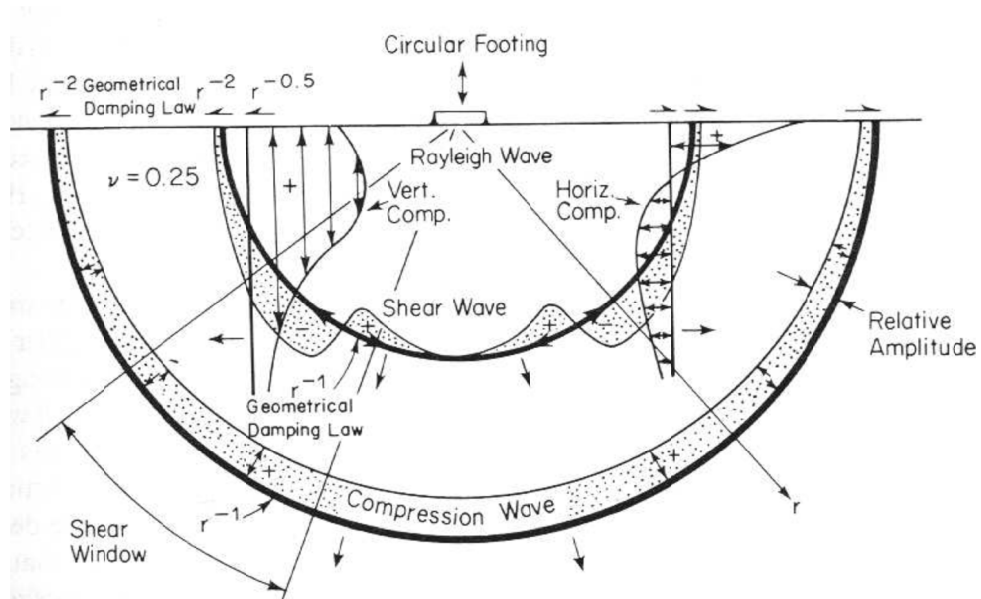
Figure 2-4: Distribution of stress waves from a point source on a homogeneous, isotropic, elastic half-space. The particle motion is visualized at a distance of approximately 2.5 wavelengths from the source. The different wave types are drawn in proportion to the velocity of each wave, from Richart et al. [20].

wavelength from the source, approximately 67% of the induced energy from point source on a homogenous half-space propagates as Rayleigh waves [20]. Thus, R-waves can be detected even at large distance. Unlike P-waves, which are dominated by in-plane motions, R-waves result in large amplitude out-of-plane motions, which is usually the quantity being measured at the free surface.

2.4 INTERACTION OF SURFACE WAVES WITH A SURFACE-BREAKING CRACK

2.4.1 Overview

Scattering of surface waves caused by a surface-breaking crack (or slot) has been extensively studied through experimental studies and numerical simulation since the late 1970's. Kino [21], Auld [22] and Achenbach *et al*. [23] developed approximate scattering theories to evaluate the surface-breaking or near surface defects. Tien *et al*. [24] investigated the near-field scattering of surface waves from a surface-breaking crack based on the approximate scattering theory developed by Kino [21], and measured reflection coefficients of incident surface waves to explore behavior of fracture crack extension in ceramics. Jungerman *et al*. [25] explored reflection of surface waves using a pulsed acoustic laser probe to characterize surface defects in an aluminum sample. Cooper *et al.* [26, 27] experimentally investigated surface waves interacting with a surface-breaking crack using non-contact sensors (Laser). Achenbach and his colleagues [28-30] obtained analytic solutions for scattering field of surface waves interacting with a single surface-breaking crack. Based on the scattering theory, reflection and transmission coefficients of surface waves in the far-field of a crack were presented in terms of the normalized crack depth (h/λ, crack depth normalized by wavelength of surface waves). Hirao *et al*. [31] investigated scattering of surface waves by a surface-breaking crack through numerical simulations (finite element method) and experimental measurements in a wide frequency range (h/λ= 0~3.0). Yew *et al*. [32] measured transmission coefficients of surface waves across a surface-breaking crack through experimental studies. They pointed out difficulties to interpret the signal data measured in near-field of a crack. Masserey and Mazza [33] observed oscillations in reflection and transmission coefficients of surface waves across a surface-breaking crack measured in near-field of the crack. Jian *et al*. [34] discussed a mechanism of signal enhancements in the near-field

14

of a crack, and oscillation in surface wave reflection and transmission coefficients by means of multiple reflected and transmitted waves at the crack.

2.4.2   Near-field scattering of surface waves by a surface-breaking crack

A single surface-breaking crack normal to the free surface causes scattering of surface waves at the crack, and attenuates incident surface waves by diffraction, reflection, transmission, and mode conversion [31]. Jian *et al*. [34] showed near-field scattering of surface wave interacting with a surface-breaking crack using numerical simulation (FEM). **Figure 2-5** shows calculated B-scan images representing in plane (a) and out-of plane (b) displacements of scattered surface wave at a 11.8 mm deep surface breaking crack in an aluminum specimen. Velocity of P-, S- and surface waves (C_P, C_S, and C_R) in the aluminum is 6300, 3100, and 2900 m/s, respectively. The center frequency of incident surface waves is around 500 kHz. Consequently, h/λ covered in the study was approximately 2 *(~11.8 mm/5.8 mm)*. Propagation paths of dominant waves are summarized in Appendix A. A surface wave interacting with a surface-breaking crack provides valuable information about the depth of the crack.
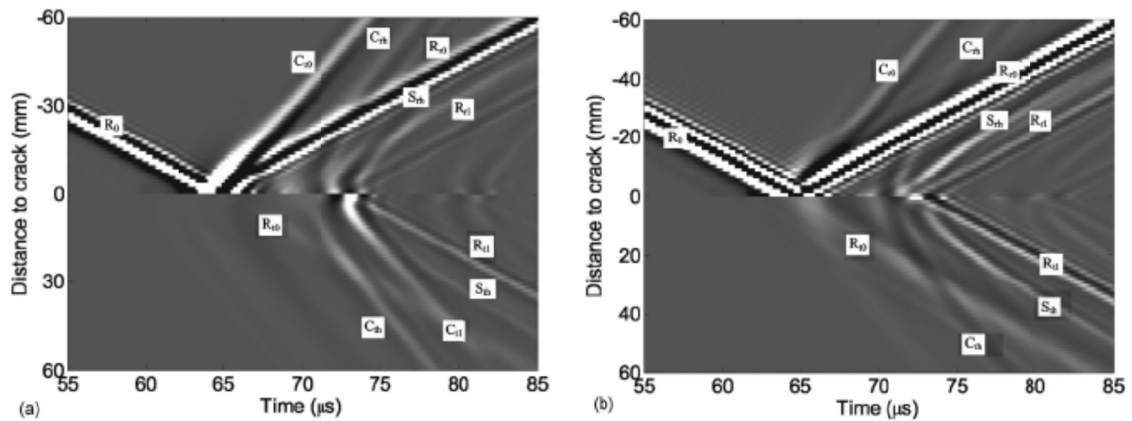
Figure 2-5: B-scan images of in-plane (a) and out-of-plane (b) displacement of surface waves interacting with a surface-breaking crack of depth 11.8mm.(after Jian et al. [34]).

15

2.5   NDT METHODS FOR CRACK DEPTH ESTIMATION IN CONCRETE

Based on the scattering theory, previous researchers have developed several NDT methods to estimate the depth of surface-breaking crack in solid medium. The currently available NDT methods are divided into two categories according to the principle of the methods: the time-of-flight (TOF) and surface wave transmission (SWT) method.

2.5.1   The TOF method

Cooke [35] suggested an analytical method in the time domain to estimate the depth of surface-breaking cracks by monitoring the time of flight from the source to the receiver (time-of-flight method, TOF). Any intervening crack lengthened the path because the surface waves have to travel down the crack face and up the other side. Morgan [36] attempted to relate time-dependent features, occurring in the reflected pulse, to the corner discontinuities at the top and the bottom of a slot. However, the limited frequency bandwidth of the surface-wave wedge transducer was not effective to generate short pulse for separating out the expected echoes from a slot in aluminum. Cooper *et al.* [26, 27] investigated acoustic pulse interactions with a machined slot in aluminum using lasers, by which short-duration surface waves (70 ps to 40 ps) could be generated. They demonstrated that the time difference between directly reflected surface waves (R_r) and the mode-converted waves S_{rh} (see **Figure 2-6** and Appendix A) is related to the depth of a surface-breaking crack as follows,

$$\Delta t = \frac{h}{C_R} + \frac{h}{C_S \cos\theta_c} + \frac{h\tan\theta_c}{C_R} \qquad \text{Equation 2-1}$$

where θ_c is the critical angle in which the backscattered components of shear waves are mode-converted into surface waves S_{rh} at the surface of solid medium. According to Jian et al.[37], $\tan\theta_c$ converges to C_s/C_P.

16
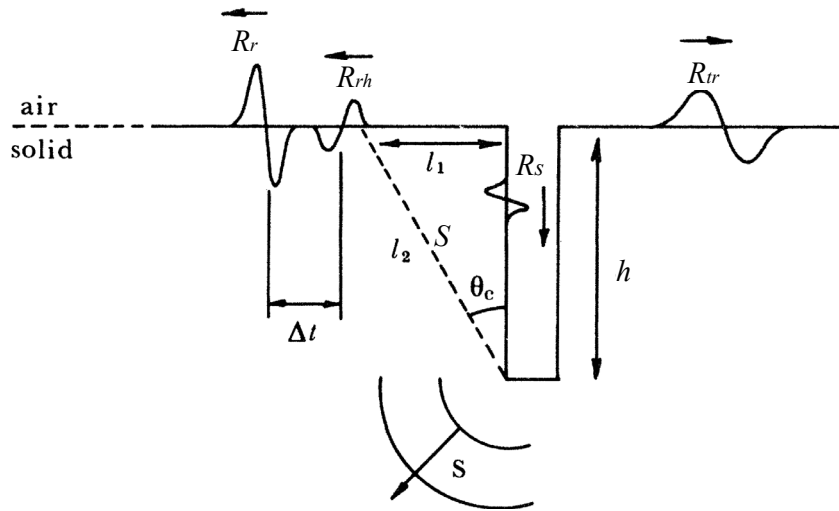
Figure 2-6: Physical processes involved when an incident Rayleigh pulse interacts with a slot to produce reflected and transmitted surface pulses (after cooper et al. [27]).

In addition, Jian et al. [37] estimated the depth of a slot in an aluminum bar through measuring arrival time of R_{tl} (see **Figure 2-7**). If C_R is known, the depth of slot can be expressed as follows,

$$h = 2\left[\frac{t_{R_{tl}}}{C_R} - (l + x_2)\right].$$

Equation 2-2
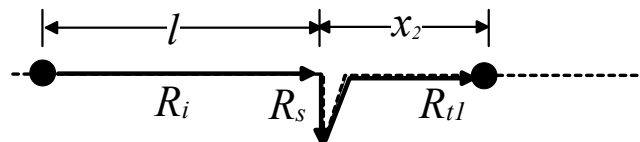
Figure 2-7: Schematic explanation of surface wave propagation (after Jian et al.[37].)

However, it is difficult to directly apply the TOF method developed for metals to heterogeneous concrete material due to high attenuation of ultrasonic waves in concrete. In addition, the TOF method is not effective when the wavelength of incident surface

17

waves becomes larger than the crack depth because the waves no longer travel along the crack boundaries but pass under the crack.

For concrete, Sansalone *et al*. [4] demonstrated that a time-of-flight diffraction (TOFD) method using impact-induced P waves is effective to determine the depth of a surface-breaking crack. An impact on concrete surface generates P wave with spherical wave front (**Figure 2-8** (a)). When the P waves attain to a surface-breaking crack, portions of the P waves are reflected by the crack face, and diffracted from the crack tip. The diffracted P waves propagate to the opposite side of the crack. In the TOFD method, two sensors are located at the either side of a surface-breaking crack as shown in **Figure 2-9** (a) [2-4]. Transient waves can be generated by an impact source from one side of the crack, and received by a sensor on the opposite side of the crack. The depth can be calculated from the measured travel times of ultrasonic waves (see **Figure 2-9** (b)) using equation as follows,

$$d = \sqrt{\left[\frac{(C_p \times \Delta t)^2 + H_1^2 - H_2^2}{2 \times C_p \times \Delta t} \right]^2 - H_1^2} \qquad \text{Equation 2-3}$$

where H_1 is the distance between the impact position and the crack; and H_2 is the distance between the crack and the receiver. When H_1 and H_2 are equal to H, the equation simplifies to:

$$d = \sqrt{\left(\frac{C_p \times \Delta t}{2} \right)^2 - H^2} \qquad \text{Equation 2-4}$$

The accuracy of the TOFD results depends on determination of arrival time of the diffracted waves, and valid assumption of crack geometry. However, the TOFD method may not always provide reasonable crack depth estimation in the field application [6]. Infiltration of dust/water in the cracks, and shape of crack tips may affect accurate arrival time determination of diffracted waves [5].

18
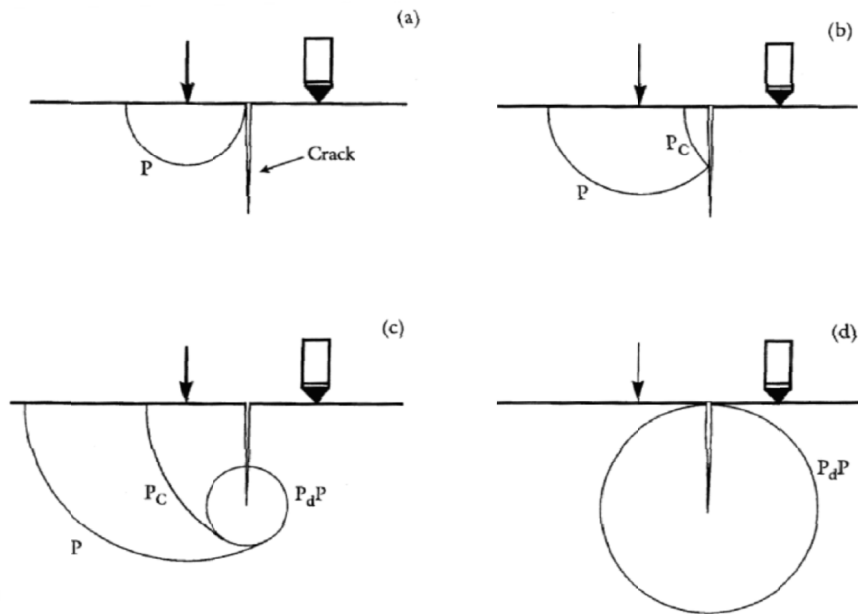
Figure 2-8: Schematic illustrations of the propagation of impact generating stress waves: (a) P-wave generated by impact; (b) P-wave being reflected from edge of crack; (c) diffracted waves generated by P-wave incident on crack tip; and (d) propagation of the diffracted P-wave. (after Sansalone et al. [4]).
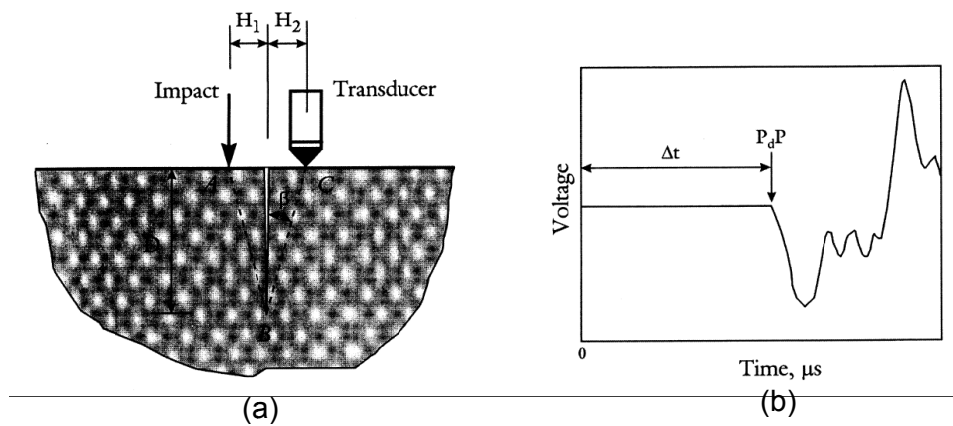
Figure 2-9: Experimental technique for determining the depth of a surface-breaking crack: (a) schematic of test configuration; and (b) recorded waveforms showing P-wave arrivals (after Sansalone et al. [4]).

19

2.5.2 The SWT method

2.5.2.1 *Principle of the SWT method*

The SWT method is based on measurement of surface wave transmissions across a surface-breaking crack in the frequency domain. In the SWT method, two sensors are located on the either side of the crack according to the self-calibrating (SC) procedure [7-9] (see **Figure 2-10**). The SC procedure is effective in reducing the experimental variability caused by inconsistent source input and receiver coupling. The transmission coefficient of surface waves is defined as spectral amplitude ratio between the transmitted surface waves (R_{tr}) and the incident surface waves (R_i) in the frequency domain. The depth of a surface-breaking crack can be estimated from the pre-established relationship between transmission coefficient and crack depth.
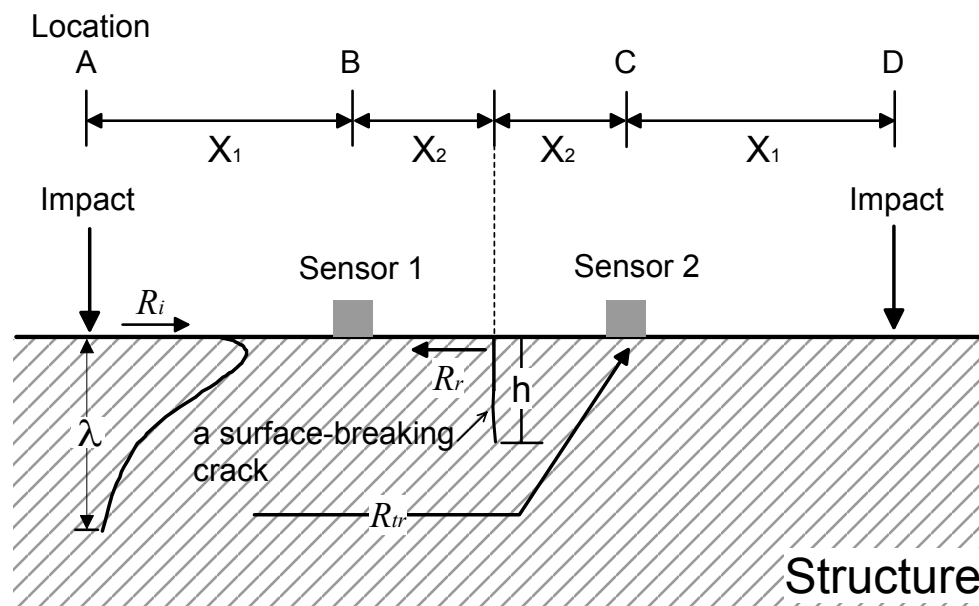
Figure 2-10: Wave path of surface waves interacting with a surface-breaking crack and test setup for the SWT method using the self-calibrating procedure.

20

2.5.2.2 *Transmission function*

Previous researchers demonstrated that the transmission coefficient of surface waves is a good indicator of estimating the depth of a surface-breaking crack in solid materials. **Figure 2-11** (a) is a plot representing the surface wave transmission coefficient in function of the normalized crack depth (h/λ: crack depth normalized by wavelength of surface waves) according to available data sets collected from previous studies. Achenbach and his colleagues [28-30] obtained the analytic solution of the scattering field of surface waves caused by a surface-breaking crack. Hirao *et al.*[31] presented transmission coefficients in a wide range of h/λ ($h/\lambda \in [0, 3]$) based on finite element numerical simulations (FEM) and experimental measurements. Yew *et al.* [32] verified the transmission function given by Achenbach and his colleagues through experimental measurements from aluminum specimens. Cheng and Achenbach [38] also demonstrated that transmission coefficients measured in far-field of a crack ($x_2 \sim 5\lambda$) converge
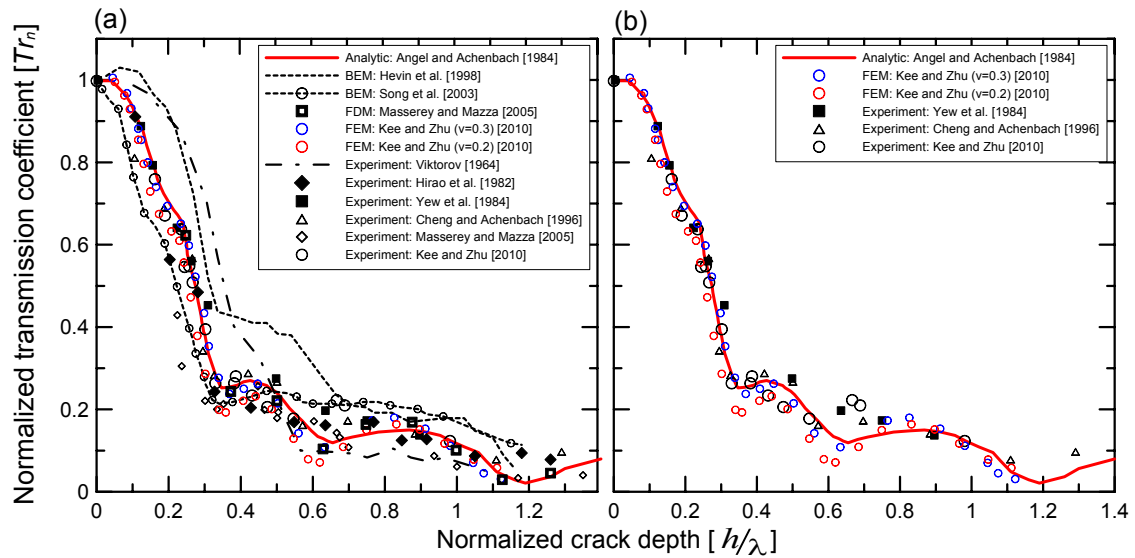
Figure 2-11: Normalized transmission coefficient versus normalized crack depth: (a) from available data in previous studies (b) from the data in approximate far-field region.

21

to the analytical solution [28-30] (see **Figure 2-11** (b)). Masserey and Mazza [33] obtained transmission functions through numerical simulations (finite difference method) and experimental studies from aluminum specimens. For concrete, a heterogeneous material, the SWT method has been proven sensitive to the depth of surface-breaking cracks [7, 8, 39-41]. Hevin *et al*. [39] obtained the transmission ratio of a surface wave in the frequency domain using boundary element method (BEM), and calculated averaged transmission functions from many different sensor locations. Song *et al.* [8] obtained the *Tr* and *h/λ* relation based on numerical simulations (BEM) and experimental studies in laboratory. Shin *et al*. [41] proposed the spectral wave-energy transmission method in crack-depth estimation problem for concrete. Kim *et al*. [42] proposed a self-calibrating frequency response function to improve isolating the surface wave components from the accompanying noise. Chai *et al*. [43] studied the feasibility of impact-generated Rayleigh waves for measuring deep surface-breaking cracks in concrete structures.

2.5.2.3   *Near-field effects*

All curves in **Figure 2-11** (a) show similar trends that *Tr* decreases with increasing *h/λ*. However, differences between these curves are also obvious. Previous researchers [34, 40, 44, 45] noticed that near-field scattering effects (signal enhancement and oscillation in transmission coefficients) significantly affect transmission measurements when sensors are located too close to the crack. The signal enhancement is mainly due to interference effect of bulk waves (i.e., mode converted P- and S-waves in front of a surface-breaking crack, and bulk waves generated from a crack tip) and direct contribution of incident surface waves.

On the other hand, **Figure 2-11** (b) shows that the transmission function based on approximate far-field measurements tends to converge to the analytical solution [28-30]. Yew *et al.* [32] suggested that the distance of sensors from the crack should be comparable to, or larger than *h* to minimize the near-field effect. Cheng and Achenbach

[38] observed that *Tr* converged to the far field analytical solution when sensors were located 5λ from the crack opening.

2.5.2.4   *The self-calibration procedure*

The surface wave transmission coefficient across a surface-breaking crack can be measured by using the self-calibrating procedure (see the setup in **Figure 2-10**). Previous researchers [7-9] have demonstrated that the self-calibrating procedure is effective in reducing experimental variability caused by inconsistent source input and sensor coupling in surface wave measurements. The surface wave transmission ratios were measured from two opposite directions, and processed in the frequency domain. The transmission between B and C (see **Figure 2-10**) is defined as

$$\left|\mathbf{Tr_{BC}}(f)\right| = \left|\sqrt{\frac{\mathbf{S_{AC}S_{DB}}}{\mathbf{S_{AB}S_{DC}}}}\right|,$$ Equation 2-5

where $\mathbf{Tr_{BC}}$ is the transmission coefficient of surface waves propagating across the wave path BC, and $\mathbf{S}_{ij}$ is the Fourier transform of the time-domain signal generated by an impact source located at i and measured by a sensor located at j. Further, $\mathbf{Tr_{BC}}$ is normalized by $\mathbf{Tr_{BC,0}}$ from a crack free region to eliminate effects caused by geometric attenuation and material damping as follows:

$$\mathbf{Tr_n} = \mathbf{Tr_{BC}} / \mathbf{Tr_{BC,0}}.$$ Equation 2-6

2.5.3   Limitations of the SWT method

However there are still challenges when applying the SWT method to concrete structures, which are discussed as follows.

- ***Near-scattering of surface waves by a surface-breaking crack***: One challenge is related to near-field scattering of surface waves due to a surface-breaking crack. Prior research on near-field scattering has focused on the case where crack depth

23

h is greater than wavelength λ of surface waves (i.e., $h/\lambda > 1$). Near-field scattering of surface waves has still not been completely understood in the frequency range of the *SWT* method (i.e., $0 \le h/\lambda \le 1/3$), where transmission coefficients monotonically decrease with increasing h/λ.

- ***Effects of distributed surface-breaking cracks***: There has been very few studies for more realistic problems involving near scattering of surface waves by distributed surface-breaking cracks. One possible reason is complexity caused by the interaction of surface waves between multiple cracks. In this study, the author provides a preliminary results on effects of distributed surface-breaking crack on transmission coefficient of surface waves through numerical simulations and experimental studies using Plexiglas specimens.

- ***Interference of surface waves and higher-order Lamb waves in a free plate***: The SWT method was originally proposed for the half-space (or very thick solid medium compared to the wavelength of incident surface waves). In fact, it is difficult to directly apply the theory to plate-like structures with a finite thickness due to contribution of higher-order Lamb waves. The higher-order Lamb waves are consequences of constructive and destructive interference of coupled P and S waves guided in a plate with finite thickness [46]. According to Lamb wave theories, possible higher order Lamb modes and their excitability are functions of frequency and thickness of the plate [17, 47]. In this dissertation, appropriate source-sensor arrangements and frequency-thickness ranges are proposed to minimize contribution of multiple Lamb wave modes for calculation of the transmission coefficients.

24

- *Effects of crack width, and external loading on transmission measurement of surface waves in concrete*: Most results were obtained using a well-defined crack (or notch) in laboratory. In facts, there is a critical gap to apply the theory to surface-breaking cracks in concrete structures subjected to external loadings where the cracks are generally ill-defined, and partially closed. To apply the theory to real problem, effects of internal stresses on acoustic parameters of surface waves should be investigated.

- *Inconsistent coupling problem of conventional contact sensors:* Inconsistent coupling condition of conventional contact sensors (e.g., accelerometers) prevent obtaining reliable, consistent, and rapid transmission measurements. Temporary sensor mounting methods, such as wax, adhesive and magnetic mounts, will induce a low resonant frequency, which significantly affect experimental measurements if center frequency of input signal is close to resonance frequency of sensors. On the other hand, permanent mounting cannot meet the requirement of rapid NDT test. In addition, rough surface on concrete in field structures make it difficult to obtain good coupling between contact sensors and concrete. As a solution of this problem, using non-contact air-coupled sensor is proposed in this dissertation.

- *Lack of a repeatable wave source*: A steel ball or hammer is usually used as an impact source to generate incident stress waves in concrete structures. However, these human-controlled methods cannot generate consistent inputs, nor be used to inaccessible areas in structures. Therefore, developing a computer-controlled source is needed to improve consistency, accuracy, and test speeds in surface wave measurement. In this dissertation, the author proposes to use piezoelectric sensors as a cost-effective and repeatable impact source.

- ***Lack of available data measured from in-situ concrete structures***: Care is needed to apply the SWT method to in-situ concrete structures. Particularly, unevenly distributed cracks with high density may increase near-field effects [34, 45], and interaction of surface waves between multiple surface-breaking cracks [48]. Validity of the simplified SWT method for in-situ concrete structures will be discussed in more detail in this study. The air-coupled SWT method will be used for rapid acoustic scanning of large concrete structures. 2D image technique is developed to efficiently show the results from large test areas.

2.6   SUMMARY

This chapter provided fundamental background of the SWT method, and air-coupled sensing techniques in civil engineering. First, properties of surface waves were summarized, and then, available NDT techniques for estimating the depth of a surface-breaking crack were briefly described. Based on the literature review, limitations of the current SWT methods for concrete materials are summarized as follows:

- *Near-scattering of surface waves interacting with a surface-breaking cracks*
- *Effects of distributed surface-breaking cracks*
- *Interference of surface waves and higher-order Lamb waves in a free plate*
- *Effects of crack widths, and external loadings on transmission measurement of surface waves in concrete*
- *Inconsistent coupling problem of conventional contact sensors*
- *Lack of a repeatable impact source for concrete*
- *Lack of available data measured from in-situ concrete structures*

PART II THEORETICAL STUDIES

Chapter 3   Near-Field Effect of Sensors

Near-field wave scattering caused by a crack affects the reliability and consistency of surface wave transmission measurements. Prior studies on near-field scattering have focused on the case where crack depth h is greater than wavelength λ of surface waves (i.e., h/λ >1). Near-field scattering of surface waves remains not completely understood in the range of h/λ for the SWT method (i.e., 0 ≤h/λ≤1/3), where the transmission coefficient is sensitive to crack depth change and monotonically decreases with increasing h/λ. In this chapter, near-field scattering of surface waves caused by a surface-breaking crack is investigated using experimental tests and numerical simulations for 0 ≤h/λ≤1/3.

3.1   INTRODUCTION

Using nondestructive evaluation (*NDE*) methods to estimate the depth of a surface-breaking crack (SWT method) has been extensively investigated by many researchers in recent decades. Previous researches on the SWT method are summarized in Chapter 2. **Figure 3-1** shows transmission functions (i.e., surface wave transmission coefficient versus normalized crack depth curves) developed by previous researchers. Although these curves show similar trends that *Tr* decreases with increasing *h/λ*, the differences between the curves are also obvious. In this chapter, the author attempts to explain discrepancies between these transmission functions given by the previous researchers, and improve accuracy of crack-depth estimation using the SWT method.

One reason for the discrepancies is related to the near-scattering effects of surface waves by interaction with a surface-breaking crack (near-field effects of sensors: hereafter referred to as 'near-field effect'). Note that 'near-field effect' in this study means near-field effect of sensors. Near-field scattering caused by the interaction between surface waves and a surface-breaking crack has been investigated by many researchers

28

[34, 44, 45]. Prior studies [34, 44, 45] on the near-field effect have focused on deep cracks where the depth of crack h is greater than wavelength λ of surface waves (i.e., h/λ >1). For the crack depth range used in the SWT method, i.e., $0 < h/\lambda < 1/3$, where the transmission coefficient monotonically decreases with increasing h/λ, the near-field scattering of surface waves remains not fully understood. Yew et al. [32] suggested that the location of sensors should be comparable to, or larger than the crack depth to minimize the near-field effect. However, this finding was only based on empirical observation and narrow range of h/λ. Cheng and Achenbach [38] observed that Tr converged to the far field analytic solution when sensors were located 5λ from the crack opening. Nevertheless, in field testing, the criteria of 5λ are not always satisfied due to size limitation of structures.
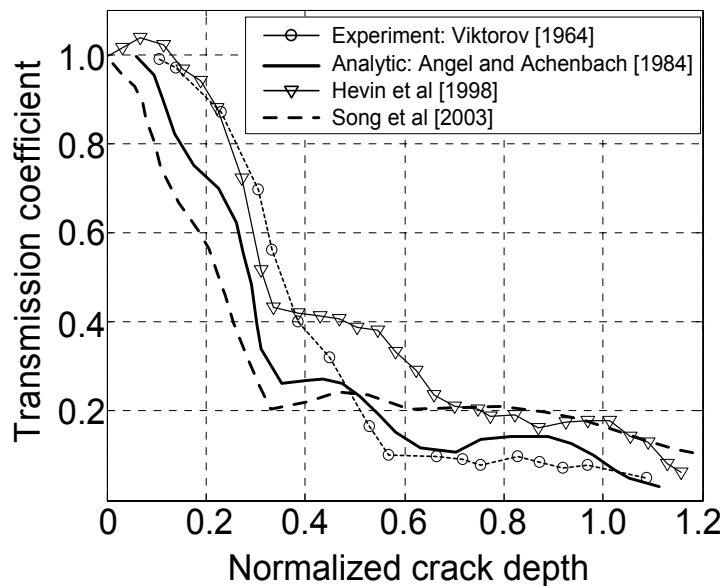
Figure 3-1: Transmission coefficient versus normalized crack depth from literature review.

In this chapter, the near field scattering of surface waves caused by a surface-breaking crack is thoroughly investigated for the crack depth range of $0 < h/\lambda < 1/3$. First, effects of sensor locations on surface wave transmission coefficients across a surface-

breaking crack are studied experimentally. Data are collected from Plexiglas and concrete specimens using air-coupled sensors to improve accuracy and test speed. As a result, the variation of transmission coefficients is expressed in terms of the normalized crack depth (h/λ) as well as the normalized sensor location (x/λ). The validity of finite element models is also verified by comparing experimental results with numerical simulations. Second, a series of parametric studies are performed using the verified finite element model to obtain complete understanding of near field scattering of surface waves in various solid materials with different mechanical properties and geometric conditions. Finally, a guideline for selecting appropriate sensor arrangements to obtain the reliable crack depth using the SWT method is suggested.

3.2   NUMERICAL SIMULATION

3.2.1   Model description

Commercial finite element analysis software (*ABAQUS Standard v 6.7.1, 2007,*[49]*)* was used to simulate the transient behavior in solids. Although the specimens are better simulated using 3D models, 2D models were developed with material properties corresponding to Plexiglas and concrete to save computing time. **Table 3-1** lists material properties and model parameters for 12 models. The 12 models include 11 FEM models with the crack depth varying from 0 to 100 mm, and a small domain 3D model developed to check the validity of 2D models. A comparison between 2D and 3D models are presented in section 3.4.3.

Finite element (FE) models studied in this chapter are summarized in **Table 3-1**. **Figure 3-2** (a), and (b) shows a finite element model for Plexiglas and concrete specimens. Plexiglas specimens were modeled using rectangular plane stress element

Table 3-1: Finite element models and parameters

Model No.	v	E [GPa]	ρ [kg/m^3]	T [μs]	Element type	h [mm]
Model 1	0.22	33.6	2400	40	4AX[(i)]	
Model 2	0.22	33.6	2400	60	4AX	
Model 3	0.22	33.6	2400	80	4AX	
Model 4	0.22	33.6	2400	100	4AX	0, 10,20, 30,40,50,60,70,8 0,90,100
Model 5	0.22	33.6	2400	120	4AX	
Model 6	0.22	33.6	2400	140	4AX	
Model 7	0.33	33.6	2400	60	4AX	
Model 8	0.22	33.6	2400	60	4PS[(ii)]	
Model 9	0.33	5.8	1200	60	4AX	
Model 10	0.33	5.8	1200	60	4PS	
Model 11	0.22	33.6	2400	60	4PE[(iii)]	
Model 12	0.33	5.8	1200	60	C3D8[(iv)]	0, 20

Note: 4AX[(i)]: 4-node Axi-Symmetric element; 4PS[(ii)]: 4-node Plane Stress element; 4PE[(iii)]:4-node Plane Stain element, and C3D8[(iv)]: 8-node 3D element.

(CPS4) (FE model 10); whereas for concrete specimens, four-node axisymmetric element (CAX4) was used (FE models 1~6). Infinite (energy absorbing) boundaries were placed at the outer edge to simulate a solid half space. Material properties were assumed homogeneous and linear-elastic. This assumption is valid and reasonable for Plexiglas and concrete specimens within the frequency range in this study, (center frequency f_c ~13kHz). The material properties of the Plexiglas were selected as Young's modulus E of 5800 MPa, Poisson's ratio v of 0.33, and mass density ρ of 1200 kg/m^3. The corresponding velocities of P-, S-, and surface waves were 2328, 1347, and 1240 m/s, respectively. In contrast, the material properties of concrete are Young's modulus of 33630 MPa, Poisson's ratio of 0.22, and mass density of 2400 kg/m^3. The corresponding velocities of P-, S-, and surface waves in concrete models are 4050, 2420, and 2215 m/s, respectively. These material properties were chosen to simulate normal concrete. In

31
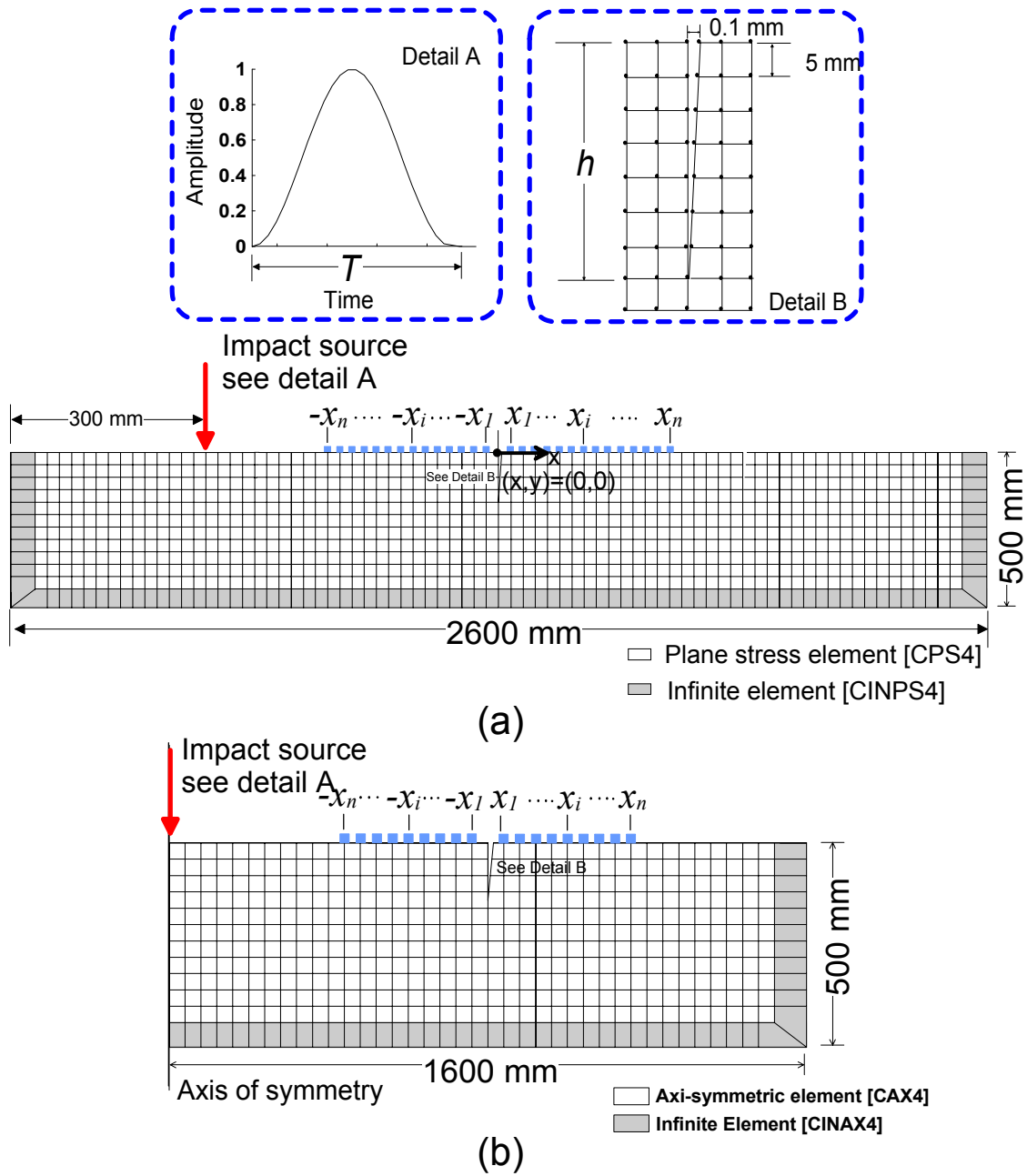
Figure 3-2: A finite element model used for numerical simulations of Plexiglas (a) and concrete (b) models.

addition, FE models 7, 9, 10, 11, and 12 were used to investigate effects of Poisson's ratios and element types. Details are shown in section 3.4.3.

Mesh size of model l_e and time increment Δt_{fem} during numerical integration procedure were carefully determined to obtain the accurate response calculation [50]. The mesh size was designed as 5 mm so that at least 10 elements could participate to express the minimum wavelength λ_{min} [51]. In addition, the time increment Δt_{fem} for integration was determined as 1 μs which is small enough to prevent a propagation of disturbance through a grid size during one time step.

For the FE models of using plane stress and plane strain elements, an impact source was applied on the free surface at the location of x=-1000 (see **Figure 3-2** (a)). Transient impact point source was applied on the free-surface of half-space at the axis of symmetry (i.e., r=0) (see **Figure 3-2** (b)). The force function of the transient impact source is as follows:

$$f(t) = \sin^2(\pi t / T), \qquad 0 \leq t \leq T,$$
$$= 0, \qquad T < t.$$

Equation 3-1

where T is the duration of impact. Note that the quadratic force function in

Equation 3-1 was verified effective to simulate the transient contact forces by previous researcher [52]. The quadratic force function generates vertical displacement and velocity of surface waves with C^1, and C^0 continuity, respectively; thus, Gibbs phenomenon (i.e., spurious oscillation due to discontinuity) does not interfere with response of vertical displacement and velocity calculated from FEM analysis [52]. To study the near field effect caused by the crack tip scattering, various sensor locations on the surface of the concrete are investigated.

3.2.2   Near-field scattering of surface waves

3.2.2.1   B-scan images of near-scattering fields

Near-field scattering of surface waves caused by a surface-breaking crack in Plexiglas and concrete was investigated through numerical simulations (FEM) in this section. To eliminate the effect of geometric attenuation, the surface response in the near-scattering field of the crack was normalized by the corresponding response in a crack-free model as follows:

$$V_{hn}(x/\lambda, t) = \frac{V_h(x/\lambda, t)}{V_0(x/\lambda, t)},$$ Equation 3-2

where $V_h(x/\lambda, t)$ is the out of plane component of the surface velocity response in the near-scattering field of the crack with depth h, x/λ is the normalized sensor location from the crack opening (i.e., the distance of sensors from a crack opening x normalized by the wavelength of surface waves λ), and t is time. $V_0(x/\lambda, t)$ is the surface velocity response from a crack-free model.

Figure 3-3 (a) and (b) show B-scan images representing surface velocity from FE model 2, which represents two concrete models with a surface-breaking crack with depths of 20 mm ($h/\lambda\sim0.15$), and 100mm ($h/\lambda\sim0.76$), respectively. Consistent with observations from previous researchers [34, 40], mode converted waves (R_i-R_s-P) as well as transmitted-, and reflected surface waves (R_i-R_t, and R_i-R_r) are clearly observed in the near-scattering field of surface waves, where R_i, R_t, R_r, and R_s are incident, transmitted, reflected surface waves, and surface skimming waves [34].

In addition, **Figure 3-4** shows B-scan images representing surface velocity from FE models 1, 3, and 5 in **Table 3-1**. To investigate the effects of the crack depth and frequency contents of the incident surface waves on a near-scattering field, velocity responses were obtained from the numerical models with crack depth h =10 and 70 *mm*
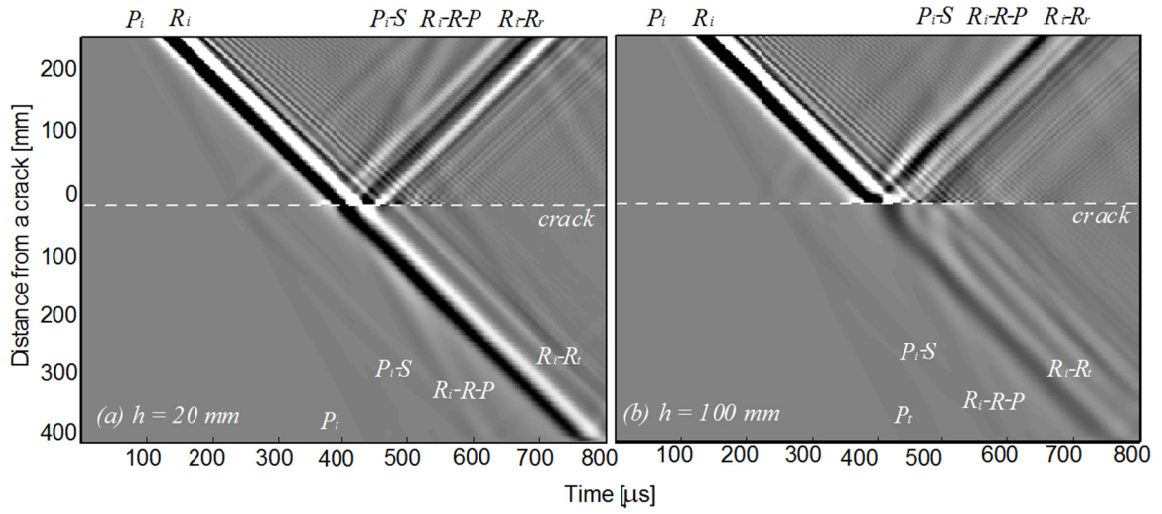
Figure 3-3: B-scan image of near-scattering field of surface waves caused by a surface-breaking crack in FE model 2: (a) h=20 mm (h/λ~0.15), (b) h=100 mm (h/λ~0.76). Note locations of a crack were denoted as dash lines.

and impact duration time T=40, 80 and 120 μs, respectively. Consequently, six B-scan images corresponding to h/λ of 0.12, 0.81, 0.06, 0.41, 0.04 and 0.27 were obtained and are presented in **Figure 3-4**.

When h is much smaller than λ, e.g., h/λ=0.12 in **Figure 3-4** (a), the dominant wave components are the reflected surface waves (R_r), and the transmitted surface waves (R_t) after the incident waves (R_i) interact with the crack. The low frequency components of the surface waves can transmit through the crack; while most of high frequency components are reflected back by the crack. On the other hand, when h/λ ~1.0 (deep crack), most portions of the R_i are reflected by the crack, as shown in **Figure 3-4** (b).

In **Figure 3-4** (a), and (b), the mode-converted P-waves with a velocity of approximately 4000m/s (P_r) are observed along with R_r. However, when the impact duration T increases to 80 and 120 μs, as shown in **Figure 3-4** (c)~(f), the mode-converted bulk waves are not distinguishable from surface waves. In addition, R_r waves
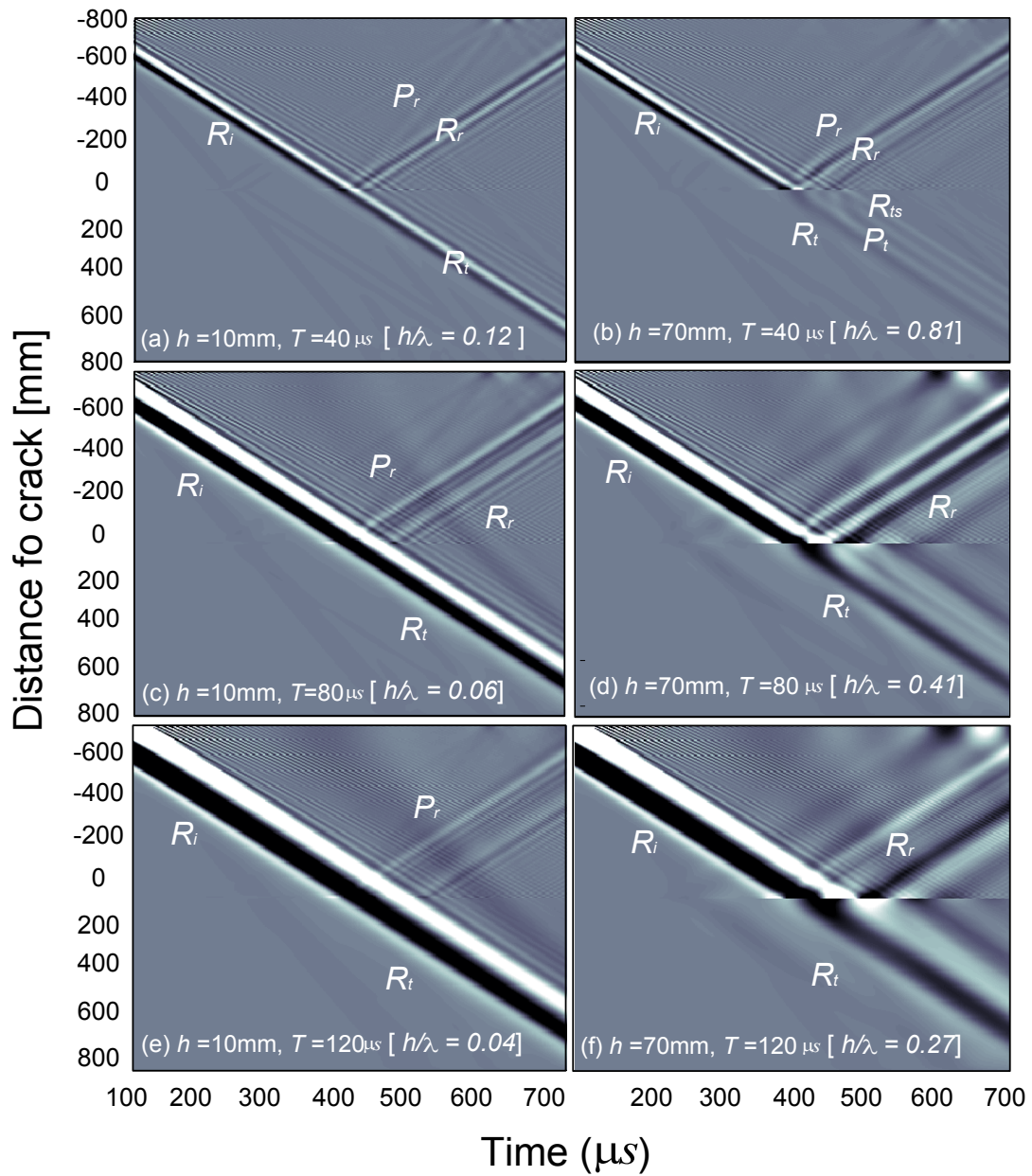
Figure 3-4: B-scan images of wave propagating on solid models with various h/λ: (a) 0.12, (b) 0.81, (c) 0.06, (d) 0.41, (e) 0.04 and (e) 0.27. (a)-(f) represent six models with two crack depths h=10 mm [(a),(c), and (e)], and 70 mm [(b), (d), and (f)], and three source duration times T=40 μs [(a), and (b)], 80 μs [(c), and (d)], and 120 μs [(e), and (f)].

interferes with the incident surface waves in the near region of the crack, as shown in **Figure 3-4** (a) and (b). In addition to the reflected and transmitted surface waves, secondary waves, which include bulk waves: P_{ts}, P_{rs}, S_{ts} and S_{rs} and surface-skimming waves: R_{ts} and R_{rs} are generated by crack tip scattering.

3.2.2.2 *Amplitude in near field*

To obtain more complete and quantitative properties of the near-field scattering field caused by a surface-breaking crack, the **a**mp**l**ification **c**oefficient (*APC*) curve was defined. It is the peak amplitude ratio between the vertical velocity obtained on a cracked model (V_h) and that on a crack free model (V_0) as follows:

$$APC(x/\lambda) = \frac{\max(V_h(x/\lambda, t))}{\max(V_o(x/\lambda, t))} \qquad \text{Equation 3-3}$$

Figure 3-5 shows amplification coefficient curves versus normalized distance x/λ from the crack opening for various crack depths obtained from the verified FE models. Analysis shows that the APC curves depend on the distance from the crack x, the crack depth h and wavelength λ. When $h/\lambda \leq 1/3$, *APC* curves are continuous in the vicinity of the crack. In the backward scattering field, *APC* curves show very small oscillation (1%) when $x/\lambda \leq 0.2$. In the forward scattering field, *APC* curves decrease sharply from the upper peak at the location of the crack and then gradually reach an asymptote with increasing x/λ. This value is the surface wave transmission coefficient in the far-field. Signal enhancement and oscillations in near-scattering field can be explained from two aspects: *(i) particles around a crack are easier to move than the solid region without a crack because of lower stiffness around a surface-breaking crack; and (ii) interaction between direct surface waves, and mode converted bulk waves and secondary surface waves results in constructive and destructive interference in near-field* [34, 40].
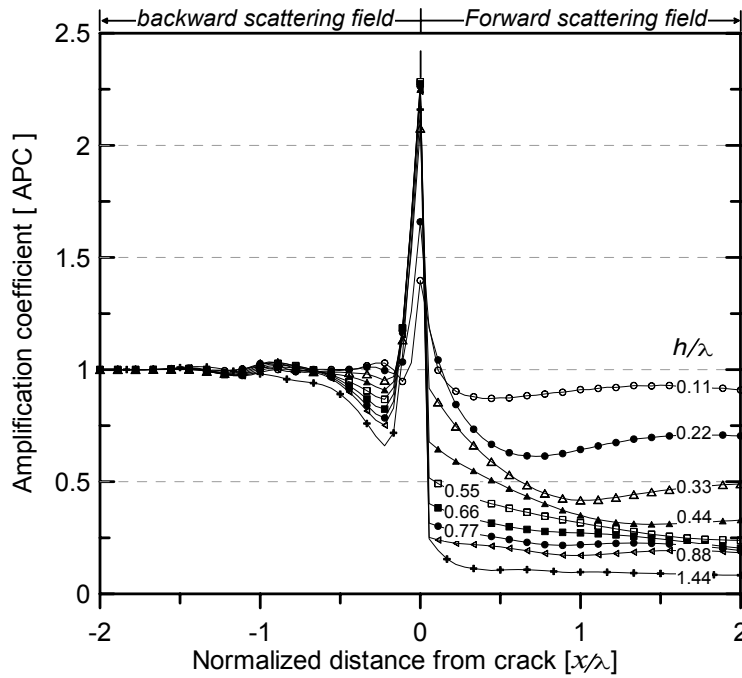
Figure 3-5: Amplification coefficient varies with the normalized distance from crack (x/λ) for different h/λ.

Based on the results shown in **Figure 3-5**, in the range of $h/\lambda = 0\sim1/3$, the near field size can be approximately expressed as

$$a_n / \lambda = 1.8 h / \lambda + 0.1 \qquad for \quad h / \lambda \leq 1/3, \qquad \text{Equation 3-4}$$

where a_n is the near field size measured from the crack opening.

To reduce the effects of crack tip scattering, surface wave transmission should be measured in the far-field region, i.e., the sensor to crack spacing should be larger than a_n calculated from Equation 3-4.

3.3 CALCULATION OF TRANSMISSION COEFFICIENT

3.3.1 Transmission function

The surface wave transmission across a surface-breaking crack is defined as

$$\mathbf{Tr}(f,h) = \mathbf{S}_b(f,h) / \mathbf{S}_a(f,h),$$ Equation 3-5

where $\mathbf{Tr}$ is the transmission coefficient in function of frequency and crack depth, and $\mathbf{S_a}$ and $\mathbf{S_b}$ are Fourier transforms of the time domain signals measured at locations of A and B, respectively (**Figure 3-2**). The sensor locations of A and B are determined based on observation concerning near-field size in the previous section. To eliminate geometric attenuation effects, the transmission coefficient $\mathbf{Tr}(f,h)$ is normalized by the value obtained from a crack free model $\mathbf{Tr}(f,0)$.

Figure 3-6 shows the normalized transmission coefficient Tr_n versus h/λ relationship measured using sensors located at plus and minus 650 mm ($\sim 5\lambda$) from a crack mouth. The sensors are regarded as in far-field region according to Cheng and Achenbach (1996) [38]. Note that length of FE models were 2600 mm. The data in Figure 3-6 were obtained from FE models with T of 60 μs and h varying from 0 to 100 mm, and have frequency range of 10 to 25 kHz (i.e., half-band width with center frequency 17 kHz). To investigate the effect of Poisson's ratio v, transmission curves with v of 0.3, and 0.2 were calculated from FE models; and shown as lines with circles and squares in **Figure 3-6**, respectively. For comparison purposes, the analytic result given by Angel and Achenbach (1984)[30] for v of 0.3 was also illustrated using line in Figure 3-6. The transmission curve of v of 0.3 measured in far-field region shows very good agreement with the analytic curve. This can be regarded as verification of the validity of FE models considered in this study. On the other hand, the transmission coefficients for v of 0.2 are lower than those for v of 0.3; however, effects caused by Poisson's ratio on transmission functions appear insignificant compared to the other critical factors (i.e., h, x, and λ).
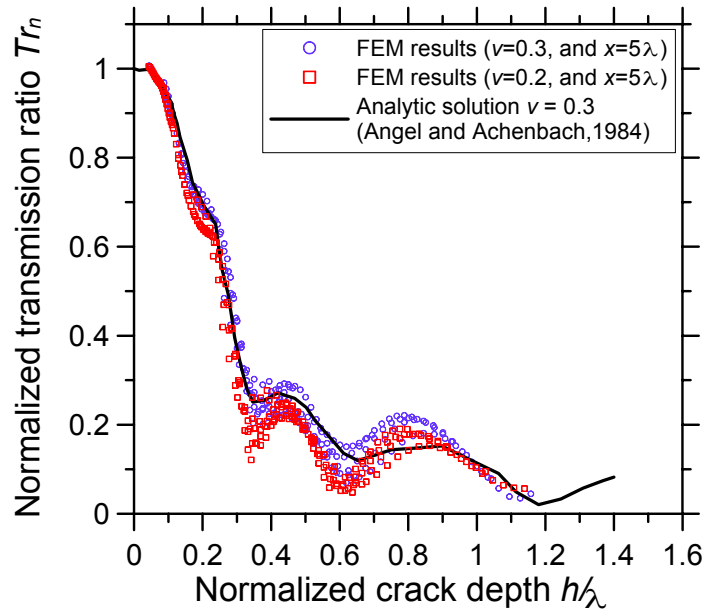
Figure 3-6: Normalized transmission coefficient versus normalized crack depth relation based on FE models and the analytic solution in far-field regions ($x=5\lambda$).
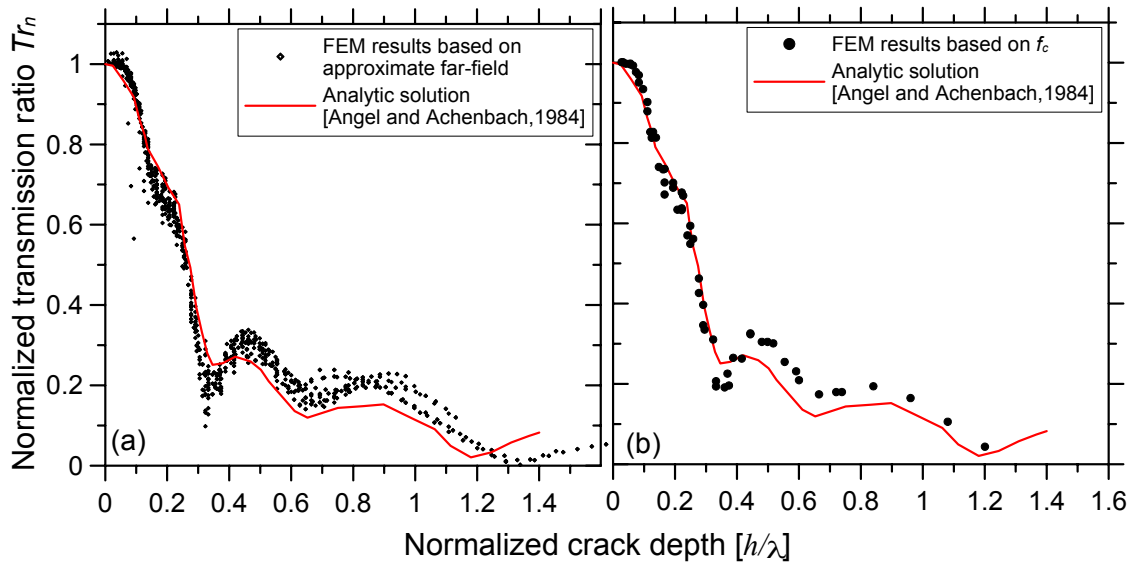
Figure 3-7: Normalized transmission coefficient versus normalized crack relation based on FE models in the approximate far-field region. The far-field analytic solution is also shown.

Figure 3-7 (a) shows the Tr_n and h/λ relationship based FE models with T varying from 40 to 140 μs and h varying from 0 to 150 mm. The sensors are located in the approximate far-field region obtained by Equation 3-4. For example, for T=60 μs and h=50mm, the sensor location x was 110mm (a_n=103.5 mm with λ=135 mm for T=60 μs). Overall the data in **Figure 3-7** (a) indicate that the FEM results match the analytic curve fairly well, especially in the range of h/λ=0 ~ 1/3. Scattering of FEM data may come from two aspects: different Poisson's ratio 0.2 versus 0.3 and near-field effects. The criterion given by Equation 3-4 is just an approximation to the true far field. Nevertheless, the data scattering has been significantly decreased when it is compared with previous research without considering near-field effects.　caused by the fact that Equation 3-4 is based on approximate near-field size [39]. The near-field effect may be a possible reason why the transmission curves obtained by other researchers Song *et al*. [8] are different from the analytic results

3.3.2   Simplified algorithm

The depth of a crack can be estimated using the inversion process of the surface wave transmission function from the established surface wave transmission curve. To accurately evaluate the depth of crack, it is important to obtain a reliable surface wave transmission measurement. Signals have the highest energy at their center frequencies. Therefore, measurements around the center frequencies should provide the most reliable results. Based on this assumption, the author proposed a simplified algorithm to calculate the surface wave transmission. Instead of calculating wave transmission for all frequencies, we calculated Tr at the center frequency only, as shown below

$$\mathbf{Tr}_n(f_c,h) = \mathbf{Tr}(f_c,h)/\mathbf{Tr}(f_c,0), \qquad\qquad \text{Equation 3-6}$$

where f_c is center frequency of input signal $\mathbf{S}_a(f, 0)$.

With the measured surface wave transmission ratio at the center frequency, h/λ can be directly found from the established Tr_n- h/λ curve. If the surface wave velocity is

known, the wavelength λ can be calculated, and then the crack depth can be determined. **Figure 3-7** (b) shows the transmission function versus h/λ based on measurements at center frequency f_c. The point source has impact duration ranging from 40 to 140 μs, and the crack depth h varies from 0 to 150 mm at intervals of 10 mm. **Figure 3-7** (b) shows good agreement between the center frequency measurement and the analytic solution, especially in the sensitive region where $h/\lambda \leq 1/3$.

3.4   EXPERIMENTAL SETUP

Near field scattering of surface waves caused by a surface-breaking crack was investigated through a series of experimental tests. The tested materials include a homogeneous material, Plexiglas, and a heterogeneous but statistically isotropic material, concrete. The surface wave transmission functions were obtained using a pair of air-coupled sensors in conjunction with a modified self-calibrating procedure to improve signal consistency and test efficiency.

3.4.1   Preparation of test specimens

A Plexiglas (Poly methyl methacrylate, PMMA) specimen of dimension 1200 x 300 x 25 mm was prepared for surface wave transmission measurements. In this study, the Plexiglas specimen was held in upright position as shown in **Figure 3-8**. A notch-typed crack was created using a hand saw in the Plexiglas specimen, with the crack depth h increasing from 0 to 30 mm with increments of 5 mm, as shown in **Table 3-2**. In this study, specimens are named based on the material and crack depth, e.g., P5 is a Plexiglas specimen with a crack depth of 5 mm. A hand saw made approximately 0.5 mm wide cracks, consequently, resulting in the width-to-depth ratio of all cracks implemented in this study smaller than 0.1. According to Masserey and Mazza [33], this value is small
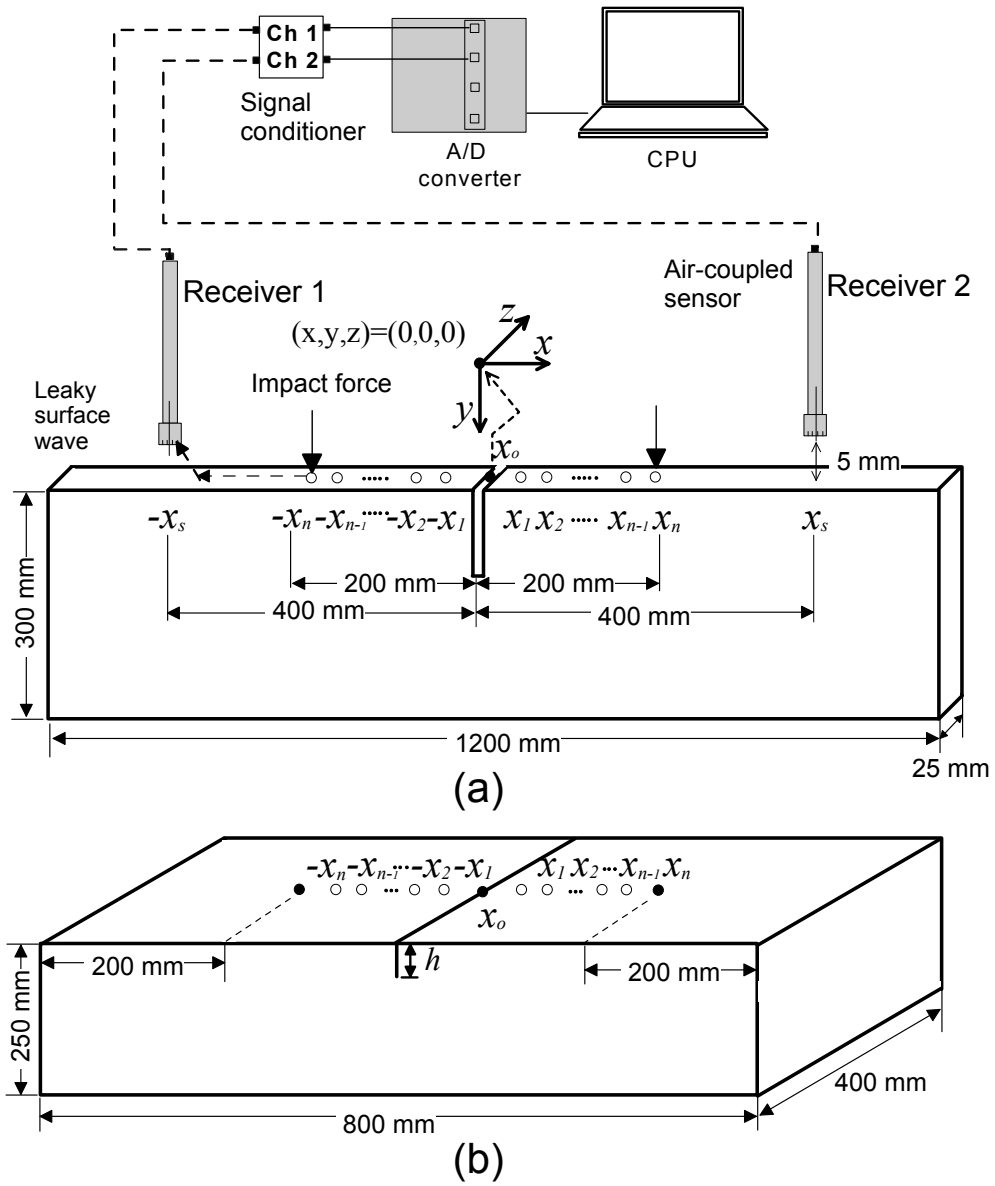
Figure 3-8: Experimental setup and data acquisition system for laboratory experiments; (a) for Plexiglas specimens and (b) for concrete specimens. Note that x_i is a location of an impact source and x_s is the location of the sensor.

Table 3-2: Specimens for laboratory experiments.

Mark	h [mm]	f_c [kHz]	C_R [m/s]	h/λ_c
C0-1	0	17[a]		-
C0-2	0	35[b]	2200	-
C20-1	20	17		0.15
C20-2	20	35		0.32
P0	0			-
P5	5			0.06
P10	10			0.12
P15	15	14[c]	1245	0.18
P20	20			0.24
P25	25			0.30
P30	30			0.36

Note: the center frequency f_c was determined through the Fourier transform
of incident surface waves generated by dropping a steel ball with diameters of
(a)13mm, (b) 8 mm, and (c) 6.35 mm.

enough to neglect the effect of the crack width on transmission coefficients of surface waves, so that the experimental results can be directly compared to the theoretical analysis results. To obtain the phase velocity of surface waves, a dispersion curve was obtained through the Multichannel Analysis of Surface Waves (MASW) method [53, 54]. Experimental results showed the phase velocity converged to 1245 m/s when the frequency is greater than 15 kHz, which agrees with the theoretical value based on 2D wave propagation model (i.e., generalized plane stress approximation) [55, 56].

Two concrete specimens with dimensions of 800 x 400 x 250 mm were cast in a laboratory. The specimen C0 did not contain a crack, whereas the specimen C20 has a 20 mm deep surface-breaking crack (refer to **Table 3-2**). The thickness of these specimens is 250 mm, which is larger than the 2 times of the surface wave wavelength used in this study. Concrete was made of Portland cement type I/II, river sand, and gravel with a maximum size of 10 mm. A notch-typed crack with a depth of 20 mm was created in the specimen by inserting a 0.2 mm thick metal sheet into the form before casting concrete.

The sheet was removed from the concrete 12 hours later. The density of concrete was 2350 kg/m^3 obtained from the average of five concrete cylinders (10 cm diameter by 20 cm height) cast at the same time as the concrete specimens. The phase velocity of surface waves in concrete is approximately 2200 m/s based on the MASW test when frequency is greater than 10 kHz.

3.4.2 Test setup, data acquisition, and signal processing

A schematic view of the test setup for the Plexiglas specimens is shown in **Figure 3-8** (a). The test setup of concrete specimens is shown in **Figure 3-8** (b). Two air-coupled sensors (PCB model No. 377B01) were used to measure leaky surface waves propagating on the surface of specimens. Detailed descriptions of the air-coupled sensing technique have been given by Zhu [13].

Previous researchers [7-9] demonstrated that the self-calibrating procedure was effective to eliminate experimental variations caused by impact sources and receiver coupling in the SWT test. In this study, a modified self-calibrating (MSC) procedure was used to measure the surface wave transmission across a surface-breaking crack from multiple locations (see **Figure 3-8**). In the MSC procedure, an impact point source moves from $-x_n$ to x_n on the specimen surface, and the generated surface waves are recorded by two sensors fixed at both sides of the crack at locations of $-x_s$ and x_s. Note that moving an impact source is more beneficial to test efficiency and signal consistency than moving sensors, especially for contact sensors (e.g., accelerometers). When impact sources are applied at positions $+x_i$ and $-x_i$, the transmission coefficient of surface waves is defined as

$$\mathbf{Tr}(h, x_i) = \sqrt{\frac{\mathbf{S}(x_s, -x_i)\mathbf{S}(-x_s, x_i)}{\mathbf{S}(-x_s, -x_i)\mathbf{S}(x_s, x_i)}}, \qquad \text{Equation 3-7}$$

where $\mathbf{S}(x_s, x_i)$ is the Fourier transform of the signal recorded by the sensor at x_s with the impact source at x_i. Note that Equation 3-7 is equivalent to the definition given by

Achenbach *et al.*[9], Popovics *et al.*[7] and Song *et al.*[8] based on the self-calibrating procedure according to source-receiver reciprocity [57].

In addition, to improve signal consistency, five repeated signal data sets were collected from the same test location. These five transmission functions were then arithmetically averaged in the frequency domain. To evaluate the quality of obtained signals, the signal coherence function defined in Equation 3-8 was used to check consistency of signal data

$$\mathbf{SC}_{12}(f) = \frac{\left|\sum \mathbf{G}_{12}(f)\right|^2}{\sum \mathbf{G}_{11}(f) \times \sum \mathbf{G}_{22}(f)}, \qquad \text{Equation 3-8}$$

where $\mathbf{G}_{12}(f)$, $\mathbf{G}_{11}(f)$ and $\mathbf{G}_{22}(f)$ are the cross spectrum and auto spectrum functions between sensor outputs $\mathbf{S}(x_s, -x_i)$, and $\mathbf{S}(-x_s, -x_i)$, caused by an input at $-x_i$. Similarly, $\mathbf{SC}_{21}(f)$ can also be calculated from signals $\mathbf{S}(-x_s, x_i)$, and $\mathbf{S}(x_s, x_i)$. Similarly, $SC_{21}(f)$ can also be calculated from signals by the right impact at $+x_S$. The averaged $SC(f)$ is defined as

$$\mathbf{SC}(f) = \sqrt{\mathbf{SC}_{12}(f) \times \mathbf{SC}_{21}(f)}. \qquad \text{Equation 3-9}$$

The value of $\mathbf{SC}(f)$ ranges from 0 to 1.0. A value close to 1.0 indicates good signal quality and repeatability. Therefore, the signal coherence function can be used to select the acceptable frequency range of a transmission ratio curve.

The measured surface wave transmission coefficient $\mathbf{Tr}_h$ was further normalized by $\mathbf{Tr}_0$, which is the transmission coefficient obtained from crack free regions. This procedure will eliminate material attenuation and the geometric spreading effect caused by a point source. The normalized transmission coefficient $\mathbf{Tr}_n$ is defined as

$$\mathbf{Tr}_n(h, x) = \frac{\mathbf{Tr}_h(x)}{\mathbf{Tr}_0(x)}. \qquad \text{Equation 3-10}$$
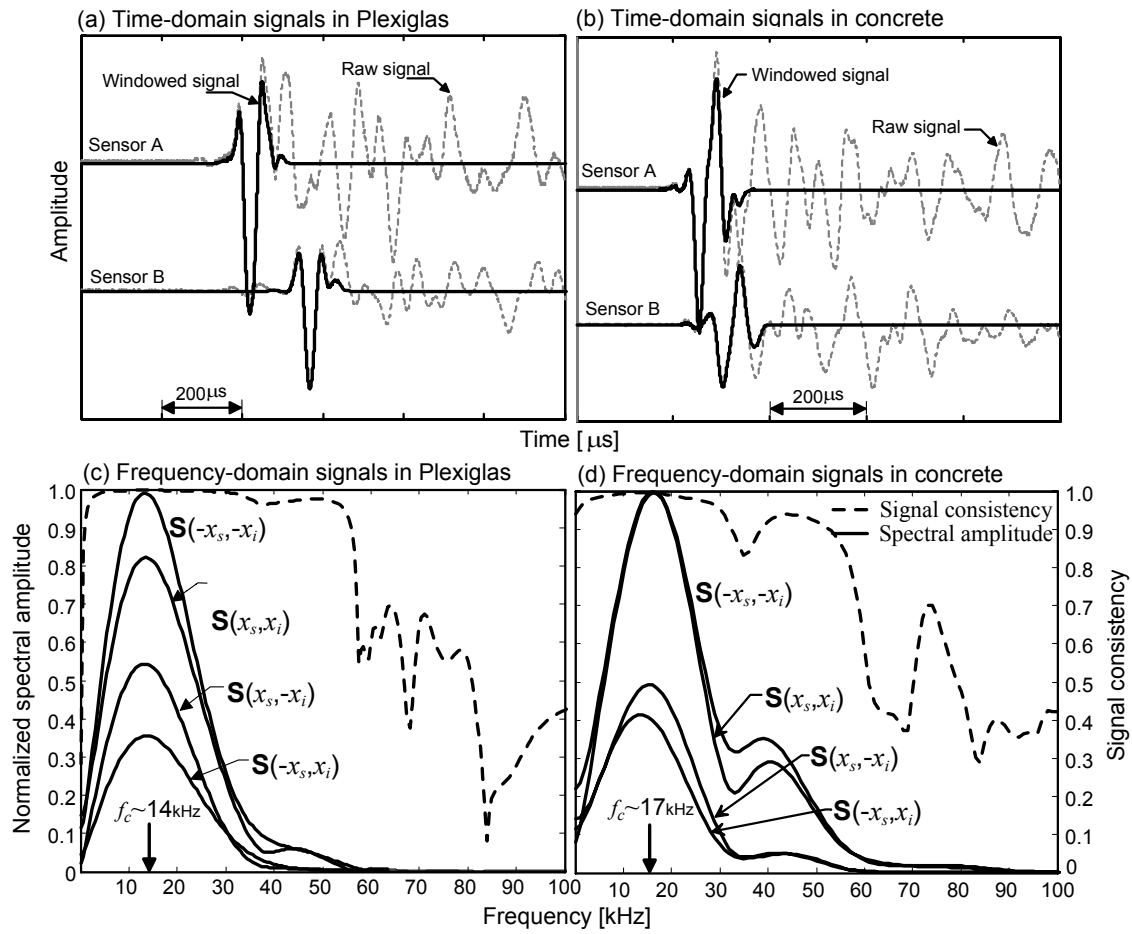
Figure 3-9: Typical signal from Plexiglas and concrete specimens: (a) typical time-domain signals from a Plexiglas specimen (P10) using a steel ball with a diameter of 6.35 mm (b) typical time-domain signal from concrete specimen (C20) using a steel ball with a diameter of 8 mm, (c) and (d) normalized spectral amplitude, and signal consistency calculated using windowed signals shown in (a) and (b), respectively.

All analyses were performed in the frequency domain. A *Hanning* window was applied to the time domain signals to extract the surface wave component.

For Plexiglas specimens, the transient force was generated by dropping a 6.35 mm diameter steel ball with guided by a plastic tube. The impact force generated incident surface waves with a center frequency around 14 kHz, and provided good signal consistency up to 30 kHz. The center frequency of incident surface waves was determined from the Fourier transform of the windowed signal measured in the backward scattering field (see **Figure 3-9** (a) for the specimen P10). For concrete specimens, steel balls with diameters of 13 and 8 mm were used. The center frequencies of the incident surfaces were around 17 kHz and 35 kHz, and the acceptable frequency ranges were up to 35 kHz and 60 kHz, respectively. **Figure 3-9** (b) shows typical received signals corresponding to the center frequency of 17 kHz. The acquired signals were digitized at a sampling rate of 10 MHz using an NI-USB 5133 oscilloscope.

In **Figure 3-9** (d), it is also noted that signals from reciprocal locations, such as $S(x_s, x_i)$ versus $S(-x_s, -x_i)$, and $S(-x_s, x_i)$ versus $S(x_s, -x_i)$, show good agreement with each other. It indicates the experimental setup is almost symmetric about the center line between two sensors. Signals in **Figure 3-9** (c) show some degrees of asymmetry, but the effects of asymmetry on transmission calculation will be cancelled by using Equation 3-7.

3.5   EFFECTS OF SENSOR LOCATIONS

3.5.1   APC curve

Figure 3-10 shows *APC* versus x/λ curves from experimental and numerical simulation results on Plexiglas specimens, where x/λ is the normalized distance from a crack opening. The experimental data were measured from the Plexiglas specimens P10 ($h/\lambda \sim 0.12$), and P30 ($h/\lambda \sim 0.36$), and the numerical simulation results were from the

48
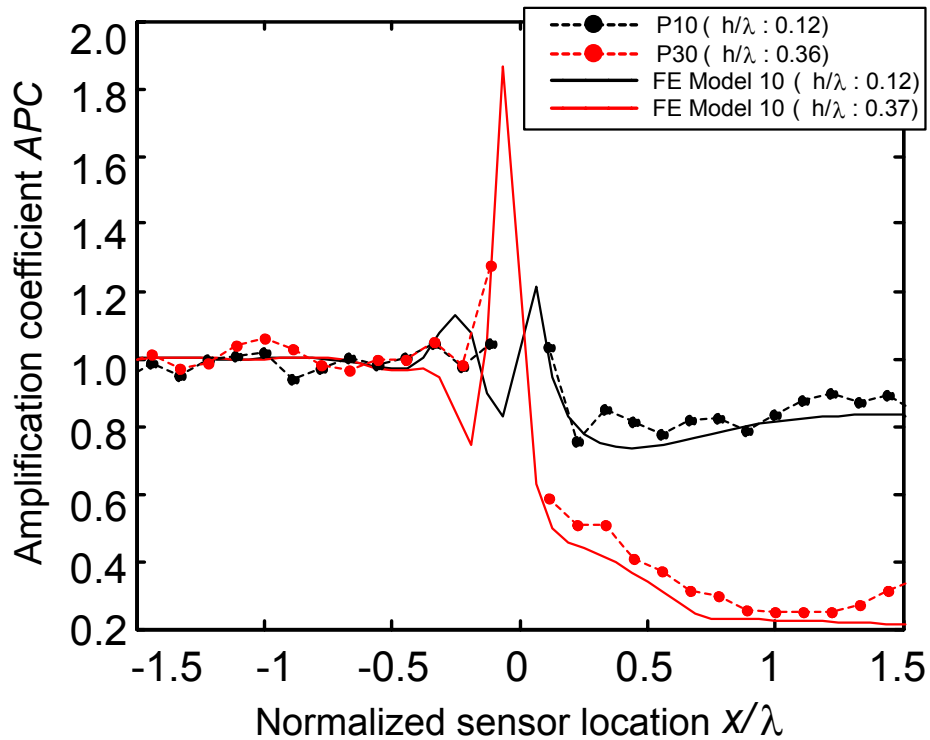
Figure 3-10: Amplification coefficient versus the normalized sensor location x/λ obtained from Plexiglas specimens (P10, and P30) and the FE model 10.

Plexiglas FE model 10 with crack depths of 10 mm ($h/\lambda \sim 0.12$), and 30 mm ($h/\lambda \sim 0.37$) (refer to **Table 3-1** and **Table 3-2**). Experimental data from the Plexiglas specimens are presented as solid circles with dash lines, while the numerical simulation results from the FE model 10 are plotted using solid lines. **Figure 3-10** shows good agreement between the experimental measurements and the numerical simulations.

3.5.2 Tr_n versus x/λ

Effects of near-field scattering of surface waves on the surface wave transmission were investigated in the frequency domain. **Figure 3-11** shows the transmission
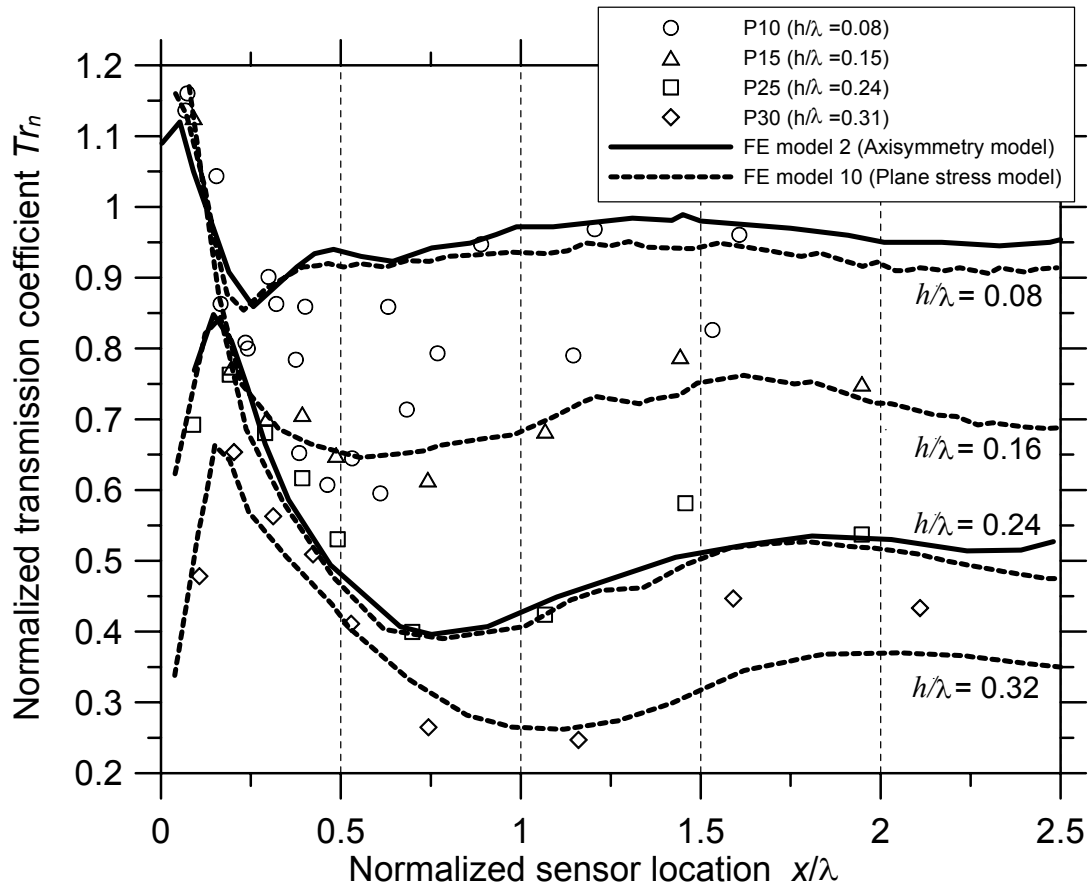
Figure 3-11: Transmission coefficients versus normalized sensor location (x/λ: sensor to crack opening spacing normalized by the wavelength of incident surface waves) obtained from Plexiglas specimens through the laboratory experiments and numerical simulations on FE model 10. For comparison, results from concrete models (FE model 2) are also shown as solid lines.

50

coefficients versus normalized sensor location x/λ obtained from the Plexiglas specimens in the laboratory experiments. The transmission coefficients calculated at the center frequencies for the Plexiglas specimens of P10 ($h/\lambda \sim 0.08$), P15 ($h/\lambda \sim 0.15$), P25 ($h/\lambda \sim 0.24$), and P30 ($h/\lambda \sim 0.31$) are depicted as circles, triangles, squares, and diamonds in **Figure 3-11**. For comparison purposes, the transmission coefficients obtained from the FE model 10 (h/λ of 0.08, 0.16, 0.24, and 0.32) are also shown in **Figure 3-11** as dash lines. All transmission coefficients were calculated in the frequency domain as defined in Equation 3-7 and Equation 3-10 [7, 8]. Overall, the experimental transmission coefficients obtained from the Plexiglas specimens match well with numerical analysis results. This good agreement verifies the validity of the FE models used in this study. Furthermore, both experimental studies and numerical simulations clearly reveal that the surface wave transmission coefficient depends not only on the depth of a crack and the wavelength of surface waves, but also on the distance of sensors from the crack opening in the near-scattering field. When measurements are taken at points located too close to a crack opening (e.g., x/λ is less than 0.2~0.3), the transmission coefficient is significantly higher than those measured in the far-field suggested by Cheng and Achenbach [38], and Angel and Achenbach [30]. The enhancement in transmission coefficient measurements in the near-scattering field was also pointed out by Richart *et al*. [20]. In addition, the transmission coefficient shows oscillatory behavior in the near field and gradually converges to a constant value with increasing x/λ ($x/\lambda \sim 2$). Consistent with observation of prior researchers [30, 31, 33], the normalized crack depth (h/λ) is the most critical parameter to determine transmission coefficients of surface waves in the far-field region.

Figure 3-12 shows the transmission coefficients and normalized sensor location x/λ obtained from the concrete specimens. Transmission coefficients were obtained from the concrete specimen of C20-1 using a 13 mm diameter steel ball and C20-2 using a 8 mm diameter steel ball. The corresponding center frequencies are 17 kHz and 35 kHz, and the normalized crack depths are $h/\lambda=0.15$ and $h/\lambda=0.32$ respectively. For comparison

51
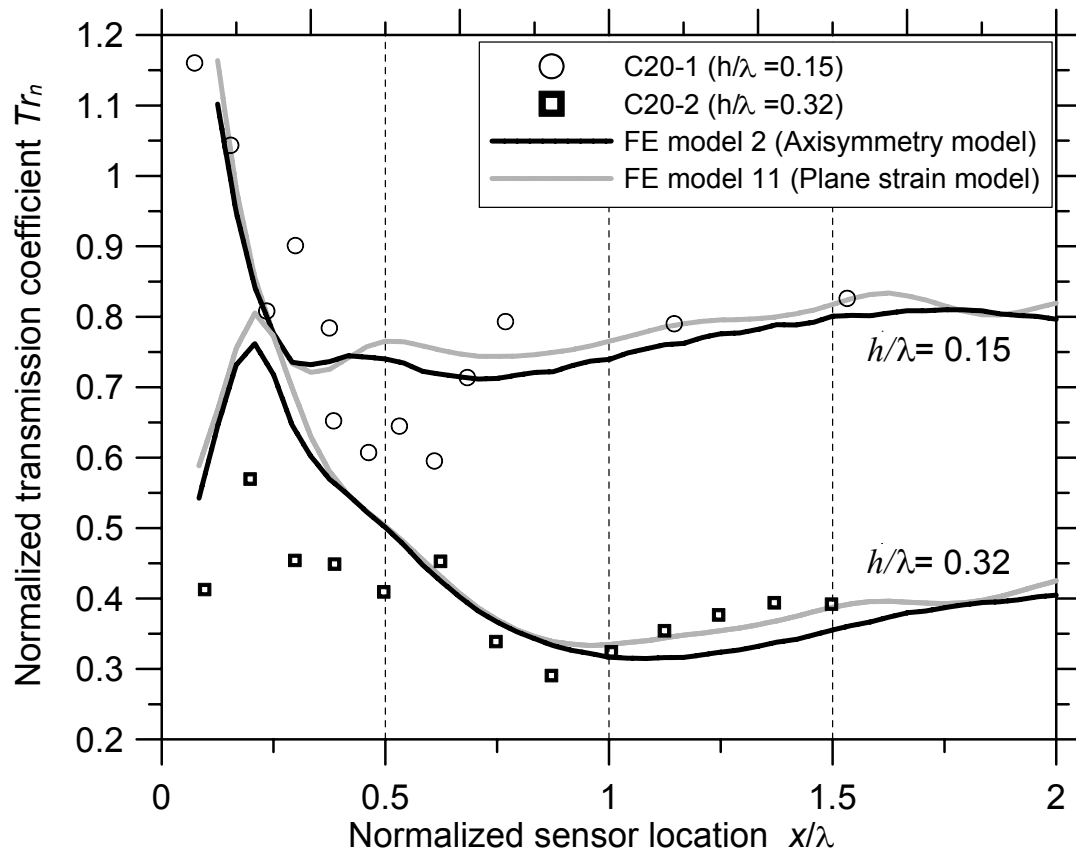
Figure 3-12: Transmission coefficient versus normalized sensor location obtained from concrete specimens and FE model 2.

purposes, Tr_n calculated from the FE Model 2 for h/λ of 0.15, and 0.32 (solid lines) are also shown in **Figure 3-12**. Overall, the experimental data show similar trend as the numerical transmission curve, such as *(i) enhancement of transmission coefficients for x/λ < 0.5*; *(ii) oscillation of transmission coefficients with varying sensor location*; and *(iii) convergence into the constant transmission coefficient when x/λ is close to 2*. However, the difference between the experimental and numerical transmission curve is larger than that in the Plexiglas case, particularly in the near field region. This difference might be partly caused by the inhomogeneity of concrete materials and wave scattering by coarse aggregates, and also caused by contribution of multiple reflected waves from bottom. The second term will be discussed in more detail in Chapter 5.

3.5.3   Parametric study

To obtain general conclusions of the near field effects, a series of parametric studies was performed using the FE models which have been verified in the previous section. The FE models used in the parametric study are summarized in **Table 3-1**. The main variables are (*i*) crack depth h, $0 \leq h \leq 100$ mm, (*ii*) duration of impact T, $40 \leq T \leq 140$ μs, (*iii*) Poisson's ratio v of 0.22 and 0.33, and element type of 4-node axisymmetric (4AX), plane stress (4PS), plane strain (4PE) and 3D brick (C3D8) elements.

Figure 3-13 (a) shows the Tr_n and x/λ relations for h/λ = 0.11, 0.22, 0.33, and 0.45 obtained from FE Models 1~ 6, with the impact duration T =40, 60, 80, 100, 120, and 140 μs. Different combinations of T and h give various h/λ values, and one h/λ may correspond to several T and h combinations, as shown in **Figure 3-13** (a). For a given h/λ, all Tr_n versus x/λ curves converge to a constant value with increasing x/λ, although frequency contents of the impact sources (T) are different. This result indicates that the Tr_n and x/λ relationship is mainly controlled by h/λ. The frequency bandwidth of the incident surface waves has little effect on it.

53
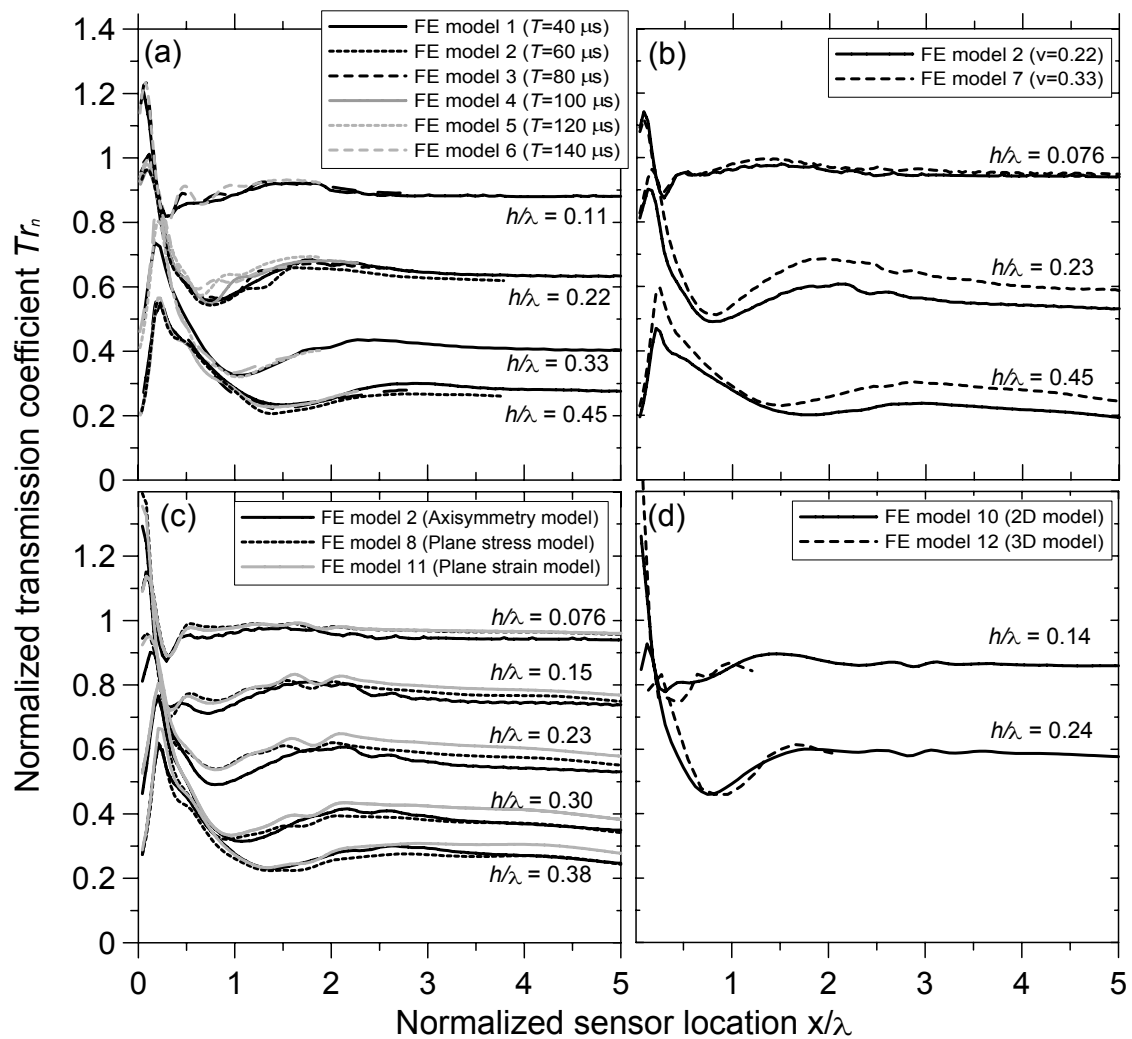
Figure 3-13: Normalized transmission coefficient Trn versus normalized sensor location from a crack opening x/λ. All curves were obtained from parametric studies using FE models to investigate effects of various parameters on the variation of Tr_n with increasing x/λ. (a) frequency contents of incident surface waves (T), (b) Poisson's ratio v of the solid media, (c) selection of element types, and (d) 2D model versus 3D model.

Figure 3-13 (b) shows the effect of Poisson's ratio v on the Tr_n and x/λ relation. The FE Models 2 (v=0.22) and 7 (v=0.33) have the same material properties and geometric conditions except for Poisson's ratios. Tr_n and x/λ relations for different h/λ (i.e., 0.076, 0.23, and 0.45) obtained from the FE Models 2 and 7 are depicted using solid lines and dashed lines, respectively. It is found that the model with the higher Poisson's ratio v=0.33 gives higher Tr_n than the model with the lower Poisson's ratio (v=0.22) for the same x/λ. The effect of Poisson's ratio increases as h/λ is greater. However, the Tr_n versus x/λ curves (i.e., signal enhancement, and oscillation) are still similar despite of different Poisson's ratios.

Figure 3-13 (c) shows the Tr_n and x/λ relations for various h/λ (0.076, 0.15, 0.23, 0.30, and 0.38) obtained from the axisymmetric model (model 2), the plane stress model (model 8), and plane strain model (model 11). As shown in **Table 3-2**, the FE model 2 is the same as model 8 and model 11 except for the element types. The results in **Figure 3-13** (c) demonstrate that variation of transmission coefficients from three different models shows fairly good agreement with each other in the near-scattering field of a surface-breaking crack (x/λ<2), especially between plane strain and plane stress models. For three cases, Tr_n converges to a constant value with increasing x/λ.

In addition, the combined effects of critical material properties (v, E, and ρ) and element types on Tr_n and x/λ relations are also shown in **Figure 3-13**. Note that the material properties for FE Model 2 correspond to a normal concrete, whereas those of FE Model 10 are for Plexiglas. Despite of the difference in material properties, Tr_n and x/λ relations from these two models show good agreement with each other.

Figure 3-13 (d) compares Tr_n and x/λ curves obtained from 2D (FE model 10) and 3D models (FE model 12) for two h/λ (0.14, and 0.24). Results from 2D models were extended to x/λ=5, while results from 3D models were presented in ranges of x/λ < 2 because of a limitation in size of 3D models. Nevertheless, in the near-scattering field of

55

a surface-breaking crack, results from 3D models show good agreement with those from 2D models. This demonstrates validity of 2D models in this study.

Based on this parametric study, although many parameters affect the near-field scattering by a surface-breaking crack, the most critical parameters on determination of transmission coefficients are the crack depth h/λ and sensor location x/λ.

3.5.4   Guidelines on selecting sensor locations in the SWT method

The experimental studies and numerical simulations show that the signal enhancement and oscillatory behaviors of transmission coefficients are due to the near field interaction of surface waves with the surface-breaking crack, which makes difficult to obtain consistent transmission measurements in near field region. Cheng and Achenbach [38] proposed $x > 5\lambda$ as an approximate far field guideline. However in practice, this criterion is not always satisfied due to the limitation of specimen geometry. In this section, the errors caused by near field effects in surface wave transmission measurements are evaluated by comparing to the results from far-field measurements. A guideline for selecting sensor locations is proposed based on error analysis.

Figure 3-14 shows errors of transmission coefficient (EOT) caused by the near-field effect. In this study, EOT is defined as follows:

$$EOT(h/\lambda, x/\lambda)[\%] = \frac{Tr_n(h/\lambda, x/\lambda) - Tr_n(h/\lambda, \infty)}{Tr_n(0, \infty)} \times 100,$$

Equation

3-11

where Tr_n is the normalized transmission coefficients determined by using

Equation 3-7 and Equation 3-10. EOT indicates the deviation of transmission coefficients measured at a specific sensor location from those measured in the far-field. Converged transmission coefficients mentioned in the previous section (see also **Figure 3-13**) were regarded as the far-field measurement. The negative

56

and positive sign of EOT indicate under- and over-estimation of transmission measurement respectively.
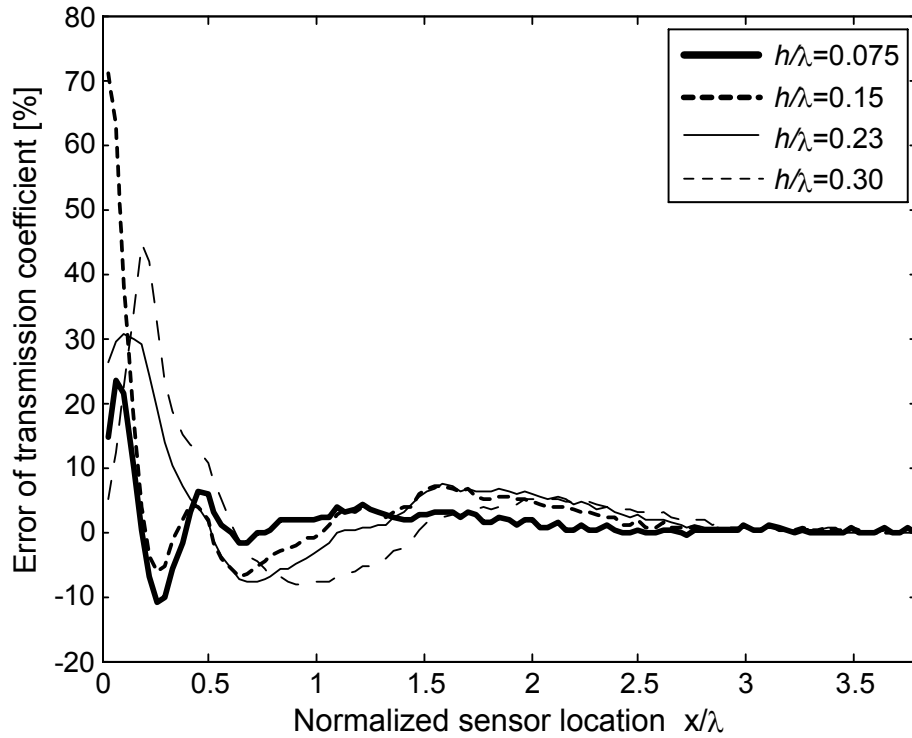
Figure 3-14: Errors of transmission coefficient as a function of the normalized sensor to crack spacing (x/λ).

Figure 3-14 reveals that EOT is less than 5% for $x/\lambda > 2.0$. In the h/λ range of interest for crack depth estimation, i.e., $h/\lambda = 0.1 \sim 0.3$, the sensitivity of transmission function with respect to h/λ is greater than 2.0. Therefore, 5% of errors in the transmission measurement will lead to less than 2.5% error in h/λ estimation. Note that the sensitivity of transmission function was obtained from the first derivative of the transmission function for surface waves across a surface-breaking crack suggested by Angel and Achenbach[30] with respect to the h/λ. In contrast, *EOT* varies within ±10% when sensors are located between 0.5λ and 1.5λ from the crack opening ($0.5 < x/\lambda < 1.5$).

57

Likewise, the error of h/λ is approximately less than 5% when h/λ is in the range from 0.1 to 0.3.

3.6   CONCLUSIONS

The near-field scattering of surface waves caused by a surface-breaking crack is thoroughly investigated within the crack depth range of $0 < h/\lambda < 1/3$ in which transmission coefficient is sensitive to crack depth variation. Conclusions based on experimental studies and numerical simulations are drawn as follows:

1) Results from experimental studies and numerical simulations reveal that the transmission function (Tr_n) of surface waves across a surface-breaking crack is affected not only by the crack depth h, and the wavelength of incident surface waves λ, but also by the sensor location from the crack opening x. Strong signal enhancement and oscillation of transmission coefficient are observed when sensors are located within 0.5λ away from the crack opening. The oscillatory behavior of transmission coefficients becomes weaker as sensors are located approximately 1.5λ from the crack, and almost disappears when sensors are 3.0λ away from the crack.

2) Numerical simulations and experimental measurements show good agreement in surface wave transmission function calculation, especially for the Plexiglas specimens, a type of homogeneous material. For the concrete specimens, material heterogeneity and wave scattering by coarse aggregates in concrete decrease the agreement between numerical and experimental transmission curves in the near scattering field. The degree of agreement improves in the far-field.

3) To obtain reliable and consistent transmission coefficient, measurements should be performed in the far-field. Analyses in this study show that surface

58

wave transmission coefficients converge to a constant value in the far-field for large x/λ. Transmission coefficients in far-field measurements also converge to the analytical solution based on steady-state analysis given by Angel and Achenbach [30].

4) Near-field effects induce errors in surface wave transmission measurements. Error analysis shows that the error in transmission coefficient depends on the normalized sensor locations (x/λ). When $x/\lambda > 2.0$, the error is around 5%, and the corresponding error in crack depth estimation is about 2.5% of the wavelength λ of incident surface waves.

Chapter 4   Surface Wave Transmission across Distributed Cracks

There have been very few studies for more realistic problems involving near scattering of surface waves by distributed surface-breaking cracks. One possible reason is complexity caused by the interaction of surface waves between multiple cracks. In this study, first, interaction of surface waves between two surface-breaking cracks with various crack spacing a and the same depth h in Plexiglas was investigated through experimental studies using non-contact sensors (air-coupled sensors, and a laser vibrometer), and numerical simulations (Finite Element Method). Second, effects of crack spacing a, and the number of cracks N on the transmission coefficients of surface waves Tr_n are studied using the Plexiglas specimens and the verified FE models. As a result, transmission coefficients of surface waves across various distributed surface-breaking cracks are presented in terms of normalized spacing a/h, the number of crack N, and normalized crack depth h/λ. Analysis show that for the very small crack spacing (a/h < 0.2), the distributed cracks can be regarded as a single surface-breaking crack. However, for a/h ranging between approximately 1 and 6, the transmission coefficient of surface waves is significantly affected by interaction between cracks. For the same h/λ within [0.1, 0.25], transmission coefficients reaches the lowest value when a/h is between 2 and 3. When a/h is large (a/h > 6), transmission coefficients obtained from experiments, and numerical simulations agree with the theoretical results based on non-interaction crack assumption.

4.1   INTRODUCTION

Scattering of surface waves caused by a single surface-breaking crack (or slot) has been extensively studied by experimental studies and numerical simulation since late 1970's. However, there have been very few experimental works for more realistic problems involving distributed surface-breaking cracks in a solid medium. The dispersion and scattering of surface waves caused by non-interacting distributed surface-breaking

60

cracks has been studied by Zhang and Achenbach [58]. In their research, they analytically studied phase velocity and attenuation coefficients of surface waves across uniformly distributed surface-breaking crack with the same depth based on the non-interaction assumption (i.e., crack spacing is large enough so that there is no interaction between cracks). Recently, Pecorari [59, 60] suggested an effective field approach to model the dispersion and attenuation of surface waves across distributed cracks. Until now, no exhaustive theoretical model describing the interaction of surface waves between distributed surface cracks has been developed. This is mainly due to the complexity of surface wave interaction between individual surface-breaking cracks.

In this chapter, near-field scattering of surface waves interacting with distributed surface-breaking cracks was investigated through experimental measurements using non-contact sensors (air-coupled sensors and a laser vibrometer), and numerical simulations (FEM). Section 4.2 contains a brief description of FE models for numerical simulations. An experimental program conducted in this study is described in section 4.3.1, and test setup and data acquisition systems for air-coupled sensors and a laser vibrometer are shown in section 4.3.2. Verification of the FE models is shown in section 4.4.1. Based on the results from experimental studies and numerical simulations, interaction of surface waves between individual surface-breaking cracks are investigated in section 4.4.2. In addition, effects of crack spacing a, and the number of cracks N on the transmission coefficients of surface waves are discussed for a wide range of normalized crack depth h/λ in section 4.4.3.

4.2 NUMERICAL SIMULATION

4.2.1 Model description

Finite element method (FEM) was used to simulate the transient behavior and near-field scattering of surface waves caused by distributed surface-breaking cracks in Plexiglas specimens. The main purpose of numerical simulation in this study is to investigate wide range of variables which could not be completely covered by the experimental program. The main variables in the numerical simulation are *crack depth h, crack spacing a, and the number of crack N*.

To save computational cost, 2D FE models with distributed surface-breaking cracks were developed using rectangular plane stress elements (CPS4) in a finite element package (ABAQUS *v 6.7.1*) as shown in **Figure 4-1**. Plane stress elements (CPS4) have been verified to effectively simulate the transient behavior of surface waves across a surface-breaking crack in Chapter 3. In this chapter, the FE model was extended to investigate near-field scattering of surface waves interacting with distributed surface-breaking cracks.
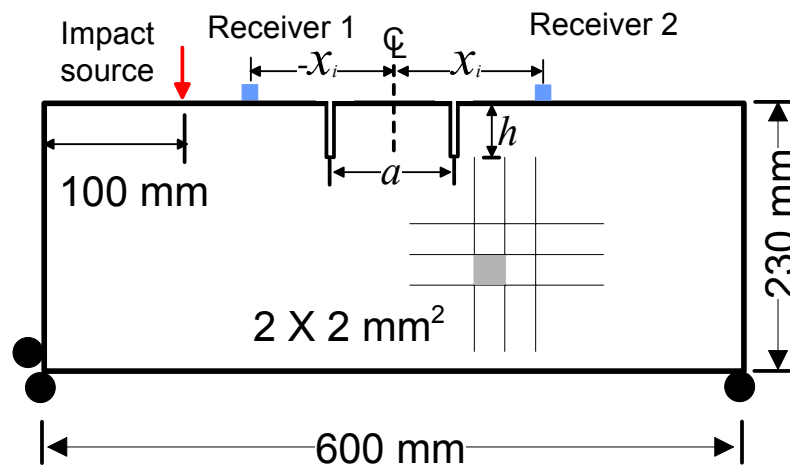
Figure 4-1: A finite element model containing two surface breaking cracks with the spacing *a*, and the same depth *h*.

4.2.2 Determination of surface wave transmission

Transmission coefficients of surface waves across distributed cracks were investigated in the frequency domain. Parameters affecting the surface wave transmission include frequency f, crack depth h, crack spacing a, and the number of crack N. The surface wave transmission coefficient Tr is defined as the frequency response ratio between the cracked model and the crack free model as follows:

$$\mathbf{Tr}_n(f,h,a,N) = \frac{\mathbf{S}_2(h)}{\mathbf{S}_1(h)} \bigg/ \frac{\mathbf{S}_2(0)}{\mathbf{S}_1(0)}, \qquad \text{Equation 4-1}$$

where $\mathbf{S}_1$ and $\mathbf{S}_2$ are the Fourier transforms of the vertical velocity responses measured by at receivers 1 and 2 (see **Figure 4-1**). Similar to the procedure described in Chapter 3, a window function (hanning window) with a length of two times of the signal period was used to extract the surface wave components before the Fourier transform [7, 8].

4.3 EXPERIMENTAL PROGRAM

4.3.1 Preparation of test specimens

Two series of Plexiglas (Poly methyl methacrylate, PMMA) specimens with sizes of $600 \times 230 \times 6.35$ mm^3 (series A), and $1200 \times 300 \times 25.4$ mm^3 (series B) were prepared for measuring near-scattering field of surface waves and surface wave transmission across various distributed cracks in laboratory. In this study, the Plexiglas specimen was held in upright position as shown in **Figure 4-2**. The Plexiglas specimens of series A include five specimens, in which three have two surface-breaking cracks, one has a single crack and one does not contain any crack. All cracks have the same depth of 8 mm, and crack spacings of 0, 8, 24, and 48 mm. Similarly, the specimens of series B include 10 specimens with various numbers of cracks of 1, 2, 3, and 4 and one specimen without crack. The cracks have the same depth of 15 mm, and various spacings of 0, 15,

63
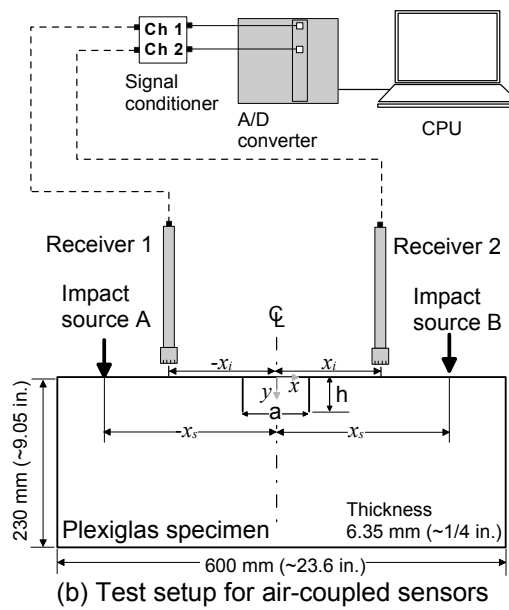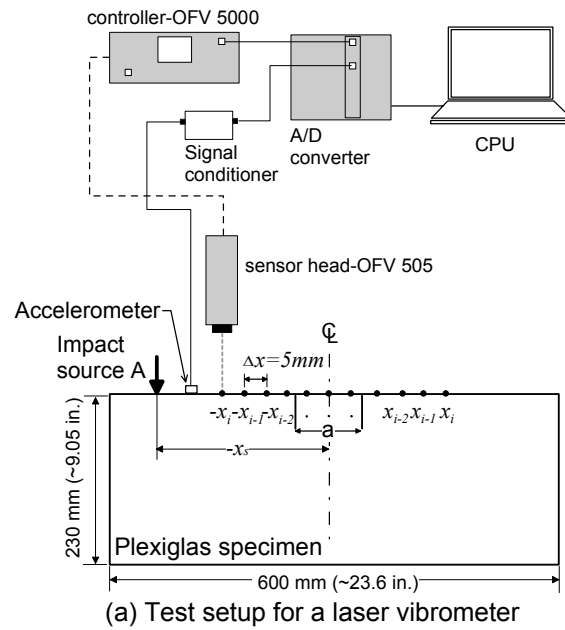
Figure 4-2: Experimental setup and data acquisition system for (a) a laser vibrometer, and (b) air-coupled sensors on the Plexiglas specimen series A with an impact source having duration T around 40 μs ($\lambda\sim50$ mm).

Table 4-1: Properties of Plexiglas specimens for experiments

Plexiglas Specimens		Specimen size	Crack spacing a [mm]	Crack depth h [mm]	# of cracks N	a/h	Center frequency f_c
Series A	*A0-0-0* (no crack)	600 X 230 X 6.35 [mm³]	0	0	0	0	25 kHz
	A1-0-8 (single)		0		1	0	
	A2-8-8		8	8	2	1	
	A2-24-8		24		2	3	
	A2-48-8		48		2	6	
Series B	*B0-0-0* (no crack)	1200 X 300 X 2.54 [mm³]	0	0	0	0	15 kHz
	B1-0-8 (single)		0		1	0	
	B2-15-15		15		2	1	
	B2-45-15		45		2	3	
	B2-90-15		90		2	6	
	B3-15-15		15	15	3	1	
	B3-45-15		45		3	3	
	B3-90-15		90		3	6	
	B4-15-15		15		4	1	
	B4-45-15		45		4	3	
	B4-90-15		90		4	6	

Note : A2-24-8 means a Plexiglas specimen series **A** containing **2** surface-breaking cracks with a spacing of **24** mm and a depth of **8** mm.

45, and 90 mm. Consequently, this test program covers four spacing-to-depth ratios (a/h=0, 1, 3, and 6) of distributed surface-breaking cracks in Plexiglas. The Plexiglas specimens are summarized in **Table 4-1**. The specimens are named based on test variables. For example, A2-24-8 indicates the Plexiglas specimen series **A** having **2** surface-breaking cracks with a spacing **24** mm, and a depth **8** mm. A hand saw was used to generate surface-breaking cracks perpendicular to the free surface of specimens. The width of all cracks is approximately 0.5 mm. The width-to-depth ratios of cracks used in this study are around 1/16 and 1/30 for series A and B, respectively. Note that these values are small enough to ignore effects of the crack width on transmission coefficients

of surface waves according to Masserey and Mazza [33]. Therefore, the results from the experimental study can be directly compared with analytic results. The phase velocity of surface waves obtained from the spectral analysis of surface wave (SASW) test converges to 1245 m/s when frequency is greater than 15 kHz. This velocity is compatible with the value calculated based on generalized plane stress approximation [55]. This also demonstrates that the thickness of specimens and frequency range ($H/2\lambda_R$ >1) implemented in this study are appropriate to generate surface waves.

4.3.2 Test setup and data acquisition

4.3.2.1 Using a laser vibrometer

A schematic view of the test setup for the Plexiglas specimen series A is shown in **Figure 4-2** (a). A laser vibrometer by Polytec (sensor head-OFV 505 and controller-OFV 5000) was used to measure vertical velocity responses in near-field scattering of distributed-surface breaking cracks in Plexiglas specimens. The specimens were moved to scan the surface of specimens from x_i = -200 to 200 mm at an interval of 5mm, where x_i is the distance of the sensor from the midpoint between two cracks (see **Figure 4-1** (a)). An accelerometer was installed near the impact point to calibrate the impact force amplitude.

4.3.2.2 Using air-coupled sensors

To measure surface wave transmission, two air-coupled sensors (PCB model No. 377B01) were located at $-x_i$ and x_i from the centerline of the specimens (see **Figure 4-2** (b)). In this study, x_i varies from 10 to 150 mm at an interval of 10 mm to investigate the effects of sensor locations on transmission coefficients. The impact source was applied at x_S = ±200 mm. Test setup for the Plexiglas specimen series B is the same as that for the specimens series A, except that the impact source was located at x_S = ±300 mm. The air-

coupled sensing technique has been described in more detail in another publication [40] and Chapter 6.

To reduce experimental variability in the surface wave measurement, signal data were acquired through the self-calibrating procedure [7-9]. The surface wave transmission ratios were measured from opposite directions, and averaged as follows:

$$Tr = \sqrt{\frac{\mathbf{S}(-x_S, x_i)\mathbf{S}(x_S, -x_i)}{\mathbf{S}(-x_S, -x_i)\mathbf{S}(x_S, x_i)}} ,$$
Equation 4-2

where $S(\pm x_S, \pm x_i)$ are the Fourier transform of the time signal data $V(\pm x_S, \pm x_i)$ generated by impact sources at $\pm x_S$ and recorded by the sensors located at $\pm x_i$. Note that

Equation 4-2 is equivalent to the Equation 3-7 in Chapter 3 using source-receiver reciprocity.

In addition, five repeated signal data sets were collected at the same test location to improve signal consistency. These five transmission functions were then arithmetically averaged in frequency domain. Signal consistency was evaluated using signal coherence function shown in Equations 3-8 and 3-9 in Chapter 3. The **SC**(f) ranges from 0 to 1.0. A value close to 1.0 indicates good signal quality and repeatability. The signal coherence function was used to determine the acceptable frequency range of a transmission ratio curve.

Transient forces were generated by dropping a steel ball guided by a plastic tube. The ball diameters are 3mm and 6.35 mm for the Plexiglas specimen series A and B respectively. They generate incident surface waves having center frequencies around 25 kHz, and 15 kHz, and provide good signal consistency up to 50 and 30 kHz. The acquired signals were digitized at a sampling frequency of 1 MHz using an NI-USB 5133 oscilloscope.

67

4.4   RESULTS AND DISCUSSION

4.4.1   Validity of FE model

The validity of the finite element model was investigated by comparison with experimental results. Each vertical velocity response $V_y(x/\lambda, t)$ calculated from the finite element model and measured by a laser vibrometer on the free surface of the Plexiglas was normalized by its negative peak value $\min(V_y(x/\lambda, t))$, where x is the distance from the midpoint between two cracks, and t is time. **Figure 4-3** compares the normalized vertical velocity response of signal data obtained from the FE model and the Plexiglas specimen A1-0-8 (refer to **Table 4-1**). The six signal data sets were measured at six locations ($x = \pm 20, \pm 60,$ and ± 100 mm) on the free surface of the specimen. The first arrivals are P waves, and then, mode converted S waves (PS: P waves to S waves) follow. In the backward scattering field ($x<0$), the incident surface waves (R_i), the reflected waves (R_r) from a crack and from the left boundary of the specimen are clearly seen in the time domain. In the forward scattering field, transmitted surface waves (R_{tr}) across a crack, and reflected surface waves from the plate boundary can be seen in the time domain. The normalized velocity (normalized by the negative peak value of incident surface waves) responses from FE model match well with signals from experimental measurements using a laser vibrometer. In particular, main pulses of surface waves (R_i, and R_{tr}) from the FE models show very good agreement with the corresponding measurements from the Plexiglas specimen A1-0-8. This demonstrates the validity of FE models used in this study for investigating the scattering problems of surface waves interacting with surface-breaking cracks (or slots).

68
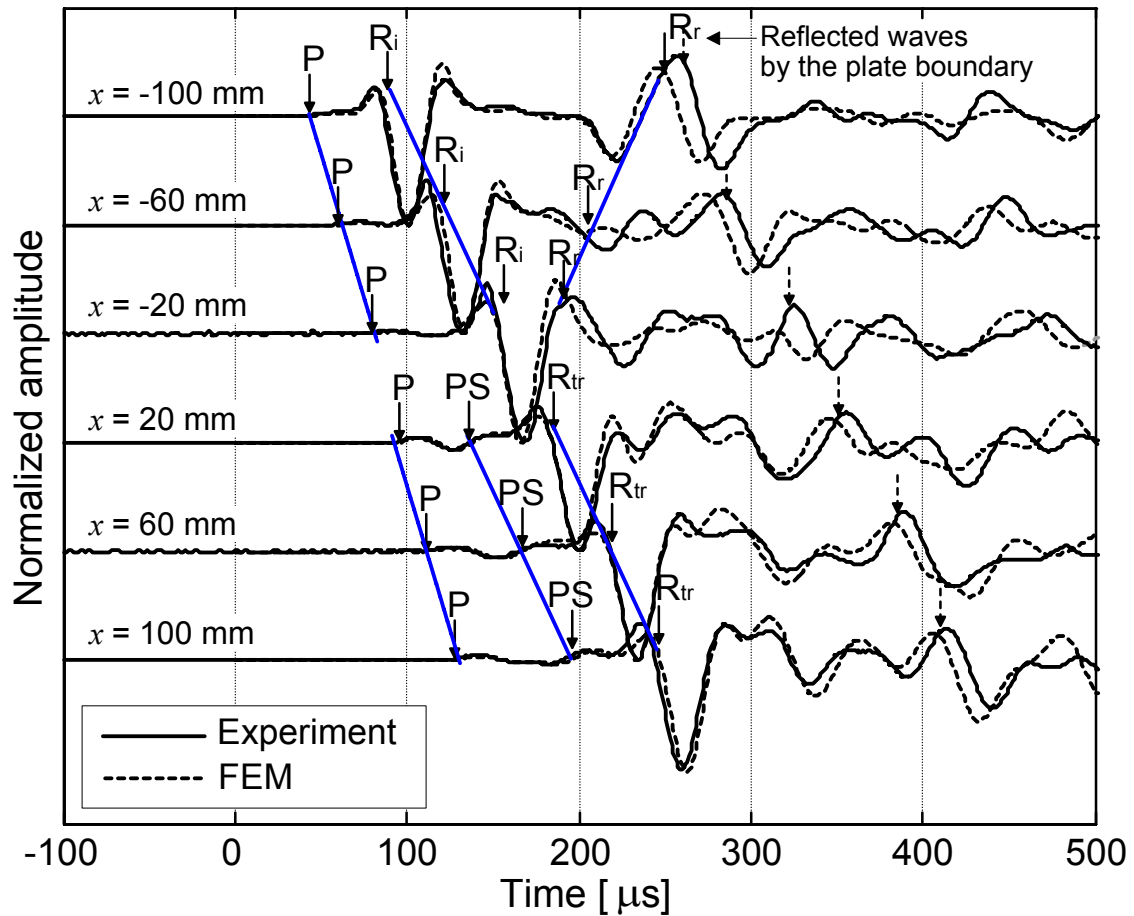
Figure 4-3: Comparison of responses in near-scattering fields measured using a laser vibrometer from the Plexiglas specimen of P0-8 and from FE model.

4.4.2 Interaction of surface waves between individual cracks

Near-field scattering of surface waves interacting with two cracks with the same crack depth h was investigated. The vertical velocity responses $V_y(x,t)$ were obtained from numerical simulations (FEM) and experimental measurements using a laser vibrometer described in the sections 2 and 3.

Figure 4-4 and **Figure 4-5** show the B-scan images representing the near-field scattering of surface waves interacting with two surface-breaking cracks obtained from

69

the FE analyses and experiments, respectively. It can be seen that the experimental measurements agree with the numerical simulations well. In all models and specimens, the cracks have the depth of 8mm, and spacings of 0, 8, 24, and 48 mm. Consequently, four crack-spacing-to-depth ratios a/h of 0, 1, 3, and 6 are covered in **Figure 4-4** and **Figure 4-5**. Interaction of surface waves between two cracks substantially affects the backward and forward scattering field of surface waves. **Figure 4-4** (a) and **Figure 4-5** (a) illustrate the scattering field by a single surface-breaking crack. The reflected surface waves (R_r) by a surface-breaking crack, the transmitted waves (R_{tr}) across the crack, and reflected surface waves by the plate boundary (R_{2i}) are clearly seen. The dark color in the B-scan images indicates the negative amplitude of waves, and the light color for positive amplitude. **Figure 4-4** (b) and **Figure 4-5** (b) show surface waves scattered by two cracks with small spacing (a/h=1). The surface waves trapped between two cracks generate multiple reflections and transmissions into the backward and forward scattering fields. Increasing crack spacing to 24 mm (a/h=3) results in complex near-scattering field before and after cracks, as shown in **Figure 4-4** (c) and **Figure 4-5** (c). In the backward scattering field, the reflected waves from the first (R_{r1}) and the next crack (R_{r2}) interfere with each other. In the forward scattering field, the transmitted surface waves are blurred and have lower amplitude. These will further affect determination of transmission coefficients of surface waves across the cracks. **Figure 4-4** (d) and **Figure 4-5** (d) show that further increasing the crack spacing to 48 mm (a/h=6) results in two separated waves in the backward scattering field, each of which is reflected by the first (R_{r1})and the second cracks (R_{r2}), and there is no strong interference between these waves.
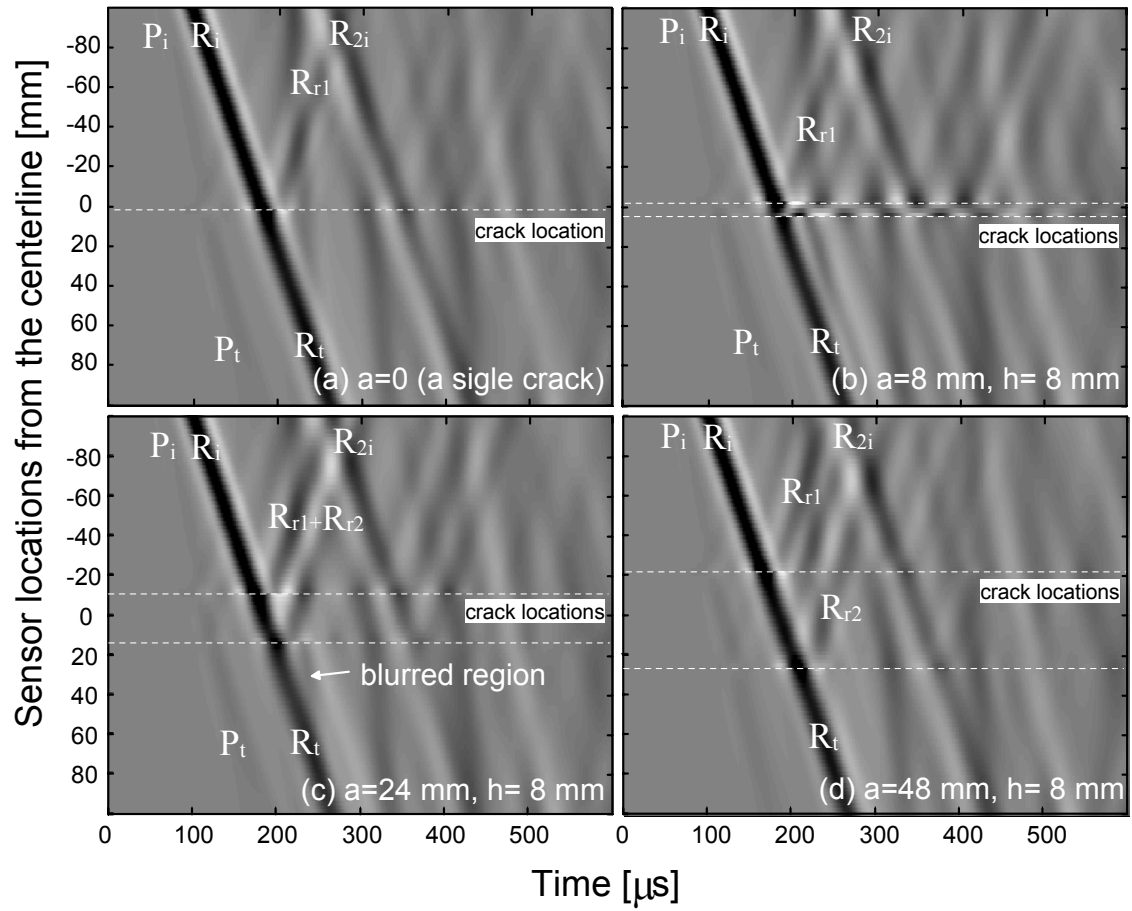
Figure 4-4: Surface wave response $V_y(x,t)$ in near-scattering fields caused by two surface-breaking cracks obtained from FE models with crack depth h=8mm: (a) a/h=0 (single crack); (b) a/h=1; (c) a/h=3 ; and (d) a/h=6.

71
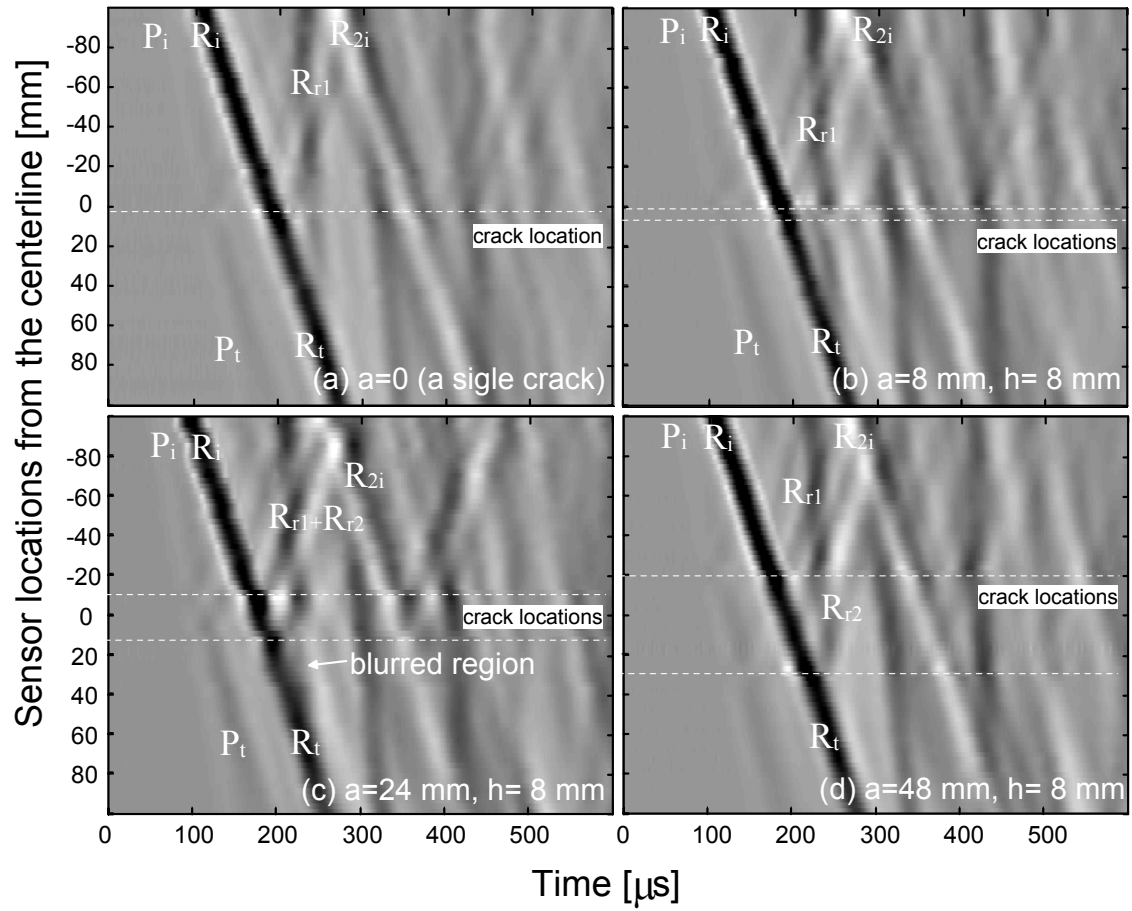
Figure 4-5: Surface wave response $V_y(x,t)$ in near-scattering fields caused by two surface-breaking cracks (h=8mm) measured using a laser vibrometer from Plexiglas specimens: (a) a/h=0 (single crack); (b) a/h=1; (c) a/h=3 ; and (d) a/h=6.

Figure 4-6 shows signal amplification coefficients versus the normalized distance x/λ for the same crack depth h of 8mm and crack spacings a of 0, 8, 16, 24, 48, 72 and 96 mm. The signal **a**mplification **c**oefficient (APC) was obtained using Equation 3-3 in Chapter 3. The *APC* curves are strongly affected by the crack spacing a even though the crack depth are the same. In addition, effects of the crack spacing on near-field scattering of surface waves also depend on near-field size a_n. The near-field sizes a_n has been Shown in Chapter 3. It was found that a_n depends on crack depth h, and wavelength λ of incident surface waves. In this study, for h=8mm and λ=50 mm, a_n is approximately 20 mm. When a=8 mm, which is smaller than half of a_n, the *APC* curve is similar to that measured from a single crack model (a=0 mm). The *APC* curve shows oscillatory behavior in the near field region, and then converges into a constant value in the far field for large x/λ. When the crack spacing a increases but is less than $2a_n$ (a=16 mm and 24 mm in **Figure 4-6**) the forward scattering field from the first crack tip interferes with the backward scattering field from the second crack tip. Consequently, complex near-field scattering forms in the region between two cracks, as shown in **Figure 4-4** and **Figure 4-5**. This interaction affects transmission measurement of surface waves across distributed surface-breaking cracks. When the crack spacing a further increases to 48, 72, and 96 mm ($a/a_n \sim$ 2.5, 3.5, and 5), interaction of surface waves between cracks gradually decreases so that the cracks can be regarded as two separated cracks. In this case, the previous surface wave transmission theories for a single crack may still be applied to each single crack. For example, if the surface wave transmission ratio after the first crack is Tr, then the transmission after the second crack will converge to Tr^2 in far field.
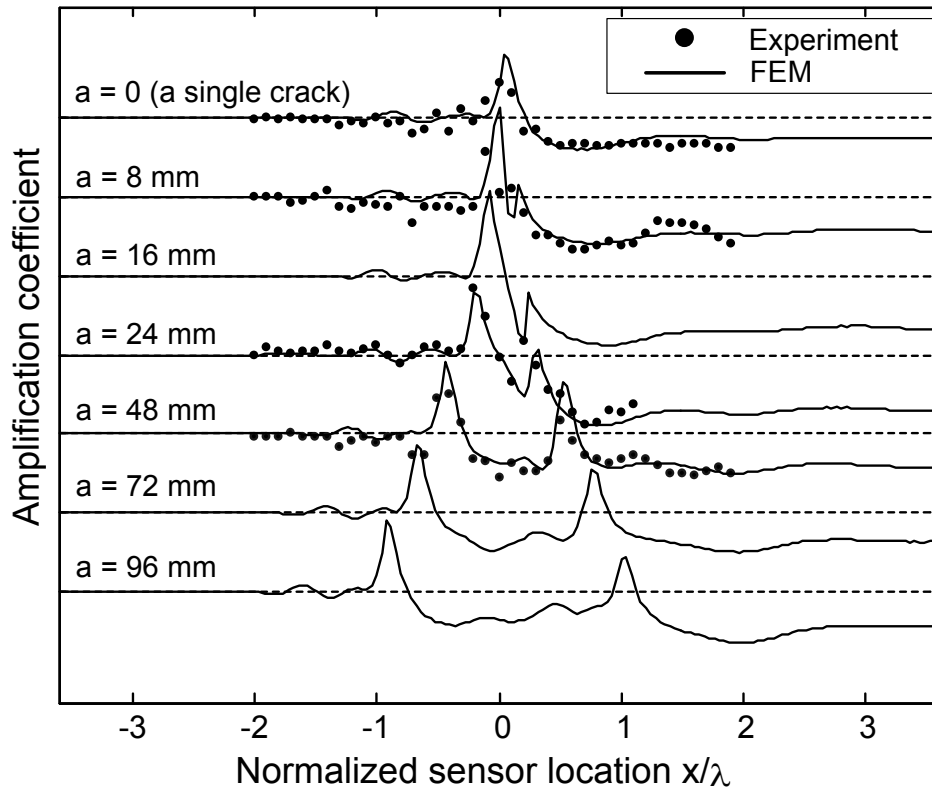
Figure 4-6: Amplification coefficients versus normalized sensor location (x/λ) obtained from FE models and experiments: λ=50mm and h/λ=0.16.

4.4.3　Transmission coefficients Tr_n

In this section, transmission coefficients of surface waves across distributed surface-breaking cracks were calculated in the frequency domain as described in previous sections 2.2 and 3.2.

4.4.3.1　Effects of sensor locations on Tr_n

To obtain better understanding of near-field scattering by distributed cracks, effects of sensor locations on Tr_n were investigated through FE analyses and experimental measurements by air-coupled sensors. **Figure 4-7** (a), and (b) present the relationship between Tr_n and the normalized sensor location x/λ. Tr_n measured from the

Plexiglas specimens series A (A1-0-8, A2-8-8, A2-24-8 and A2-48-8) are presented with solid circles, and the results obtained from corresponding FE models with solid lines. Note that to avoid overlapping the plots, the results from A1-0-8 and A2-24-8, and those from A2-8-8 and A2-48-8 are plotted in **Figure 4-7** (a) and (b), respectively. The experimental measurements show good agreement with FE models. Consistent with observations by previous researchers [34, 40], the near-field scattering by a crack ($x/\lambda < 0.5$) results in strong enhancement and oscillation in transmission coefficients; while Tr_n tends to converge to a constant value when sensors are located far from the crack opening (i.e., $x/\lambda > 1.0$). The approximate near-field size for a single crack ($x/\lambda \sim 1.5$) is effective on distributed cracks. In this study, sensor locations are chosen as $x/\lambda \sim 1.5$ to ensure far-field measurements.
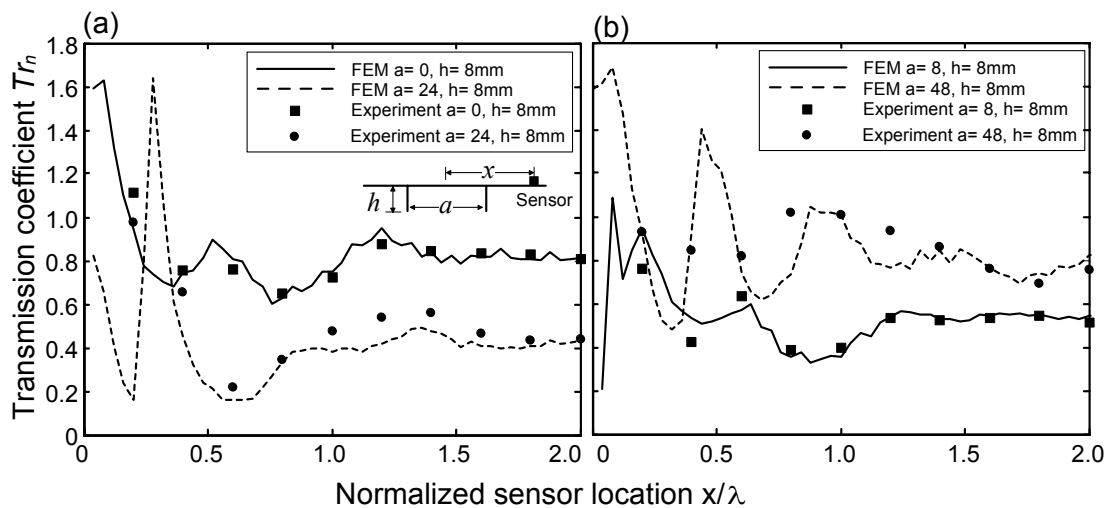
Figure 4-7: Normalized transmission coefficient versus normalized sensor location (x/λ) obtained from FE models and experiments: λ=50mm and h/λ=0.16.

75

4.4.3.2   Effects of crack spacing a/h

Among the parameters which affect surface wave transmissions, preliminary analyses by the authors [48] indicated that the normalized crack spacing a/h has the largest influence on $Tr_n(f_c)$ for a given number of cracks N. **Figure 4-8** shows the variation of $Tr_n(f_c)$ with crack spacing a/h based on FE analyses and experimental measurements, where $Tr_n(f_c)$ is the normalized transmission coefficient at center frequency. Solid squares in **Figure 4-8** (a) are results from the specimens A1-0-15, A2-8-8, A2-24-8, and A2-48-8, and solid circles in **Figure 4-8** (b) are of the specimens B1-0-15, B2-15-15, B2-45-15, and B2-90-15. For comparison purposes, $Tr_n(f_c)$ from corresponding FE analyses are presented as dashed-line with open squares and open circles at **Figure 4-8** (a) and (b). The experimental results show very good agreement with those from FE analyses. For the same crack depth h, $Tr_n(f_c)$ has the minimum value around a/h =2~3, and tends to converge to a constant value Tr^2 when a/h is greater than 6. This is consistent with the results from the previous study based on non-interaction approximation.
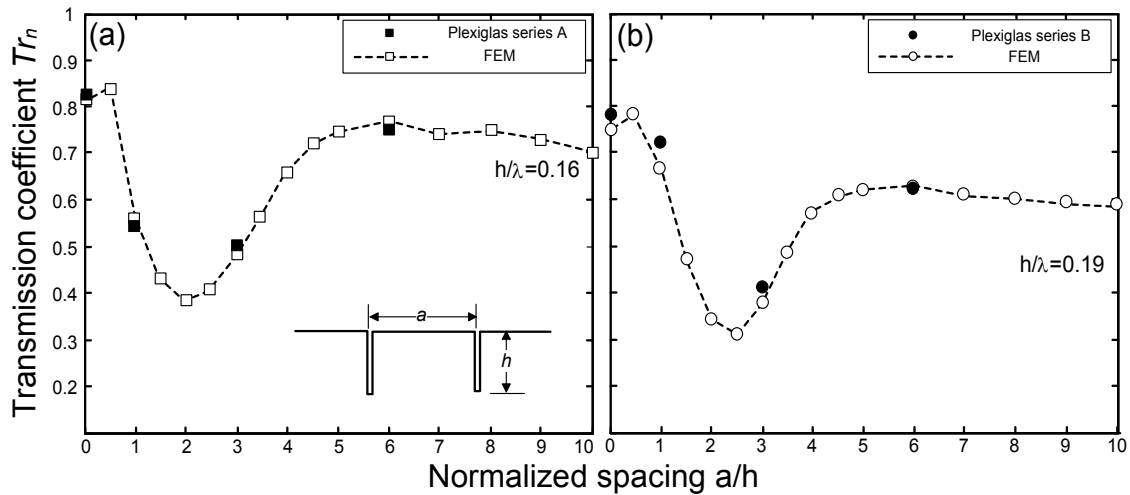
Figure 4-8: Normalized transmission coefficient versus normalized sensor spacing obtained from experimental studies and FE models for: (a) h/λ~0.16, and (b) h/λ~0.19.
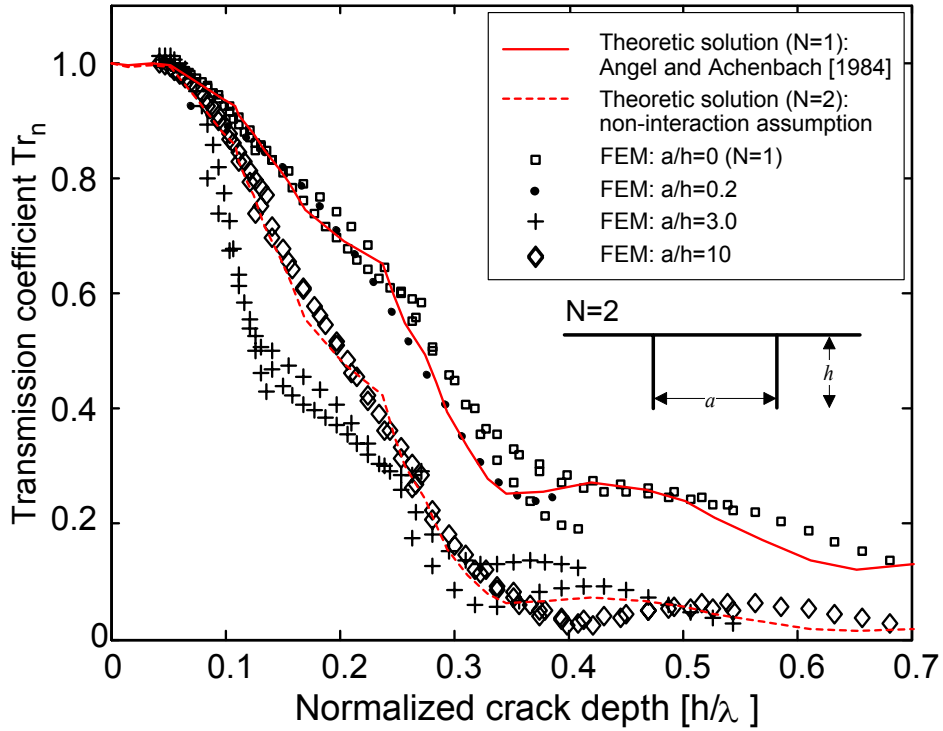
Figure 4-9: Effects of crack spacing a/h on surface wave transmission coefficient.

Figure 4-9 shows Tr_n-h/λ curves for different crack spacings (a/h= 0, 0.2, 3, and 10). The transmission curves for different a/h were obtained by combining the transmission coefficients from five FE models with different h (5, 10, 15, 20, and 25 mm) in frequency range from 10 to 30 kHz. Consequently, for the same a/h, there are overlap h/λ regions. For comparison purposes, the analytic solution of $Tr_n(f_c)$ for a single surface-breaking crack given by Angel and Achenbach [30] is presented as a solid line. $Tr_n(f_c)$ based on the non-interaction assumption (i.e., $Tr_n(f_c, h, N=2)= [Tr_n(f_c, h, N=1)]^2$) is also shown as a dash line in the same figure. For a single crack (a/h=0), the transmission from FEM analyses show good agreement with the analytic solution. When the crack spacing is very small (e.g., a/h~0.2), $Tr_n(f_c, h, N=2)$ is close to the single crack transmission curve. For very large crack spacing (a/h=10), the FEM results converge to the dash line

based on the non-interaction theory. For a/h=3, the interaction effect appears most significant when h/λ is approximately between 0.1 and 0.25.

4.4.3.3   Effects of the number of distributed cracks N on Tr$_n$

Figure 4-10 shows $Tr_n(N)$ versus N curves obtained from FE analyses and experimental measurements from the Plexiglas specimens series B ($a/h=1, 3,$ and 6 with h = 15mm, f_c=15 kHz; h/λ~0.18), where $Tr_n(N)$ is the transmission across N cracks. $Tr_n(N)$ is further normalized by the single crack transmission $Tr_n(1)$. Results from Plexiglas specimens corresponding to a/h of 1, 3, and 6 are presented as solid circles, solid squares and solid triangles, respectively. The surface wave transmission curve based on non-interaction theory is also presented as a solid line in **Figure 4-10**. Consistent with the observations from the two-crack analysis, transmission coefficients of surface waves across three, and four surface-breaking cracks also have the lowest values when $a/h=3$. In addition, the Tr_n-N curve converges to the non-interaction solid line Tr^N when a/h =6.

4.4.3.4   Two surface-breaking cracks with different crack depth h

Figure 4-11 shows the transmission coefficients $Tr_n(f_c)$ versus crack depth ratio h$_1$/h$_2$ between two cracks, where h$_1$ and h$_2$ are the depth of two surface-breaking cracks (see the illustration in **Figure 4-11**). The results in **Figure 4-11** were obtained using the verified FE models. The depth of the second crack h_2 was fixed to 30 mm, while h_1 varies from 0 to 30 mm at an increment of 6 mm. In addition, four crack spacings of 6, 90, 150, and 270 mm were taken into account to investigate the combination effects of a/h_2 and h_1/h_2. The center frequency of incident surface waves in FE analyses was approximately 10 kHz, thus h_2/λ is around 0.24. **Figure 4-11** shows influence of the crack depth ratio h_1/h_2 on transmission coefficients in conjunction with the normalized crack spacing a/h_2.

When h_1/h_2 is sufficiently small (e.g., 6/30), $Tr_n(f_c)$ was dominated by the lager crack depth. In this case, interaction of surface waves between two cracks seems

78

ignorable. However, increasing h_1/h_2 causes higher interaction between two cracks. In this case, effects of h_1/h_2 on $Tr_n(f_c)$ should be understood along with the coupling effects of a/h_2. When a/h_2 is large enough (e.g., $a/h_2=9$), these two surface-breaking cracks can be regarded as two separated cracks so that the transmission coefficient of surface waves across these two cracks converges to $Tr_1 \times Tr_2$, where Tr_1 and Tr_2 are the ransmission coefficients separately calculated from a single crack problem. In addition, when a/h_2 is very small (e.g. $a/h_2 =0.2$), increasing h_1/h_2 does not have much impact on $Tr_n(f_c)$.
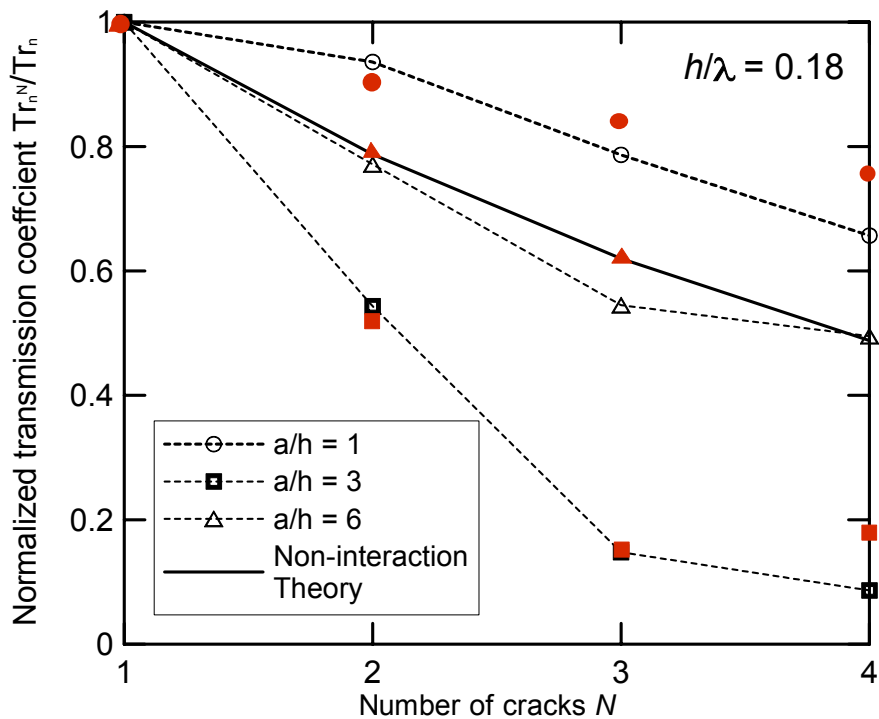
Figure 4-10: Effects of crack spacing a/h on surface wave transmission coefficient for multiple cracks. The dash lines with circles, squares, and triangles are results from numerical simulation (FEM) of a/h=1, 3, and 6, respectively; solid circles, solid squares, and solid triangles were obtained from experiments using Plexiglas specimens with a/h=1, 3, and 6, respectively; and the solid line is corresponding to the theory based on non-interaction assumption.
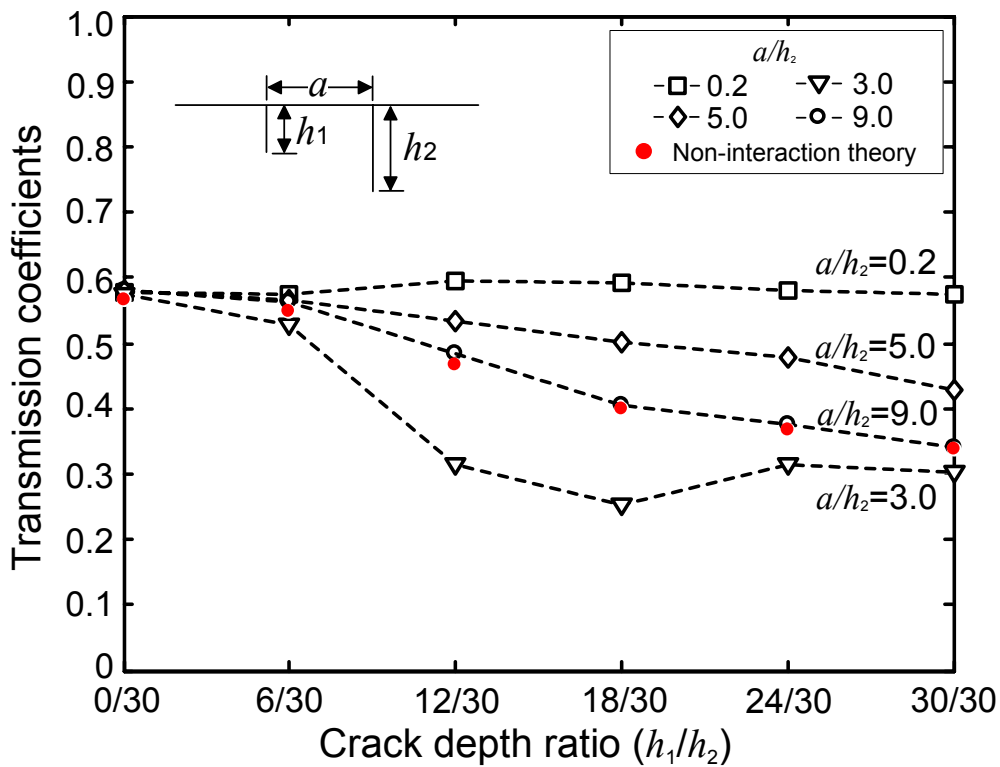
Figure 4-11: Effects of crack spacing a/h on transmission coefficient for two cracks with different crack depths.

4.5 CONCLUSIONS

In this study, near-field scattering of surface waves interacting with distributed surface-breaking cracks was investigated through experimental studies, and numerical simulations (FEM) by considering interaction of surface waves between individual cracks. The conclusions from this study are summarized as follows:

(1) Experimental measurements and numerical simulations (FEM) conducted in this study show that interaction of surface waves between individual cracks becomes significant when the normalized crack spacing a/h is smaller than the threshold value ($a/h \sim 6$). When crack spacing a is less than two times a_n, the forward scattering field caused by the first crack interferes with the backward

scattering field caused by the next crack, resulting in a complex near-scattering field between the cracks.

(2) Interaction of surface waves between individual cracks significantly impacts transmission of surface waves across distributed surface-breaking cracks. Tr_n reaches a minimum value when a/h is between 2 and 3 for the same crack depth h. For very large a/h, the transmission coefficients tend to converge to a constant value.

(3) Tr_n of surface waves decreases with increasing number of cracks N. For large crack spacing a (i.e., non-interaction assumption), Tr_n across N cracks converges to $(Tr_1)^N$.

(4) For the two crack models, the crack depth ratio h_1/h_2 also affects Tr_n in conjunction with the normalized crack spacing a/h_2. When h_1/h_2 is very small, Tr_n is dominated by the lager crack. For very large a/h_2 (e.g., $a/h_2=9$), Tr_n across two cracks converges to $Tr_1 \times Tr_2$ where Tr_1 and Tr_2 are the transmission separately calculated from a single-crack problem. For very small spacing a/h_2, Tr_n converges to Tr_2 which is determined by the larger crack.

Chapter 5   Effects of Multiple Modes of Lamb Waves

The purpose of this chapter is to extend the surface wave transmission (SWT) method to crack-depth estimation problems in plate-like structures. The author investigated near-field scattering of impact-induced surface waves interacting with a surface-breaking crack through experiments and numerical simulations (FEM) using Plexiglas specimens. Based on the results in this study, appropriate source-sensor configurations and frequency-thickness ranges were proposed to reduce contribution of multiple modes of Lamb waves in calculation of transmission coefficients.

5.1   INTRODUCTION

The SWT method was originally proposed for the half-space (or solid medium having a large thickness compared to the wavelength of incident surface waves), in which the transmission function can be determined based on transmission coefficients of fundamental modes (i.e., Rayleigh-like waves in plates [17]). In fact, it is difficult to directly apply the theory to the plate-like structures with a finite thickness because of *(i) contribution of multiple modes (also called higher order modes) of Lamb waves, and (ii) dispersion of fundamental surface waves.* The multiple modes are consequences of constructive and destructive interference of coupled P and S waves guided in a plate with a finite thickness [46]. According to Lamb wave theory, possible multiple modes and their excitability are in function of frequency-thickness (*f-H*: frequency of input source, and thickness of a plate) [17, 47]. In a thick plates (or high frequency input), individual reflection mode is identifiable in the time domain. In this case, the seismic reflection theory allows calculating arrival time of multiple modes, and fundamental modes are separated in the time domain. However, in thin plates (or low frequency input), dispersion of surface waves and interaction of individual reflection modes become

82

significant. In this case, resolving all contributing modes is difficult using a simple signal analysis technique.

The purpose of the study in this chapter is to extend the SWT method to determine the depth of a surface-breaking crack in plate-like structures. The author investigated near-field scattering of impact-induced surface waves interacting with a surface-breaking crack in Plexiglas specimens having various thicknesses (50, 100, and 200 mm), and crack depths (0, 10, 20, 30, and 40 mm). In the experimental study, non-contact air-coupled sensors are used to improve signal consistency and test efficiency in transmission measurements. Based on the research in this study, a practical guideline to select appropriate input frequency for a given thickness of plates, and sensor-receiver configurations are discussed to reduce contribution of multiple modes in calculation of transmission coefficients. The validity of the proposed guideline is verified through experimental studies and comparison analyses with theoretic solution given by previous researchers.

5.2 LAMB WAVE THEORY

Lamb waves are propagating resonances guided in a free plate, which are consequences of multiple reflections of coupled longitudinal and transverse motions, and have infinite set of modes [46, 61]. The resonance modes can be split up into two systems of symmetric (S) and antisymmetric (A) modes, whose velocities depend on relationship between frequency and plate thickness. The infinite sets of individual symmetric (S) and antisymmetric (A) modes can be determined from Rayleigh-Lamb frequency equations as follows:

$$\frac{\tan(\beta H/2)}{\beta} + \frac{4k^2 \tan(\alpha H/2)}{(\beta^2 - k^2)^2} = 0 \qquad \text{for S mod}es \qquad \text{Equation 5-1}$$

$$\beta \tan(\beta H/2) + \frac{(\beta^2 - k^2)^2 \tan(\alpha H/2)}{4k^2 \alpha} = 0 \qquad \text{for A modes} \qquad \text{Equation 5-2}$$

83

where $\alpha^2 = k^2 - k_p^2$, $\beta^2 = k^2 - k_s^2$, and k_p and k_s are compression and shear wavenumber, and H is a thickness of a plate. **Figure 5-1** shows the frequency spectrum of Plexiglas (v=0.33), which is effective to predict possible Lamb wave modes for any given frequency-thickness.

Dominant Lamb modes for a force excitation can be determined using the concept of excitability. The particle displacement for each Lamb mode is proportional to the amplitude of the excitation force of that mode, where the frequency-dependent constant of proportionality is represented by excitability function [47]. In a 2D problem, excitability can be defined as the ratio of particle displacement to excitation force per unit length, thus has a unit of m^2/N. The 2D excitability function for symmetric and antisymmetric Lamb modes generated by a line source was given by Wilcox [47] as follows:

$$E_{zS} = \frac{i}{8\mu} \frac{\alpha[(\beta^2 - k^2)\sinh(\beta d/2)\sinh(\alpha d/2)]}{k(k^2 + \beta^2)\cosh(\alpha h)\sinh(\beta d) - 8k\alpha\beta\sinh(\alpha d)\cosh(\beta d)} \quad \text{for S modes}$$

Equation 5-3

$$E_{zA} = \frac{i}{8\mu} \frac{\alpha[(\beta^2 - k^2)\cosh(\beta d/2)\cosh(\alpha d/2)]}{k(k^2 + \beta^2)\sinh(\alpha h)\cosh(\beta d) - 8k\alpha\beta\cosh(\alpha d)\sinh(\beta d)} \quad \text{for A modes}$$

Equation 5-4

where E is modulus of elasticity, v is Poisson's ratio, and μ is shear modulus [$\mu = E/2(1+v)$].

Figure 5-2 is the 2-D excitability function of Plexiglas (v=0.33) represented in function of normalized frequency (fH/C_R), where C_R is the velocity of Rayleigh wave (=1240 m/s for Plexiglas). For the high frequency-thickness range ($fH/C_R > 2.0$), coupled surface waves (combination of A_0 and S_0 modes) are of most prevalence. In the very low frequency-thickness range (i.e., $fH/C_R < 0.5$), the A_0 mode is dominant. In the transitional region ($0.5 < fH/C_R < 2$), multiple modes show considerable energies at certain combinations of the excitation frequency and thickness.

84
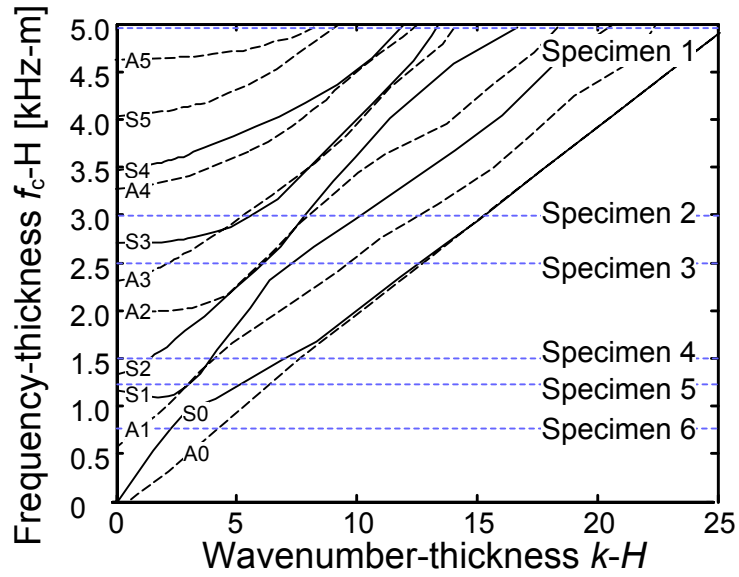
Figure 5-1: Frequency spectrum for the Rayleigh-Lamb frequency equation of Plexiglas (v=0.33).
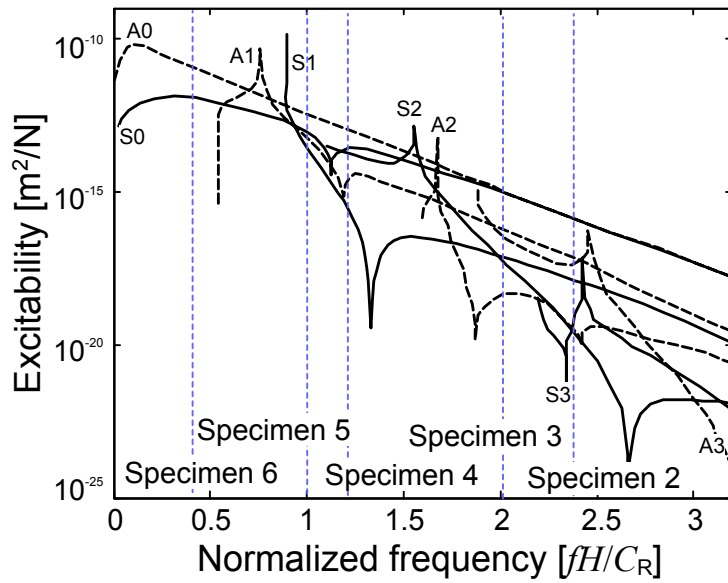
Figure 5-2: Out-of plane excitability functions for the first four symmetric and antisymmetric modes calculated for Plexiglas (v=0.33).

5.3   NUMERICAL SIMULATION

5.3.1   Model description

Numerical simulation of transient behavior of surface waves and Lamb waves in Plexiglas specimens was performed using finite element method (FEM). Previous researchers [51] have demonstrated that FEM is effective to simulate propagation of Lamb waves in a free plate. The main variables in the numerical simulation are thickness of the plate H, duration of the impact source T (frequency contents of excitation forces), and crack depth h.

2D FE models with a surface-breaking crack were developed using rectangular quadratic plane stress elements (CPS4R) implemented in a finite element package (ABAQUS *v 6.7.1, 2007*) as shown in **Figure 5-3**. Specifics for the FE models and loading scheme are available in Chapters 3 and 4.
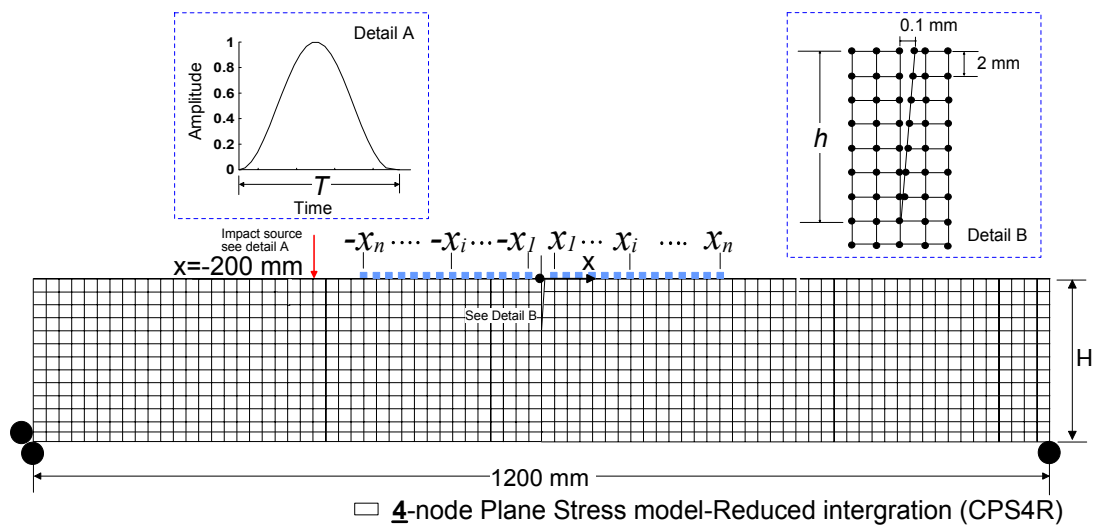
Figure 5-3: FE model for numerical simulations**.**

5.3.2   Determination of surface wave transmission

Transmission coefficients of surface waves across a surface-breaking crack are investigated in the frequency domain. The surface wave transmission coefficient Tr is defined as the frequency response ratio between the cracked model and the crack free model as follows,

$$\mathbf{Tr}_n = \frac{\mathbf{S}_b(f,h)}{\mathbf{S}_a(f,h)} / \frac{\mathbf{S}_b(f,0)}{\mathbf{S}_a(f,0)} \qquad \text{Equation 5-5}$$

where S_a and S_b are the Fourier transforms of the vertical velocity responses measured by sensors located at before and after a crack respectively. A window function (hanning window) with size of 2 times period was applied at the minima of surface wave components before the Fourier transform [7, 8].

5.4   EXPERIMENTAL PROGRAM

5.4.1   Preparation of specimens

Plexiglas specimens with a length of 1220 mm, a width of 6.4 mm and different thicknesses of 50, 100, and 200 mm were prepared in laboratory. Each Plexiglas specimen contained a surface-breaking crack with different depths of 0, 10, 20, 30, and 40 mm. The specimens were set upright position as shown in **Figure 5-4**. Steel balls with three different diameters were used to generate impact-induced surface waves with different frequency contents. The width of the specimens (=6.4 mm) is small enough compared to wavelengths of incident surface waves so that stress wave propagation can be explained as generalized plane stress theory [55]. In this study, six different levels of f_c-H caused by various combinations of thicknesses and frequency contents were covered, where f_c is center frequency of incident surface waves. Frequency-thicknesses of the Plexiglas specimens were denoted as dashed lines in the frequency spectrum in **Figure**

5-1. The properties of the Plexiglas specimens and impact sources are summarized in **Table 5-1**.
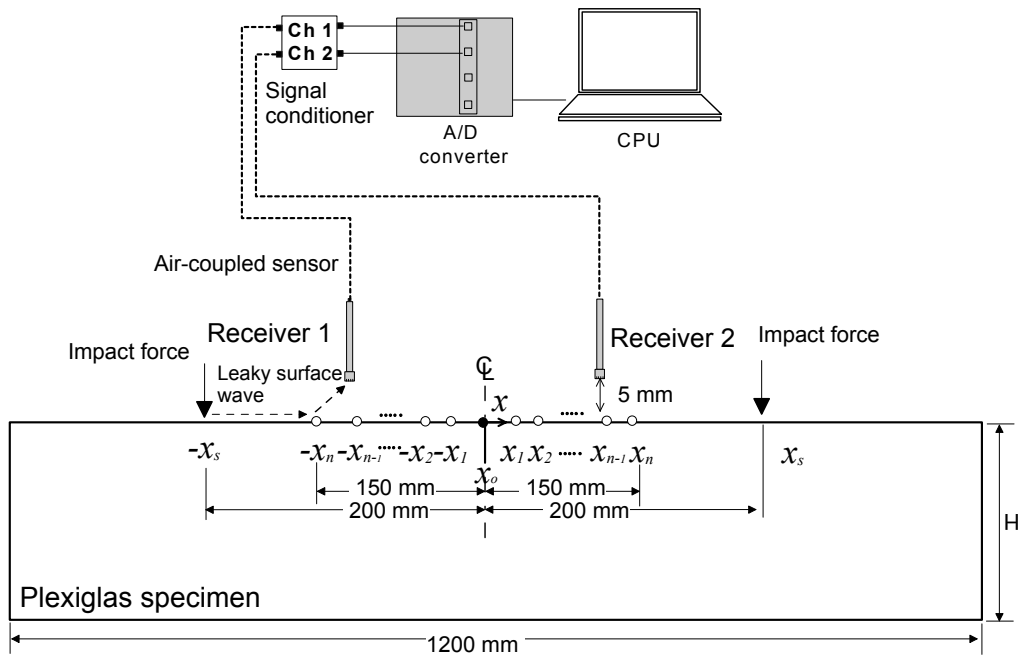
Figure 5-4: Test setup and data acquisition system for air-coupled sensors.

Table 5-1: Properties of Plexiglas specimens for experiments

Specimens	Specimen size			h [mm]c	f_c [kHz]
	L [mm]	W [mm]	H [mm]		
#1			200		25
#2			200		15
#3			100		25
#4	1200	6.3	100	0,10,20,30,40	15
#5			50		25
#6			50		10

5.4.2 Test setup, data acquisition, and signal processing

Two air-coupled sensors (PCB model No. 377B01) were used to measure surface waves propagating on a free surface of Plexiglas specimens. Transmission coefficients of surface waves were measured using a test setup based on the self-calibrating procedure [7, 9]. To investigate the effects of sensor locations of transmission measurements of surface waves, the distance of each sensor from a crack opening ($\pm x_i$) varies from ± 10 to ± 150 mm at an increment of ± 10 mm (see **Figure 5-5**). Typical time signals measured in six crack-free Plexiglas specimens using air-coupled sensors located at $x_i=\pm 70$ mm are shown in **Figure 5-5**. Original signals and windowed signals were drawn as dash lines and solid lines respectively. Similar to the numerical signals, windowed signals were obtained by applying a hanning window with size of 2 times period at the minima of surface wave components. Transmission coefficients were calculated in the frequency domain using Equation 5-6.

$$\mathbf{Tr}_h = \sqrt{\frac{\mathbf{S}(x_{S1}, x_i)\mathbf{S}(x_{S2}, -x_i)}{\mathbf{S}(x_{S1}, -x_i)\mathbf{S}(x_{S2}, x_i)}} \qquad \text{Equation 5-6}$$

where Tr_h is transmission coefficients measured from a specimen with a crack depth of h, and $\mathbf{S}(x_{s1}, x_i)$ is the Fourier transform of the windowed time signal generated by an impact source at x_{s1} and measured by the air-coupled sensor at x_i. Previous researchers [7-9, 40] demonstrated that the self-calibrating procedure is effective to eliminate experimental variability caused by impact source and sensors.

In addition, Tr_h was further normalized by Tr_0 obtained from crack-free specimens to eliminate the geometric attenuation and material damping, resulting in normalized transmission coefficient Tr_n. In addition, to improve signal-to-noise level, spectral coherence curves were also calculated based on five repeated signal data collected at the same location using Equation 3-9.
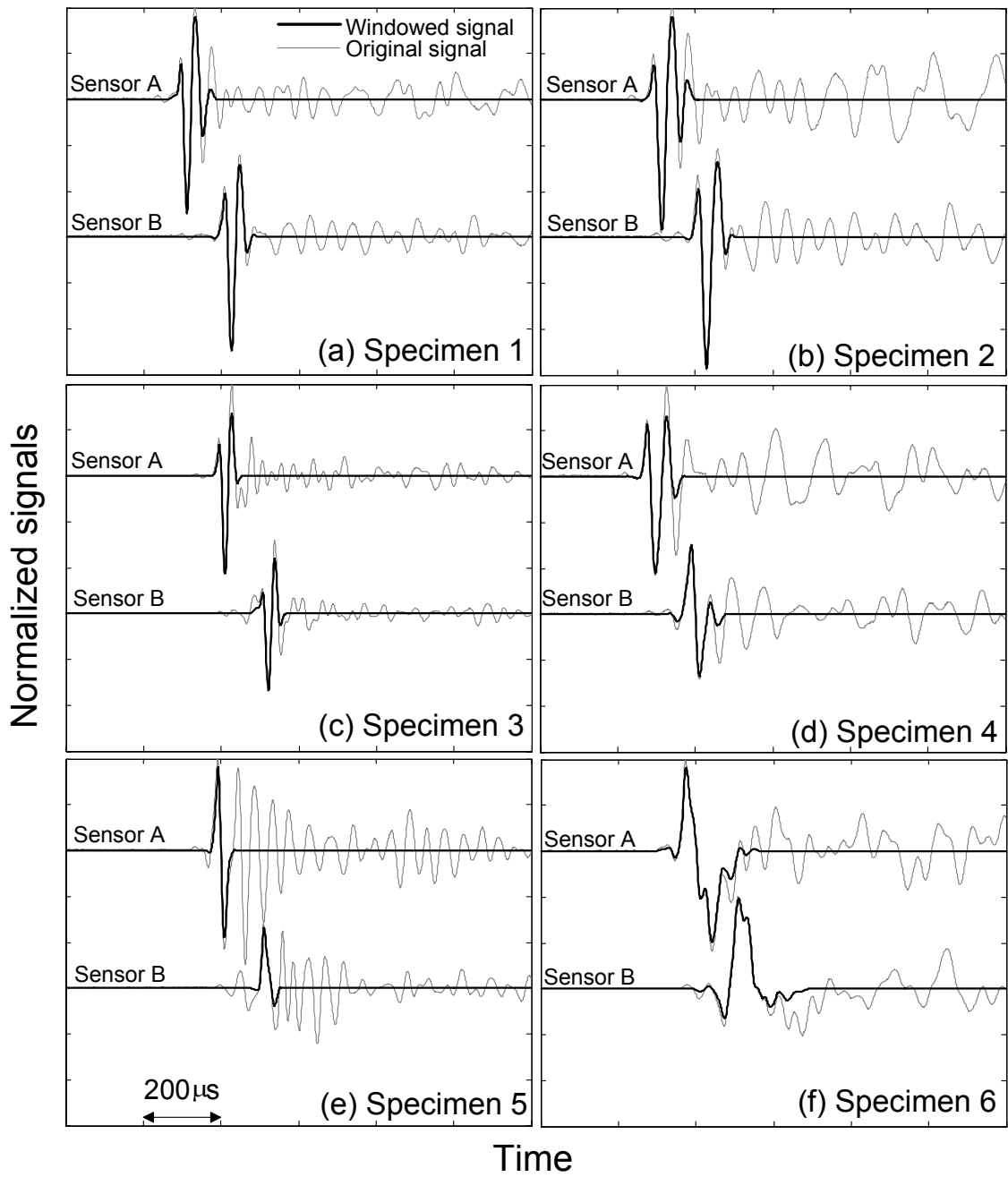
Figure 5-5: Original signal and windowed time signal data measured in Plexiglas specimens using air-coupled sensors A and B located at $x_i = \pm 70$ mm by applying an transient impact at $x_s = -200$ mm (see **Figure 5-4**).

90

5.4.3 Comparison of signals from experiments and FE models

Comparison analyses were carried out to check the validity of the finite element models. The normalized out-of plane velocity responses ($V_y(x_i, t)/\max(V_y(x_i, t))$) obtained from the finite element model were compared to the measured signal data using a laser vibrometer. Test setup of using the laser vibrometer is shown in Figure 4-2(a). **Figure 5-6** is a plot representing the time-domain signal data obtained from the Plexiglas specimens 1 and 5 and corresponding FE models. The solid lines are measured signal data at seven locations (x=0, ±50, ±100, and ±150 mm), and the dashed lines are for the calculated signal data from FE analyses. For comparison purposes, first arrivals of the multiple reflected waves are shown as solid lines (blue). Note that arrival time of individual reflected waves can be determined by using seismic reflection theory (see Appendix B). The overall trend of the measured time-domain signals shows good agreement with those from FE analyses. For the specimen 1 (f_cH/C_R~4.0), main pulses of surface
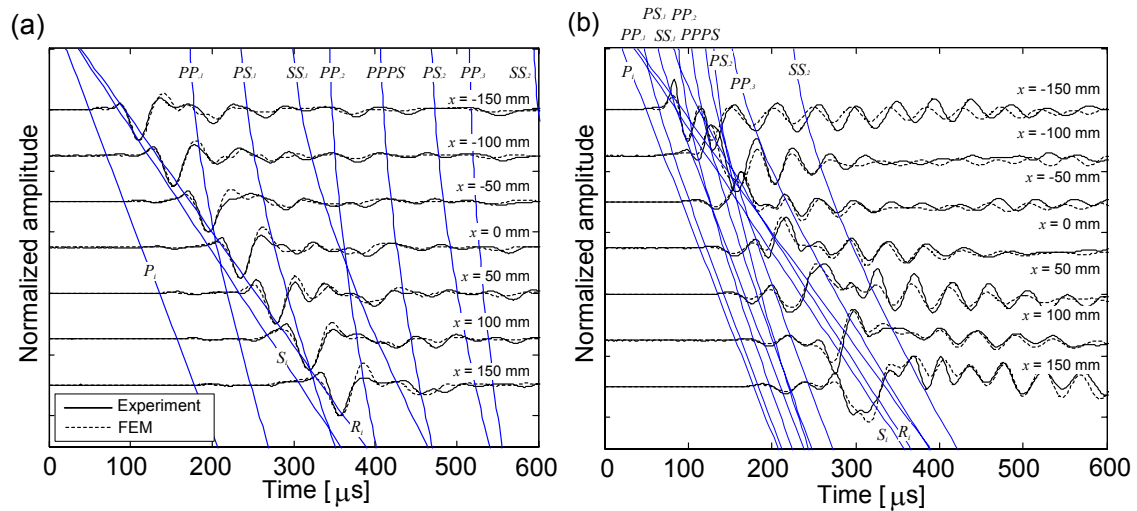
Figure 5-6: Comparison of time-domain signals from the crack-free Plexiglas specimens with corresponding FE models: (a) the Plexiglas specimen 1 with H=200mm and f_c=25 kHz, and (b) the Plexiglas specimens 5 with H=50mm and f_c=25 kHz.

waves calculated using FE models are matching well with the corresponding measurements from the Plexiglas specimens. For the specimen 5 ($f_c \sim f_{IE}$), resonant behavior of higher-order Lamb wave mode (i.e., S1 mode) was clearly observed in the calculated signals and measured signals. The good agreements in the time-domain signals verify the validity of the FE models used in this study.

5.5   NEAR-SCATTERING FIELD OF SURFACE WAVES IN A FREE PLATE

In this section, near-scattering field of surface waves in a free plate is explored using the verified FE models to better understand interference of direct surface waves and multiple reflected waves. **Figure 5-7** (a) and (b) are B-scan images representing impact-induced stress wave fields for the crack-free specimens with thicknesses of 200 and 50 mm. For comparison purposes, first arrivals of possible wave modes were calculated based on seismic reflection theory and presented as dash lines. Direct P, S and surface waves are denoted as P_i, S_i, and R_i. In addition, first several modes caused by multiple reflections of coupled P and S waves are denoted as PP_n, SS_n, PS_n, and $PPPS_n$, where PP and SS are reflected P and S waves (P-P, and S-S), PS is mode converted waves (P-S), and n is the number of reflections in a free plate. For specimen 1 (H=200 mm), individual reflected waves can be separated in the time-domain: whereas for specimen 5 (H=50 mm), individual reflected waves are no longer distinguishable, but constructive and destructive interference of individual mode results in several resonant modes.
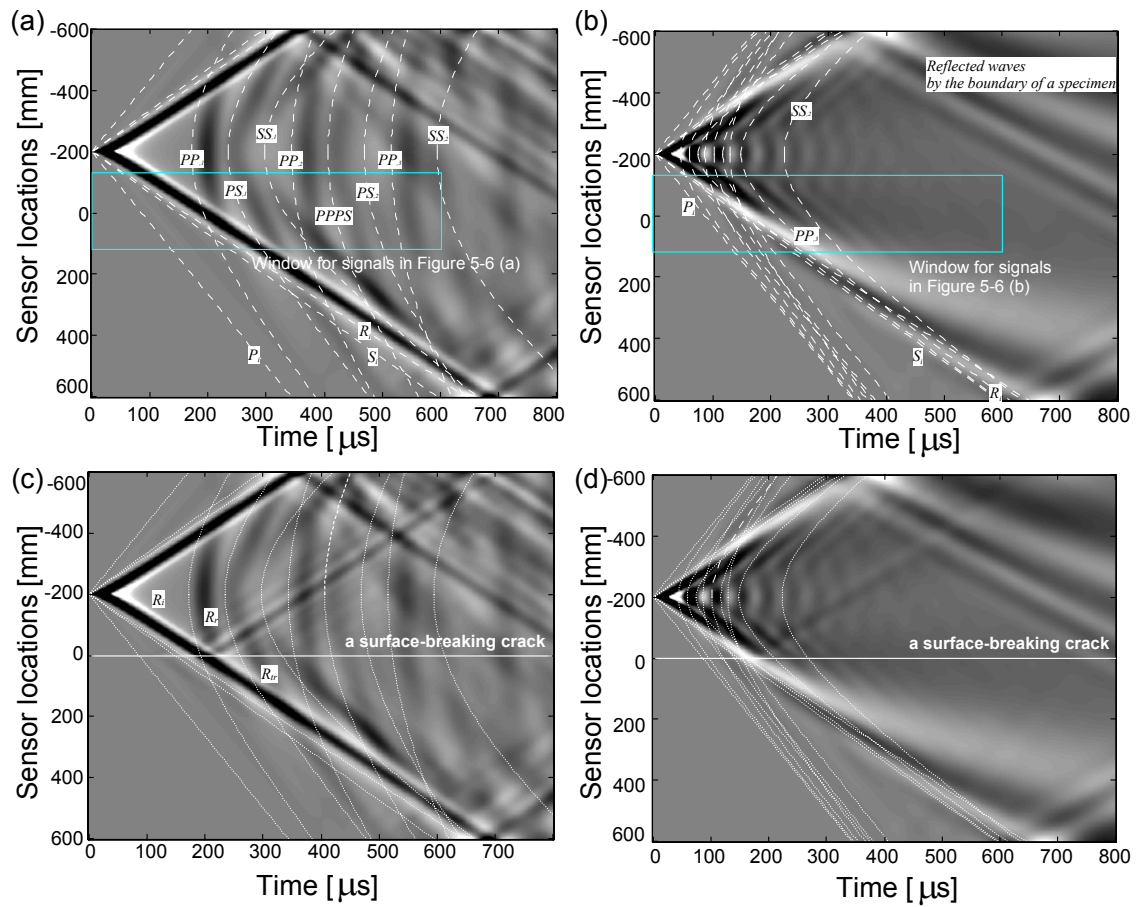
Figure 5-7: B-scan images representing near-field scattering of surface waves across a surface-breaking crack in Plexiglas specimens: (a) *H*=200mm, *f*c=25 kHz, and *h*=0, (b) *H*=50mm, *f*c=25 kHz, and h=0, (c) *H*=200mm, *f*c=25 kHz, and *h*=10 mm, (d) *H*=50mm, *f*c=25 kHz, and *h*=10 mm.

Figure 5-7 (c) and (d) are B-scan images of near-scattering fields of surface waves for the specimens 1 and 5 having a depth of 10 mm. Consistent with observations from previous researchers [34, 40], mode converted waves (R_i-R_s-P) as well as transmitted-, and reflected surface waves (R_i-R_t, and R_i-R_r) are clearly observed in the near-scattering field of surface waves, where R_i, R_t, R_r, and R_s are incident, transmitted, reflected surface waves, and surface skimming waves [34]. Previous researchers showed that a surface-breaking crack cause near-field effects in transmission measurements (i.e., transmission

93

enhancement when sensors are located too closed to a crack). In addition, for a free plate, contribution of multiple modes may affect transmission coefficients of surface waves.

5.6   TRANSMISSION MEASUREMENT

This section serves to quantitatively investigate near-field effects and interference of surface waves with higher-order Lamb waves on transmission measurements of impact induced surface waves.

5.6.1   Effects of sensor locations on Tr_n

Figure 5-8 (a)-(c) present normalized transmission coefficients of center frequency $Tr_n(f_c)$ versus normalized sensor location x/λ measured from the Plexiglas specimens and FE models corresponding to specimens 1, 2 and 6, respectively. First, consistent with previous researches [34, 40, 44], transmission coefficients are significantly enhanced when sensors are located in the near-field of a surface-breaking crack. For comparison purposes, near-field size calculated using Equation 3-4 was also pointed out by arrows in the same figures. Although obtained from the numerical simulation in high frequency-thickness range, the equation was still effective to determine near-field size in low-frequency range (specimen 6). In addition, for the specimens 1 and 2 (high frequency-thickness regions), further increasing x/h resulted in oscillatory behavior in transmission coefficients. Oscillation is also observed in a half-space model, shown as blue dash lines in **Figure 5-8** (a) and (b). However, amplitude of oscillation in a plate model is higher than in a half-space model. It can be seen that this is mainly construction interference of multiple reflected waves (i.e., $PP_{,1}$ and $PS_{,1}$) and direct surface waves as seen in **Figure 5-6** (a).

94
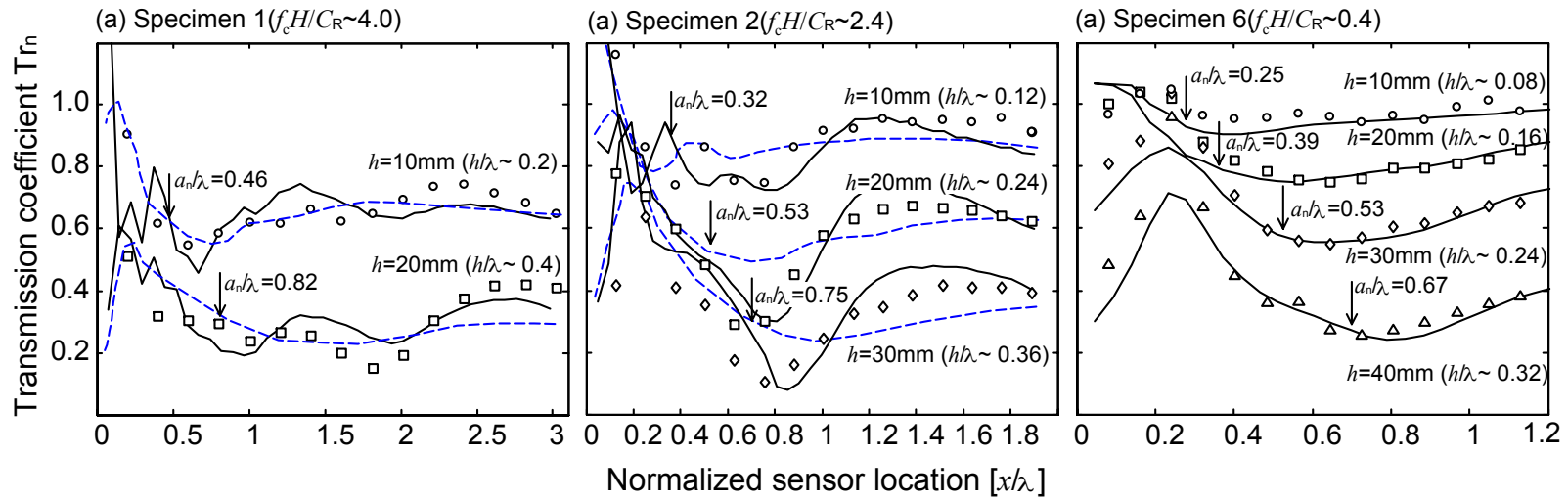
Figure 5-8: Transmission coefficient versus normalized sensor location obtained from experiments and numerical simulations: (a) H=200mm and f_c=25 kHz, (b) H=200mm and f_c=15 kHz, and (c) H=50mm and f_c=10 kHz. Note – : numerical results from a plate model, and ---: numerical results from a half space model described in Chapter 3.

95

5.6.2 Tr_n versus h/λ for thick plates (or high frequency region)

For thick plates, individual reflected waves are identifiable in the time domain when main pulses of surface waves arrives at a sensor earlier than multiple reflected waves. The arrival times of incident surface waves t_R and reflected waves t_M (e.g., PP_n, SS_n, and PS_n), can be expressed in terms of sensor location from a source a_i, wave velocities (C_R, C_P, and/or C_S), and thickness of plates H (see Appendix B). In the backward scattering field, incident surface waves can be completely separated from any multiple reflect waves when sensors are located according to Equation 5-7,

$$t_R + T < t_{PP,1} \quad \text{in the backward scattering field} \qquad \text{Equation 5-7}$$

where $t_{PP,1}$ is first arrival time of PP,1 (see Appendix B). In the forward scattering field, Equation 5-7 may not provide a practical sensor-receiver configuration for the SWT method except for very thick plates. However, as seen in **Figure 5-7**, attenuation of $PP_{,1}$ is apparent with moving a sensor farther from a source, while PS,1 still remain considerable energy at a certain distance. This implies that PS,1 is more critical in the forward scattering field. Therefore, Equation 5-8 may provide a reasonable a_i for the sensor in the forward scattering field.

$$t_R + T < t_{PS,1} \quad \text{in the forward scattering field} \qquad \text{Equation 5-8}$$

where $t_{PS,1}$ is first arrival time of PS,1 (see Appendix B).

Equations 5-7 and 5-8 mean that a_i is dependent of several parameters (i.e., H, T, and material properties (E, v, and ρ) of a plate). For the Plexiglas specimen 1 in a frequency range of 20 to 40 kHz, a_i for separating surface waves from the first earlier modes PP_1, and PS_1 are as follows

$$
\begin{aligned}
a_i &< 0.17\,m \\
a_i &< 0.30\,m
\end{aligned}
\qquad \text{Equation 5=9}
$$

96
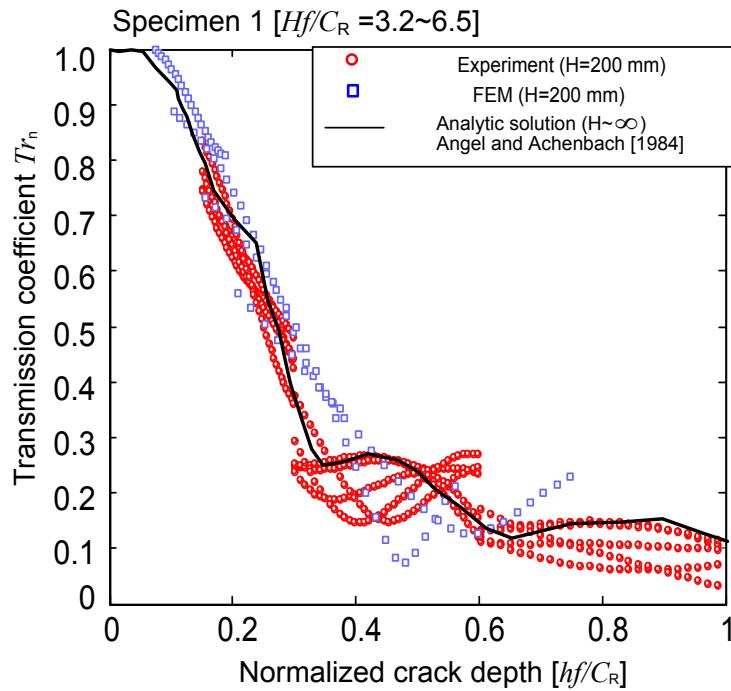
Figure 5-9: Transmission coefficient versus normalized crack depth obtained from experiments and numerical simulations for the high frequency-thickness range. All transmission coefficients were measured by sensors located at 60-100mm to minimize the near-field effect and interference of direct surface waves and multiple reflected waves.

Figure 5-9 shows the Tr_n and h/λ relation obtained from Plexiglas specimen 1, and corresponding FE models. All transmission coefficients were obtained in a frequency range of 20 to 40 kHz, which covers a frequency-thickness range fH/C_R of 3.2 to 6.5. The transmission coefficients shown in **Figure 5-9** were obtained at the sensors located $x_i = \pm60\sim\pm90$ mm, in which surface waves are well separable to PP_1 in the backward scattering field, and to PS_1 in the forward scattering field. The results from experiment and numerical simulations show fairly good agreement with the analytic solution given by Angel and Achenbach (1984). The analytic solution was obtained on the ideal far-field in the semi-infinite model. This demonstrated that the sensor locations from Equation 5-7, and Equation 5-8 are effective to reduce interference of surface waves and multiple reflected waves from the bottom surface in the free-plate.

97

Figure 5-10 presents effects of multiple modes (especially PS$_1$) on transmission calculation. The transmission coefficients Tr_n shown in **Figure 5-10** (a) were calculated for frequencies of 25, 30, and 35 kHz from the Plexiglas specimen 1. For **Figure 5-10** (b), Tr_n were corresponding to frequencies of 10, 15, and 20 kHz from the Plexiglas specimen 2. Tr_n presented as solid squares were obtained from the sensors located x_i = ±100~±150 mm in **Figure 5-10** (a), and x_i = ±110~±150 mm in **Figure 5-10** (b), respectively, in which multiple reflected waves (PS$_1$) interfere with the direct surface waves in the forward scattering field (see **Figure 5-7** (c)). For comparison purposes, Tr_n from sensors at x_i = ±60~±100 mm and x_i = ±80~±100 mm were also presented as open circles in **Figure 5-10** (a) and (b). It can be seen that contribution of PS$_1$ may increase experimental variability and magnitude of Tr_n, especially in a range of $1/3 < h/\lambda < 1.2$.
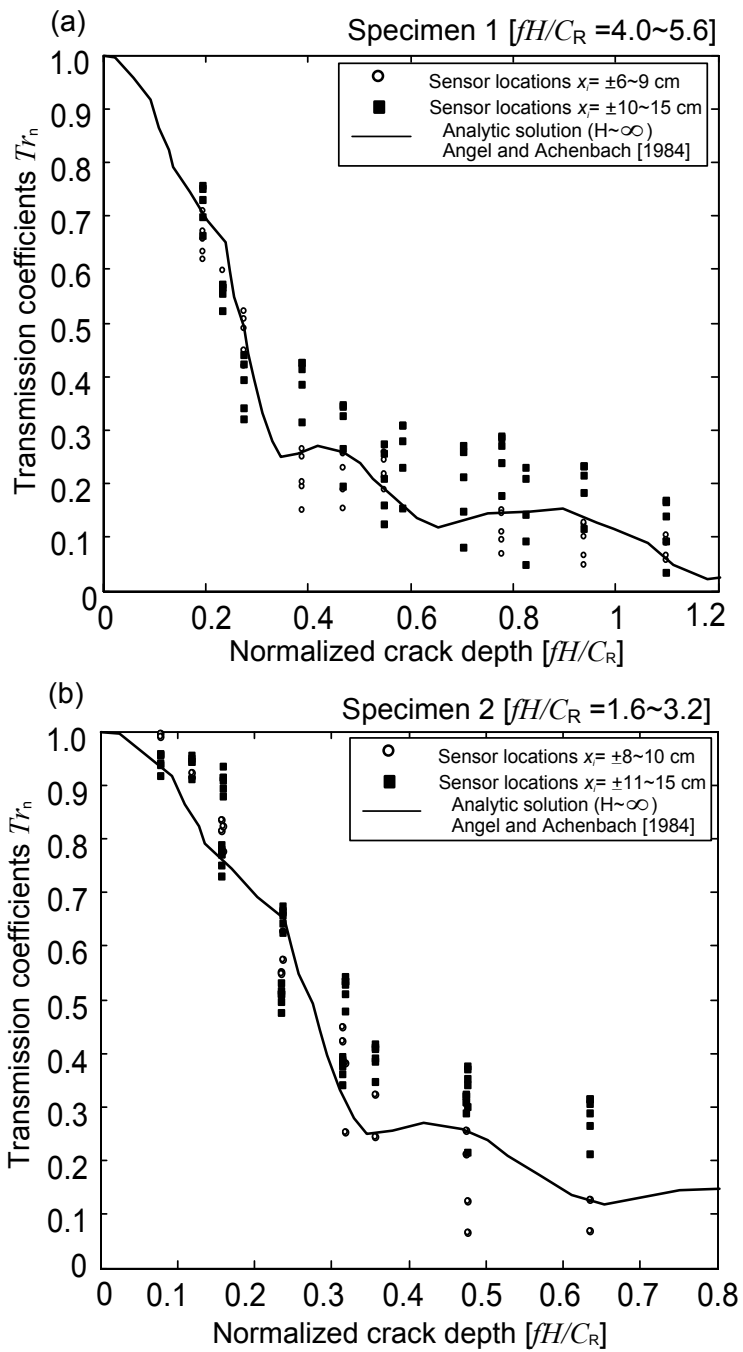
Figure 5-10: Transmission coefficient versus normalized crack depth obtained from various sensor locations in (a) the Plexiglas specimen 1, and (b) specimen 2.

5.6.3 Tr_n versus h/λ for medium thickness ($1.6 < f\text{-}H/C_R < 2.0$)

Decreasing $f\text{-}H/C_R$ results in narrower range of a_i from Equation 5-7 and 5-8, which makes more difficult to separate surface waves from multiple reflected waves. **Figure 5-11** shows the Tr_n and h/λ relation obtained from Plexiglas specimens 3 and 4 having a thickness of 100 mm (see **Table 5-1**). All transmission coefficients were calculated for frequencies of 20, 25, and 30 kHz from the Plexiglas specimen 3, and 15, 20, and 25 kHz from the Plexiglas specimen 4. This covers $f\text{-}H/C_R$ in a range of 1.2 to 2.2. In addition, the Tr_n were obtained from different sensors located $x_i = \pm 60, \pm 80, \pm 100, \pm 120,$ and ± 140 mm to investigate effects of sensor locations.

Variations of the transmission coefficients are significant, especially in a range of h/λ of 1/3 to 1.2. Furthermore, for the same h/λ, Tr_n are very sensitive to the location of sensors due to contribution of multiple modes. In this case, the analytic solution for thick plates cannot be used for estimation of a crack-depth. Moreover, too many variables affect the transmission function. One reasonable approach is to define and use a transmission function resulting from the propagation of all contributing modes for the fixed sensor location. This concept is applied to evaluate the depth of surface-breaking crack in a concrete slab in Chapter 6.
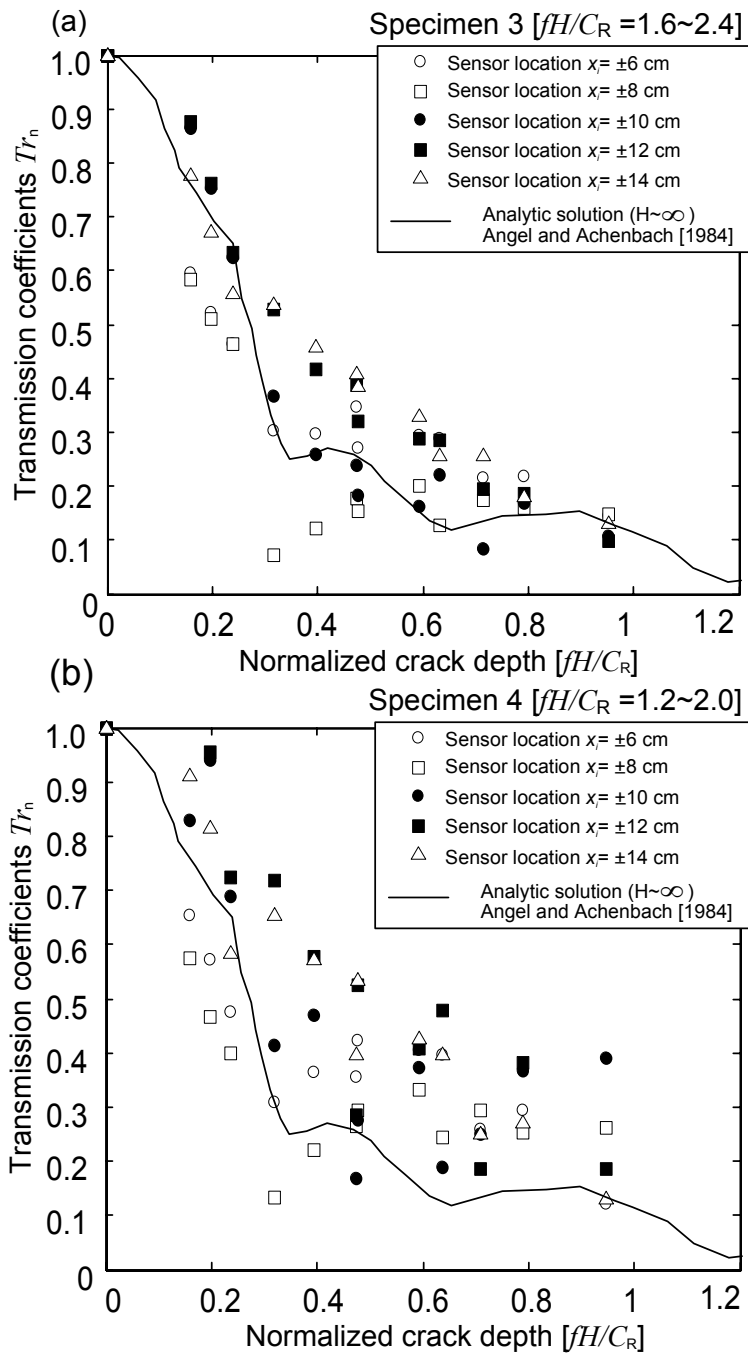
Figure 5-11: Transmission coefficient versus normalized crack depth obtained from various sensor locations in (a) the Plexiglas specimen 3, and (b) specimen 4.

101

5.6.4 Tr_n versus h/λ for resonance region $0.5 < f\text{-}H/C_R < 1.6$

The resonance region is defined as $0.5 < f\text{-}H/C_R < 1.6$ according to the excitability function of individual higher order Lamb wave modes (see **Figure 5-2**). In this region, constructive and destructive interference of multiple reflection modes results in resonance modes, especially higher excitability in the frequency of S1 zero group velocity. As shown in **Figure 5-7** (b), the resonance modes overlap into direct surface waves in the time domain. One simple way to reduce interference effects is to resolve all contributing modes in the frequency domain; however, this needs a large number of sensors [51]. Moreover, contribution of higher-order modes to transmission coefficients is significant because of high excitability of resonance modes. Generally, higher-order modes are not as sensitive as fundamental modes to the depth of surface-breaking crack. Therefore, it is reasonable to avoid this frequency-thickness range in the transitional region for the SWT method based on a limited numbers of sensors.

5.6.5 Tr_n versus h/λ for thin plates ($fH/C_R < 0.5$)

For very low frequency, the fundamental Lamb wave modes are dominant. Spectral energy distribution of waves reveals that direct surface waves are dispersive, and A_0 Lamb mode is dominate in this case. **Figure 5-12** shows the Tr_n versus h/λ obtained in the fH/C_R in a range between 0.28 and 0.48. Transmission coefficients were measured from a group of the Plexiglas specimen 6, and were presented in function of h/λ, where $\lambda = C_{ph,Ao}/f$. Phase velocity of the fundamental Ao mode $C_{ph,Ao}$ was obtained from a dispersion curve calculated by SASW (Spectral Analysis of Surface Waves) [62], and presented in **Figure 5-13**. $C_{ph,Ao}$ measured by air-coupled sensors shows good agreement with those obtained from FE models and analytic solution using Equation 5-2. A transmission curve of Ao Lamb mode obtained using numerical simulation (the hybrid BEM) by Cho and Rose [63], and analytic solution by Angel and Achenbach [30] are also presented in the same figure. For the same h/λ, the experimental results from impact-
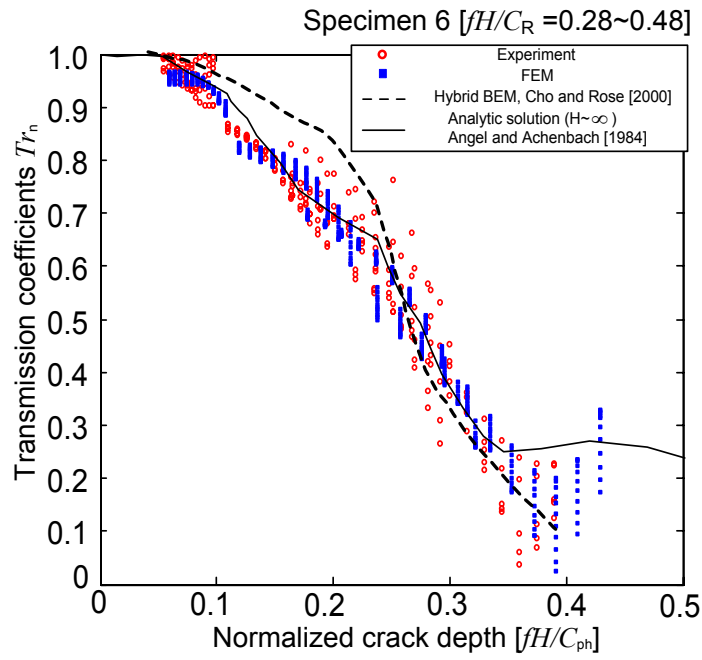
Figure 5-12: Transmission coefficient versus normalized crack depth obtained from experiments for the low frequency-thickness range.
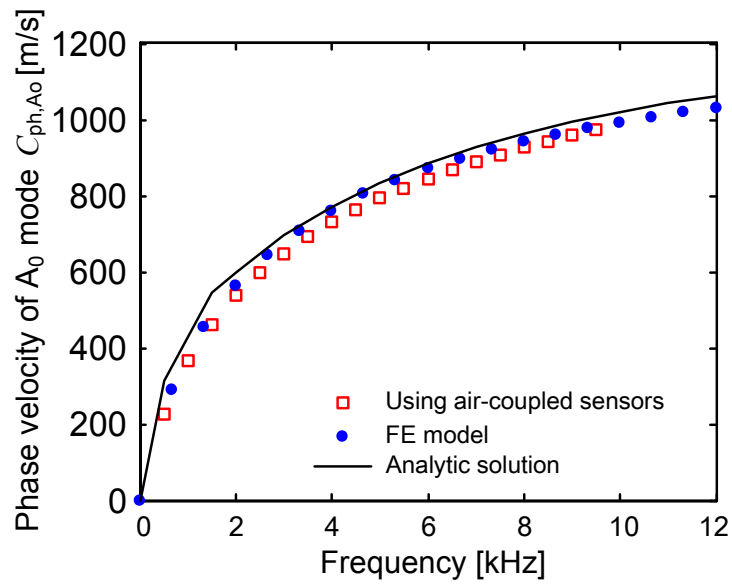
Figure 5-13: Phase velocity of A_0 Lamb wave mode versus frequency.

103

induced surface waves matched with transmission coefficients of A_0 Lamb waves by Cho and Rose [63], especially in $0.2 < h/\lambda < 0.4$. Furthermore, the experimentally measured Tr_n shows good agreements with analytic solution of Tr_n for surface waves in half-space. It can be seen that the transmission curve based on half-space is also effective to estimate the depth of surface-breaking crack in plate-like structures.

5.7   CONCLUSIONS

Near-field scattering of surface waves interacting with a surface-breaking crack in a free-plate was investigated in this study. Through experimental studies and numerical simulations (FEM), effects of multiple-reflected waves by the bottom of a free-plate on transmission coefficient of direct surface waves across a surface-breaking crack were examined in a wide range of frequency-thickness (f-H), and different sensor locations. As a result, appropriate source-sensor arrangements and frequency-thickness ranges were proposed to minimize interference of direct surface waves with the multiple-reflected waves. The specific conclusions obtained from this study are summarized as follows:

1) Consistent with previous studies obtained from a half-space model, near field scattering significantly increases transmission coefficients of surface waves measured in the Plexiglas specimens with finite thicknesses. Observations in this study show that an approximate near-field size a_n determined from a half-space was effective to minimize near-field effects in a free-plate in high (f-$H/C_R > 2$) and low frequency-thickness ranges (f-$H/C_R < 0.5$).

2) In addition to the near-field effect, for the specimens 1 and 2 in the high frequency-thickness f-H ranges, increasing sensor location-to-crack depth ratio x/h causes oscillatory behavior in transmission coefficients. This is mainly due to constructive interference of multiple reflected waves (particularly PS_1) with direct surface waves. For the high frequency-thickness range (f-$H/C_R > 4$), the seismic

104

reflection theory can be used to determine sensor locations to avoid the interference effect.

3) For the high-frequency range (f-H/C_R >2), the Tr_n and h/λ relation from experiment and numerical simulations based on sensor location ($a_n < x < a_i$) show fairly good agreement with the analytic solution calculated in the ideal far-field on the half-space model.

4) For low frequency-thickness range (f-H/C_R <0.5), antisymmetric Lamb wave mode (A_0) have most prevalence. Results from experimental studies and numerical simulation (FEM) demonstrated that the Tr_n versus h/λ based on the half-space is also effective to estimate the depth of surface-breaking crack in plate-like structures in low-frequency range. In this range, phase velocities of dispersive surface waves were determined by SASW (spectral analysis of surface waves).

5) For the transitional range of frequency-thickness (0.5< f-H/C_R <2), construction and destruction interference of the multiple-reflected waves result in resonance modes at certain frequency-thickness (i.e., cut-off frequency-thickness of higher order Lamb waves). Considerable energies are imparted by resonance modes, which are not informative on the depth information of a surface-breaking crack.

PART III APPLICATION TO CONCRETE (LAB TEST)

Chapter 6   Air-coupled Sensing Technique for Concrete NDT

6.1   INTRODUCTION

Air-coupled ultrasonic transducers have been widely investigated for non-contact NDT of solid materials since early 1970's. The practical advantages and limitations of using air-coupled sensors in nondestructive material inspections have been recognized for a long time [64]. The main advantages of using air as the couplant are the lack of contamination of materials under study, and the potential for rapid scanning due to elimination of direct contact. Therefore, air-coupled ultrasonic technique enables a number of inspections that were previously unavailable. For example, air-coupled sensors can be used for the inspection of materials that could not be immersed in water or that would be damaged by physical contact with an ultrasonic transducer: which includes wood assessment [65], paper products [66], food [67], propellants and explosives [64] and advanced composite materials in the aerospace engineering [68].

Recently, the non-contact air-coupled sensing techniques have been proposed as a possible solution for rapid scanning of large concrete structures in civil engineering. Leaky surface waves and Lamb waves in concrete structures have been successfully measured by Zhu and Popovics [10-13]. Zhu's studies have shown that air-coupled sensors can be used in many NDT methods for concrete, e.g., SASW (Spectral Analysis of Surface Waves) [13], MASW (Multi-channel Analysis of Surface Waves) [13], Impact-echo (IE) [11], surface wave attenuation [12], and ultrasonic wave measurements [13]. Furthermore, air-coupled sensors have also been used to characterize the material properties of asphaltic concrete [15]. Ryden *et al*. [14] applied a multichannel array of microphones to measure asphalt concrete pavements and softer granular pavement using leaky air-coupled surface waves.

A fundamental background of air-coupled sensing technique for concrete NDT is summarized in this chapter. Section 6.2 describes fundamentals of air-coupled sensors for

application to concrete structures. Test setup to measure leaky surface waves using air-coupled sensors is described in Section 6.3. Furthermore, the self-calibrating procedure to obtain the transmission coefficient and the phase velocity of the surface waves using air-coupled sensors is discussed in Section 6.4. Accuracy of air-coupled sensors is also compared with the conventional contact sensors (accelerometers) in Section 6-5. In addition, effects of open traffics on applicability of air-coupled sensors to field inspections of concrete bridge decks are discussed in section 6.6.

6.2   AIR-COUPLED SENSORS

Transducers for the generation and reception of acoustic waves are heart of an air-coupled ultrasonic NDE system. Grandia and Fortunko [64] summarized the electro-acoustic air transducers, and their frequency regions (see **Figure 6-1**). The most commonly used air-coupled sensors are based on *(i) piezoelectric and (ii) electrostatic designs*.

A piezoelectric air transducer uses a quartz or man-made ceramic crystal structure, which exhibits a permanent polarization. These sensors are inherently resonance devises, and require special backing to obtain suitable damping coefficients. The application of a matching layer limits the overall bandwidth of the device; which generates narrow bandwidth. Although having very low sensitivity levels, the piezoelectric air transducers are very durable and are able to measure very high amplitude pressure ranges. Conversely, the floor noise level on this type of sensor is generally very high. Therefore, this design is suitable for shock and blast pressure measurement applications.

In contrast, electrostatic or capacitance transducers have much broader bandwidths and high sensitivities. The class of electrostatic transducers includes (i) the condenser microphone, (ii) the solid-dielectric microphone, and (iii) the new wide-band, capacitive transducer, which is made using silicon-micro-machining techniques [64].

108
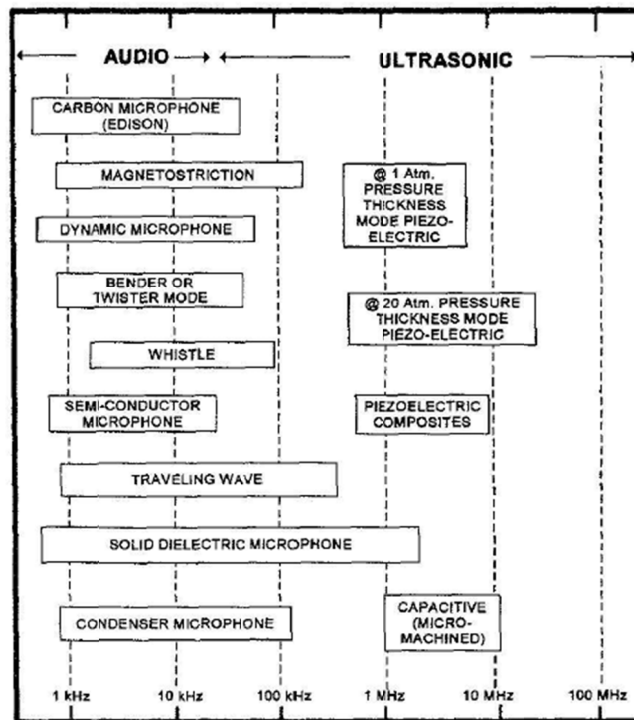
Figure 6-1: Frequency range of various air-coupled sensors (after Grandia and Fortunko [64]).

At low frequencies below 100 kHz, condenser microphones can be a good choice to generate and receive ultrasound in air. A condenser microphone (see **Figure 6-2**) operates on a capacitive design [69]. The cartridge from the condenser microphone utilizes basic transduction principles and will transform the sound pressure to capacitance variations, which are then converted to an electrical voltage. This is accomplished by taking a small thin diaphragm and stretching it a small distance away from a stationary metal plate, called a "back plate." A voltage is applied to the back plate to form a capacitor. In the presence of oscillating pressure, the diaphragm will move which changes the gap between the diaphragm and the back plate. This produces an oscillating voltage from the capacitor, proportional to the original pressure oscillation. The back plate voltage can be generated by two different methods. The first is an externally polarized

109

microphone design where an external power supply is used. The power source on this traditional design is 200 volts. The second or newer design is called a prepolarized microphone design. This modern design utilizes an "electret" layer placed on the backplane, which contains charged particles that supply the polarization.
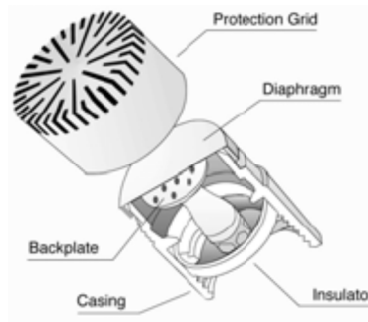
Figure 6-2: Structure of a condenser microphone (after PCB piezotronics, INC. [69]).

Comprehensive theoretical studies by Zhu *et al*. [10] showed that for a typical impulse force with duration between 50 and 200 μs, the excitability of leaky surface waves in air-concrete interface is between 1.0 to 0.1Pa/kN, which is equivalent to the sound pressure level of 95 to 75 dB. The normal room noise level is in the range of 40-60 dB, which is below this leaky Rayleigh wave level. In addition, low frequency waves, usually below 100 kHz, are used in concrete structures in civil engineering. In this light, *condenser microphones* are a good choice for concrete NDT.

In this study, air-coupled sensors of PCB model No. 377B01 were selected to measure leaky surface waves propagating along the concrete surface. The microphone (PCB No. 377B01) is modern prepolarized free-field pressure, and random incidence precision condenser microphone. This model can operate from constant current (2 to 20 mA) ICP® sensor signal conditioners and coaxial cables. The sensors have following properties: nominal diameter of 6 mm; ± 2 db flat frequency response over 4 Hz to 80 kHz; resonance frequency around 83 kHz. The specifincation is also summarized in **Table 6-1**. The microphone was connected to the prepolarized microphone preamplifier

(PCB 426B03), which is powered by a constant current (2 to 20 mA) ICP® sensor power supply. The specification of the PCB 426B03 is summrized in **Table 6-2**.

Table 6-1: Specification of the condenser microphone (PCB 377B01) [70].

Model number	Microphone (PCB 377B01)
Diameter	¼''
Responses	Free-field
Frequency responses (± 2 dB)	4 Hz to 90 kHz
Open circuit sensitivity (at 250 Hz)	2.5 mV/Pa
Polarization Volatage	0 V
Dynamic range -3% Distortion Limit *	170 dB
Dynamic range-catridge thermal Noise	30 dB (A)
Operating temprature	$-40 \sim 120^{o}C(-40\sim 248\ ^{o}F)$

Note: * 20 μPa

Table 6-2: Specification of the preamplifier (PCB 425B03) [70].

Model number	Preamplifier (PCB 426B03)
Diameter	¼''
Gain (attenuation)	-0.25 dB
Frequency responses (±0.25 dB)	2 Hz -100 kHz
Electrical noise (A-weight)	<2.5 μV
Electrical noise (Flat) *	<6 μV
Output Voltage (max)	8 Vpk
Costamt current excitation	2 - 20 mA
Operating temprature	$-30 \sim 60^{o}C\ (-22\sim 140\ ^{o}F)$
Output connector	10-32 Jack
TEDS IEEE P1451.4	Yes

Note: * 20 Hz-20 kHz

6.3 AIR-COUPLED SENSING OF SURFACE WAVES IN CONCRETE

This section summarizes air-coupled sensing of surface waves in concrete. Figure 6-3 shows the testing setup for measuring air-coupled leaky surface wave in concrete. The test setup has been verified effective to measure the transmission coefficient and the phase velocity of surface waves in the test region BC. The whole testing system includes an impact source, air-coupled sensor and a data acquisition system. An impact point source is applied at the surface to generate surface waves in concrete. The resulting motion at each surface point of the solid causes an acoustic wave to "leak" into the surrounding air. Testing scheme for air-coupled leaky surface wave detection is shown in **Figure 6-4**. The superposed leaky waves that emanate from each point in motion form wave-fronts of leaky bulk waves and surface waves. A sensitive air-coupled sensor or microphone is placed above the concrete surface at height h_s. The horizontal projection of spacing between the source and sensor is X_1.
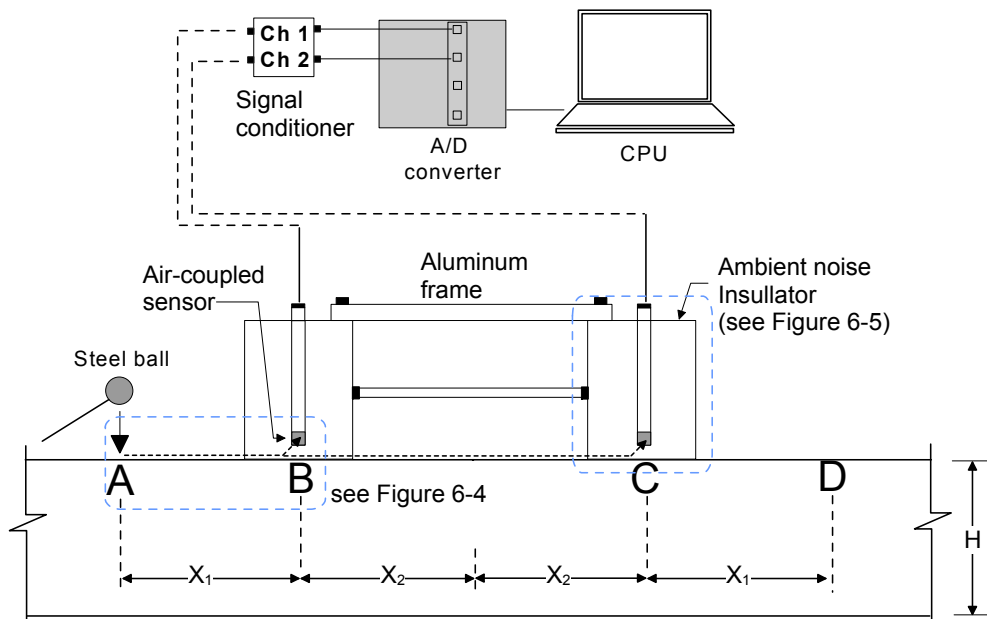
Figure 6-3: Test setup of the air-coupled surface wave measurement.
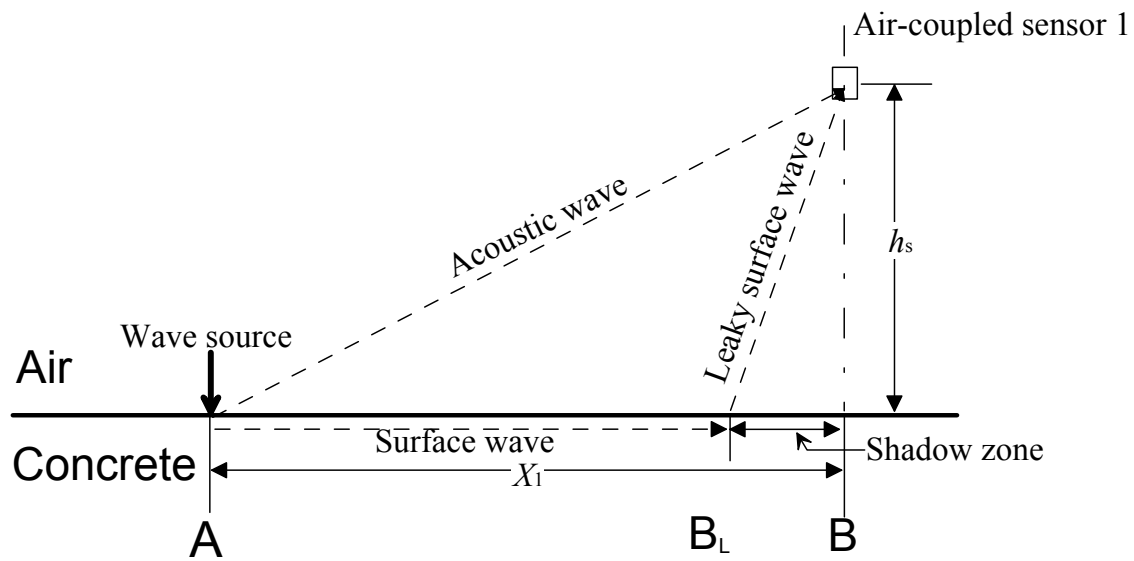
Figure 6-4:Testing scheme for air-coupled leaky surface wave detection (after Zhu and Popovics [12]).

In addition to leaky waves (P-, S- and surface waves), the air-coupled sensor also senses the direct acoustic waves generated by the source. The direct acoustic wave pressure P_F is in the same order of leaky Rayleigh waves P_{LR}. Depending on measuring locations, P_F may be larger or smaller than P_{LR}. The direct acoustic wave does not provide any information about the mechanical properties of the solid, and may make signal interpretations difficult; therefore it needs to be eliminated or suppressed. One solution is to increase the source-receiver spacing X_1, so that the acoustic waves arrive much later than leaky waves and thus can be separated in time due to the large differences between C_{air} and C_{LR}. Another solution is to use directional air-coupled sensors, which attenuate waves that have large incident angle. Increasing X_1 also increases the incident angle of acoustic waves. In this study, the air-coupled sensors were shielded by a sound insulation device shown in **Figure 6-5** to reduce the effects of direct acoustic waves and ambient noise.

113

Detail A
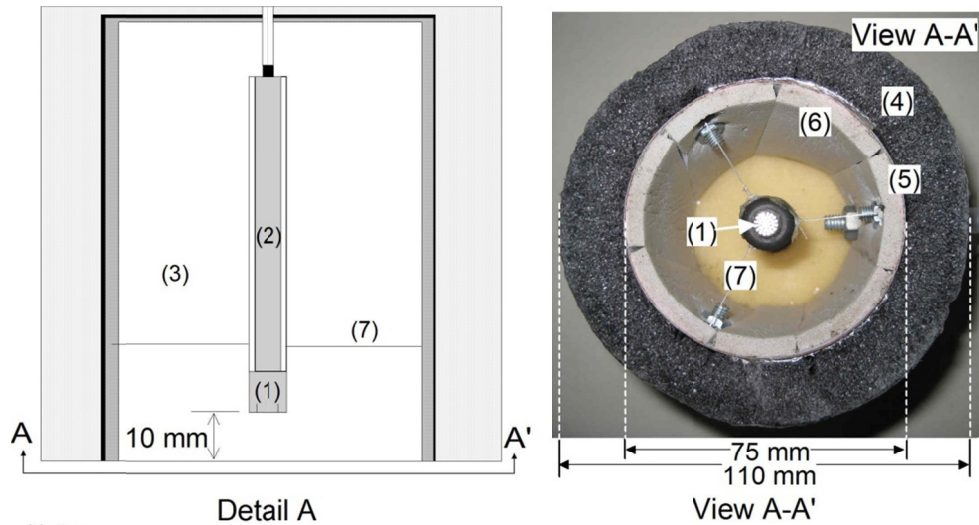
Note:
(1) Microphone (2) Preamplifier (3) Void (air) (4) Soft foam
(5) Rigid form (steel) (6) Soft foam (7) string

Figure 6-5: Sound insulation device to reduce the effects of direct waves and ambient noise.

The leaky angle θ for surface waves determined by Snell's law as

$$\sin(\theta) = \frac{C_{air}}{C_{LR}} ,$$

Equation 6-1

where C_{air} and C_{LR} are the acoustic wave velocities in air and leaky Rayleigh wave velocity in solids. For concrete, the normal values of C_{air} and C_{LR} are 343 m/s and 2000 ~ 2200 m/s, respectively. Thus θ varies between 8 to 10 degrees. Since most air-coupled sensors have a sensing field angle larger than 10 degrees, the leaky surface waves can be effectively detected if the sensor is installed with its axis normal to the testing surface.

The expected arrival times for leaky surface and direct acoustic waves can be calculated from the equations

$$t_{LR} = \frac{X_1}{C_{LR}} + h_s \sqrt{\frac{1}{C_{air}^2} - \frac{1}{C_{LR}^2}} ,$$

Equation 6-2

$$t_{air} = \frac{\sqrt{X_1^2 + h^2}}{C_{air}} .$$

Equation 6-3

114

A shadow zone exists nearby the sensor region, where no leaky surface waves can be detected, as shown in **Figure 6-4**. The shadow zone size is $h_s \tan(\theta)$. The shadow zone complicates data analysis, and reduces the effective testing region. Therefore, the shadow zone should be minimized. Because the leaky angle θ is relatively stable, which varies around 8 to 10 degrees for normal concrete, the only way to minimize shadow zone size is to reduce the sensor height h_s. For leaky surface wave sensing, larger X_1 and smaller h_s is recommended to reduce negative effects of the direct acoustic waves and shadow zone.

6.4   SELF-CALIBRATING PROCEDURE FOR AIR-COUPLED SENSING

6.4.1   Transmission measurement of surface waves

The self-calibrating procedure was originally proposed by Achenbach *et al*. [9] to eliminate effects of coupling layer of contact sensors [71]. Furthermore, previous researchers verified that the self-calibrating procedure is also effective to minimize experimental variability caused by sensors, and sources in surface wave transmission measurement [7, 8] in concrete.

The self-calibrating procedure for air-coupled sensors is described as follows. First, the stress waves, generated by the impact source at A (see Figure 6-3 and **Figure 6-4**), will propagate throughout the solid, and leaky surface waves will be measured first by the near sensor located at B, and then by the far sensors located at C, denoted as $\mathbf{S}_{AB}$ and $\mathbf{S}_{AC}$, respectively. Likewise, the leaky surface waves, generated by the impact source at D, can be measured by air-coupled sensors B and C, denoted as $\mathbf{S}_{DB}$ and $\mathbf{S}_{DC}$. The measured signals measured by air-coupled sensors can be decomposed by terms in the frequency domain as follows,

$$\mathbf{S}_{AB} = \mathbf{I}_A \mathbf{d}_{AB_L} \mathbf{d}_{airB} \mathbf{R}_B$$

$$\mathbf{S}_{AC} = \mathbf{I}_A \mathbf{d}_{AB_L} \mathbf{d}_{B_L C_L} \mathbf{d}_{airC} \mathbf{R}_C$$

$$\mathbf{S}_{DC} = \mathbf{I}_D \mathbf{d}_{DC_R} \mathbf{d}_{airC} \mathbf{R}_C \qquad\qquad \text{Equation 6-4}$$

$$\mathbf{S}_{DB} = \mathbf{I}_D \mathbf{d}_{DC_R} \mathbf{d}_{C_R B_R} \mathbf{d}_{airB} \mathbf{R}_B$$

where $\mathbf{S}_{ij}$ is the Fourier transform of the measured time domain signal generated by impact source at i and measured by a sensor located at j, $\mathbf{I}_i$ is the generating response term that describes the type of wave source at i, $\mathbf{R}_i$ is the receiving response term that describes the type of receiver located at i, $\mathbf{d}_{ij}$ is the signal transmission function between locations i and j, and $\mathbf{d}_{airi}$ is the signal transmission function of leaky surface wave through air for air-coupled sensor located at i. Finally, transmission function between locations B and C can be calculated by averaging signals obtained from opposite sides as follows,

$$\mathbf{Tr}_{BC} = \sqrt{\frac{\mathbf{S}_{AC}\mathbf{S}_{DB}}{\mathbf{S}_{AB}\mathbf{S}_{DC}}} = \sqrt{\mathbf{d}_{B_L C_L}\mathbf{d}_{C_R B_R}} \ , \qquad\qquad \text{Equation 6-5}$$

when the shadow zone is small, $\sqrt{\mathbf{d}_{B_L C_L}\mathbf{d}_{C_R B_R}} \approx \mathbf{d}_{BC}$. The sensor coupling effect $\mathbf{d}_{airB}$ and $\mathbf{d}_{airC}$ will be cancelled using the self-calibrating method.

6.4.2   Phase velocity measurement of surface waves

Phase velocity of surface waves is also used for NDT of concrete structures [72-74]. The test setup shown in Figure 6-3 can be used to measure the phase velocity of surface wave through SASW. The phase differences between $\mathbf{S}_{AB}$ and $\mathbf{S}_{AC}$ by source A and between $\mathbf{S}_{DB}$ and $\mathbf{S}_{DC}$ by source D are presented as follows,

$$\Delta\phi_L(f) = 2\pi f \Delta t_L(f) = 2\pi f \left[\frac{BC}{C_{LR}(f)} + (h_{s2} - h_{s1})\sqrt{\frac{1}{C_{air}(f)^2} - \frac{1}{C_{LR}(f)^2}} \right]$$

<div align="right">Equation 6-6</div>

$$\Delta\phi_R(f) = 2\pi f \Delta t_R(f) = 2\pi f \left[\frac{CB}{C_{LR}(f)} + (h_{s1} - h_{s2})\sqrt{\frac{1}{C_{air}(f)^2} - \frac{1}{C_{LR}(f)^2}} \right]$$

<div align="right">Equation 6-7</div>

where $\Delta\phi_L(f)$ and $\Delta\phi_R(f)$ are the phase difference, and $\Delta t_L(f)$ and $\Delta t_R(f)$ are the time difference of surface waves between S_{AB} and S_{AC}, and between S_{DB} and S_{DC}, respectively. Equations 6-6 and 6-7 imply that different height between sensors A and B may cause large errors in calculation of the phase velocity of leaky surface waves through solid region BC (the second terms in Equations). Therefore, it is recommended to average $\Delta\phi_L(f)$ and $\Delta\phi_R(f)$ to eliminate the effects of air as follows,

$$C_{LR}(f) = \frac{BC}{(\Delta t_L + \Delta t_R)/2} = 2\pi f \frac{BC}{(\Delta\phi_L + \Delta\phi_R)/2} \qquad \text{Equation 6-8}$$

6.5 AIR-COUPLED SENSORS VERSUS ACCELEROMETERS

This section compares signal data measured by using air-coupled sensors and accelerometers on a crack-free region in a reinforced concrete beam. **Figure 6-6** shows locations of air-coupled sensors and accelerometers on the reinforced concrete beam having dimensions of $8280 \times 530 \times 1060$ mm^3 (**L**ength X **W**idth X **D**epth). Detail information of the beam (e.g., reinforcement bar detail, concrete mixing properties, and fabrication procedure) is available in the other publication [75]. A steel ball having a diameter of 13 mm was applied perpendicular to the width direction, which results in surface waves with a center frequency of 17 kHz. The dimension perpendicular to the direction of wave propagation H is larger than two times the wavelength of incident surface waves λ_R (i.e., $H/\lambda_R \sim 4.5$). In this case, fundamental modes are dominant in the time, and frequency domain (see Chapter 5).
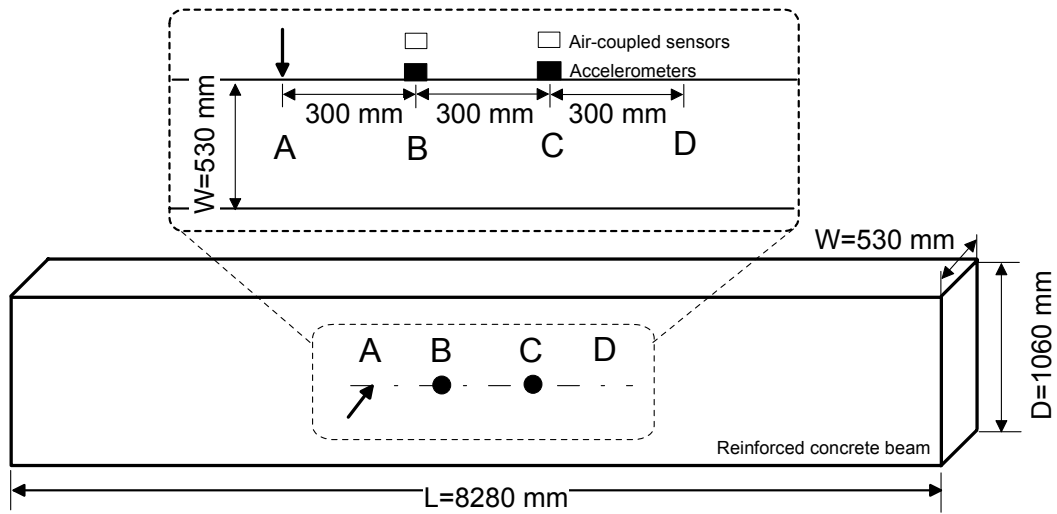
Figure 6-6: Locations of air-coupled sensors and accelerometers placed on a reinforced concrete beam [75].

Accelerometers directly measure the surface wave response on the beam specimen, while the air-coupled sensors measure air-pressure disturbance caused by leaky surface waves propagating on the surface. When the air- coupled sensors are placed very close to the surface, the pressure responses are proportional to the surface responses. **Figure 6-7** (a) shows typical time domain signals measured by two air-coupled sensors in a crack free region on the concrete beam. The raw signal data and windowed signal data are presented as dash lines and solid lines, respectively. For comparison purposes, the time-domain signal data measured by accelerometers at the same location are also shown in **Figure 6-7** (b). Strong adhesive was used to ensure good contact condition between sensors and concrete surface.
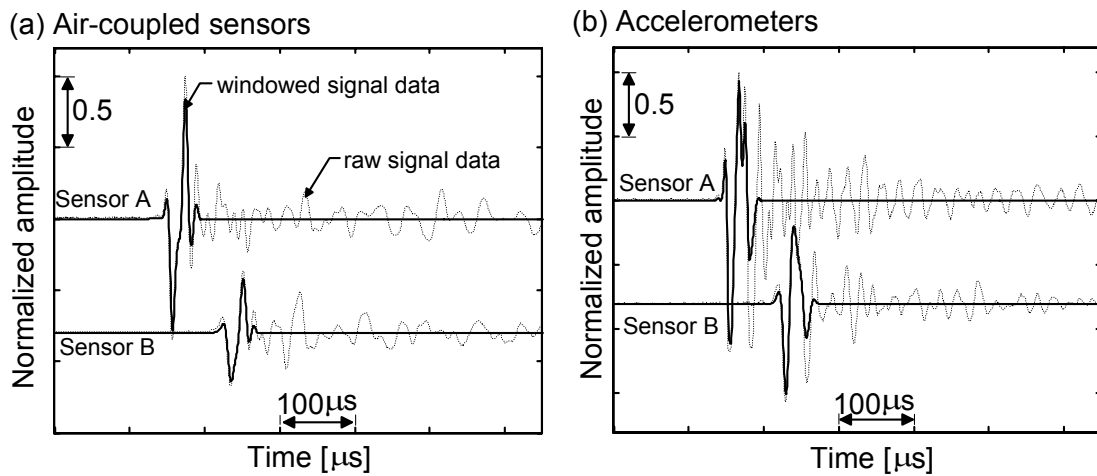
Figure 6-7: Typical time-domain signals measured from the reinforced concrete beam by using: (a) air-coupled sensors, and (b) accelerometers.

Figure 6-8 (a) and (b) show the transmission coefficient and the signal coherence function of the windowed time-domain signals shown in **Figure 6-7** (a) and (b), respectively. The transmission coefficients and signal coherence of surface waves were obtained by using Equation 6-5 and Equation 3-9, respectively. Both the air-coupled sensors and accelerometers give good signal coherence (greater than 0.98) in the frequency range of 5 kHz to 20 kHz. In this frequency range, measurements from the air-coupled sensors and from accelerometers show good agreements in transmission coefficients, especially around the center frequency (~17 kHz). In addition, **Figure 6-9** (a) and (b) shows the average phase velocity of the surface waves measured by air-coupled sensors and accelerometers, respectively, and obtained by using Equation 6-8. In the frequency range of 5 kHz to 20 kHz, the phase velocity of surface waves from air-coupled sensors was comparable to that from accelerometers. This results shows that air-coupled sensors provide the same accuracy as accelerometers in the useful frequency range for concrete NDT of using stress waves.

119
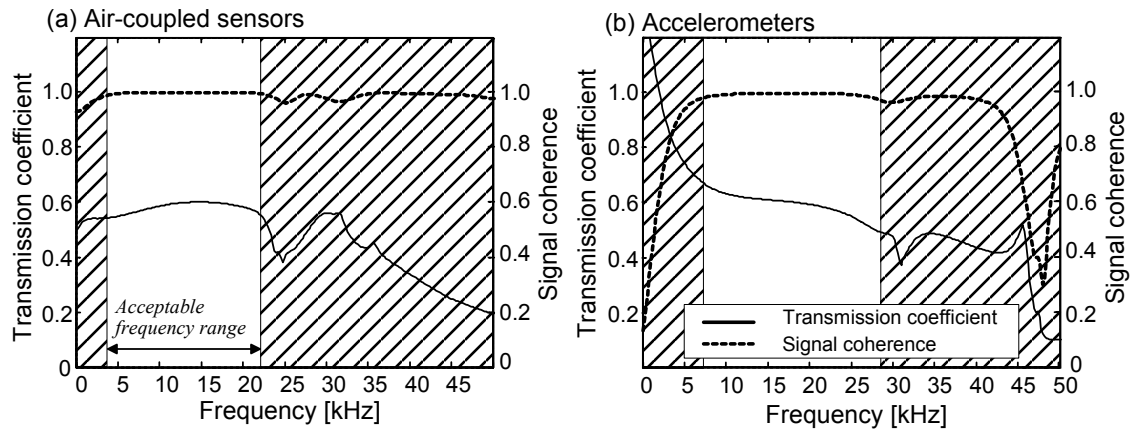
Figure 6-8: Typical transmission coefficient and signal coherence in the frequency domain of the signals measured using air-coupled sensors (a) and accelerometers (b) shown in Figure 6-7 (a) and (b), respectively.
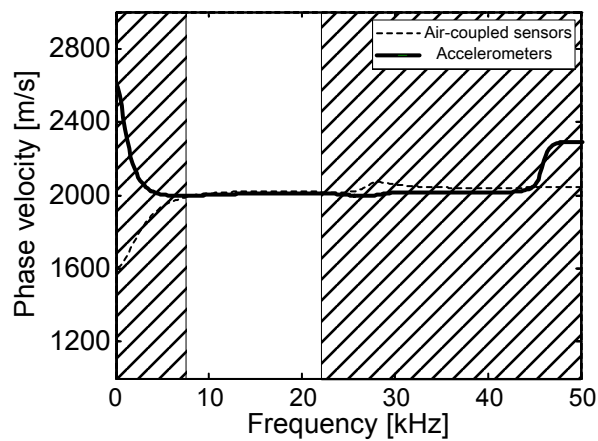
Figure 6-9: The phase velocity of surface waves of the surface waves measured using air-coupled sensors (dash line) and accelerometers (bold line).

6.6   EFFECTS OF TRAFFIC ON AIR-COUPLED SENSING

Effects of traffic noise and structural vibration are of concerns in measurements of stress waves in field testing of concrete structures using air-coupled sensors. This section provides a preliminary result obtained as a part of the research project of SHRP 2 Renewal Project R06-A. The air-coupled sensing technique developed in this chapter was

120

applied to evaluate a concrete bridge deck located at the intersection of I-66 and US 15 in Virginia (see **Figure 6-10** (a)). The test was performed on the right lane of the south bound bridge, while the left lane was still open to traffics (see **Figure 6-10** (b)).
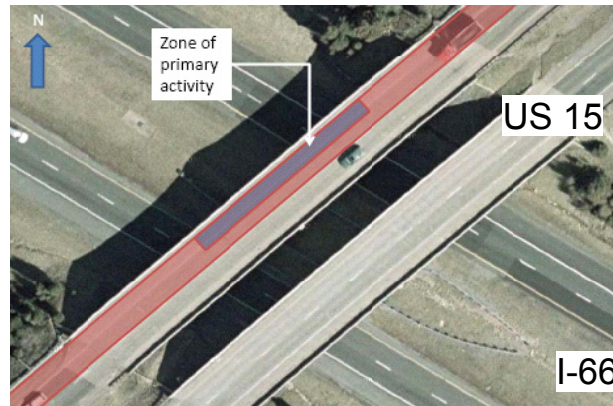
(a)

(b)

Figure 6-10: The test bridge located at the intersection of I-66 and US 15 in Virginia: (a) location of the bridge, and (b) overview of the testing site under partial traffic control.

Figure 6-11 shows typical time-domain signals obtained on the concrete bridge deck using air-coupled sensors. Test setup for the field application was the same as shown in Figure 6-3 with x_1=200mm, and x_2=100 mm. Compared to the typical signal data obtained in the laboratory (**Figure 6-7** (a)), low-frequency noise contaminates the

time domain signals. As shown in **Figure 6-12**, the frequency domain signals clearly show very high low-frequency components, which is mainly due to structural vibration, and traffic noise caused by vehicles. The low-frequency noise may not interfere with leaky surface waves having a center frequency of approximately 17 kHz. However, it makes signal processing (e.g., applying a window function) difficult in calculation of transmission coefficient and phase velocity of surface waves. Generally low-frequency noise lower than 1 kHz can be appropriately suppressed by a simple signal processing technique (e.g., applying a high-pass filter or a band-pass filter). **Figure 6-13** shows the time-domain signal after eliminating low-frequency components lower than 2 kHz.
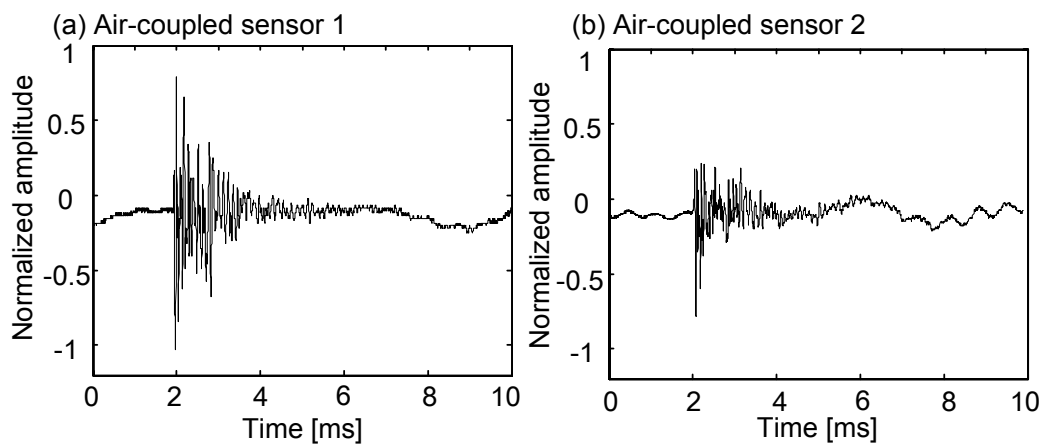
Figure 6-11: Typical time-domain signals measured by air-coupled sensors 1 (a) and 2 (b) on the concrete bridge deck with traffic.
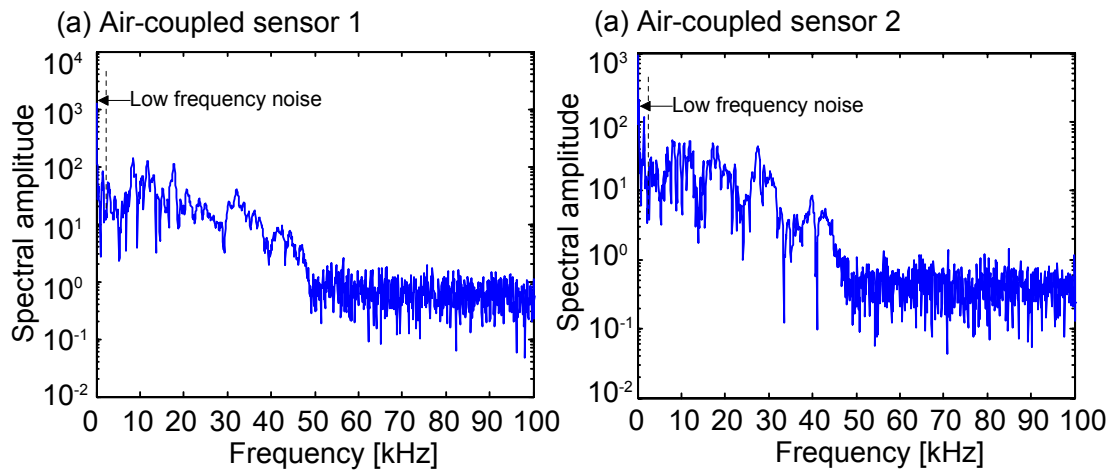
Figure 6-12: Frequency spectra of the time signals shown in Figure 6-11 (a) and (b).
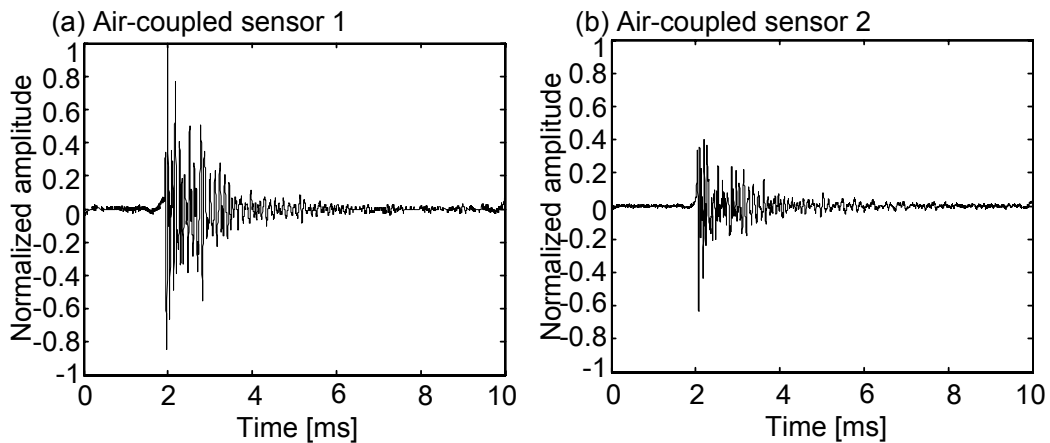
Figure 6-13: Time-domain signals for air-coupled sensors 1 (a) and 2 (b) after eliminating low-frequency components lower than 2 kHz.

In addition, **Figure 6-14** shows the transmission coefficients and the phase velocity of surface waves. The surface wave components were extracted from the time-domain signals by applying a hanning window. Signal coherence function shows good consistency in a frequency range of 10 to 30 kHz, also implies good signal-to-noise ratio in the frequency range. In this range, the transmission coefficients and the phase velocity show reasonable values for normal concrete. The preliminary results in this chapter show

123

the potential of applying air-coupled sensors to concrete structures with open traffics. However, it is noteworthy that features of traffic noise depend on a number of factors [76, 77] (e.g., types and driving speed of vehicles, road surface types, pavement types (Asphaltic concrete, or Portland cement concrete), humidity, and temperature variation). Therefore, more studies are still needed to better understand effects of open traffics on applicability of air-coupled sensors to in-situ concrete structures.
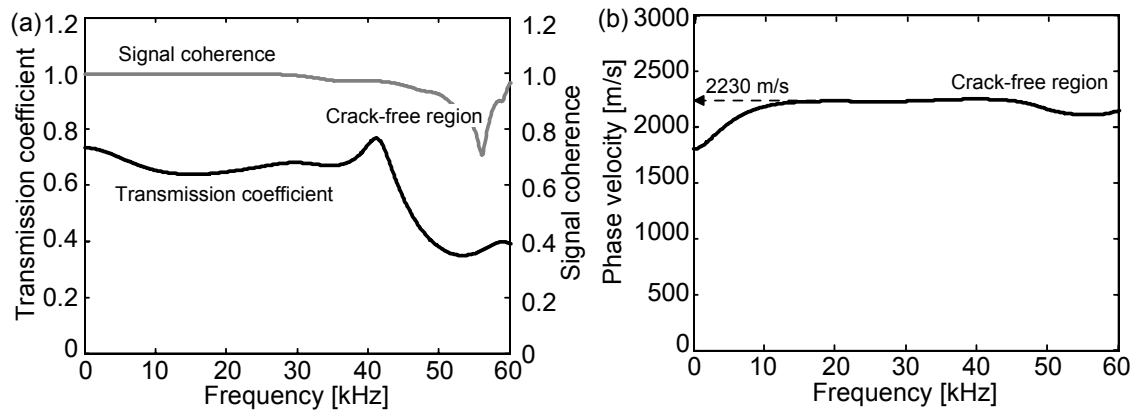
Figure 6-14: The transmission coefficient and signal coherence function (a), and the phase velocity (b) of surface waves presented in the frequency domain.

6.7 CONCLUSIONS

This chapter provides a fundamental background of air-coupled sensing technique for NDT of concrete structures. The conclusions obtained in this chapter are summarized as follows;

(1) *Condenser microphones* are a good choice for concrete NDT.

(2) The conventional self-calibrating procedure, originally developed for contact sensors, is still effective to determine the transmission coefficient of surface waves measured by air-coupled sensors when air-coupled sensors are placed very close to the surface. In addition, the self-calibrating procedure is

effective for minimizing the effects of different heights h_s in air-coupled sensors 1 and 2.

(3) Difference in height of sensors 1 and 2 may cause substantial errors in calculation of the phase velocity of surface waves measured by air-coupled sensors. Using the average phase velocity, shown in Equation 6-8, is effective in eliminating the effects of air in the calculation of the phase velocity of leaky surface waves in concrete.

(4) Comparison studies demonstrated that the transmission coefficient and the phase velocity of surface waves measured by air-coupled sensors have good agreement with those measured by accelerometers. This demonstrated that air-coupled sensors can provide the same accuracy as accelerometers in the useful frequency range for concrete NDT of using stress waves.

(5) A preliminary result in this chapter demonstrated that low-frequency noise lower than 1 kHz could be effectively suppressed by a simple signal processing technique, and the signals measured by air-coupled sensors in in-situ concrete structures resulted in good signal-to-noise in a frequency range of 10 to 30 kHz. This shows the potential of application of air-coupled sensors in in-situ concrete structures even under traffic. However, more comprehensive research is still needed to completely understand effects of traffic on application of air-coupled sensors to in-situ concrete structures due to complex features of traffic noise.

Chapter 7 Application of the Air-coupled SWT Method to Concrete

7.1 INTRODUCTION

The self-calibrating procedure described in Chapter 2 has been verified effective to reduce the experimental variability caused by types of impact source and receiver in surface wave measurement. The setup is based on the assumption that effects of coupled sensors on the surface wave measurements are insignificant, and coupling of the sensors during test remains consistent [7]. However, inconsistent coupling conditions of conventional contact sensors (e.g., accelerometers) make it difficult to present reliable and consistent measurements. Furthermore, temporary sensor mounting methods, such as adhesive and magnetic coupling, may induce a low resonance frequency which depends on the mounting stiffness of the contact sensors. The errors caused by this mounting resonance cannot be eliminated by the self-calibrating technique. On the other hand, permanent mounting method of contact sensors cannot meet the requirement of rapid NDT test and is difficult to apply to concrete. In addition, rough surface on concrete and environmental variations (e.g., moisture, temperature variation, and chemical attacks) in field structures are challenges to obtain good coupling between contact sensors and concrete.

One solution for the coupling issue in ultrasonic testing is using non-contact sensors that include laser vibrometers and air-coupled sensors. However, using a laser vibrometer generally requires expensive equipment for signal control and data acquisition. Moreover, a laser vibrometer poses difficulties in measuring stress waves on rough concrete surface due to high scattering and low reflection from irregular concrete surface. In contrast, air-coupled sensors have been successfully used to measure leaky surface waves, and Lamb waves propagating in concrete by previous researchers (see Chapter 6). Compared to contact sensors, the air-coupled sensors eliminates sensor

126

coupling problems, and thus gives more consistent measurement results, and the non-contact features enable rapid scanning of concrete structures in civil engineering.

In this chapter, the author uses air-coupled sensors described in Chapter 6 to measure surface wave transmission coefficient across a surface-breaking crack (i.e., air-coupled SWT method). Section 7-2 presents experimental results obtained from a series of notch-typed crack in a concrete slab. The experimental results validate the theoretic results from analytic solution given by Achenbach and his colleagues [28-30], and numerical simulations in Chapter 3. The results in this chapter show promising application of air-coupled sensors.

7.2   EXPERIMENTAL PROGRAM

7.2.1   Preparation of specimen

A concrete specimen with dimensions of 1500 ✕ 1500 ✕ 2600 mm^3 (W ✕ L ✕ T) was cast in the laboratory as shown in

Figure 7-1: . Depth of specimen was assumed large enough compared with the wavelength of surface waves so that dominant surface waves do not interfere with flexural mode of lamb waves. Notch-type cracks with depths varying from 10 to 100 mm were generated in the specimen by inserting a 0.5 mm thick metal sheet (Zinc) before casting concrete. The Zinc sheet was removed from the concrete 12 hours later. The width of crack in hardened concrete specimens measured by a crack width gauge is approximately 0.5 mm; consequently, width-to-depth ratio of cracks implemented in this study is smaller than 0.1. According to Masserey and Mazza [33], this value is small enough to ignore the effect of width of a crack on transmission coefficient of surface waves so that results from experimental study may be directly comparable with the theoretic results. Normal-weight concrete, made from normal Portland cement type I/II, river sand, and gravel with a maximum size of 10 mm, were used for the specimen. The density of concrete specimens, determined by averaging of five concrete cylinders

127

(diameter of 10 cm and height of 20 cm) cast simultaneously with concrete specimens, was 2350 kg/m^3. The phase velocity of surface waves calculated from a dispersion curve obtained through the **M**ultichannel **A**nalysis of **S**urface **W**aves (MASW) [53, 54] was converging into approximately 2200 m/s when frequency is greater than 10 kHz. The velocities of P and S waves measured by low frequency ultrasonic transducers (50 kHz) in a pitch-and-catch mode were 4100, and 2460 respectively.
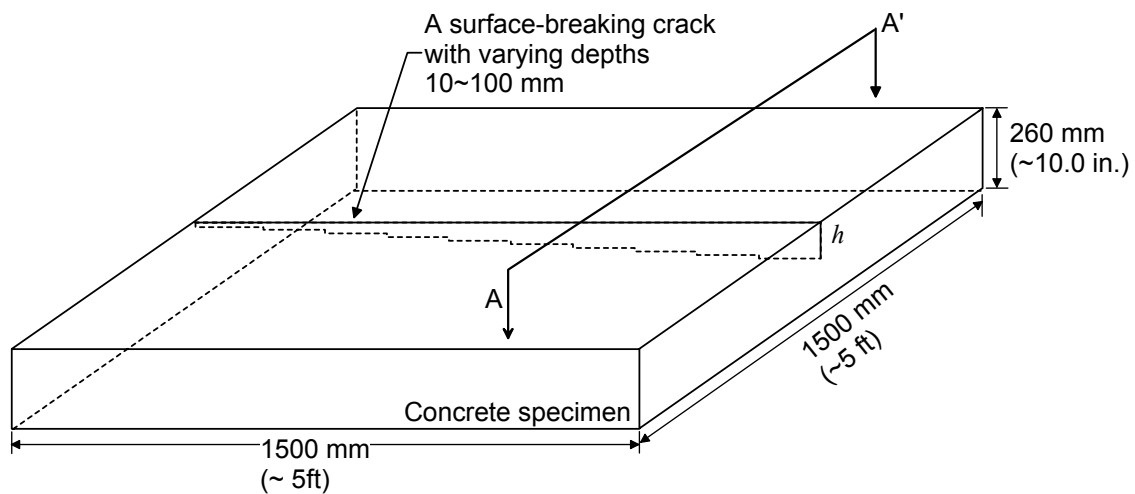
Figure 7-1: 3D view of concrete specimen having a surface-breaking crack with varying crack depths from 10 to 100 mm.

7.2.2 Test setup

A schematic view of the test setup is shown in **Figure 7-2**. Two air-coupled sensors described in Chapter 6 were used to measure leaky surface waves propagating along the concrete surface. The horizontal spacing between the sensor and the impact source was designed as 200 mm to minimize the effects of direct acoustic waves. Furthermore, the sensor was 100 mm away from the surface-breaking crack to minimize the near-field effects according to Equation 3-4. According to Zhu and Popovics [12] and discussed in Chapter 6, the air-coupled sensors should be close to the test surface to reduce ambient noise and direct acoustic wave effects. In this study, the vertical distance

between the sensors and the concrete surface, h_s, is 20 mm. Unlike a contact sensor which measures the wave right at the sensor location, an air-coupled sensor actually measures the surface wave emitted from the concrete surface at a distance of $h_s\tan\theta$, where θ is the leaky angle determined by the Snell's law. This distance is defined as shadow zone. When this value is large, sensor locations should be corrected for shadow zone. In this study, the shadow zone size is about 3.0 mm, which is very small compared to the sensor to crack spacing 100 mm. To further reduce the effects of direct acoustic waves and ambient noise, the air-coupled sensors were shielded by a sound insulation device as described in Chapter 6.

(b)
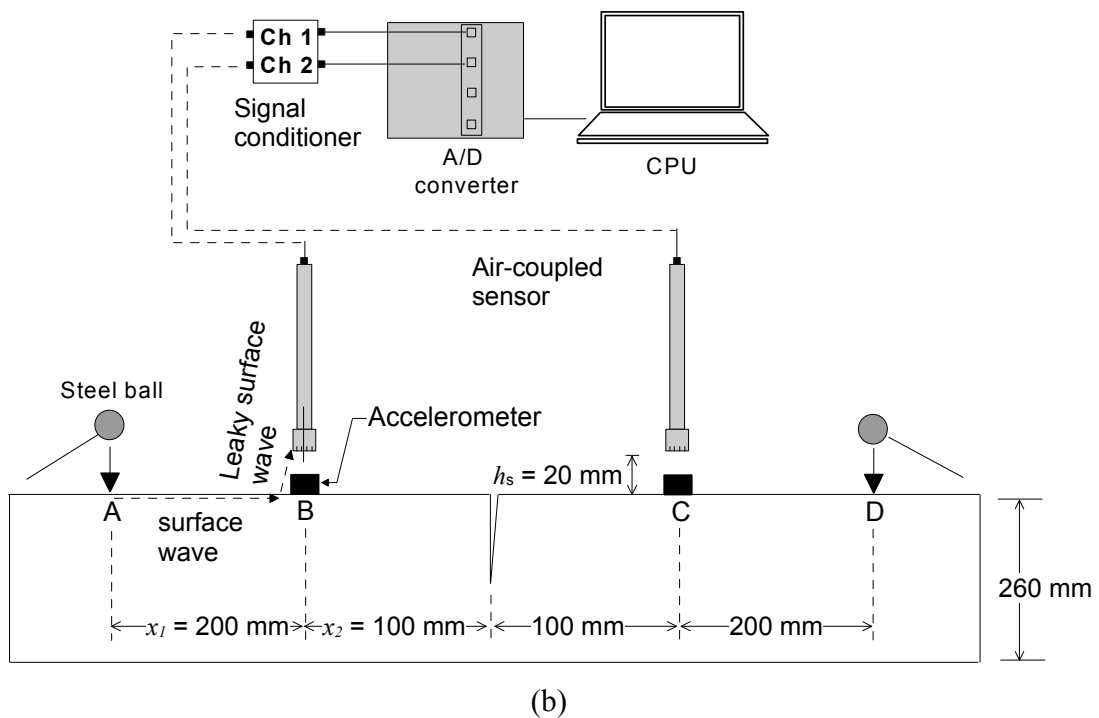
Figure 7-2: Test setup of air-coupled sensors for surface wave transmission measurements using the self-calibrating procedure (a section view of A-A' in **Figure 7-1**).

7.2.3   Data acquisition

The self-calibrating technique was used to measure surface wave transmission across a crack in concrete. The test setup is shown in **Figure 7-2**. The self-calibrating procedure for air-coupled sensors was described in Chapter 6. First, surface waves generated by an impact load at location A were recorded by sensors at locations B and C. The signals are denoted as S_{AB} and S_{AC}. Consequently, the wave transmission between locations B and C can be calculated from these two signals and denoted as Tr_{BC}. To eliminate the unsymmetrical effect caused by sensor coupling, an impact load is then applied at location D, and the signals recorded by the sensors at locations B and C are denoted as S_{DB} and S_{DC}. The transmission ratio between locations C and B is defined as Tr_{CB}. The average surface wave transmission function shown in Equation 6-5 was used in this study.

As described in Chapter 3, the signal coherence function was used to check signal consistency of measured signal data, and select the acceptable frequency range of a transmission curve. Five repeated signal data sets were collected at the same test location. These five transmission functions were then arithmetically averaged in frequency domain. The averaged $SC(f)$ was determined using Equation 3-9. The averaged $SC(f)$ ranges from 0 to 1.0. A value close to 1.0 indicates good signal quality and repeatability.

The measured surface wave transmission ratio Tr was normalized by Tr_0, which is the transmission ratio obtained from crack free regions (see Equation 3-10). This procedure will eliminate the geometric effect caused by a point source. All analyses are performed in the frequency domain. A *Hanning* window is applied to the time domain signals to extract the surface wave components.

Three steel balls with different diameter (7 mm, 12 mm, and 14 mm) were used as impact sources. They generate incident surface waves with center frequencies around 25, 20 and 18 kHz. The acquired signals were digitized at a sampling frequency of 10 MHz using an NI-PXI 5105 oscilloscope.

130

7.3   RESULTS AND DISCUSSION

7.3.1   Typical signal measured using air-coupled sensors

Figure 7-3 shows typical time domain signals measured by two air-coupled sensors. **Figure 7-3** (a) presents signals obtained from a crack-free region of the concrete specimen, where the incident waves were generated by a source with impact duration T approximately 60 µs. Note that the impact duration T was measured from a peak-to-peak time difference of surface waves in the time-domain. The acoustic waves were completely separated from the leaky surface waves. In **Figure 7-3** (b), clear incident and transmitted surface waves were also obtained from the crack region (h = 40 mm). Therefore, the surface wave components can be easily extracted from the signals by using a hanning window.
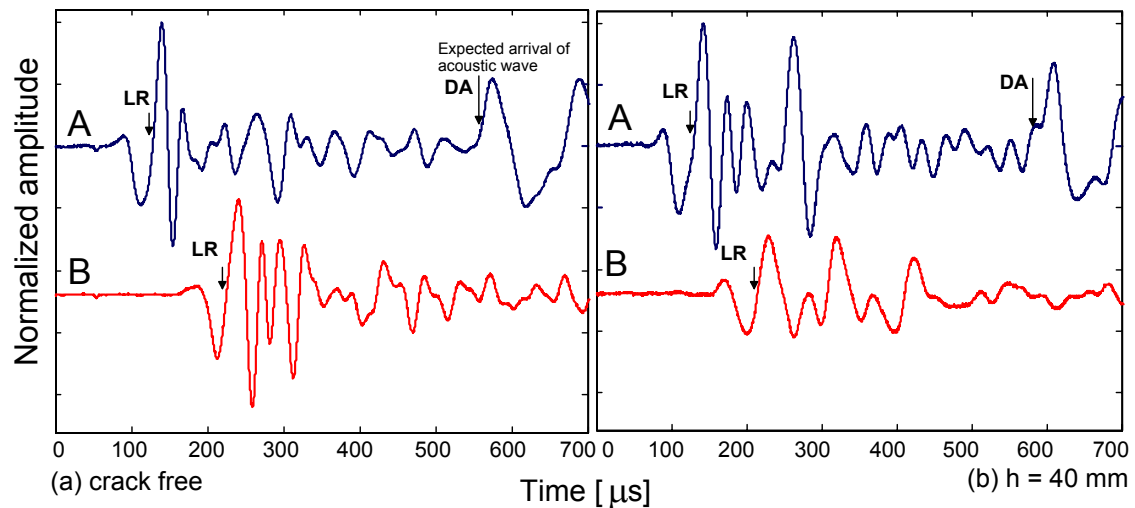
Figure 7-3: Typical signals measured by air-coupled sensors from a concrete specimen. The crack depths are (a) h=0mm and (b) h=40 mm. The impact duration time is T=60 µs. Note that LR=leaky surface wave and DA=direct acoustic wave.

7.3.2   Air-coupled sensor versus accelerometer in cracked region

For comparison purposes, accelerometers were also installed on the concrete surface below the air-coupled sensors at locations A and B, respectively (see **Figure 7-2**).

131

Figure 7-4 shows the surface wave transmission coefficient and signal coherence functions for signals obtained from the concrete slab with a 40 mm deep crack by using microphones (**Figure 7-4** (a)) and accelerometers (**Figure 7-4** (b)). Both measurements show constantly good consistency in the frequency range of 10 to 40 kHz. The upper limit of 40 kHz is governed by the frequency contents of impact point source. In the low frequency range (0-10 kHz), however, the air-coupled sensors show better consistency than accelerometers. The poor consistency of accelerometer measurement is associated with the low frequency resonance response that is caused by coupling problem of accelerometers. This implies that the measured transmission coefficient may be unreliable when the center frequency of incident waves falls in the low frequency range due to resonance response. In addition, coupling problem of accelerometers becomes critical when they are applied field testing. Sometimes, surface roughness and/or environmental conditions (e.g., dust, moisture, and temperature variation) will require substantial efforts for surface preparation; moreover, inappropriate coupling of sensors cannot provide reasonable signals at all.
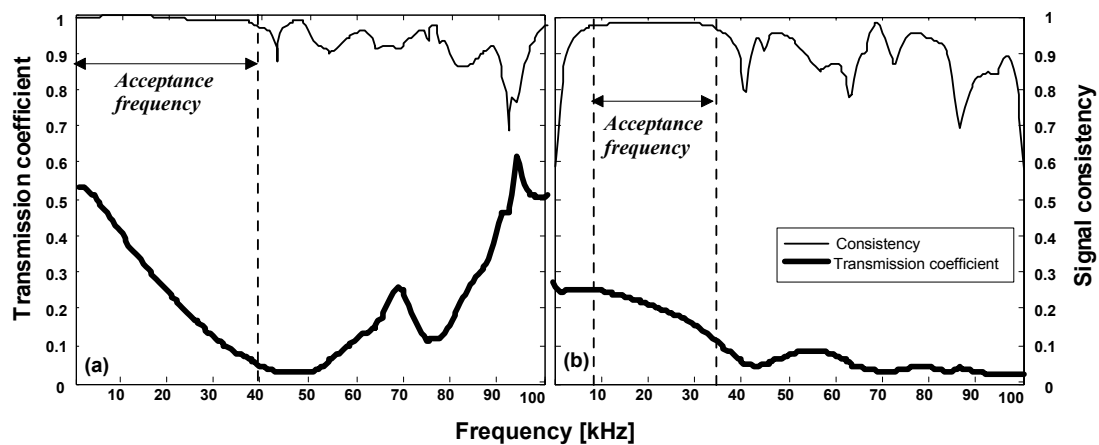
Figure 7-4: Typical transmission coefficient and signal consistency versus frequency measured by (a) air-coupled sensors and (b) accelerometers. The depth of crack was 40 mm and the incident surface waves were generated by a 12 mm diameter steel ball.

132

7.3.3 Calibration curve of transmission function using air-coupled sensor

Figure 7-5 (a) presents the normalized transmission coefficient Tr_n versus h/λ curves obtained from experiments on the concrete specimen. Signal data were collected in the approximate far-field for various crack depths. Despite of the good signal consistency of air-coupled sensors, the self-calibration procedure was used to eliminate other experimental variability caused by different impact sources and properties of sensor itself. Generally, to minimize the asymmetric properties of concrete material (surface roughness, randomly distributed air-voids, and aggregates), measurement on both side of the cracks is desirable. Three different steel balls of different diameters (7 mm, 12 mm, and 14 mm) were used to generate the incident surface wave. The experimental results show good agreement with the FEM simulation and the analytical solution, especially for shallow cracks, e.g., $h = 20$mm and 30 mm, and in the range of $h/\lambda < 1/3$. This is because the impact source contains enough low frequency energy to cover the range of $h/\lambda < 1/3$. The data corresponding to $h = 10$ mm is not presented in this paper because a steel embedment under the crack distorted surface propagation. For deep cracks, the source should contain enough low frequency wave energy to give a reliable transmission measurement in $h/\lambda < 1/3$ range. However, using long impact duration will induce boundary reflections and near field effects (Chapter 5). Effects of multiple reflections from the bottom of thin concrete plate were investigated in Chapter 8. The crack depth that can be reliably measured using the surface wave transmission method depends on the impact source, sensor arrangement and geometry (thickness and size) of the specimen. In this chapter, cracks up to 50 mm deep can be accurately estimated.
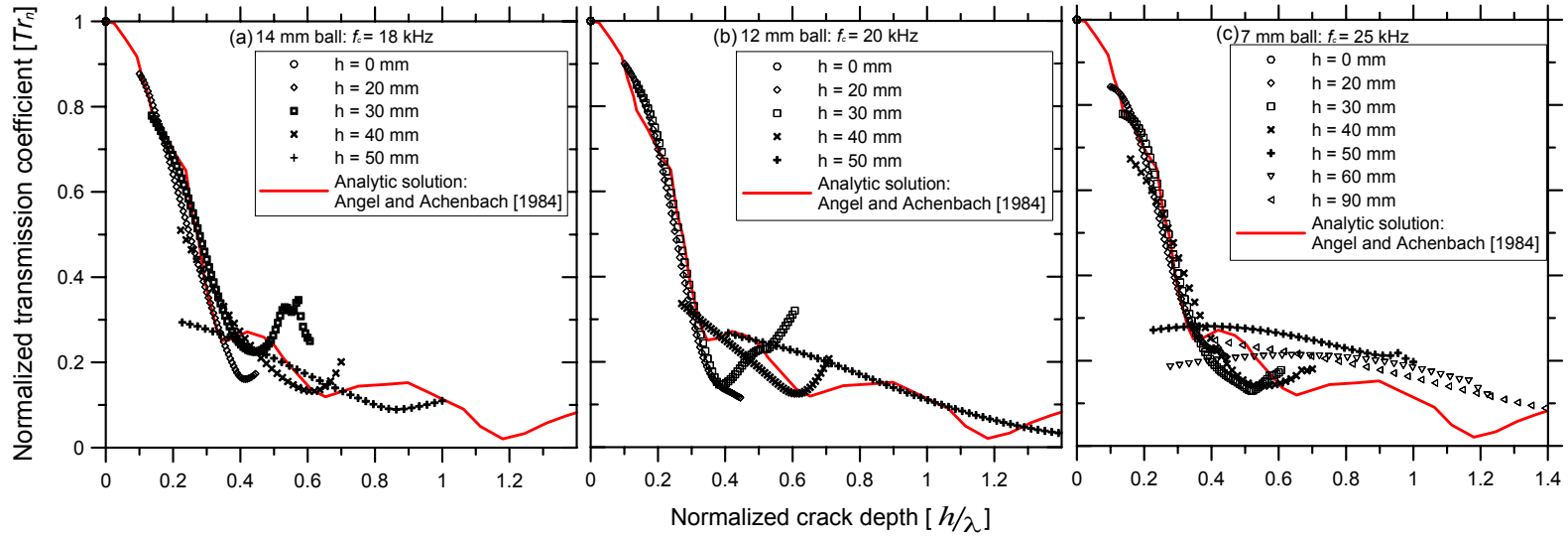
Figure 7-5: Normalized transmission coefficient and normalized crack depth relation.

7.3.4 Experimental verification of the simplified algorithm using air-coupled sensor

To verify the proposed simplified algorithm in Chapter 3 for crack depth measurement, transmission coefficients measured at the center frequencies are shown in **Figure 7-6**. The data based on measurements at three center frequencies (18 kHz, 20 kHz and 25 kHz), and crack depths (0, 20, 30, 40, 50, 60, and 70 mm). As shown in **Figure 7-6**, the experimental data are in good agreement with the analytic curve. Therefore, the simplified surface wave transmission algorithm is a promising in-situ NDT method to quickly estimate crack depth in concrete.
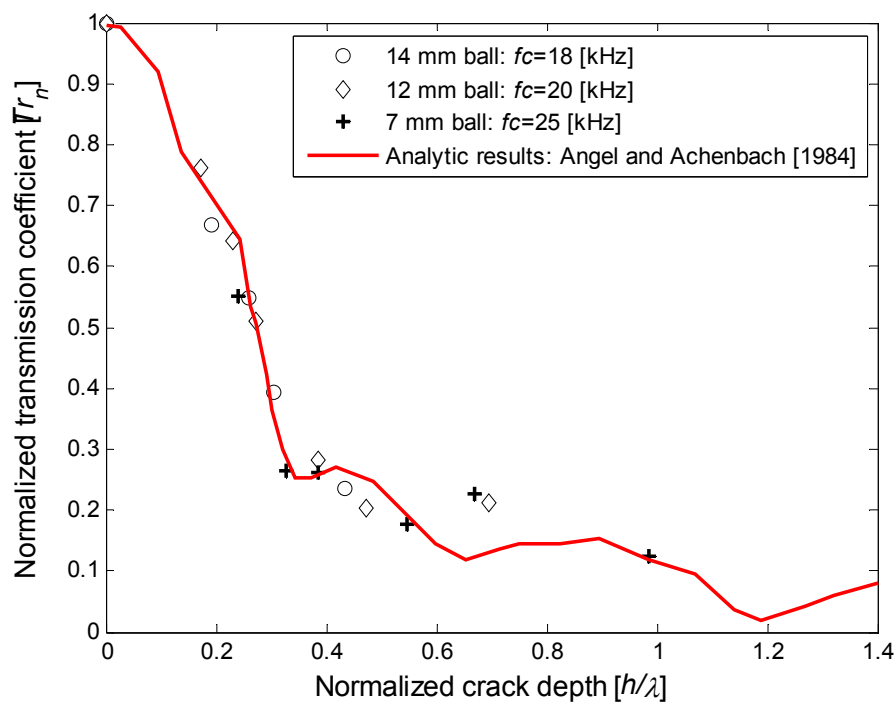
Figure 7-6: Normalized transmission coefficient based on center frequency and normalized crack depth relation

135

7.4 **CONCLUSIONS**

The study in this chapter presents the surface wave transmission method to estimate the depth of a surface-breaking crack in concrete. Experimental studies were carried out: *(i) to verify the theoretical results and numerical simulation results on concrete specimens in Chapter 3* and (ii) *to demonstrate the effectiveness of air-coupled sensing technique in concrete NDT*. The following conclusions are drawn based on the results of this study.

(1) Reliable surface wave transmission measurement can be obtained using the air-coupled sensors. Owing to the non-contact features, air-coupled sensors show better signal consistency than accelerometers in low frequency ranges. Test speed is also improved with air-coupled sensors.

(2) Experimental measurements based on the transmission values at the center frequencies show good agreement with the analytic solution. Therefore, a simplified algorithm is proposed to estimate a crack depth. Instead of trying to match the measured transmission curve with the pre-established curve at all frequencies, only the transmission at the center frequency is needed to find the corresponding h/λ. If surface wave velocity is known, the crack depth can be calculated. The simplified algorithm provides a quick in-situ NDT method for crack depth measurement.

Chapter 8   Application to Thin Concrete Plates

This chapter presents application the air-coupled SWT method to determining the depth of a surface-breaking crack in thin concrete plates. Studies in Chapter 5 showed that contribution of multiple Lamb waves may affect calculation of transmission coefficients in thin plate structures. In this case, the transmission function based on the fundamental mode (i.e., Rayleigh-like waves) may not provide accurate estimation of the crack-depth. In this chapter, a measurement model is developed to apply the air-coupled SWT method to thin concrete plates. This chapter includes appropriate configuration of a source-and-receiver, signal processing procedure, and a transmission functions for the given configuration.

8.5   INTRODUCTION

Many portions of civil infrastructure systems contain various types of plate-like concrete structural elements (e.g., concrete bridge decks, pavement systems and slabs in building structures). Monitoring of cracks in the concrete structures is important to evaluate current health condition of the structures, and if necessary, to make appropriate maintenance decision. One critical issue in field inspection is to estimate the depth of a surface-breaking crack in concrete. Accurate and reliable estimation of crack-depth will provide valuable information to evaluate structural performance of a concrete structure, and its remaining life related to durability issues.

Using nondestructive evaluation (NDE) methods to estimate the depth of a surface-breaking crack has been investigated extensively in recent decades. Comprehensive literature reviews are summarized in Chapter 2. However, studies in chapter 5 demonstrated that it is difficult to directly apply the theory to the plate-like structures with a finite thickness because of *(i) contribution of multiple modes of lamb waves, and (ii) dispersion of fundamental surface waves*. There are many variables which

can affect transmission coefficients of surface waves (e.g., thickness of plates H, duration of impact T, material properties of plates, i.e., Elastic modulus E, Poison's ratio v, and mass density ρ, and sensor locations x). Chapter 5 shows that effects of multiple modes on calculation of transmission coefficients are strongly dependent of the normalized frequency-thickness ratio (f-H/C_s: frequency-thickness normalized by shear wave velocity). In high f-H/C_s ranges, all possible contributing reflections are resolvable in the time domain. In this case, the transmission function based on fundamental modes (i.e., Rayleigh-like waves [17, 78, 79]) converges into the analytic solution obtained from a half-space model. However, as f-H/C_s decreases, contribution of multiple modes increases, which makes it more difficult to separate fundamental modes from higher modes of Lamb waves. In this case, variations of transmission coefficients are significant, and very sensitive to sensor location. Consequently, the transmission function from a half-space model [28-30] may not provide accurate solutions in crack-depth estimation problems. One simple way to minimize contribution of multiple modes in transmission calculation is to resolve all possible modes [51, 80]. However, this requires a large number of sensors. A possible alternative is to define and use a transmission function resulting from the propagation of all contributing modes for the fixed sensor location.

Theoretic studies were performed in Chapter 5 through numerical simulations (FEM) and experimental studies using Plexiglas specimens. The aim of this chapter is to extend the air-coupled SWT method to thin concrete plates (i.e., $1.2 < H/2\lambda R < 1$), practical material in civil engineering. For the purposes, the author proposes a measurement model, which includes appropriate configuration of source and receiver, and a transmission functions for the given configuration. First, a transmission function is calculated using numerical simulations (FEM) in section 8-2. Second, the theoretic curve is calibrated through experimental tests in laboratory in section 8-3. In addition, the air-coupled SWT method is compared to the other NDT methods using the phase velocity, and the time-of-flight diffraction (TOFD) of P waves in section 8-4.

8.6   NUMERICAL SIMULATION

8.6.1   Finite element model

The finite element method (FEM) was used to obtain near-scattering field of surface-waves caused by a surface-breaking crack in concrete. Concrete specimens with finite thicknesses were modeled using rectangular plane strain elements (CPE4R) in the commercial program (*ABAQUS standard v 6.7.1, 2007* [49]) (see **Figure 8-1**). For comparison purposes, a half-space model developed in Chapter 3 was used in this chapter. The finite element models for a half-space model and a plate-like structure are shown in **Figure 8-1** (a) and (b), respectively. In addition, FE models and parameters are summarized in **Table 8-1**. Specific description of developing FE models and applying a transient force function are provided in Chapter 3.

Table 8-1: Finite element models and parameters

Model No.	v	E_c [GPa]	ρ [kg/m^3]	T [μs]	h [mm]	H [mm]	Element type
Model 1						180	4AX[ii]
Model 2	0.22	33.6	2400	60	0,10,20, 30,40,50, 60,70,80, 90,100	Half-space model	4AX+4INAX[i]
Model 3	0.3					Half-space model	4AX+4INAX[i]

Note: 4AX+4INAX [i]: 4-node Axi-Symmetric element + 4 node infinite element; 4AX[ii]: 4-*node* Axi-Symmetric element; 4PE[iii]: 4-node Plane Stain element.
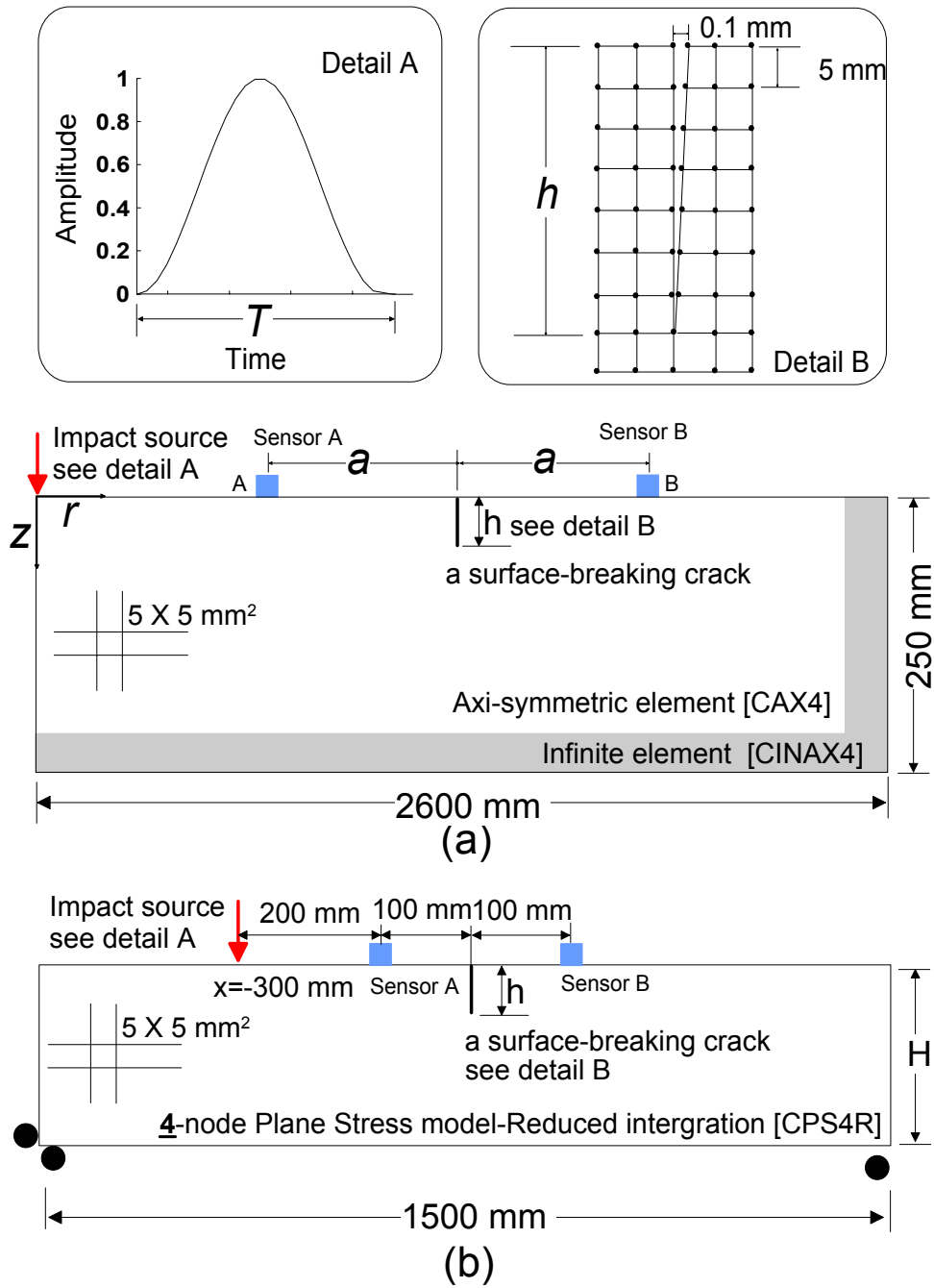
Figure 8-1: FE models: (a) for a half-space model, and (b) for a plate model.

8.6.2 Near-field scattering of surface waves

Figure 8-2 shows B-scan images representing near-scattering field of surface waves along the surface of concrete with a finite thickness of 180 mm. To investigate interaction of multiple modes and Rayleigh waves, velocity responses were obtained from the numerical models with crack depths h=0 and 30 mm.

Figure 8-2 (a) show B-scan images representing stress wave fields in crack-free specimens. In addition, first arrivals of possible wave modes in the plate were calculated using the seismic reflection theory (see Appendix B), and presented as dash lines in the same figures. Direct P, S, and surface waves were denoted as P_i, S_i, and R_i. In addition, multiple reflections of P and S waves were denoted as PP_n, and SS_n, where PP and SS are reflected P and S waves from free boundary of a plate (i.e., P-P, and S-S, respectively), and n is the number of reflections from the bottom of a free plate. Furthermore, mode conversion of P and S waves (P-S or S-P) in free boundaries of a free plate also generates infinite sets of reflection modes. First reflection waves (PS_n, and $PPPS_n$) are presented in **Figure 8-2** (a).
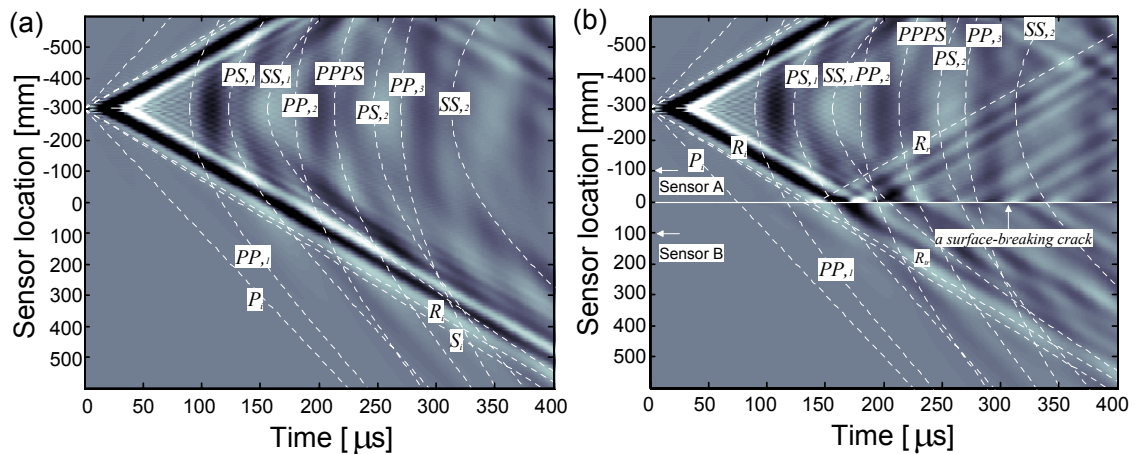
Figure 8-2: B-scan images of waves propagating on a free-plate model with a surface-breaking crack: (a) h=0 mm (crack-free model), and (b) h=30 mm.

Figure 8-2 (b) is a B-scan image representing near-scattering fields of surface waves interacting with a surface-breaking crack having a depth of 30 mm. Consistent with observations in Chapter 3, transmitted (R_t) and reflected surface waves (R_r) are clearly shown in the forward and backward scattering field. It has been well demonstrated that transmission coefficient of surface waves (R_{tr}/R_i) is a good indicator of estimating the depth of surface-breaking crack [7, 8, 40]. However, as seen in **Figure 8-2** (b), multiple reflection waves may interfere with incident surface waves R_r in the backward scattering field, and with transmitted surface waves R_{tr} in the forward scattering field and then have a significant effect on the transmission coefficients of surface waves.

8.6.3   Calculation of transmission coefficient

The surface wave transmission function across a surface-breaking crack is defined as

$$\mathbf{Tr}_n(f,h) = \frac{\mathbf{S}_b(f,h)}{\mathbf{S}_a(f,h)} \bigg/ \frac{\mathbf{S}_b(f,0)}{\mathbf{S}_a(f,0)}, \qquad \text{Equation 8-1}$$

where $\mathbf{Tr}_n$ is the transmission coefficient in function of frequency and crack depth, and $\mathbf{S}_a$ and $\mathbf{S}_b$ are Fourier transforms of the time domain signals measured at locations of A and B, respectively (**Figure 8-1**). The sensor locations of A and B are determined based on observation concerning near-field size in the previous Chapter 3.

8.6.4   *Tr*$_n$ versus *h/λ*

Figure 8-3 shows the normalized transmission coefficient *Tr*$_n$ versus *h/λ* relationship measured from the FE model 1 in **Table 8-1** with a thickness of 180 mm. The results were obtained from the sensors located ±100 mm from a crack opening. The measurement for the current sensor configuration is regarded as approximate far-field according to the findings in Chapter 3. However, multiple reflected waves interfere with surface waves in the backward and forward scattering field. For comparison purposes, the

Tr_n - h/λ curve obtained from theoretic models of a half-space given by Angel and Achenbach [30], and the Tr_n - h/λ curve from a half space model (FE models 2 and 3 in **Table 8-1**) is also shown in same figure. As discussed in Chapter 5, contribution of multiple reflection modes resulted in enhanced transmission coefficients compared to those from a half-space model in a range of h/λ 0.25 to 0.8.

The Tr_n versus h/λ curve from FE models were expressed as a mathematical formula obtained from non-linear regression as follows,

$$
\begin{aligned}
Tr_n &= 1.443e^{-5.09h/\lambda} + -0.443e^{-20.54h/\lambda} & 0 < h/\lambda \le 0.25 \\
&= 2.136e^{-2.94h/\lambda} + -5.098e^{-8.4h/\lambda} & 0.25 < h/\lambda \le 1.0
\end{aligned}
\qquad \text{Equation 8-2}
$$

In practices, once transmission coefficient is given by measurements, using an inverse technique enables to quantitatively evaluate the depth of surface breaking crack in concrete plate. A simple inverse technique will be discussed in section 8.4.1.
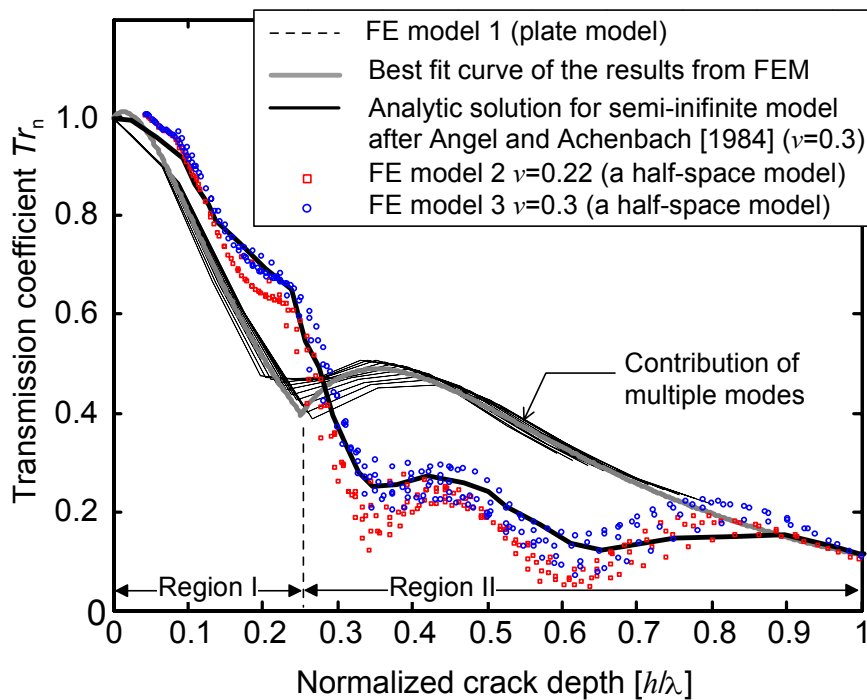
Figure 8-3: Tr_n versus h/λ obtained from FE models. An analytic solution for a half-space model given by Angel and Achenbach (1984) is also shown.

143

8.7 EXPERIMENTAL VERIFICATION

8.7.1 Preparation of specimen, and test setup

A concrete specimen with dimensions of 1500 ⨉ 1500 ⨉ 180 mm^3 (W ⨉ L ⨉ T) was cast in the laboratory (see **Figure 8-4** (a)). Notch-type cracks with depths varying from 10 to 100 mm were generated in the specimen by inserting a 0.5 mm thick metal sheet before casting concrete. The metal sheet was removed from the concrete 12 hours later. The width of crack in hardened concrete specimens measured by crack width gauge is approximately 0.5 mm. Normal-weight concrete, made from normal Portland cement type I/II, river sand, and gravel with a maximum size of 19 mm (3/4 in.), were used for the specimen. The density of concrete specimens, determined by averaging five concrete cylinders (diameter of 10 cm and height of 20 cm) cast simultaneously with concrete specimens, was 2350 kg/m^3. Phase velocity of surface waves calculated from a dispersion curve obtained through the SASW [81] was converging into approximately 2200 m/s when frequency is greater than 15 kHz. The P wave velocity measured by 50 kHz ultrasonic transducers was 4100 m/s.

A schematic view of the test setup is shown in **Figure 8-4** (b). Two air-coupled sensors (PCB model No. 377B01) were used to measure leaky surface waves propagating along the concrete surface. Detailed descriptions of air-coupled sensors are available in Chapter 6. **Figure 8-5** shows air-coupled sensors on the concrete specimen. Ambient-noise insulation device was used to reduce effects of ambient noise.

The self-calibrating technique described in Chapter 6 was used to measure the transmission coefficient Tr and the phase velocity C_{ph} of surface waves across a surface-braking crack. Tr and C_{ph} were calculated using Equations 6-5 and 6-8, respectively. Tr was further normalized by Tr_0 to eliminate geometric attenuation and material damping (see Equation 3-10). Signal coherence function was used to check signal consistency. Five repeated signal data sets were collected at the same test location to obtain signal
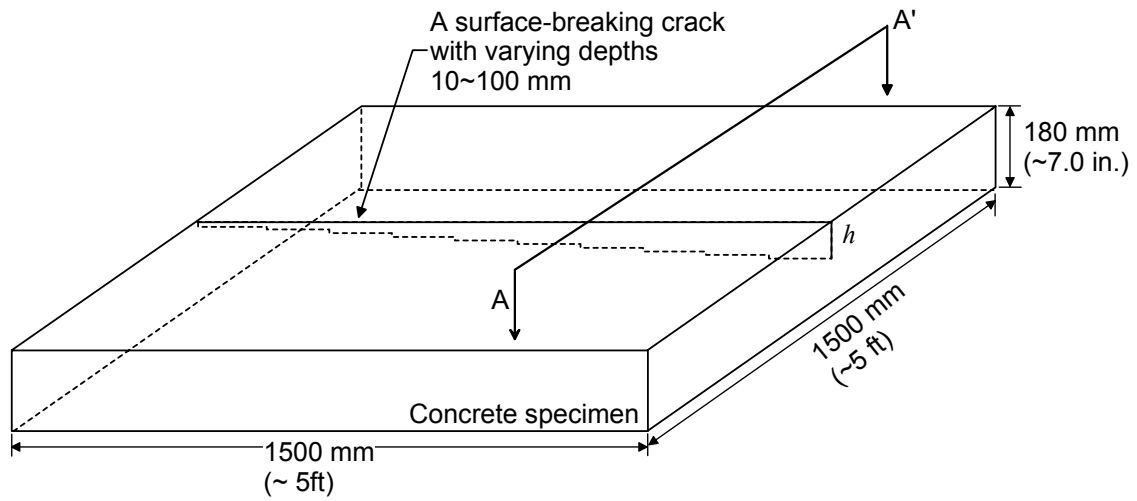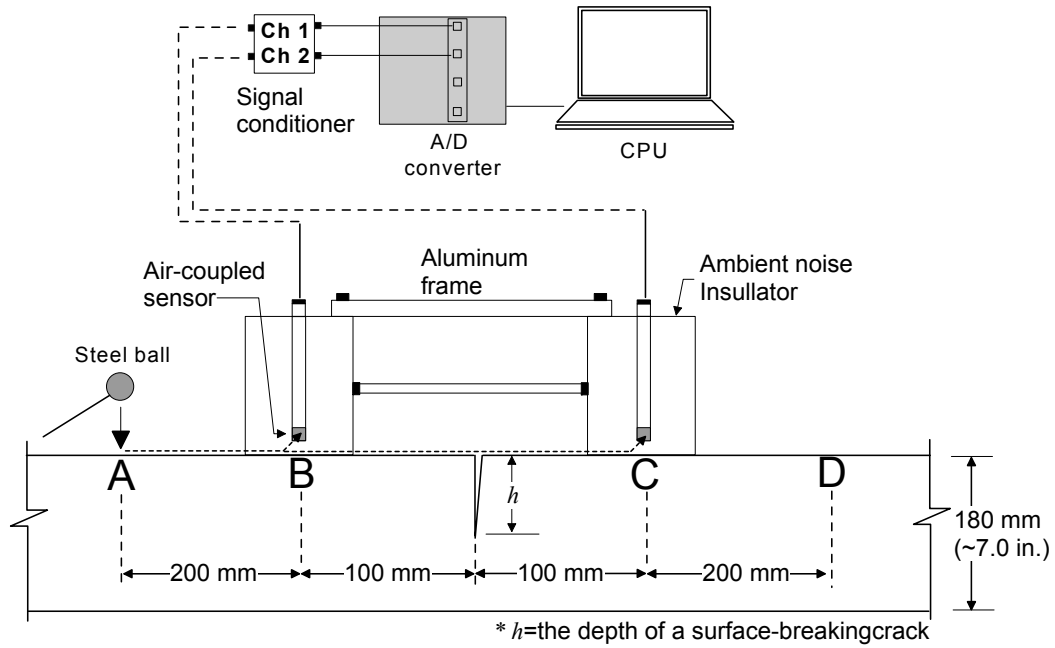
Figure 8-4: Test specimen and test setup of the air-coupled SWT method: (a) 3D view of a concrete specimen with a surface-breaking crack with varying crack depths from 10 to 100 mm and test setup of the air-coupled SWT method (a section view of A-A' in **Figure 8-4** (a)).
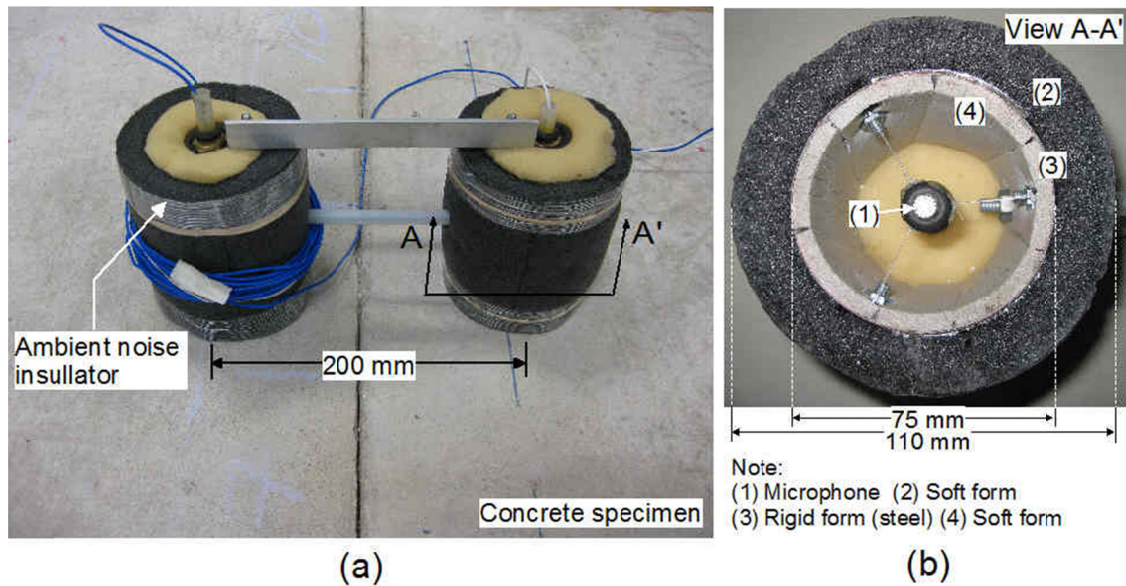
Figure 8-5: Air-coupled sensors: (a) on the concrete specimen, and (b) view from the bottom.

coherence function using Equations 3-8 and 3-9. Three steel balls with a diameter of 13, 12, and 8 mm were used as impact sources. The acquired signals were digitized at a sampling frequency of 10 MHz using an NI-USB 5133 oscilloscope.

8.7.2   Typical signal measured using air-coupled sensors

Figure 8-6 (a) and (b) show typical time domain signals measured by two air-coupled sensors measured from the crack-free region, and cracked-region with h=30mm. The incident waves were generated by using a steel ball having a diameter of 12 mm. The impact force generated incident surface waves with a center frequency around 20 kHz, and provided good signal consistency up to 30 kHz. The raw signal data and windowed signal data were presented as dash lines and solid lines.

Figure 8-6 (c) and (d) present the normalized spectral amplitude and signal consistency function of the windowed time-domain signals shown in **Figure 8-6** (a) and

(b). Spectral amplitude of the surface waves measured from cracked region is lower than those measured from the crack-free region. More discussion on quantitative evaluation is available in the next section.
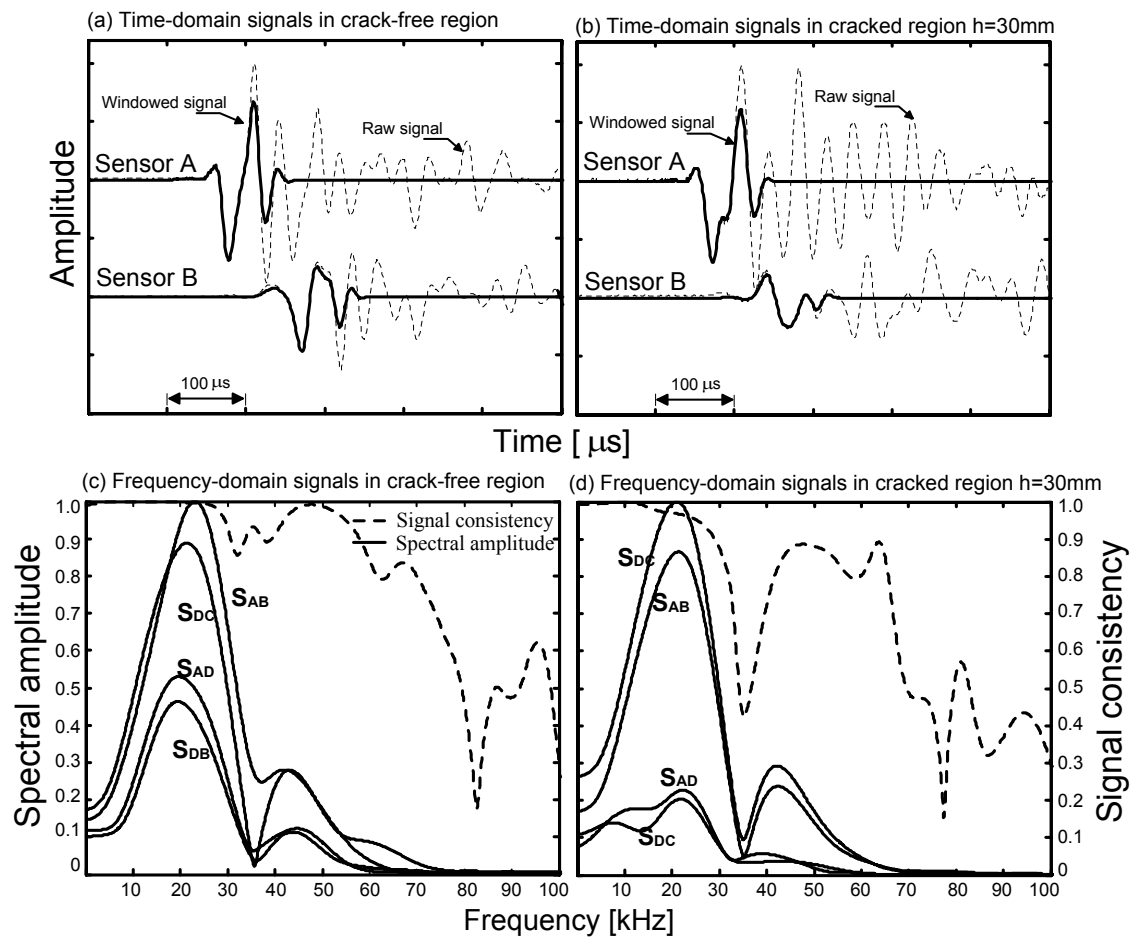
Figure 8-6: Typical signals from the concrete specimen: (a) typical time-domain signals from the crack-free region (b) typical time-domain signal from the cracked-region with *h*=30mm, (c) and (d) normalized spectral amplitude, and signal consistency calculated using windowed signals from the crack-free region, and cracked-region with *h*=30mm, respectively. Signals were generated by the 12 mm-diameter steel ball.

8.7.3   Calibration curve of transmission function

Figure 8-7 presents the normalized transmission coefficient Tr_n versus h/λ curves obtained from experiments on the concrete specimen. Signal data were collected using the setup shown in **Figure 8-4**. To minimize the asymmetric properties of concrete material (surface roughness, randomly distributed air-voids, and aggregates) and sensor setup, the self calibration procedure was used. Three different steel balls of different diameters (i.e., 8 mm, 12 mm, and 13 mm) were used to generate the incident surface wave. The transmission coefficients shown in Figure 8-7 are corresponding to two frequencies at 5 and 20 kHz. Note that 20 kHz was selected around center frequency of the incident surface waves, and 5 kHz was selected in the low frequency region where interfere with higher-order mode is minimized (see also Chapter 5). Designed crack depths were used to calculate normalized crack depths (h/λ) in the horizontal axis. The experimental results show pretty good agreement with the FEM simulation,
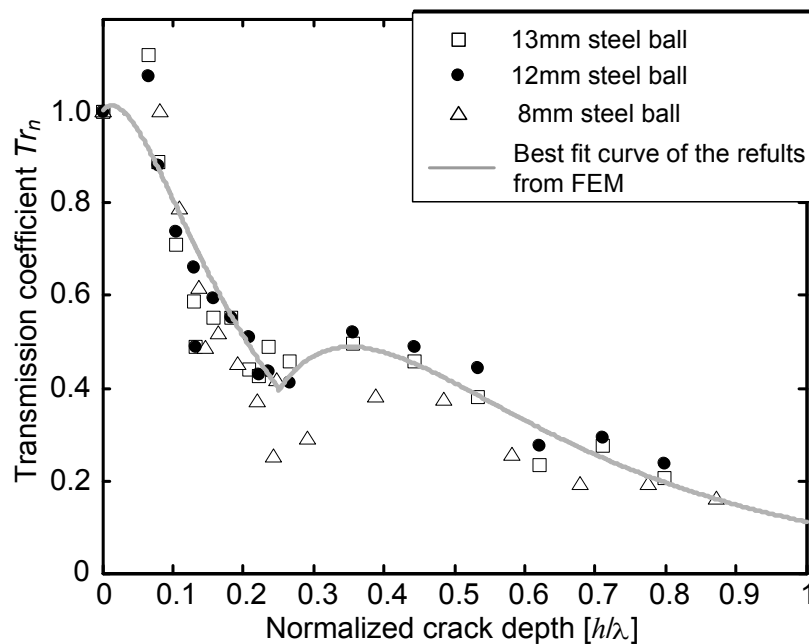
Figure 8-7: Tr_n versus h/λ obtained from experiments. A theoretic curve obtained from numerical simulation is also shown.

148

which is denoted as a bold line. Particularly, results obtained using steel balls having larger ball size (12, and 13 mm) shows better agreement with the numerical simulation than the smaller ball having a diameter of 8mm.

8.8 CRACK DEPTH ESTIMATION

8.8.1 Using Transmission coefficient Tr_n

In practical application, once transmission coefficient is calculated using Equation 6-5 and Equation 3-10, the depth of a surface-breaking crack can be estimated by inversing the transmission function. Note that the shape of curves does not ensure the unique solution for a single input of Tr_n. In this study, two inputs of measured tr_n correspond to two frequencies of 5 and 20 kHz, each of which covers the region I and region II in the transmission function (see **Figure 8-3**). The depth of a surface-breaking crack can be determined when an error function defined in Equation 8-3 results in minima.

$$Error(h) = \sqrt{\sum_{i=1}^{2}(\frac{Tr_n(f_i, h/\lambda_i) - tr_n(f_i)}{Tr_n(f_i, h/\lambda_i)})^2} \qquad \text{Equation 8-3}$$

where tr_n, is measured transmission coefficient calculated using Equation 3-10, i is an index of input values, and f_i and λ_i is frequency and wavelength with an index i. In addition, λ_i is in function of frequency and phase velocity as follows,

$$\lambda_i = f_i / C_{ph}(f_i) \qquad \text{Equation 8-4}$$

Figure 8-8 presents comparison of designed crack depth and estimated crack depth obtained using Equation 8-3. The estimated crack depths are close to the designed crack depth. This demonstrates that the measurement model described in this study is

149
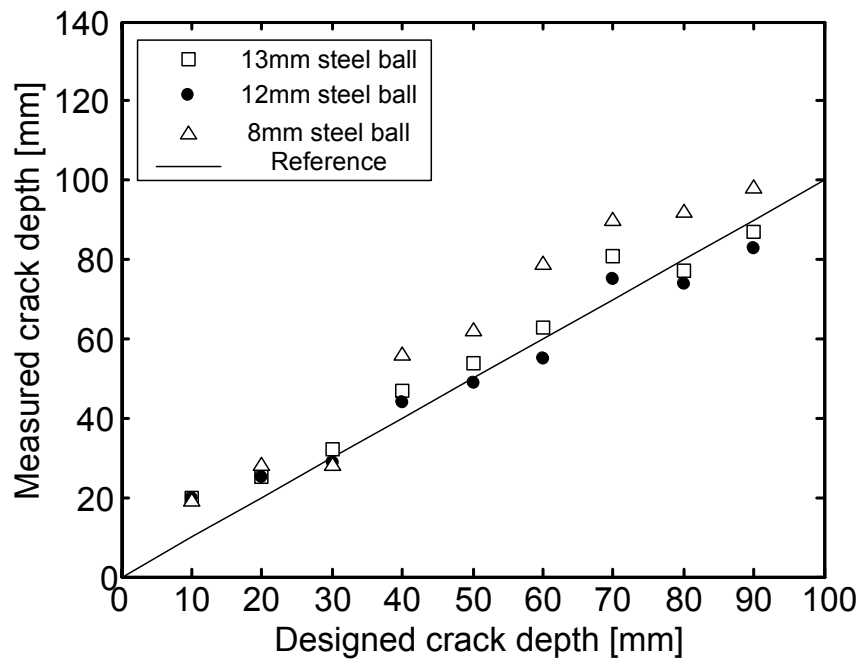
Figure 8-8: Crack depth estimation using the air-coupled SWT method.

effective to estimate the depth of a surface-breaking crack in plate-like concrete structure. Note that using larger steel balls (12 mm, and 13 mm) resulted in more accurate results than using a smaller ball (8mm).

8.8.2 Using Phase velocity C_{ph}

Figure 8-9 presents the phase velocity of surface waves C_{ph} and crack depth relation obtained from experiments and FE models. Experimental results show that the C_{ph} was not sensitive to the crack depth h in the range considred in this study (i.e., $0 \leq h \leq 100$ mm). Results from numerical simulation show the similar trend that C_{ph} does not change much until the crack depth becomes greater than 110 mm. This results is consistent with observation by previous researchers [82]. They showed that the time difference of surface waves between two sensors (or phase velocity) remains stable when

150

h/λ <0.8. It can be seen that C_{ph} is not a sensitive acoustic parameter to estimate the depth of shallow cracks in thin concrete plates.
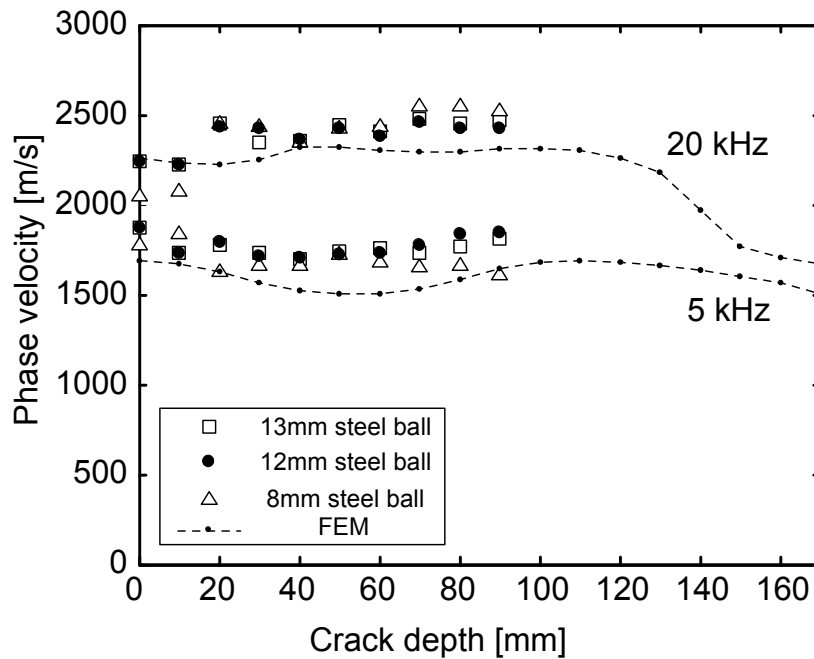
Figure 8-9: Phase velocity versus crack depth in frequencies of 5 and 20 kHz.

8.8.3 Using TOFD of P waves

For comparison purposes, the depth of a surface-breaking crack was also estimated by the time-of-flight diffraction of P waves (i.e., TOFD method). In the TOFD method, two sensors are located at the either side of a surface-breaking crack. Ultrasonic waves are sent from one sensor from one side of the crack, and received by the other sensor on the opposite side of the crack. The depth can be calculated from the measured travel times of ultrasonic waves. As shown in **Figure 8-10**, two different setups were used to estimate the depth of a surface-breaking crack in concrete using the TOFD method.

First, **Figure 8-10** (a) shows the test setup of using two ultrasonic transducers with a center frequency of approximately 50 kHz. Two sensors were used as a source and a receiver in the pitch-and-catch mode. The depth of crack can be calculated using Equation 8-5.

$$h = \sqrt{\left(\frac{C_p \Delta t}{2}\right)^2 - (\frac{\Delta x}{2})^2}$$

Equation 8-5

where Δt is the measured travel time of P waves, and Δx is center-to-center distance between two sensors (i.e., 200 mm in this study). In addition, **Figure 8-10** (b) shows the test setup of using transient waves according to previous researchers [3]. Incident waves were generated by applying impact using steel ball with a diameter of 8 mm. The generated waves were measured by two accelerometers. The depth of crack can be calculated using Equation 8-6.

$$h = \sqrt{\left(\frac{C_p \Delta t + x_1}{2}\right)^2 - (\frac{\Delta x}{2})^2}$$

Equation 8-6

where x_1 is sensor-to-source distance (100 mm in this study).

Figure 8-11 shows estimated crack depths obtained using Equations 8-5 and 8-6. The test setup of using ultrasonic transducers resulted in large errors in crack-depth estimation. This is mainly due to difficulties to pick first-arrival of diffracted waves in the receiver. In contrast, the estimated crack depth from the test setup of using transient waves show better agreement with the designed depths than using ultrasonic transducers. However, compared to the results from the air-coupled SWT method, the estimated crack depth by the TOFD method tends to overestimate results, especially for cracks with shallow depths.
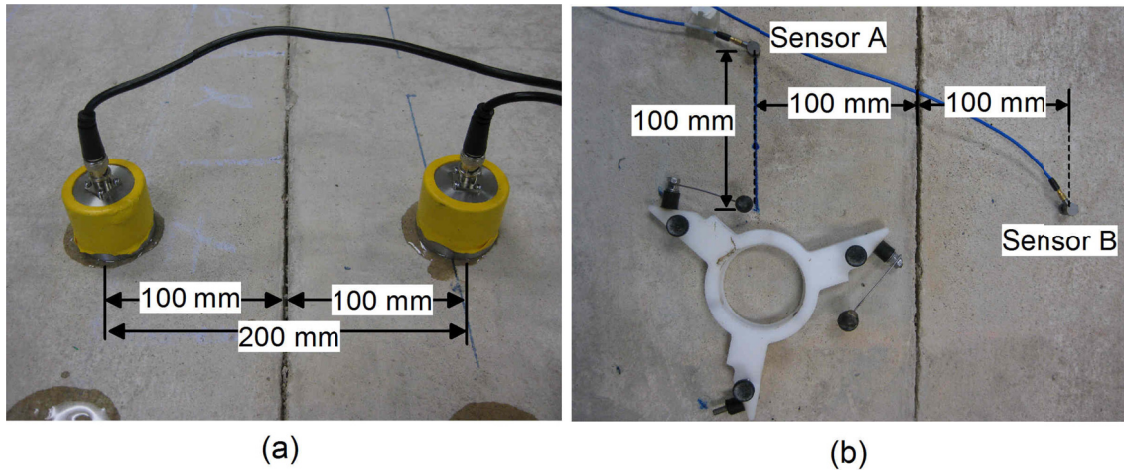
Figure 8-10: Testing setup of TOFD method: (a) using ultrasonic sensors (50 kHz), and (b) using transient waves.
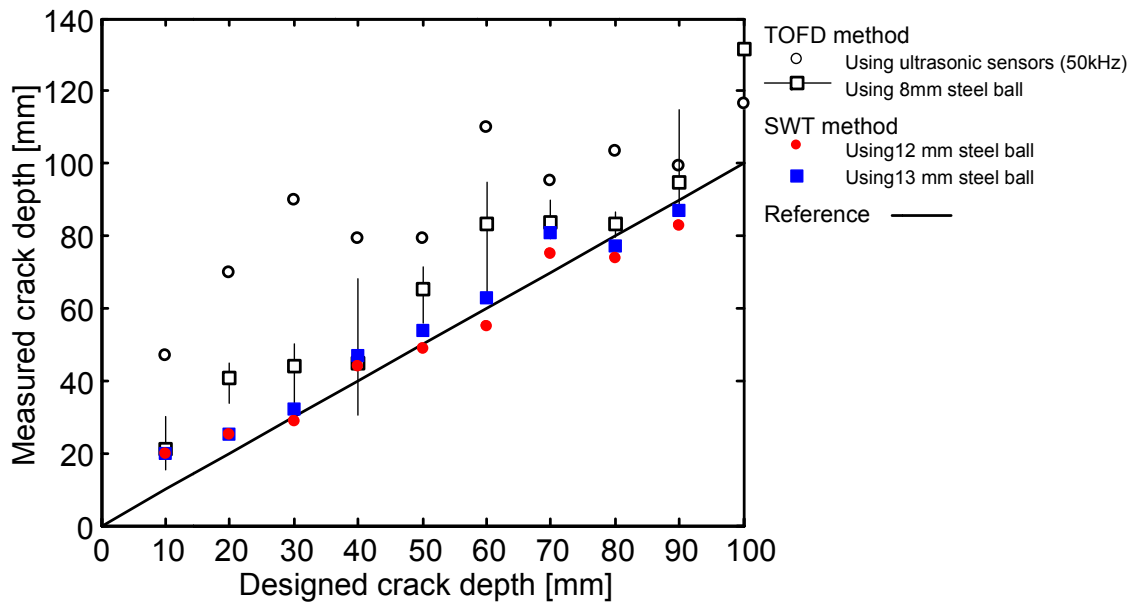
Figure 8-11: Crack depth estimation using the TOFD method. For comparison purposes, results from the air-coupled SWT method were also shown.

8.9   CONCLUSIONS

In this study the air-coupled SWT method was extended to thin concrete plates. First, the effects of multiple modes of lamb waves on calculation of transmission coefficient of surface waves were investigated using numerical simulations (FEM), and reliable transmission function (Tr_n-h/λ curve) was defined. Second, experimental studies were carried out to verify the numerical simulation results. Third, the effectiveness of the air-coupled SWT method was demonstrated through comparison analyses with other NDT methods: using the phase velocity of surface waves, and the time-of-flight diffraction of P waves. The following conclusions are drawn based on the results of this study.

1) Surface wave transmission measurement is affected by the contribution of multiple modes (i.e., multiple reflections by the bottom of a free-plate). When f-H/C_s is less than 2, the contribution of multiple modes increases, which makes it difficult to separate fundamental modes from multiple modes. In this case, variations of transmission coefficients are significant, and very sensitive to sensor location. As an alternative, the author developed a measurement model which includes sensor-to-source configuration, reliable transmission function, and signal processing procedure.

2) The surface wave transmission curve based on the FEM analyses and the experimental studies show good agreement. It verifies that the measurement model proposed in this study is effective in estimating the depth of surface-breaking cracks in thin concrete plates.

3) In addition, for the practical applications, a simple inversion technique based on two frequencies was proposed. The estimated crack-depths calculated using the two-frequency method showed good agreement with the crack-depths.

154

4) Consistent with previous research [82], the phase velocity of surface waves C_{ph} was not a sensitive ultrasonic parameter to estimate the crack-depth h in concrete when h is smaller than or comparable to wavelength of incident surface waves.

5) The depths of cracks were also estimated using the TOFD method with two different test setups: *(i) ultrasonic transducers, and (ii) transient waves generated by impact source*. The test setup for using ultrasonic transducers resulted in very large errors in crack-depth estimation. This is mainly due to errors in selecting the first-arrival of diffracted waves in receivers. In contrast, the estimate crack depth from the test setup with transient waves showed better agreement with the selected crack depths than using ultrasonic transducers. However, compared to the results from the air-coupled SWT method, the estimated crack depth by the TOFD method tends to overestimate crack depth, especially for cracks with shallow depths.

155

Chapter 9   Surface Wave Transmission across a Partially Closed Surface-breaking Crack in Concrete

Most of studies on surface wave transmission across a surface-breaking crack were obtained by using a well-defined crack (or notch) in laboratory. In fact, the theory may not be directly applied to actual surface-breaking cracks in concrete structures subjected to external loadings where the cracks are generally ill-defined, and partially closed. The purpose of this chapter is to investigate the transmission coefficient of surface waves across a partially closed surface-breaking crack in concrete. For comparison purpose, the author also investigates the phase velocity of surface waves, with varying interfacial conditions in a surface-breaking crack.

9.1   INTRODUCTION

Most of the results on surface wave transmission across a surface-breaking crack were obtained by using a well-defined crack (or notch) in laboratory. In fact, there is a critical gap of knowledge to apply the theory to in-situ concrete structures. For in-service concrete structures subjected to external loadings, the cracks are generally ill-defined, and partially closed. Kendall and Tabor [83] investigated interfacial contact between solids using multiple methods including electrical, thermal, optical and ultrasonic assessment. Previous researchers [84, 85] have also demonstrated that ultrasonic waves are sensitive to evaluate rough surface in contact or imperfect interfaces in aluminum. Pecorari [86] investigated scattering of surface waves by a partially closed surface-breaking crack in aluminum specimen and explored effects of external loadings on reflection and transmission coefficients of surface waves. Na and Blackshire [87] investigated interaction of surface wave with a tightly closed fatigue crack in aluminum. They experimentally demonstrated that the crack interfacial waves can transmit through the crack, which affect transmission coefficient of surface waves across the crack.

156

However, similar works for concrete, heterogeneous but statistically isotropic material, have not been performed until now. Cheng and Sansalone [88, 89] carried out a series of research on 'determining the minimum crack width that can be detected using transient stress waves (i.e., impact echo)'. The minimum crack width for which stress waves are not transmitted across the crack faces was found to be 0.08 mm. The result may provide a rough idea on effects of concrete crack width (or interfacial condition in the crack) on stress wave transmission across a partially closed crack. However, more work is still needed to better understand how the interfacial conditions in a partially closed crack affect transmission of surface waves.

The purpose of this chapter is to investigate transmission coefficient of surface waves across a partially closed surface-breaking crack in concrete. Five concrete specimens were prepared in laboratory for experimental studies. The experimental program includes three test steps: *(i) monolithically increasing compressive loadings from 0 to 110 kN were applied to crack-free specimens, (ii) a point load was applied at the midsection of specimens using the three-point bending test setup until a vertical surface-breaking crack appeared, and (iii) compressive loadings same as in the first step were applied to a partially closed crack generated in the second step.* In the first and second test steps, effects of stress levels on acoustic parameters of surface waves (i.e., transmission coefficient and phase velocity) were investigated in crack-free specimens. In the third step, sensitivity of surface wave parameters to various interfacial conditions caused by compressive loadings is investigated.

9.2   EXPERIMENTAL PROGRAM

9.2.1   Preparation of specimens

A concrete specimen having dimensions of 400 X 190 X 1500 mm³ (**W X T X L**) was prepared in laboratory (see **Figure 9-1**). Normal-weight concrete, made from type I/II cement, river sand, and coarse aggregate with a maximum size of 19 mm (¾ in.),

157

were used. The design compressive strength of concrete was 20 MPa (3000 psi). Three cylinder specimens were used to measure concrete compressive strength according to ASTM C39. The measured concrete strength at the time of testing range from 22.3 MPa (3240 psi) to 23.58 MPa (3420 psi), with a mean value of 22.84 MPa (3317 psi). Two layers of longitudinal reinforcing bars (rebars) were placed to avoid abrupt collapse of concrete specimens. Four and two rebars with a diameter of 13.3 mm (3/8 in.) (No. 3) were used for top and bottom layer respectively. To generate a single vertical crack, the middle part of the top and bottom rebars were unbonded by wrapping the bar with a thin plastic film of 40 cm (15.7 in.) long (see **Figure 9-1**). This design is to ensure generating a single surface-breaking crack in concrete specimens, and also makes it easy to obtain the crack width (i.e., crack mouth opening displacement, CMOD) from measured data (strains of top and bottom rebars). Transverse rebars (No. 3) were placed to avoid shear failure and ensure the beam failed in a flexural mode.
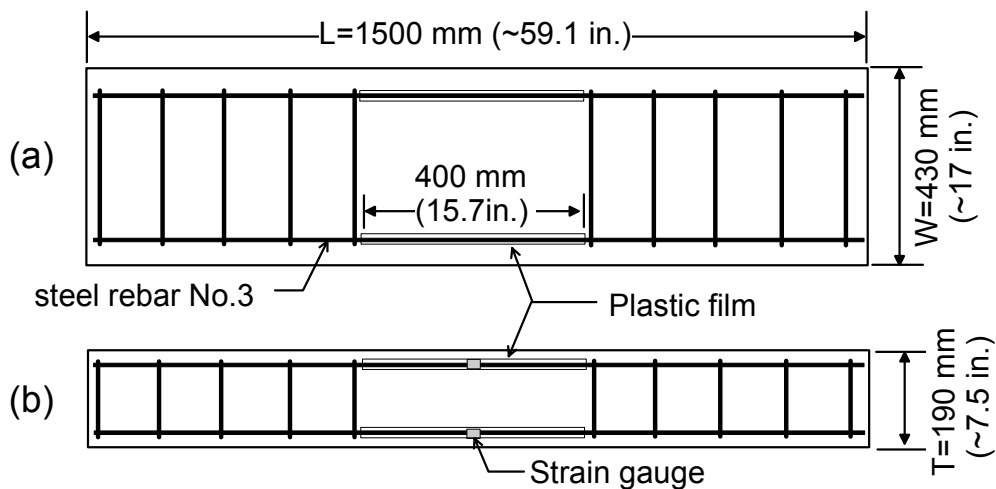
Figure 9-1: Details of a concrete specimen: (a) top view, and (b) side view.

9.2.2   Testing procedure

The testing procedure for the concrete specimen includes three steps (see **Figure 9-2**) as follows,

- Step I: apply external axial loadings P_1, and investigate effects of internal compressive stresses on the transmission coefficient and the phase velocity of surface waves in concrete specimens

- Step II: apply a point loading P_2 and generate a flexural crack (a vertical surface-breaking crack) in concrete, and investigate effects of internal tensile stresses on the acoustic parameters of surface waves in concrete specimens.

- Step III: apply external loading P_3 to partially close the crack and investigate the change of the acoustic parameters of surface waves across a partially closed surface-breaking crack.
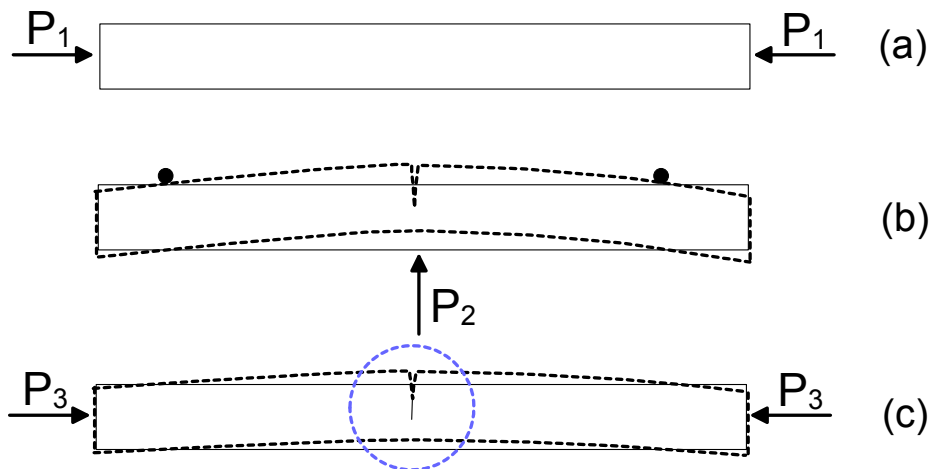
Figure 9-2: Testing procedure of the concrete specimen: (a) apply external loadings P_1, (b) apply a point load P_2 using the three-point bending setup, and generate a vertical surface-breaking crack, and (c) apply external loadings P_3 to induce various interfacial conditions in the crack.

9.2.3 Test setup to apply external loadings

External post-tensioning was applied at the ends of the concrete specimen to investigate the effects of compressive loadings on the transmission coefficient and the phase velocity of surface waves. The test setup to apply external loadings is shown in **Figure 9-3**. The compressive loads were monotonically increased from 0 to 24 kips (106.7 kN: approximately 10% of nominal compressive strength of concrete specimens) with 7 steps (0, 4, 8, 12, 16, 20, and 24 kips; or 0, 17.8, 35.6, 53.3, 71.1, 88.9, and 106.7 kN). Two loading rams (LR 1 and 2 in **Figure 9-3** (b)) controlled by a hydraulic pump were placed to apply external loadings. Magnitude of compressive loads was monitored by two load cells (LC 1 and LC 2 in **Figure 9-3** (b)) attached to the loading rams. In addition, rubber pads were used to prevent stress concentration at the concrete-steel interface.

A three-point bending system was used to generate a flexural crack (i.e., a vertical surface-breaking crack) in the specimen. A point load was applied on the specimen in the upward direction from the strong floor in the laboratory. Two bolt groups, each of which includes four 1-inch diameter high-strength rods and bolts, were used to resist the loadings applied to the specimens at one support by utilizing back-to-back channels that straddled the test specimens. Load was applied using a system that included a hydraulic loading ram, a load cell, a spherical head and plates placed intermittently between these components. A spherical head was used to ensure proper alignment of the bearing plate relative to the concrete surface during testing.

Deformation of the concrete specimen under external loadings was monitored by a static data acquisition system in the laboratory. The static instrumentation includes three load cells for loading rams (see **Figure 9-2**), four strain gauges (two on top and bottom rebars, and two on concrete top surface) (see **Figure 9-1**), and two linear potentiometers (linear pot) (see **Figure 9-4**).
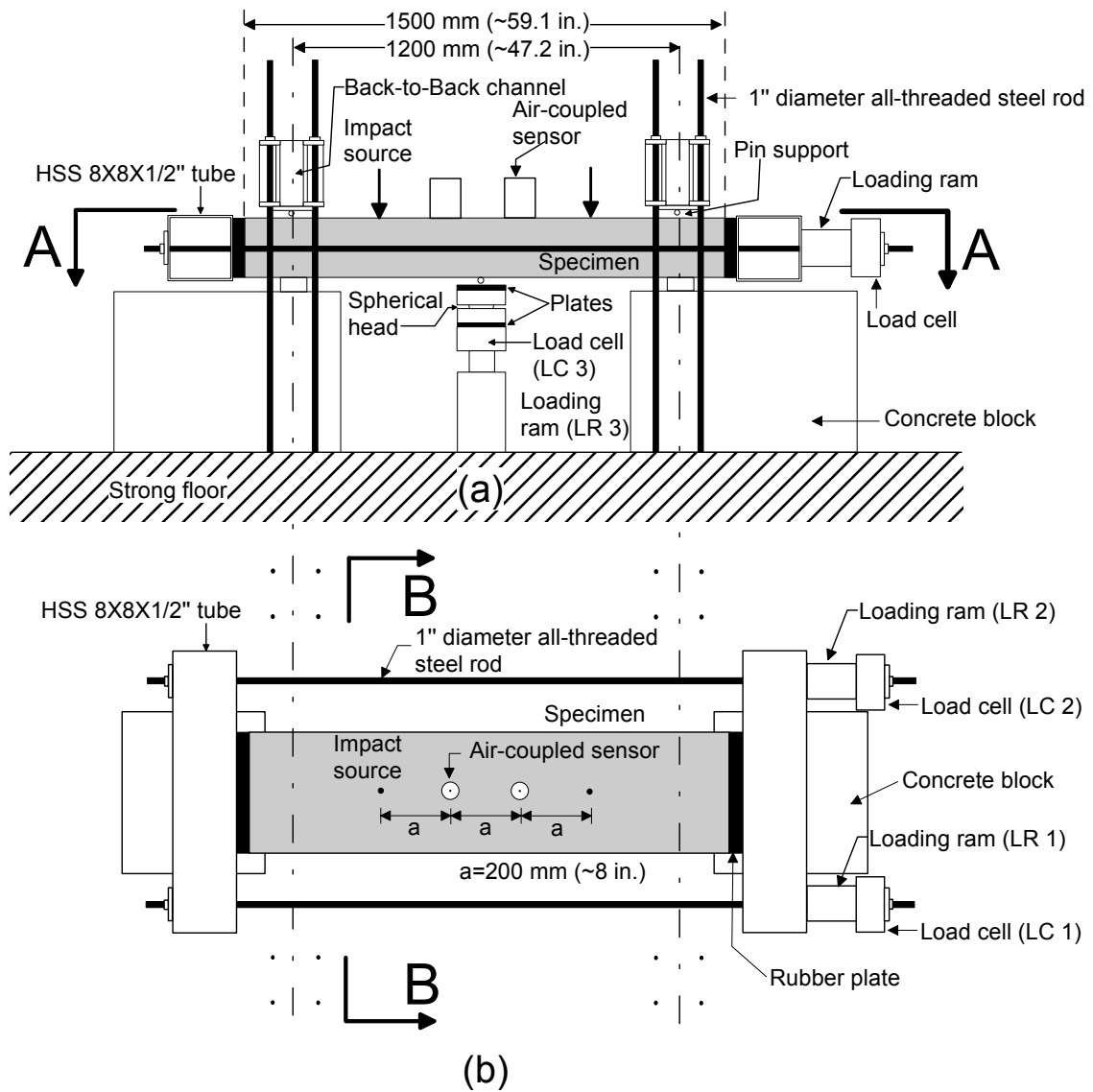
Figure 9-3: Test setup of the concrete specimen to apply compressive forces and generate a surface-breaking crack: (a) elevation view, and (b) plan view from the section A-A in (a).

161
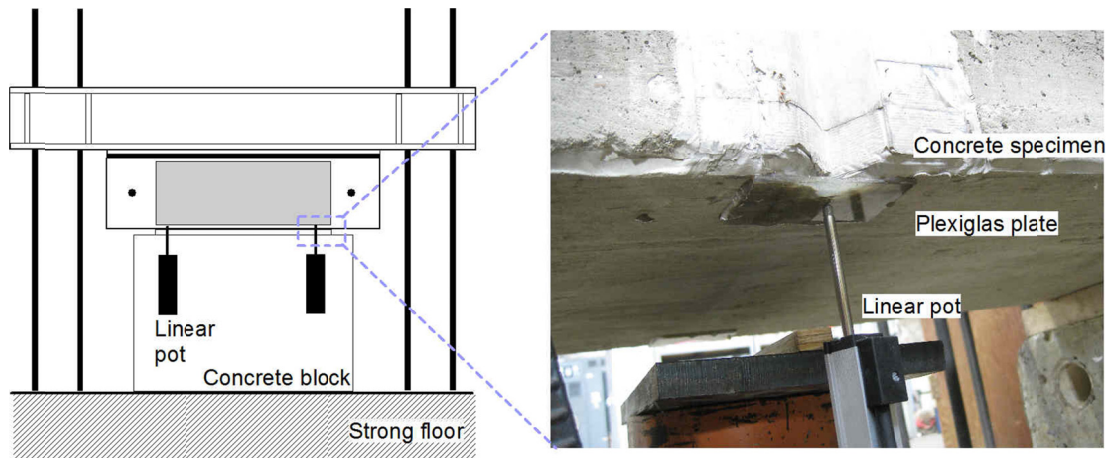
Figure 9-4: Sectional view B-B in **Figure 9-3** (b) of the test setup and location of linear potentiometers.

9.2.4   Test setup of transient stress wave measurement

Figure 9-5 shows a test setup of using air-coupled sensors for measurement of transient stress waves. Test setup in this chapter was the same as shown in **Figure 6-3**. The sensor-to-source spacing, and sensor-to-sensor spacing were kept as 200 mm during whole test steps (see **Figure 9-3**). Two air-coupled sensors described in Chapter 6 were used to measure leaky surface waves in the concrete specimen before and after cracking in the test steps described in Section 9.2.2. The surface waves were generated by hitting the concrete surface with two steel balls having diameters of 13 and 8 mm. The acquired signals were digitized at a sampling frequency of 10 MHz using an NI-USB 5133 oscilloscope. A *Hanning* window was applied to the time domain signal to extract the surface wave component before spectral analyses. To check signal-to-noise level, spectral coherence curve was calculated using Equation 3-8 based on five repeated signals collected at the same location. Transmission coefficient of surface waves was measured using a test setup based on the self-calibrating (SC) procedure, and calculated using Equation 6-5. In addition, phase velocity of surface waves was calculated by the spectral

analyses of surface waves (SASW) using the same signal data obtained from the self-calibrating procedure using Equation 6-8.
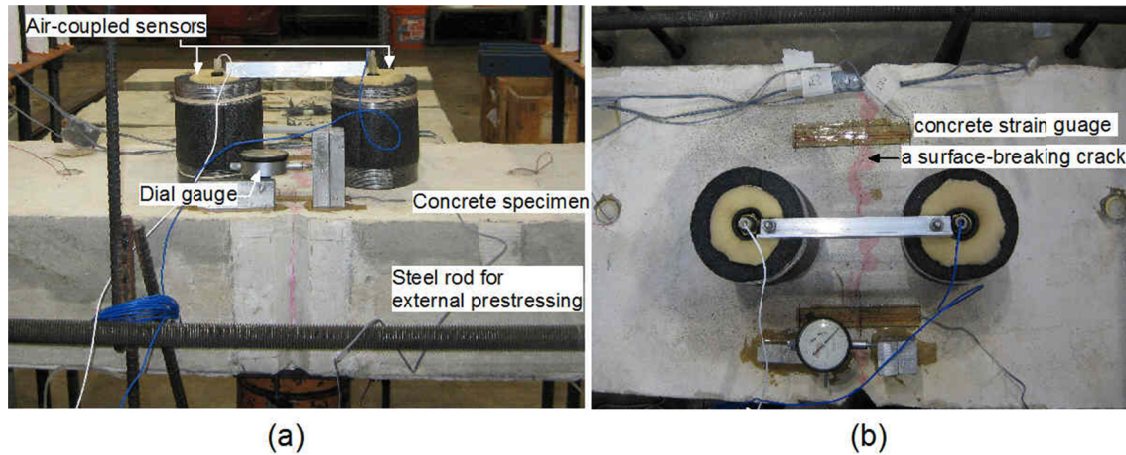
Figure 9-5: Test setup of using air-coupled sensors for transient stress wave measurement: (a) side view, and (b) top view.

9.3   BEHAVIOR OF TEST SPECIMENS

9.3.1   Step I: apply external compression before cracking

In step I, the concrete specimens were compressed by the external post-tensioning system shown in **Figure 9-3**. Applying external compression P_1 generates internal stresses at the midsection of the specimen presented as

$$\sigma = \frac{P_1}{A_g} + \frac{P_1 e}{I_g} y \qquad \text{Equation 9-1}$$

where the second term is additional stresses caused by eccentricity of applying loading (e), and A_g is gross sectional area of the concrete specimen, I_g is inertia moment based on gross concrete section, and y is distance from a neutral axis of the section. However, the strain history measured by strain gauges attached to top and bottom rebars shows that the bending mode caused by eccentricity is much smaller than the longitudinal mode during

163

the test step I (see **Figure 9-6**). Therefore the second term was ignorable, and the stress distribution was reasonably assumed a constant distribution along depth of the section. The concrete specimen behaved in a linear elastic range up to applying maximum compressive loadings in this study (approximately 10 % of the ultimate strength of the section). Effective modulus of elasticity E_{eff} in the loading direction was 3982 ksi (~27454 MPa).
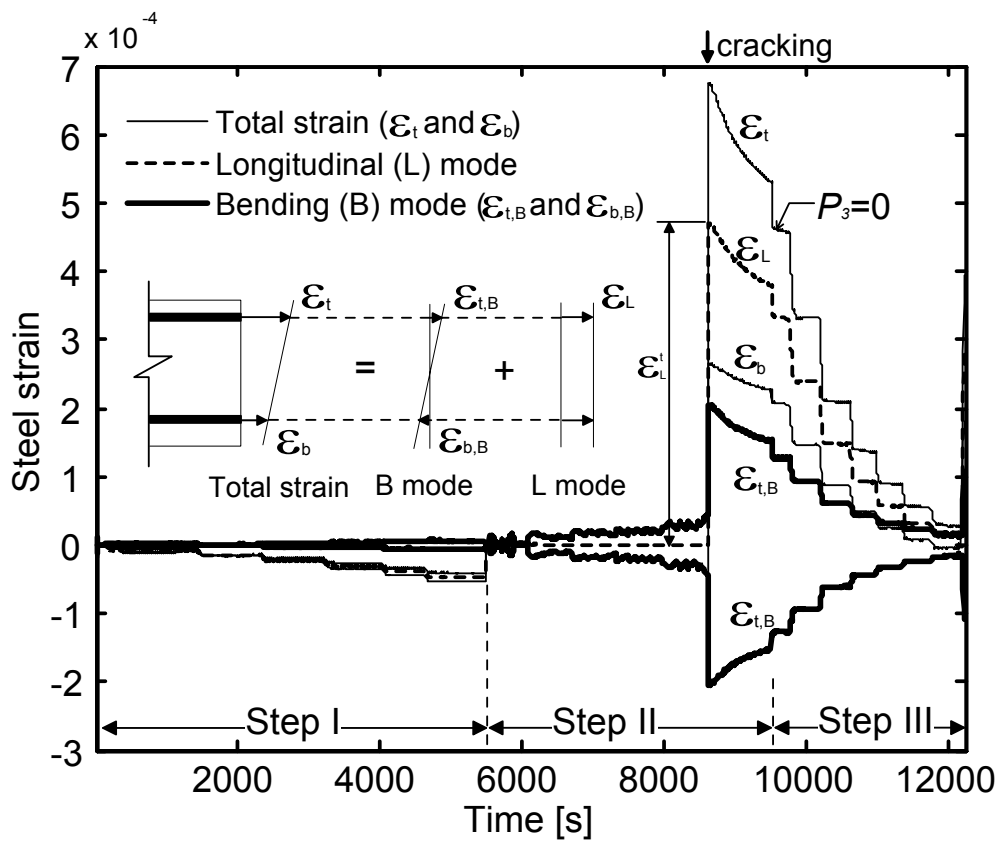
Figure 9-6: Steel strain history during test steps I, II, and III.

164
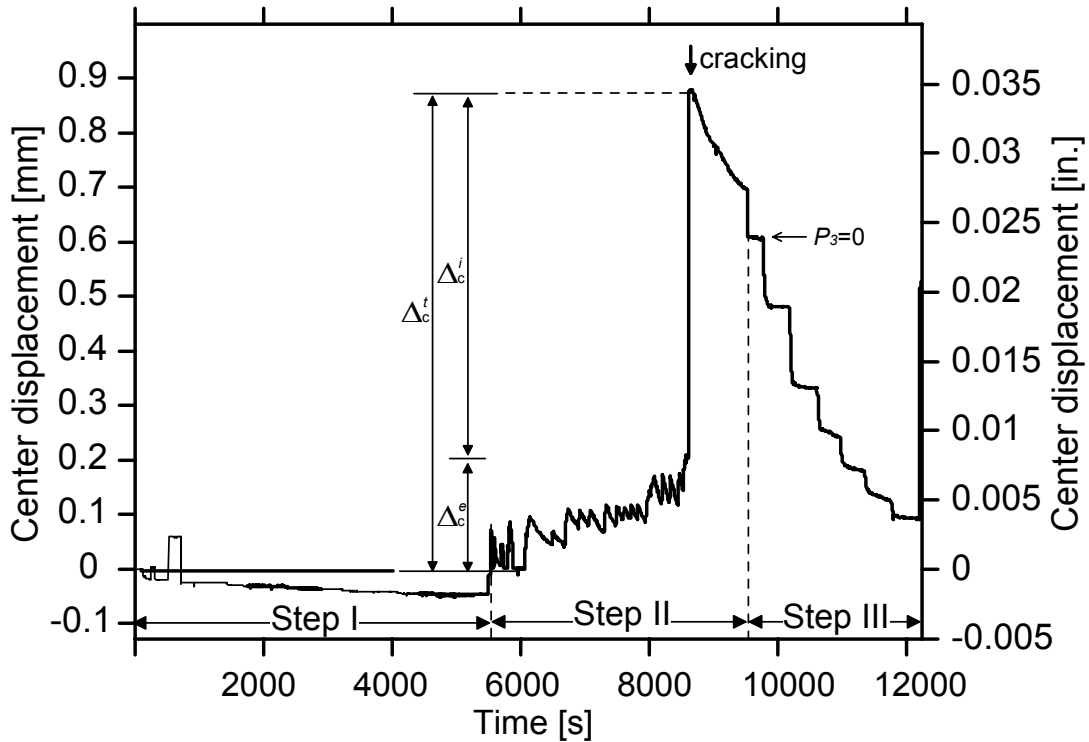
Figure 9-7: Center displacement history during test steps I, II, and III.

9.3.2 Step II: generating a vertical surface-breaking crack

After releasing all compressive loads P_1, the concrete specimens were loaded by the loading ram (LR 3) in the test setup shown in **Figure 9-3** (a). Applying an upward pointed loading P_2 generates flexural stresses along the concrete section. Distribution of stress before cracking can be obtained as follows,

$$\sigma = \frac{M}{I} y = \frac{3 P_2 l}{b H^3} y \qquad \text{Equation 9-2}$$

where l is the span length of specimen (i.e., center-to-center distance between supports), b and H is a width and a thickness of the specimen, respectively.

Figure 9-8 shows force and center displacement (P_2-Δ_c) relationship of the concrete specimen in the second test step. P_2 was measured by the LC 3 (see **Figure 9-3**), and displacement Δ_c was obtained by averaging results from two linear potentiometers

165

installed beneath the midsection of the concrete specimens (see **Figure 9-4**). For comparison purposes, P_2 was also calculated using Equation 9-3 and shown in the same figure.

$$P_2 = \frac{4EI}{l}\varphi$$

Equation 9-3

where curvature φ was calculated by measured strains from top and bottom reinforcement bars ($\varphi = (\varepsilon_{top} - \varepsilon_{bottom})/h_2$), h_2 is center-to-center distance of top and bottom rebars, EI is flexural modulus of specimens, and l is span length of specimens (=the center-to-center distance of supports). P_2-Δ_c curve shows linear elastic relation before the tensile strength of concrete is reached in the tensile side of the specimens. In the linear elastic range, P_2 based on external measurements by the LC 3 shows good agreement with internal measurements by steel strain gauges, which demonstrates the validity of the test setup and instrumentation in this study.
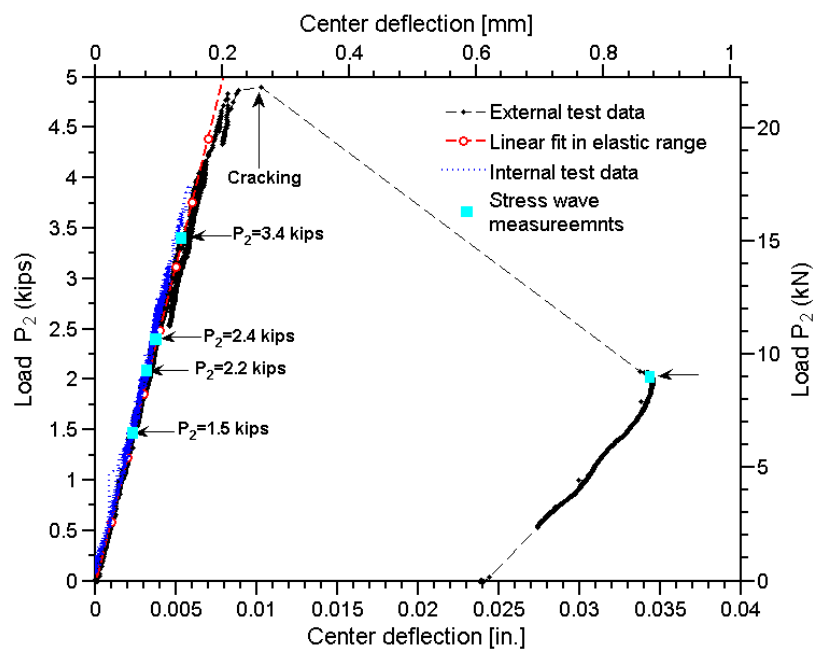
Figure 9-8: Typical force and center deflection curve in the test step.

166

The test setup was effective to generate a single vertical surface-breaking crack in the midsection of concrete specimens. However crack propagation was in a brittle manner due to low reinforcement ratio. After cracking, concrete does not provide resistance to internal stresses in the crack section, and only rebars participate in force-resisting mechanism. In addition, steel rebars in the unbounded region (see **Figure 9-1**) have a flat stain gradient; consequently, shear stresses in this region disappear after cracking. This prevents initiation of additional diagonal cracks (shear cracks) or other flexural cracks in the test region.

The behavior of the concrete specimen having a vertical surface-breaking crack can be explained through modeling the crack as a generalized plastic hinge [90]. The two halves of the specimens are both assumed to be rigid and rotate angle θ,

$$\theta = \frac{\delta}{2h}$$

Equation 9-4

where δ is crack mouth opening displacement (CMOD), and h is the depth of a surface-breaking crack. Consequently, center displacement due to cracking can be presented as follows,

$$\Delta_c = \frac{\delta l}{4h}$$

Equation 9-5

Using Equation 9-5, the initial CMOD immediately after the crack forms can be calculated using measured center displacement Δ_c^i ($=\Delta_c^t - \Delta_c^e$), which can be denoted as δ_{disp}^i. Δ_c^t is the total displacement measured by linear pots, and Δ_c^e is the displacement due to elastic deformation (see **Figure 9-7**). The superscript i means initial measurement. Note that Equation 9-5 may overestimate calculated center deflection because of effects of uncracked part in the cracked section [90]. Consequently, δ_{disp}^i can provide a lower-boundary of CMOD in this study.

In addition, the initial CMOD immediately after the crack forms can also be calculated by using strain history measured from top and bottom rebars (see **Figure 9-6**), which was denoted as δ_{strain}^i.

$$\delta_{strain}^i = \delta_{strain,L}^i + \delta_{strain,B}^i \qquad \text{Equation 9-6}$$

where $\delta_{strain,L}^i$ and $\delta_{strain,B}^i$ is CMOD caused by longitudinal and bending modes, respectively. Those can be calculated as follows,

$$\delta_{strain,L}^i = \int_0^{l_2} (\varepsilon_{t,L}^t - \varepsilon_{t,L}^e - \varepsilon_{conc})dx \qquad \text{Equation 9-7}$$

$$\delta_{strain,B}^i = \gamma \int_0^{l_2} (\varepsilon_{t,B}^t - \varepsilon_{t,B}^e - \varepsilon_{conc})dx \qquad \text{Equation 9-8}$$

where $\varepsilon_{t,L(or B)}^t$ is strain measured from top rebar at immediately after cracking in longitudinal (or bending) mode, $\varepsilon_{t,L(or B)}^e$ is measure strain in elastic range before cracking in longitudinal (or bending) mode, and ε_{conc} is the contribution of concrete. Note that ε_{conc} was assumed ignorable in the unbounded test region. Consequently, δ_{strain}^i can provide an upper-boundary of CMOD in this study. Moreover, l_2 is the length of unbounded region. γ is a constant for compensating locations of rebars expressed as follows;

$$\gamma = \frac{H\,/\,2}{H\,/\,2 - h_1} \qquad \text{Equation 9-9}$$

where h_1 is distance from concrete surface to the top surface of the top rebar.

9.3.3   Step III: applying external compression P_3

In the step III, external compression P_3 was applied to the section of the specimens after releasing all external loadings P_1 and P_2. **Figure 9-9** shows changes in CMOD with the increasing compressive loadings P_3. Applying compression contracted the specimens in the longitudinal direction and rotated the plastic hinge, which decreased CMOD. Then, CMOD in the loading step j (δ^j) can be determined by subtracting decrements of CMOD in the loading step j ($\Delta\delta^i$) from δ^i as follows,

168
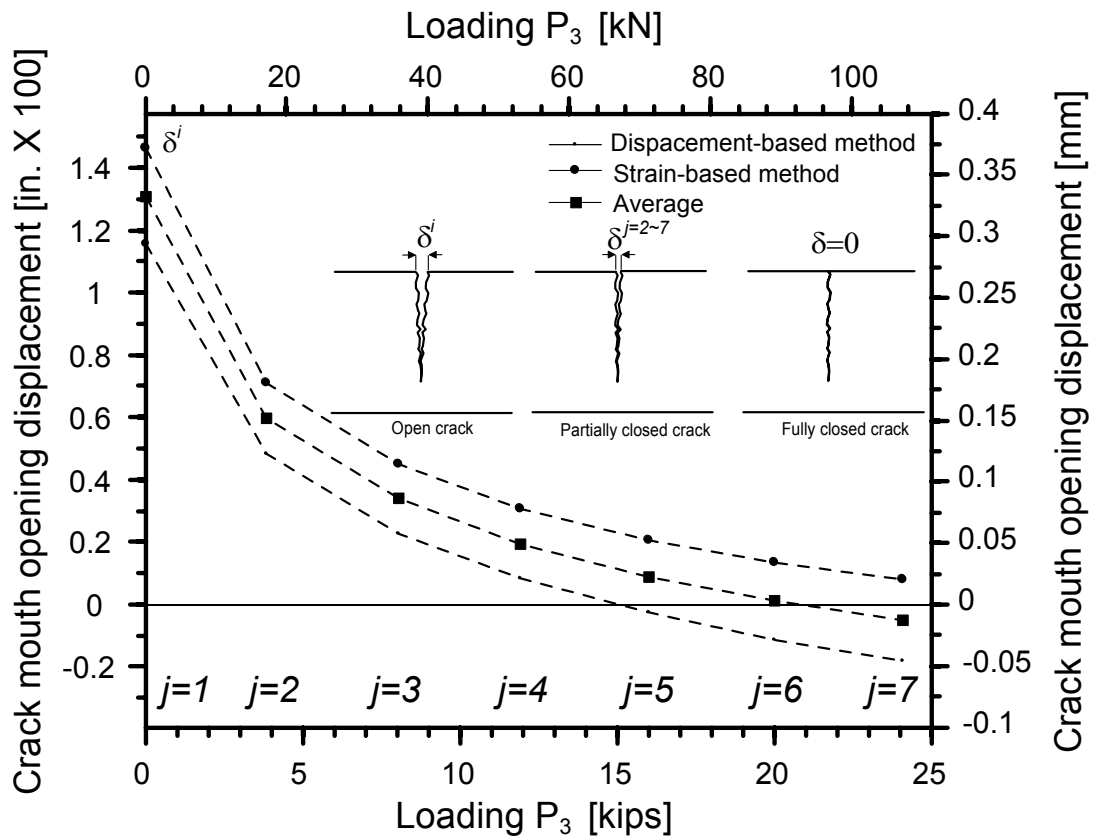
Figure 9-9: Crack mouth opening displacement versus loading P_3 in the third step of testing procedure.

$$\delta^j = \delta^i - \sum_{n=1}^{j} \Delta\delta^n$$

Equation 9-10

After test step III, the depth of crack was directly measured from a core sample extracted from the concrete specimen. The location of core extraction is shown in **Figure 9-10** (a). As shown in the **Figure 9-10** (b), the crack depth measured in the left side of the core sample and that measured in the right side of the core sample were 140, and 130 mm, respectively.

169
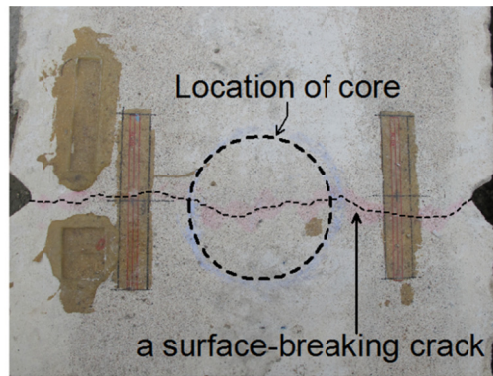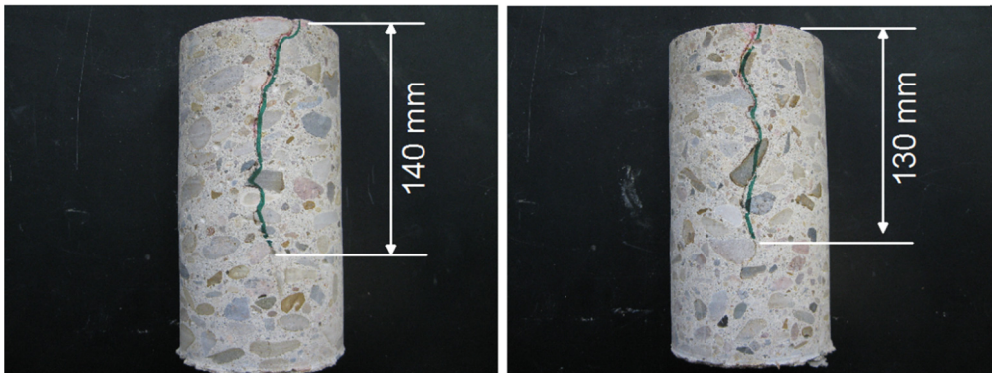
Figure 9-10: Crack depth read from a core sample extracted from the concrete specimen after test step III: (a) location of core extraction, (b) left side of the core sample with $h\sim140$ mm, and (c) right side of the core sample with $h\sim130$ mm.

9.4   RESULTS AND DISCUSSION

9.4.1   Typical signals at different test steps

Figure 9-11 shows possible paths of stress waves in three different test steps: (a) test step I and step II before cracking, (b) the test step II after cracking with a fully open crack, and (c) the test step III with a partially closed crack.

Before cracking, the measured signals show direct bulk waves (P- and S waves) and direct surface waves R_i, and then, multiple reflected waves follow the direct waves (see Appendix D for calculation of arrival times). **Figure 9-11** also includes wave paths of several multiple reflected waves (i.e., PP_1, SS_1, and PS_1). When incident surface waves (R_i) propagate across a open surface-breaking crack (see **Figure 9-11** (b)), the low frequency components of the surface waves transmit to the forward scattering field with attenuation (R_{tr}), while high frequency components is reflected back. Furthermore, existence of a vertical surface-breaking crack affects wave paths of multiple reflected waves as shown in **Figure 9-11** (b). However, applying compression decreases the CMOD, which results in different interfacial conditions on the crack surface. In this case, some portions of incident surface waves and multiple reflected waves can transmit through the interface of crack, which is called 'crack interfacial waves' [87]. Note that the crack interfacial waves may include scattering waves (V_{sc} in **Figure 9-11** (c)) caused by nonlinear features of interfacial condition in the crack [91].

Figure 9-12 and **Figure 9-13** show the time domain signals generated by a 13 mm diameter steel ball, and measured by air-coupled sensors 1 and 2, respectively, in the test step III. For comparison purposes, time signals obtained from the stress-free and crack-free specimens in the test step I are shown in the first row of the figures. **Figure 9-12** shows that time signals in the backward scattering field were not affected by existence of a surface-breaking crack and various external loadings. However, **Figure 9-13** clearly shows that time signals in the forward scattering field were very sensitive to

171

the existence of surface-breaking crack as well as loading steps (or interfacial condition of the crack). This implies that further analyses of the crack interfacial waves can provide valuable information for better understanding of interfacial condition of a crack, and effects of external loadings on surface waves across a partially close crack.
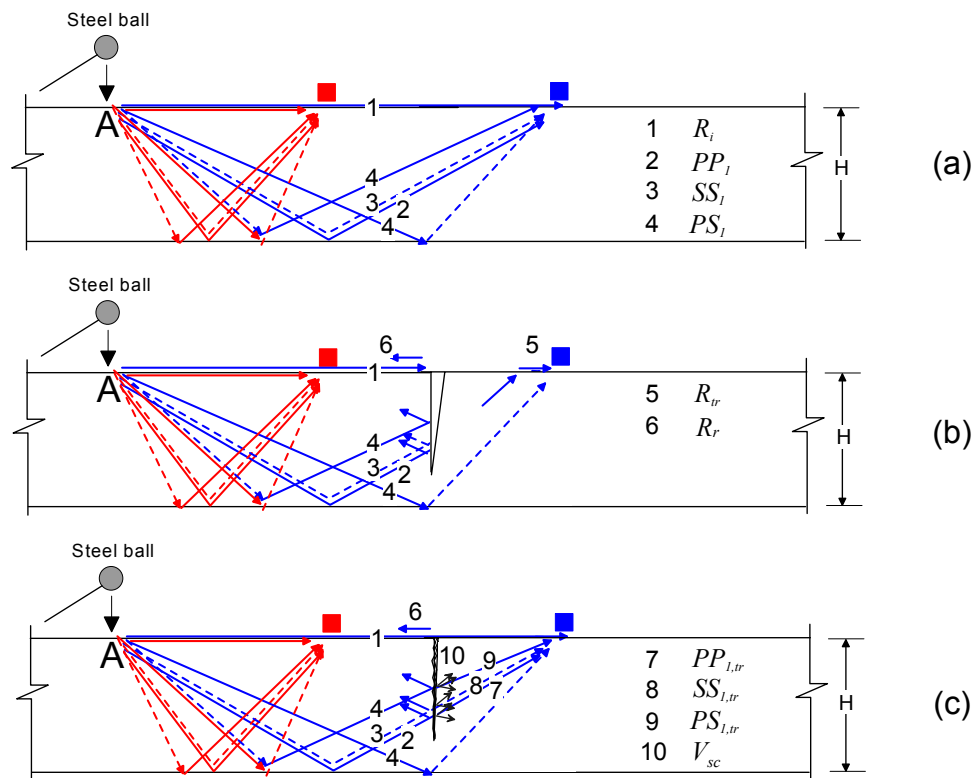
Figure 9-11: Possible paths of stress waves in different test steps: (a) steps I and II before cracking, (b) step II after cracking with a open crack, and (c) step III with a partially closed crack. Note: 1-incident surface waves, 2-multiple reflected P waves, 3-multiple reflected S waves, 4-multiple reflected coupled P and S waves, 5-transmitted surface waves, 7, 8, 9-transmitted multiple reflection waves through the crack, and 10-scattering waves caused by imperfect interfacial conditions, and nonlinear features of the crack.

172
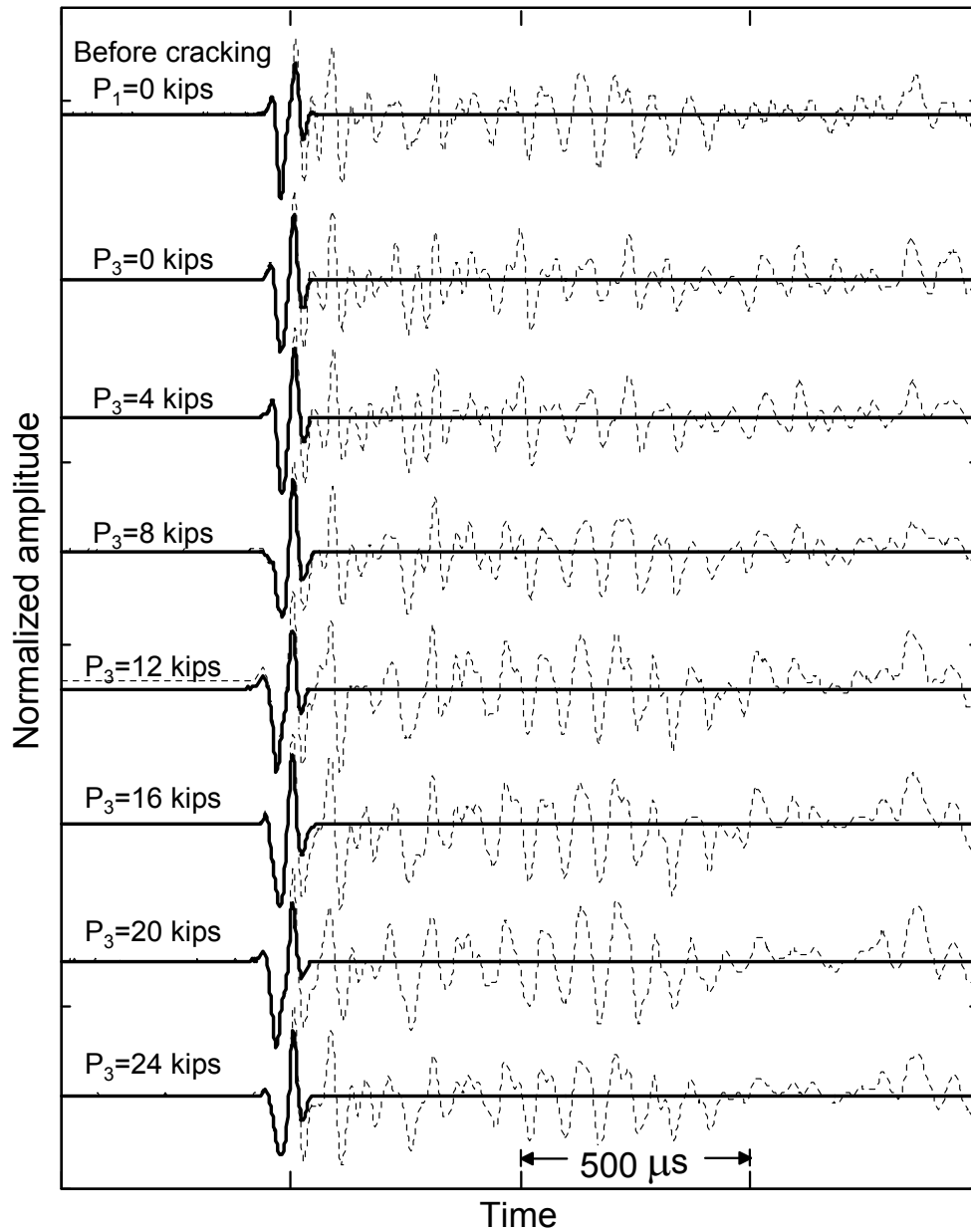
Figure 9-12: Typical time-domain signals measured in the backward scattering field using the air-coupled sensor 1 with increasing compressive forces P_3 in the test step III. All time-signals were normalized by the maxima of the reference time-signals shown in the first row.

173
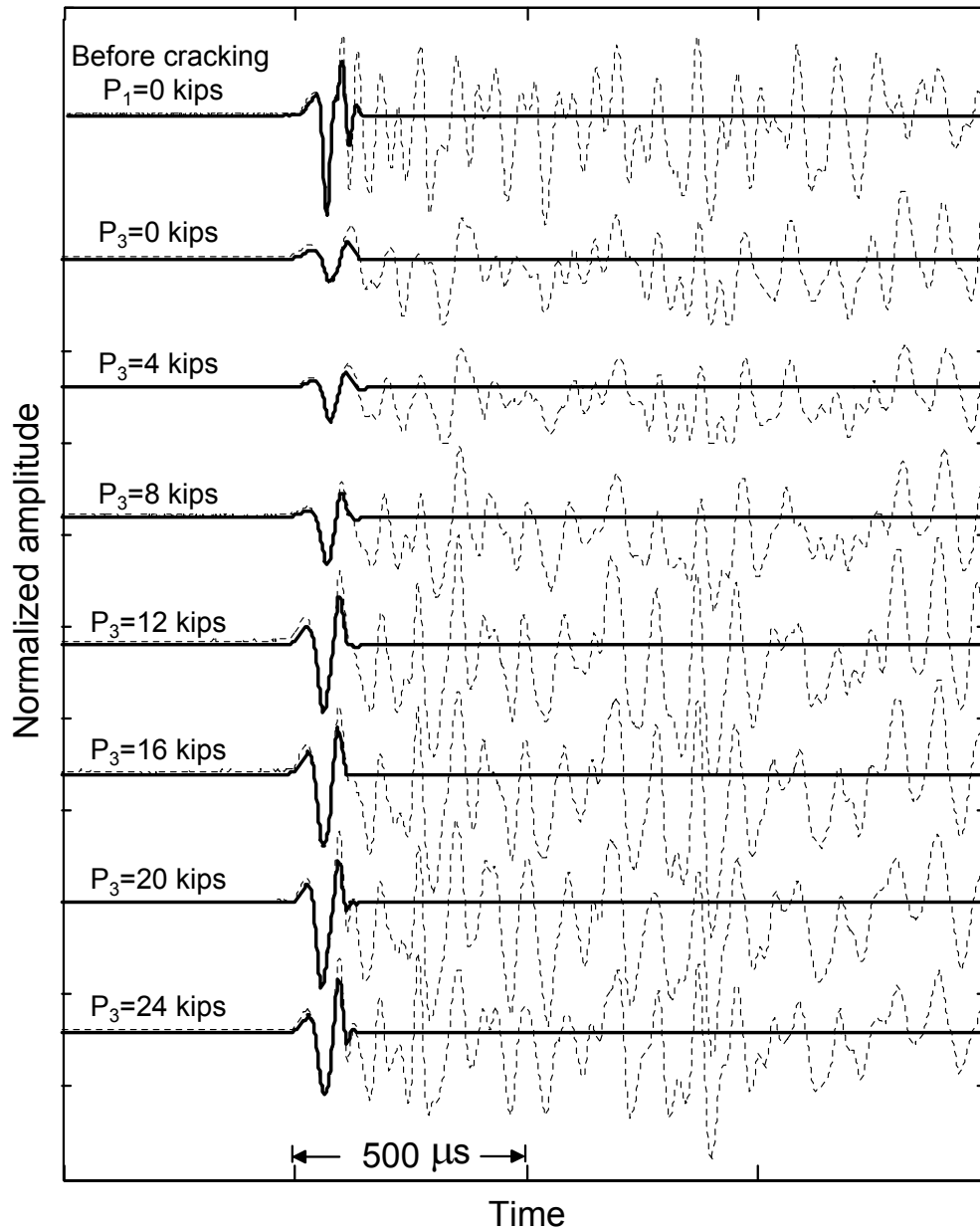
Figure 9-13: Time domain signals measured in the forward scattering field using the air-coupled sensor 2 with increasing compressive forces P_3 in the step III. All time-signals were normalized by the maxima of the reference time-signals shown in the first row in Figure 9-10.

174

9.4.2   Transmission coefficient of surface waves

Transmission coefficients $\mathbf{Tr}_h^L(f)$ measured from the cracked test region under various compressive force P_3 were normalized by the reference transmission coefficient $\mathbf{Tr}_0^0(f)$ obtained from the crack-free and stress-free specimen. The superscript L and subscript h mean the magnitude of load P_3 and the depth of the crack h, respectively. The normalized transmission coefficient $\mathbf{Tr}_n^L(=\mathbf{Tr}_h^L(f)/\ \mathbf{Tr}_0^0(f))$ was verified effective to eliminate effect of geometric attenuation and material damping [7]. **Figure 9-14** shows $\mathbf{Tr}_n^L$ of surface waves in function of frequency generated by the 13 mm diameter impact source. In crack free case, **Figure 9-14** (a) shows that $\mathbf{Tr}_n^L$ varies within ±10 % of $\mathbf{Tr}_0^0$ in a frequency range of 8 to 25 kHz with varying levels of P_1 or P_2. In contrast, after the crack formed, **Figure 9-14** (b) shows that $\mathbf{Tr}_n^L$ significantly decreases compared to the $\mathbf{Tr}_0^0$ (see a black dash line in **Figure 9-14** (b)). Consistent with previous research [30, 31, 39, 40], attenuation in the transmission function shows frequency-dependent features: higher-frequencies resulted in lower attenuation in the frequency range of 8 to 25 kHz. Moreover, **Figure 9-14** (b) also shows that $\mathbf{Tr}_n^L$ in the given frequency range gradually increases with monotonically increasing P_3 from 0 to 24 kips. This implies that some portions of incident surface waves can be transmitted through the interface of the crack (i.e., the crack interfacial waves [87]). Increasing compressive force gradually closes the concrete crack, leading to increase of interfacial stiffness in the crack [85, 92, 93]. Transmission of surface waves is then enhanced by contribution of the crack interfacial waves, which is strongly dependent on interfacial condition in the crack [93].
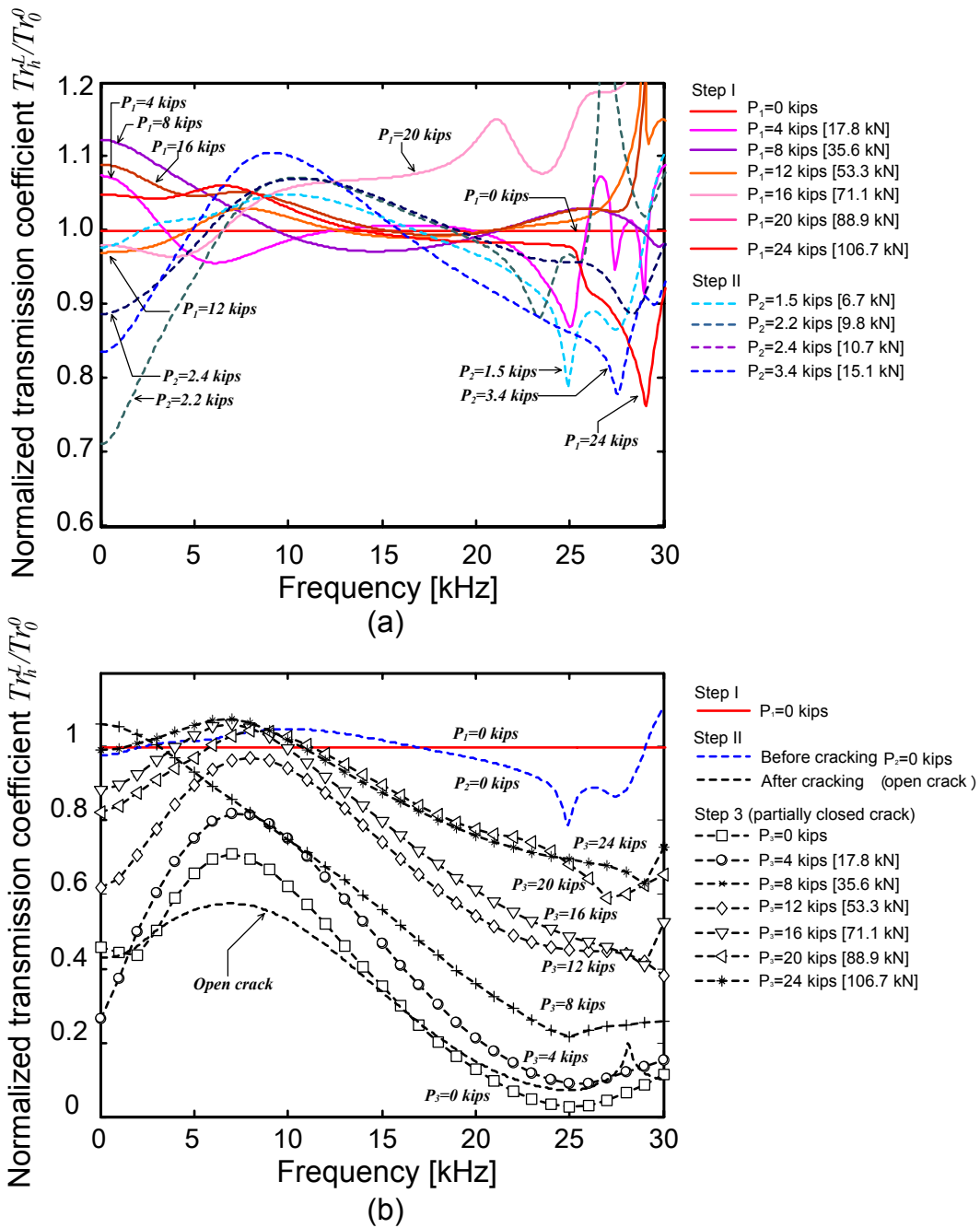
Figure 9-14: Normalized transmission coefficient of surface waves versus frequency in test steps I, II and III: (a) test steps I and II before cracking, and (b) test steps II and III after cracking.

Figure 9-15 shows transmission coefficient of surface waves presented in function of internal stress on the top extreme layer of concrete σ_t caused by external loadings P_1, P_2 or P_3. The stresses on the horizontal axis were obtained using Equations 9-1 and 9-2. $\mathbf{Tr}_n^L$ shown in **Figure 9-15** were corresponding to the frequencies 10, 15 and 20 kHz generated by the 13 mm diameter impact source, and 10, 15, 20, 25, and 30 kHz by the 8 mm diameter impact source. As expected, $\mathbf{Tr}_n^L$ measured on the crack-free specimens show only very slight increase with increasing internal compressive stresses up to 2 MPa (300 psi) (approximately 10% of nominal compressive strength of concrete specimens), in which concrete specimens were still in elastic range. Furthermore, increasing flexural stresses by increasing P_2 resulted in frequency-dependent feature of $\mathbf{Tr}_n^L$: higher frequency components tend to decrease and lower frequency components tend to decrease. On the other hand, applying monotonically increasing compressive force P_3 to the cracked specimens gradually increased $\mathbf{Tr}_n^L$ with frequency-dependent features. $\mathbf{Tr}_n^L$-σ_t relation shows that the transmission coefficient of lower frequency components was quickly converging to the $\mathbf{Tr}_0^0$. $\mathbf{Tr}_n^L$ of 10 kHz linearly increased with increasing σ_t up to 1MPa (~150psi), and after that, became stable around 80 ~ 100% of $\mathbf{Tr}_n^0$. In contrast, $\mathbf{Tr}_n^L$ at higher frequencies (= 20, 25, 30 kHz) linearly increased with the compressive force, and approached to 70 ~ 80 % of $\mathbf{Tr}_n^0$ when the compressive stress increased to 2MPa (~300psi). This implies that the high frequency components of surface waves are more sensitive to interfacial contact conditions of the crack.
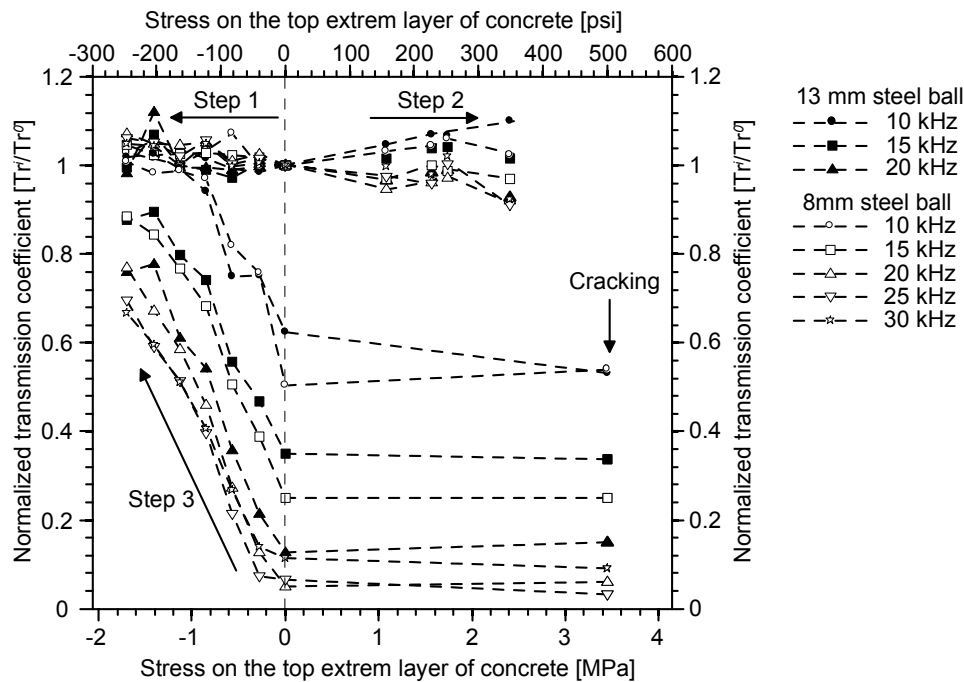
Figure 9-15: Normalized transmission coefficient of surface waves versus stress on the top extreme layer of concrete in test steps I, II and III.

9.4.3   Phase velocity of surface waves

Figure 9-16 shows the phase velocity of surface waves presented in the frequency domain. The phase velocities were calculated using Equation 6-8 based on the measured signals generated by the 13 mm diameter steel ball. Before cracking, the phase velocity of surface waves was not sensitive to changes in compressive force. Increasing compressive force only slightly increases or decreases the phase velocity. After cracking, the phase velocity decreased to approximately 75% to 80% of the phase velocity measured from the crack-free and stress-free specimens. In the test III, the phase velocity of surface waves gradually increases with the compressive force, and reaches peak value around 2250 m/s at 24 kips (~106. 7 kN). This result is consistent with the observation by previous researcher [73].

178
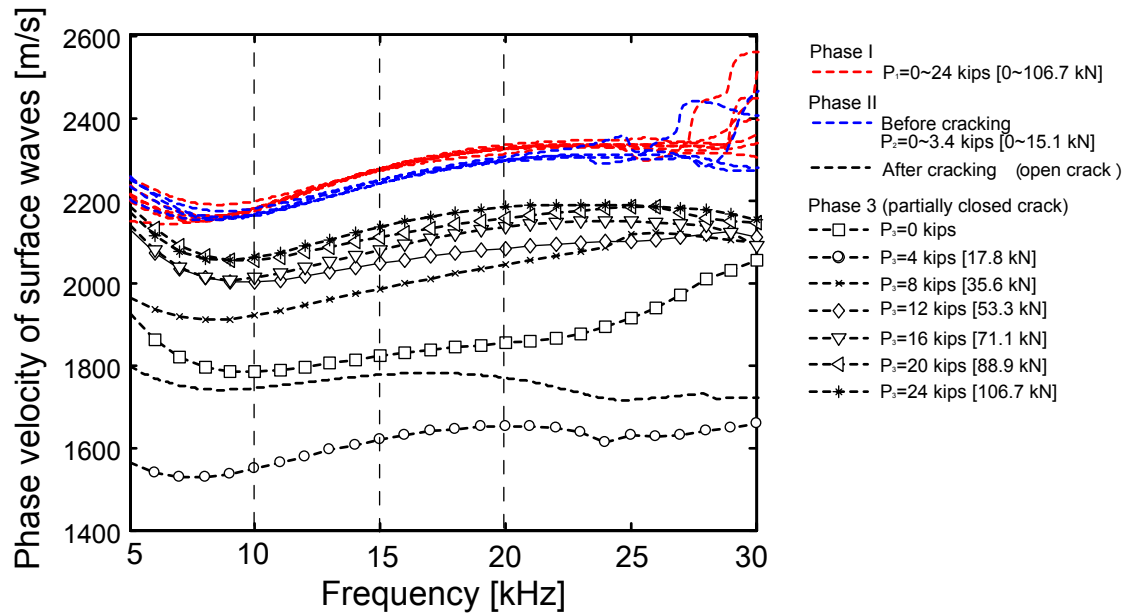
Figure 9-16: The phase velocity of surface waves versus frequency in test steps I, II and II.

Figure 9-17 shows the normalized phase velocity of surface waves $C_{ph,n}^{L}$ presented in function of internal stress σ_t on the top extreme layer of concrete. The phase velocity measured in various compressive loadings P_3 $C_{ph,h}^{L}(f)$ were normalized by the reference phase velocity $C_{ph,0}^{0}(f)$ obtained from the crack-free and stress-free specimens. $C_{ph,n}^{L}$ shown in **Figure 9-17** were corresponding to the frequencies 10, 15 and 20 kHz generated by the 13 mm diameter impact source. Consistent with previous research [94], the acoustoelastic effect was very small for the stress levels considered in this study until a surface-breaking crack appeared in the specimens. After cracking, $C_{ph,n}^{L}$ suddenly decreased to 75~85% of the $C_{ph,n}^{0}$. Furthermore, in the test step III, various interfacial conditions of a surface-breaking crack were induced by applying external loadings, and $C_{ph,n}^{L}$ were measured at each loading step. **Figure 9-17** shows that $C_{ph,n}^{L}$ $-\sigma_t$ relation appears independent of frequency. $C_{ph,N}^{L}$ at different frequencies (= 10, 15, 20 kHz) linearly increase as P_3 increases up to 0.6 MPa (100 psi). After that, $C_{ph,n}^{L}$ increases very slowly with increasing loading steps, and finally reaches to approximately 95% of $C_{ph,n}^{0}$

when σ_t reaches 2MPa (~300Psi). Compared to the transmission coefficient of surface waves $\mathbf{Tr_n}^L$, the phase velocity of surface waves $\mathbf{C_{ph,n}}^L$ is less sensitive to variations in compressive forces (or interfacial conditions in the crack).
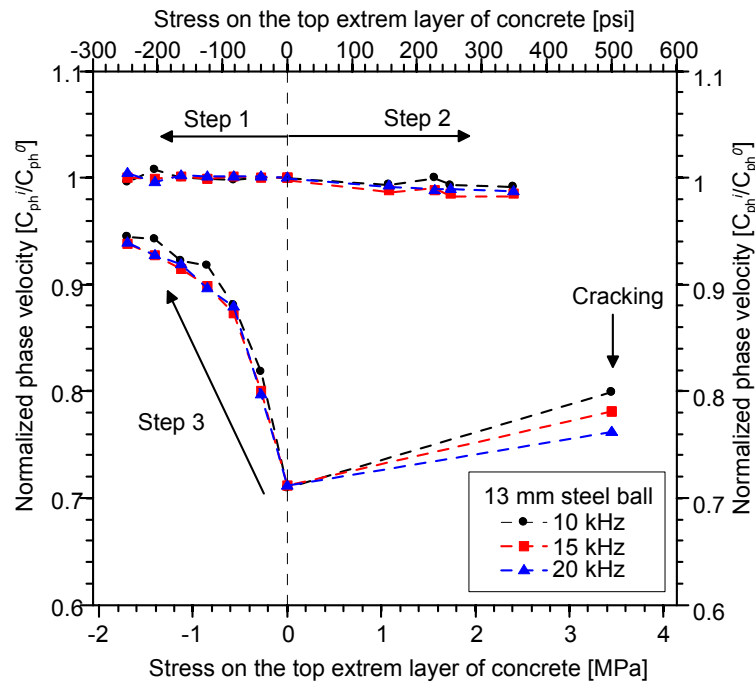
Figure 9-17: Normalized phase velocity of surface waves versus stress on the top extreme layer of concrete in the test setups I, II and III.

9.4.4 Tr_n versus CMOD, and $C_{ph,n}$ versus CMOD

The results in the previous section clearly demonstrated that acoustic parameters of surface waves (transmission coefficient, and phase velocity) are strongly dependent on the compressive force. Physically, acoustic parameters are more directly related to the interfacial condition in cracks: however, the interfacial condition in cracks is difficult to estimate on surface with a simple method. For the practical purpose, it is probably reasonable to use the CMOD as a roughly estimation of the interfacial condition of cracks in concrete.

180

Figure 9-18 shows variation of acoustic parameters of surface waves expressed in function of CMOD. **Figure 9-18** (a) shows variation of normalized transmission coefficient $\mathbf{Tr}_n^L$ with CMOD. $\mathbf{Tr}_n^L$ remains stable when CMOD is greater than 0.18 mm ($\sim 7 \times 10^{-3}$ in.). It can be seen that the SWT method may provide a consistent estimation of crack depth when CMOD is greater than 0.18 mm. However, $\mathbf{Tr}_n^L$ becomes sensitive to the interfacial condition in the crack when CMOD decreases from 0.18 mm to 0.01 mm. On the other hand, **Figure 9-18** (b) shows that $\mathbf{C_{ph,n}}^L$ monolithically increase when CMOD decreases from approximately 0.4 mm to 0.01 mm. It seems difficult to find a minimum CMOD which makes $\mathbf{C_{ph,n}}^L$ independent of CMOD. This is mainly due to high sensitivity of $\mathbf{C_{ph,n}}^L$ to the interfacial condition in cracks.

However, there are several more factors that should be taken into account to better understand effects of crack interfacial conditions on acoustic parameters of surface waves. The results from well-controlled laboratory condition may not fully represent the situation of in-situ concrete structures. The elastic behavior of the contacting faces under an applied stress may be different from the real situation. In actual cracks in concrete structures, crack interfacial condition is affected by other factors (e.g., existence of small particles (debris and dust) or infiltration of liquid, the amount of reinforcement bars, and topographical features of the rough face of cracks). In addition, further analytic work is still needed to better understand a crack opening displacement profile of a crack subjected to various loading condition, and non-linear relationship between COD and interfacial stiffness of the crack: those issues are difficult to fully understand through experimental studies.
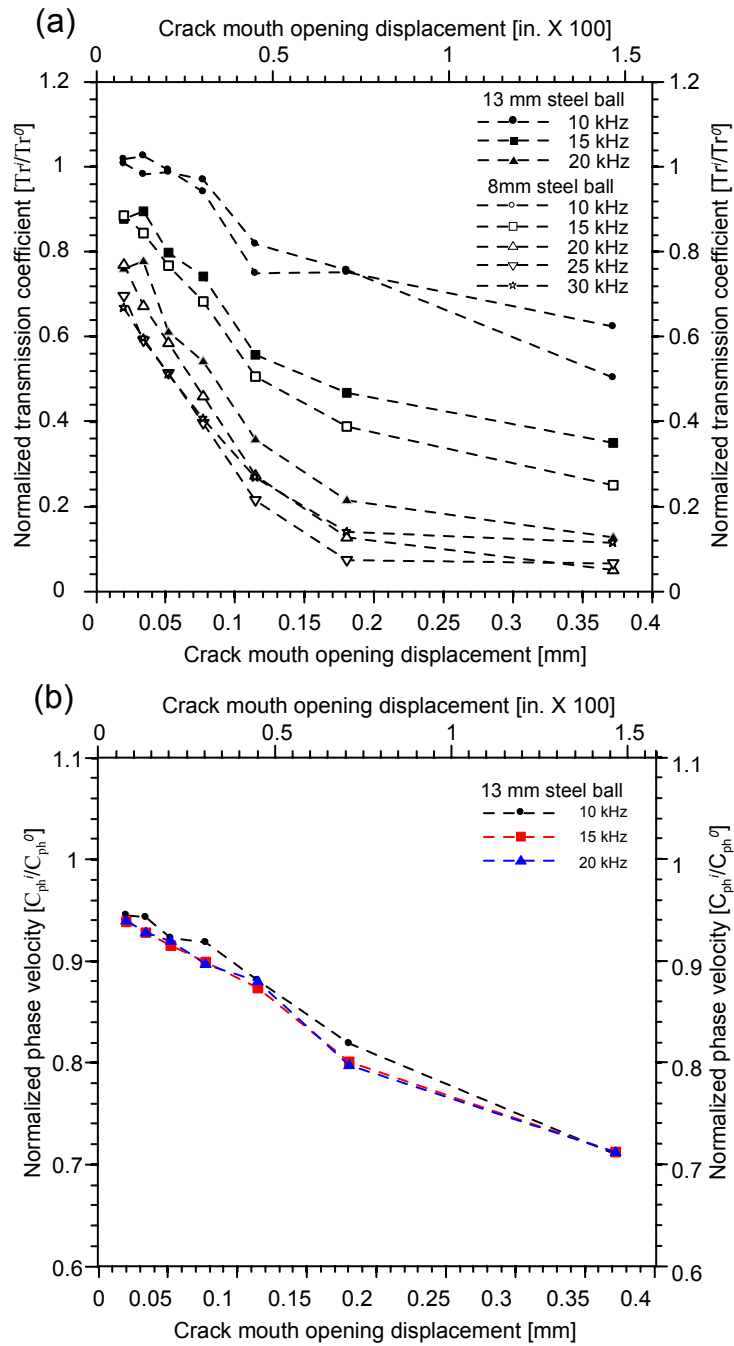
Figure 9-18: Acoustic parameters of surface waves versus crack mouth opening displacement (CMOD): (a) Tr_n -CMOD, and (b) $C_{ph,n}$ -CMOD.

182

9.5   CONCLUSIONS

In this chapter, the author experimentally investigated effects of external loadings on acoustic parameters of stress waves across a partially closed surface-breaking crack in concrete. The conclusions from in this chapter are summarized as follows:

(1) For the crack-free region, applying external loadings does not affect acoustic parameters of stress waves (the transmission coefficient and the phase velocity of surface waves, and the transmission coefficient of multiple reflected waves).

(2) After cracking, $\mathbf{Tr}_n^L$ gradually increases with monotonically increasing compressive force P_3 from 0 to 24 kips. This implies that some portions of incident surface waves can be transmitted through the imperfect interface of the crack (i.e., the crack interfacial waves). In addition, $\mathbf{Tr}_n^L$-σ_t relation shows that lower frequency components are more quickly converging to the $\mathbf{Tr}_n^0$. The frequency-dependent feature is in part due to the contribution of a bending mode. A nature of bending action results in more tightness at the bottom tip of the crack, which probably results in higher interfacial stiffness at the tip of the crack. Furthermore, non-linear relationship between COD and interfacial stiffness of cracks [93] is another possible reason. However, more analytical work is still needed to better understand the experimental observation.

(3) The phase velocity of surface waves $\mathbf{C}_{\mathbf{ph},n}^L$ suddenly decreased to 75~ 85% of the $\mathbf{C}_{\mathbf{ph},0}^0$ after a surface-breaking crack appeared on the concrete specimen. $\mathbf{C}_{\mathbf{ph},n}^L$ -σ_{eff} relation was not sensitive to change in frequencies. Compared to $\mathbf{Tr}_n^L$, $\mathbf{C}_{\mathbf{ph},n}^L$ was less sensitive to compressive loadings (or various interfacial conditions in cracks).

(5) $\mathbf{Tr}_n^L$-CMOD curves shows that $\mathbf{Tr}_n^L$ appears stable when CMOD is greater than 0.18 mm (~7 $\times 10^{-3}$ in.). Decreasing CMOD from 0.18 mm to 0.01 mm substantially grows up $\mathbf{Tr}_n^L$, in which the SWT method may not provide the reasonable crack depth estimation in concrete. On the other hand, $\mathbf{C_{ph,n}}^L$ is linearly related to CMOD. $\mathbf{C_{ph,n}}^L$ tends to monolithically increase as CMOD decreases from approximately 0.4 mm to 0.01 mm. It was difficult to find a minimum CMOD which makes $\mathbf{C_{ph,n}}^L$ independent of CMOD. This is mainly due to high sensitivity of $\mathbf{C_{ph,n}}^L$ to the interfacial condition in cracks.

Chapter 10 Using Low-Cost Piezoceramic Elements as Consistent Source and Receiver in NDT tests

The purpose of this chapter is to investigate applicability of low cost piezoceramic sensors for health monitoring of concrete in structures. The authors proposed two types of innovative sensors, i.e., surface mount sensors and embedded sensors, to generate and monitor ultrasonic waves propagating through concrete. The surface mount sensors were attached to the free-surface of the concrete specimens, and used as repeatable impact sources and receivers to measure surface waves in concrete. The proposed surface mount sensors were used to determine phase velocity and transmission coefficient of surface waves, and ultrasonic pulse velocity (UPV) on concrete surface. In addition, the embedded sensors were installed on reinforcing bars before casting concrete. The embedded sensors were used to determine UPV of acoustic waves through the concrete specimen. For comparison purposes, the performance of the surface mount sensors and embedded sensors were also compared with accelerometers, and a commercial UPV unit. The test results show that the surface mount sensors and embedded sensors are very effective in generating and monitoring ultrasonic waves through concrete. In addition, computer-controlled features of the proposed sensors significantly improved test speed, consistency and accuracy in results.

10.1 INTRODUCTION

In surface wave tests, a steel ball or hammer is often used to generate incident surface waves in concrete structures. However, the impact source controlled by a human hand is difficult to generate consistent waves. Another limitation is that it may not be used in hard-to access regions of concrete structures. Therefore, developing a computer-controlled impact source is needed to improve consistency, accuracy, and test speeds in surface wave measurement. On the other hand, ultrasonic pulse velocity (UPV) has been used to evaluate severity of existing concrete in structures since 1950s. Good coupling

between ultrasonic transducers and concrete surface is required to obtain reliable measurement of wave velocity. In nonlinear acoustic measurement, reliable coupling and amplitude measurement are more critical than in the UPV tests. Therefore, there is a need to develop a NDT method that has consistent sensor coupling with concrete.

In this study, the author developed two types of sensors, surface mount sensors and embedded sensors, using low cost piezoelectric discs (less than \$1 per element) to generate and monitor ultrasonic waves propagating through concrete. The primary purpose of the study in this chapter is to investigate applicability of the low cost piezoceramic sensors as consistent impact source and receiver for NDT of concrete structures. One concrete specimen with dimensions of 1500 X 1500 X 200 mm^3 (L X W X T) and one reinforced concrete specimen with dimensions of 1500 X 400 X 200 mm^3 were prepared in the laboratory to explore performance of the sensors proposed in this study. The surface mount sensors were attached to the surface of concrete specimens, and used as repeatable impact sources and receivers to measure surface waves propagating in concrete. In addition, the embedded sensors were installed on reinforcement bars before casting concrete. The embedded sensors were used as ultrasonic wave generators and receivers to measure ultrasound pulse velocity (UPV) of acoustic waves through concrete. For comparison purposes, the performance of the surface mount sensors and embedded sensors proposed in this study were also compared with accelerometers, and a commercial UPV unit.

10.2 DESCRIPTION OF PIEZOCERAMIC SENSORS

Piezoceramic, or also called piezoelectric ceramic, is an active element converting electrical to mechanical energy, and mechanical to electrical energy (i.e., the piezoelectricity). The piezoelectricity causes a crystal to generate mechanical vibration when electric field is applied and conversely, produce electric charges when subjected to stress.

186

10.2.1 Working principles of piezoceramic sensors

One of the most widely used piezoceramic elements is a piezoelectric disc (see
(a) and (b)). The piezoelectric disc has one layer of thin piezoceramic disc whose
thickness is much smaller than other dimensions. Generally one side of the piezoelectric
disc is attached to a metal disc (brass or steel) to reinforce the thin piezoceramic disc. The
structure and shape of the piezoelectric disc used in this study is presented in
. The piezoceramic disc is polarized in the thickness direction. When a voltage is
applied to two surfaces of a ceramic disc, the disc expands/contracts in the thickness
direction, i.e. along the axis of polarization. At the same time, the disc contracts/expands
in the transverse direction. The piezoelectric disc generates longitudinal motion when
electric field is applied to the disc as shown in
(a). Conversely, mechanical vibrations generate electric signals in receiver
mode.
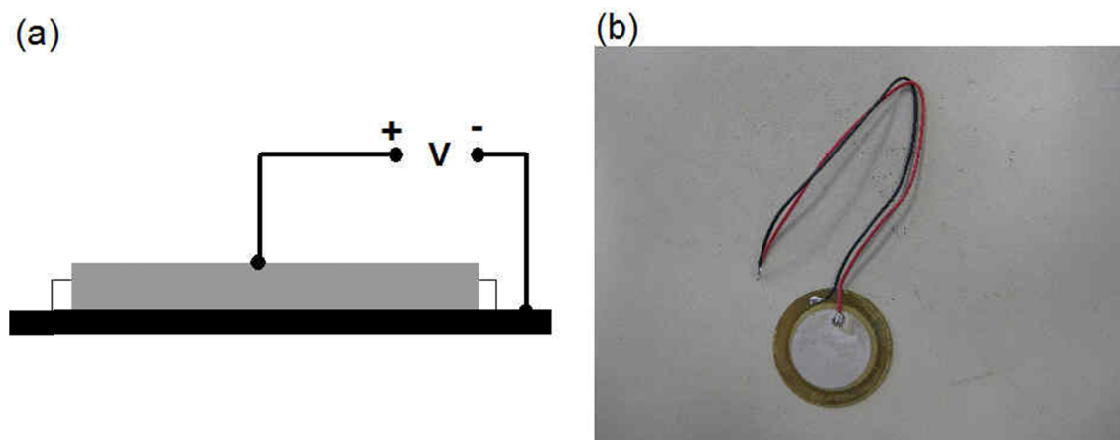
Figure 10-1: Structure of a piezoceramic sensor. (a) a piezoelectric disc with connection to
voltage, and (b) a picture of the piezoelectric disc used in this study.

10.2.2 Preparation of piezoceramic transducers

Piezoelectric discs were used in this study. The dimensions of the piezoelectric disc have a thickness of 0.2 mm and a diameter of 22 mm. To use the piezoelectric discs as ultrasonic wave generators and receivers, two wires were soldered to the electrodes on the piezoelectric disc. Overheating should be avoided to prevent depolarization of piezoceramics. In addition, electric insulation and waterproofing were needed to use the piezoelectric discs in conductive environment. This step is particularly critical for embedded piezoceramic sensors in concrete. Procedures follow the description given by Jung [95]. First, five to six layers of polyurethane coatings (M-coat A by VISHAY®) were applied to the surfaces of the piezoelectric discs. Enough time should be given to allow each coating to be fully air dry. Then, to reduce electromagnetic interference (cross talk) between the source and receiver benders, a thin layer of silver paint was applied to the disc surface to provide electrical shielding. Finally, a grounding wire was connected to the silver paint at one end, and connected to the earth ground at another end.

10.3 APPLICATION OF LOW COST PIEZOCERAMIC SENSORS

Three applications of the piezoceramic sensors are described in this section. First, the surface mount sensors were used as a repeatable impact source in surface wave measurements. Transmission coefficient and phase velocity of surface waves were obtained to evaluate the depth of a surface-breaking crack in concrete. Second, applicability of the surface mount sensor as a receiver was also investigated. Third, embedded sensors were used to determine ultrasound pulse velocity (UPV) of stress waves in concrete. The measured UPV provides information on effective stiffness of concrete, which is a good indicator of evaluating concrete in structures.

10.3.1 Using the surface mount sensors as a source in surface wave measurements

10.3.1.1 *Test specimen and test setup*

A concrete specimen was prepared to investigate applicability of the surface mount sensor as a consistent impact source of incident surface waves in concrete. A concrete specimen has dimensions of 1500 X 1500 X 200 mm^3 (L X W X T), which was actually same as the prepared for the research in Chapter 8. The concrete specimen contained an artificial surface-breaking crack with varying crack depths from 10 to 100 mm (refer to **Figure 10-2**). A procedure of making an artificial surface-breaking crack in the concrete specimen and mixing properties of the specimen were described in Chapter 8.
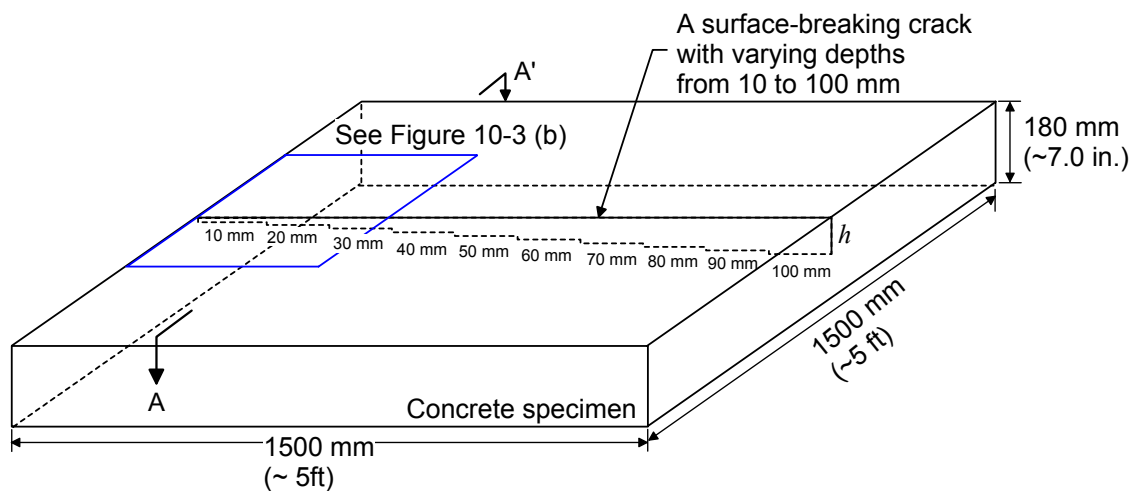
Figure 10-2: Preparation of a concrete specimen.

The surface mount piezoceramic sensors were used as a repeatable ultrasonic wave source for surface wave generation in the concrete specimen. Transmission coefficients of surface wave across a surface-breaking crack were determined by the self-calibrating procedure. **Figure 10-3** shows a source-and-receiver configuration to measure transmission coefficients of surface waves across a surface-breaking crack with a depth

(a)

(b)
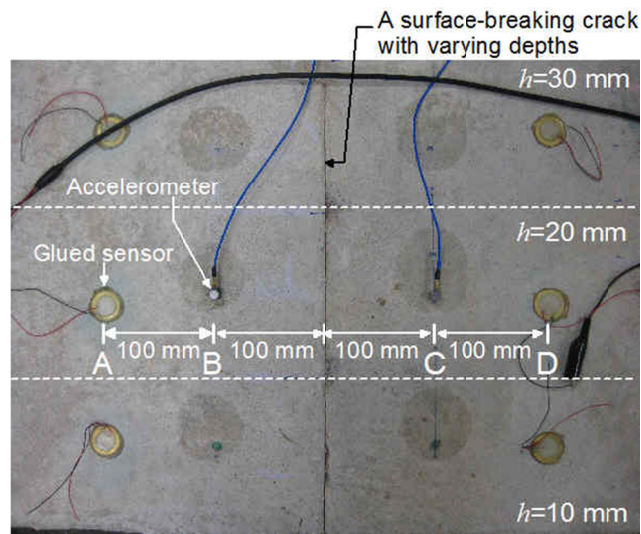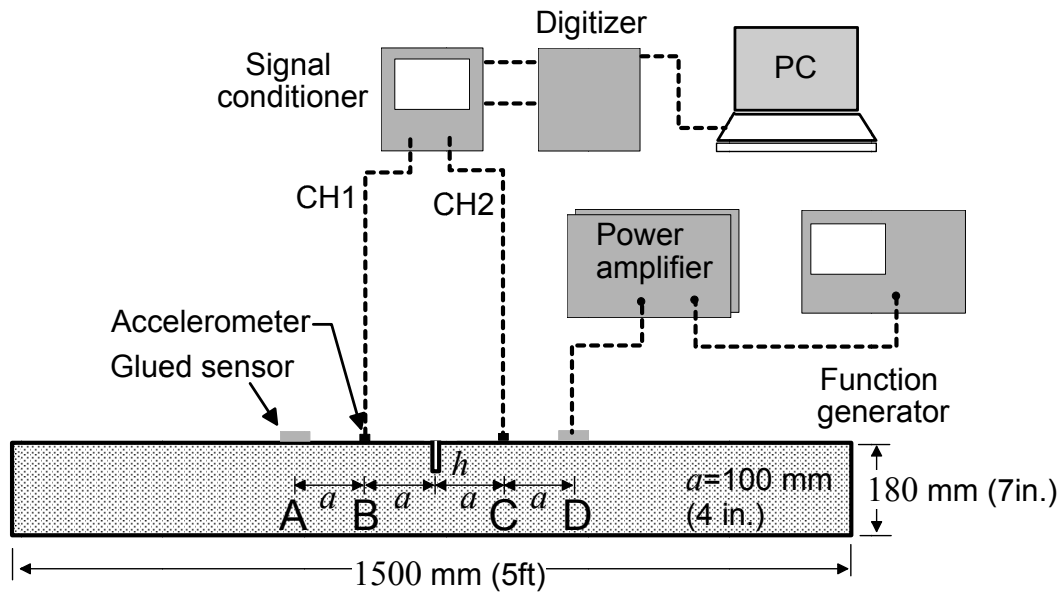
Figure 10-3: Test setup and data acquisition system of using surface mount sensors for surface wave measurements in concrete: (a) section view A-A' in **Figure 10-3**, and (b) top view of the specimen.

of 20 mm. As shown in **Figure 10-3** (b), two surface mount sensors were located at A and D and two accelerometers (PCB 352C65) were located at B and C on the concrete specimen. A function generator (EXTX/2A60) was used to drive the surface mount sensors. Gaussian functions with a duration 100 μs were used as an input signal for the function generator. The acquired signals were digitized at a sampling frequency of 1 MHz using an NI-USB 5133 oscilloscope. First, surface waves generated by the surface mount sensor located at A were recorded by accelerometers located at B and C, which are denoted as S_{AB}, and S_{AC}, respectively. Subsequently, surface waves generated by the surface mount sensor at D were measured by accelerometers at C and B, which are S_{DC}, and S_{DB}. Next, transmission coefficients of surface waves were calculated in the frequency domain using this test setup is effective in measuring transmission coefficient and phase velocity of surface waves in test region BC. In this study, transmission coefficient of surface waves was calculated in the frequency domain using Equation 6-5. In addition, phase velocity of surface waves was calculated by the spectral analyses of surface waves (SASW) using the same signal data obtained from the self-calibrating procedure using Equation 6-8.

Five repeated signal data sets were collected at the same test location to investigate repeatability of signals generated by the surface mount sensors. Signal coherence function was calculated using Equations 3-8 and 3-9. The signal coherence ranges from 0 to 1.0. A value close to 1.0 indicates good signal quality and repeatability. The signal coherence function was used to determine the acceptable frequency range of transmission coefficient and phase velocity curves.

In addition, reference signals were measured from a crack-free region in the same concrete specimen. The transmission coefficient measured from cracked regions was further normalized by the reference results to eliminate effects due to geometric attenuation, and material damping.

10.3.1.2 *Results and discussion*

Figure 10-4 (a) and (b) show the reference time-domain signals measured from crack-free test region in the concrete specimen. The surface mount sensors were used to generate incident surface waves using input signals of Gaussian functions having durations of 300 and 100 μs, respectively. Two accelerometers (PCB 352C65) were used to measure the signal data generated by the surface mount sensors. The velocity of the first arrival pulse was approximately 4100 m/s, which is corresponding to the P wave velocity of typical concrete. The main pulses of surface waves have the velocity of about 2300 m/s in **Figure 10-4**. Most energy generated by the surface mount sensors was imparted into the surface wave components. This observation demonstrates that the surface mount sensors proposed in this study are very effective in generating ultrasonic waves, especially for surface wave measurements.

For further analyses, surface wave components were extracted from the time-domain signals by applying a window function. A hanning window with a size of approximately a period was applied to the center of the negative peak in surface wave components. Windowed time domain signals were presented as bold lines in **Figure 10-4**. Subsequently, the windowed signals were converted to the frequency domain using FFT algorithm. The frequency spectra in **Figure 10-5** (a) and (b) show that the signals have the center frequencies of 20 and 45 kHz, respectively, which are within the frequency range commonly selected for ultrasonic testing of concrete.
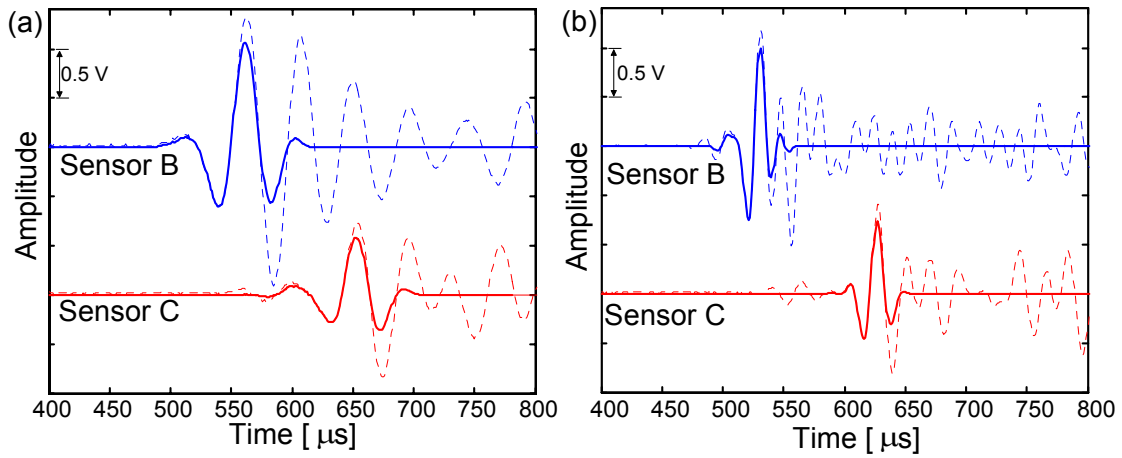
Figure 10-4: Time-domain signals generated by the surface mount piezoceramic sensors using Gaussian functions: (a) having $T=300$ and (b) $T=100$ μs as input signals. The signals were measured by two accelerometers located at B and C in **Figure 10-3** (b).
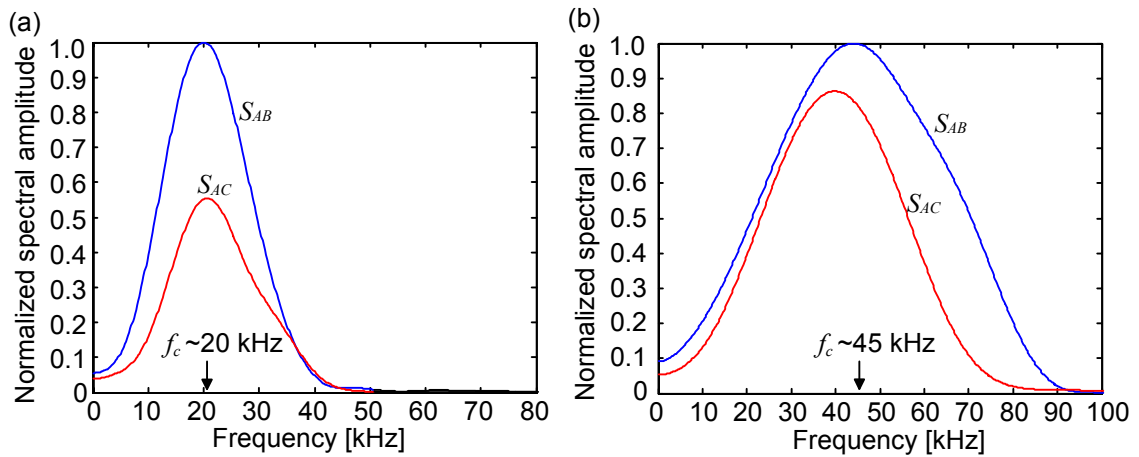
Figure 10-5: The normalized spectral amplitude versus frequency: (a) for the windowed signals in **Figure 10-4** (a), and (b) for the windowed signals in **Figure 10-4** (b).

Signal coherence functions of surface waves were calculated to investigate repeatability of the signals generated by the surface mount sensors. Signal coherence was determined using Equations 3-8 and 3-9. For example, signal coherence for the signal generated by the impact duration 100 µs is presented as a gray bold line in **Figure 10-6**, which shows very good signal consistency in a frequency range of 10 to 60 kHz. Note that a value close to 1.0 in the signal coherence indicates good signal consistency. For comparison purposes, signal coherence for the signals measured across a surface-breaking crack was presented as gray dash line at the same figure, which shows good signal consistency in a frequency range of 15 to 50 kHz. It is also note worthy that low signal consistency in a frequency range lower than 10 kHz is mainly caused by inconsistent coupling of the accelerometers.
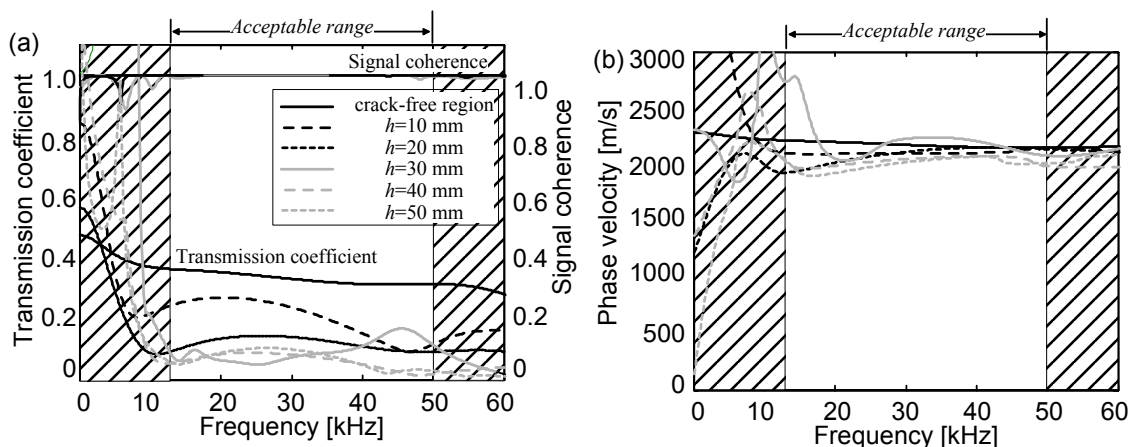
Figure 10-6: Important acoustic parameters of surface waves measured from the concrete specimen in the frequency domain: (a) signal consistency and transmission function, and (b) phase velocity of surface waves measured across a surface-breaking crack with varying depths from 0 to 50 mm.

Surface wave transmission coefficient (Tr) and phase velocity (C_R) were presented in frequency domain calculated by Equation 6-5 and Equation 6-8, respectively. For example, **Figure 10-6** (a) and (b) show Tr and C_R corresponding to the time-domain signals generated by an input signal with T=100 µs. Results measured from different test

194

regions with varying crack depths from 0 to 50 mm were presented in the same figure to investigate sensitivity of the acoustic parameters to varying crack depths. In **Figure 10-6** (b), the phase velocity of surface waves converges to 2230 m/s at the frequency range of 20 to 60 kHz. In the cracked regions, decreasing crack depths from 10 to 50 mm results in only a slight decrease in phase velocity. This result is consistent with previous research [82]. This result demonstrated that phase velocity of surface waves may not be a sensitive parameter to evaluate a surface-breaking crack with shallow depths less than 1 wavelength of incident surface waves. On the other hand, **Figure 10-6** (a) shows that transmission coefficient measured from the crack-free concrete remains constant in the acceptable frequency range. In the cracked regions, transmission coefficient significantly decreases as the crack depth increases from 10 to 50 mm. This result demonstrates that transmission coefficient of surface waves is effective in identifying and characterizing a surface-breaking crack with shallow depths.

The transmission coefficients obtained from the cracked regions were further normalized by the transmission coefficient from crack-free region to estimate the depth of the surface-breaking crack. The normalized transmission coefficients Tr_n measured across a surface-braking crack with varying crack depth from 10 to 50 mm in the concrete specimen are plotted in **Figure 10-7**. The measured Tr_n were corresponding to a frequency range of 20 to 50 kHz in an interval of 5 kHz. For comparison purposes, a theoretical solution given by Angel and Achenbach [30] was shown in the same figure. **Figure 10-7** shows that measured Tr_n–h/λ relation shows a similar trend to the theoretic solution that Tr_n monolithically decreases with increasing h/λ. However, measured Tr_n was lower than theoretical results, particularly in a useful range of h/λ <1/3. There are two possible reasons causing differences between measured and theoretical values: *(i)* the theoretic curve given by Angel and Achenbach [30] was derived from the half-space model, which may not accurately provide accurate solution for a plate with finite thickness (see also Chapter 4), and *(ii)* construction errors may cause discrepancies

195

between designed and as-built crack depths. The author observed that the as-built depths are deeper than the designed depths. However, the construction errors are not the major reason for the difference in transmission curves in **Figure 10-7**. In the author's opinion, multiple reflections of stress waves in a thin concrete plate may contribute to the errors. More work through numerical simulations is needed to explain the difference between the measured and theoretical results.
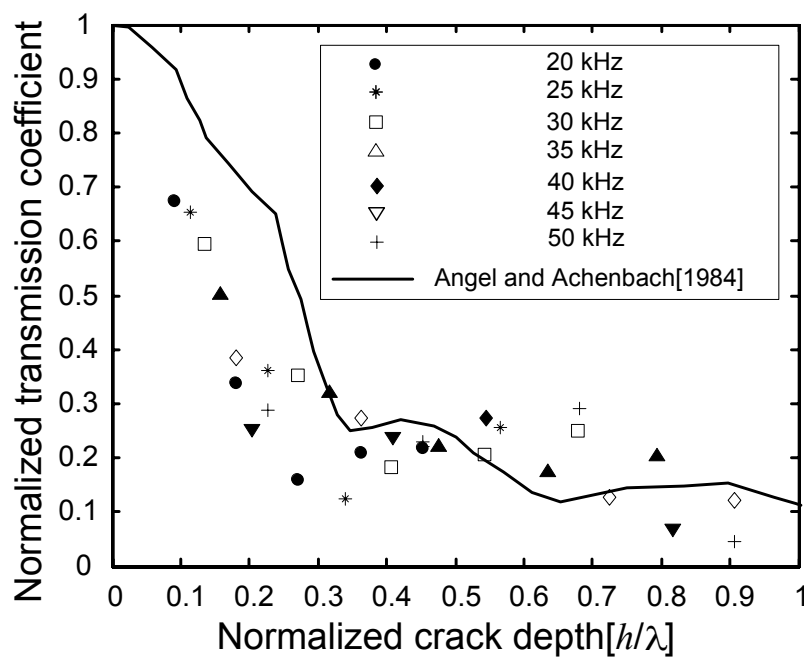
Figure 10-7: Transmission coefficient versus normalized crack depth. Analytical solution given by Angel and Achenbach [30] is also shown.

10.3.2 Using the surface mount sensors to measure wave velocity on concrete surface

10.3.2.1 *Background*

Ultrasonic pulse velocity (UPV) has been used for condition assessment of concrete structures since 1950s. However, the conventional ultrasonic setups typically need access two opposite sides of concrete structures, which is not always possible for in-situ field testing. In this study, the surface mount piezoceramic sensors were used to generate and measure ultrasonic longitudinal (P), shear (S) waves, and surface waves on concrete. The proposed low cost piezoelectric sensors have potential to be used for health monitoring of concrete structures.

10.3.2.2 *Test setup and data acquisition system*

Figure 10-8 shows the test setup of using the surface mount sensors attached on the concrete specimen 1, which is the same as that described in the previous section. The surface mount sensors located at A and B were used as a repeatable wave generator and a receiver, respectively. A function generator was used to drive the surface mount sensors in transmitter mode. Because of low sensitivity of piezoelectric discs compared to accelerometers, input signals generated by the function generator were amplified by a power amplifier (PZD 350) to 100 V, and the received signal was amplified by a preamplifier (5660C PREAMP) with a gain of 40dB. The acquired signals were digitized at a sampling frequency of 1 MHz using an NI-USB 5133 oscilloscope. For comparison purposes, an accelerometer (PCB 352C65) located at C was also used to measure signals generated by the surface mount sensor located at A. This setup is effective to measure ultrasonic pulse velocity (UPV) of direct P and S waves, and surface waves propagating in the concrete specimen. Given wave path with a constant distance (250 mm in this study), measuring wave travel time can directly provide ultrasonic wave velocity.
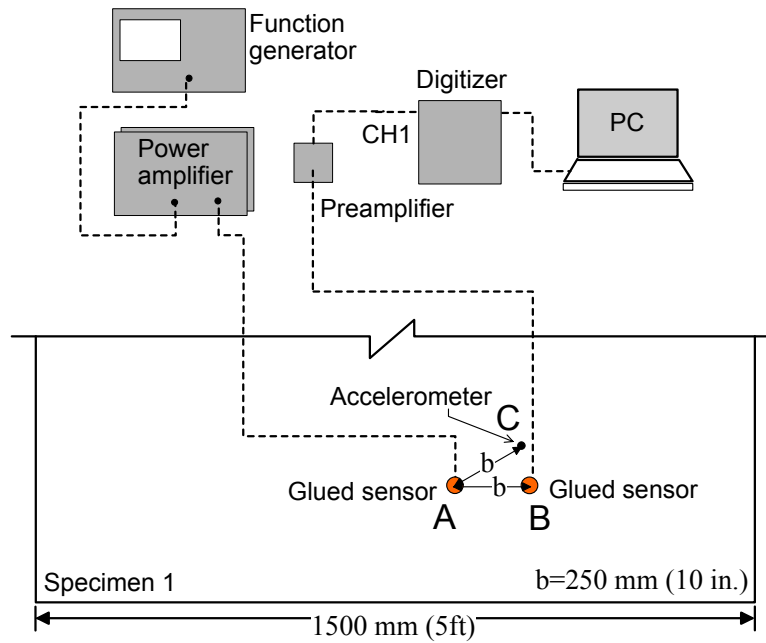
Figure 10-8: Test setup and data acquisition system of using surface mount sensors to measure wave velocity on concrete surface (top view of the concrete specimen).
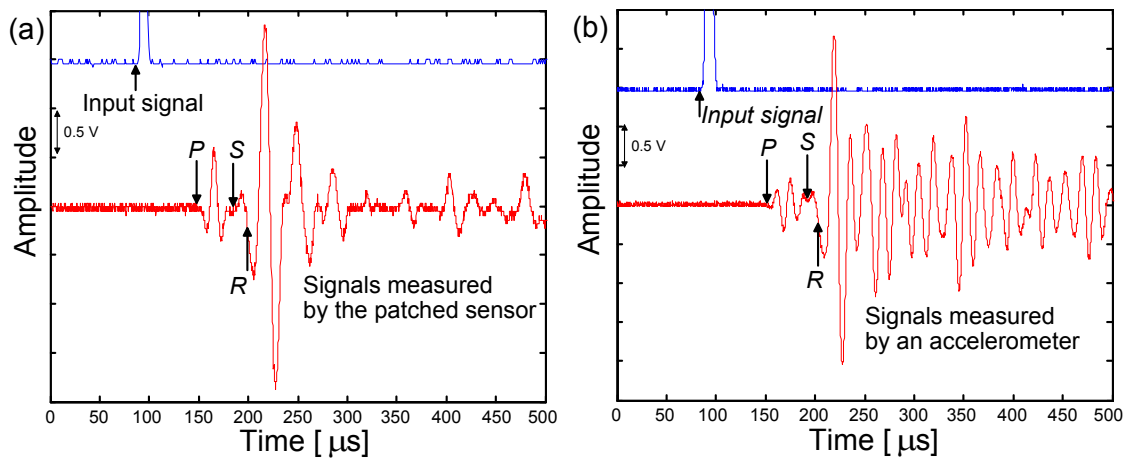
Figure 10-9: The time signals generated by the surface mount sensor located at A and measured by the surface mount sensor located at B (a), and by an accelerometer located at C (b).

198

10.3.2.3   *Result and discussion*

Figure 10-9 (a) and (b) show the time-domain signals measured by the surface mount sensor located at B and an accelerometer located at C. **Figure 10-9** (a) shows clear waveforms of direct ultrasonic waves (P, S, and surface waves). Comparing to the signal measured by the accelerometer, the piezo sensor signal has a little bit lower signal-to-noise ratio. However, the signal quality obtained by the piezosensor is still good enough to identify the arrival time of ultrasonic P, S and surface waves.

The wave velocity can be calculated by dividing a wave path L over the travel time in the concrete specimen. To obtain actual wave travel time t through the material, time delay in the measurement system t_m were subtracted from the time directly obtained from the signal t_r as follows.

$$t = t_r - t_m - t_i \qquad \text{Equation 10-1}$$

From **Figure 10-9** (a), the arrival time t_r of the first, second, and third pulses were 150.5, 188.5 and 198.5 µs, respectively. For piezoelectric discs, the time delay t_m (1.5 µs in this study) was caused by coating, cables and electronic devices, and determined by measuring travel time when the tips of the receiver and the source are in contact. The initial point of an input signal t_i was 88 µs. In this study, the distance between surface mount sensors was 250 mm. The velocities of waves were 4101, 2525, and 2293 m/s. Those values are corresponding to P, S and surface wave velocity of typical concrete, respectively. Note that P wave velocity measured by the surface mount sensor was comparable to the P wave velocity measured by a commercial UPV unit of about 4100 m/s. The results demonstrated that the surface mount sensor is effective in generating and measuring ultrasonic waves on concrete surface.

199

10.3.3   Using embedded sensors to perform UPV measurement in concrete

10.3.3.1   Background

Good coupling between ultrasonic transducers and concrete surface is required to obtain reliable measurement of wave velocity. Therefore, there is a need to develop a NDT method that has consistent sensor coupling with concrete. In this study, embedded piezoceramic sensors were used to generate and measure ultrasonic longitudinal (P) and shear (S) waves in concrete.

10.3.3.2   Test specimen, Test setup, and data acquisition system

A reinforced concrete specimen (specimen 2) having dimensions of 400 ✕ 190 ✕ 1500 mm^3 (**W ✕ T ✕ L**) was prepared in laboratory (see **Figure 10-10**). This specimen was casted at the same time when the specimen used in Chapter 9 was casted. Normal-weight concrete, made from type I/II cement, river sand, and coarse aggregate with a maximum size of 19 mm (¾ in.), were used to fabricate the concrete specimen 2. A steel cage composes of two layers of longitudinal reinforcing bars, and transverse bars were placed in concrete. The reinforcing bars have a diameter of 13.3 mm (3/8 in.) (No. 3).

Figure 10-10 shows the test setup for embedded sensors to generate and monitor ultrasonic waves through the concrete specimens in the pitch-and-catch mode. The embedded sensors located A, and B were used as signal generator, and receivers, respectively. The embedded sensors were installed to reinforcing bars before casting concrete as shown in **Figure 10-11**. Because ultrasonic waves have high attenuation in concrete, the transmitter was driven by a 200V square wave pulse generated from a pulser-receiver (Panametrics 5077PR). The receiver sensor was connected to the pulser-receiver with a gain of 40dB. The amplified receiving signals were then digitized by an NI-PXI 5101 high speed digitizer at a sampling rate of 10MHz and transferred to a laptop

computer. To improve the signal to noise ratio, for each measurement, 16 signals were averaged .
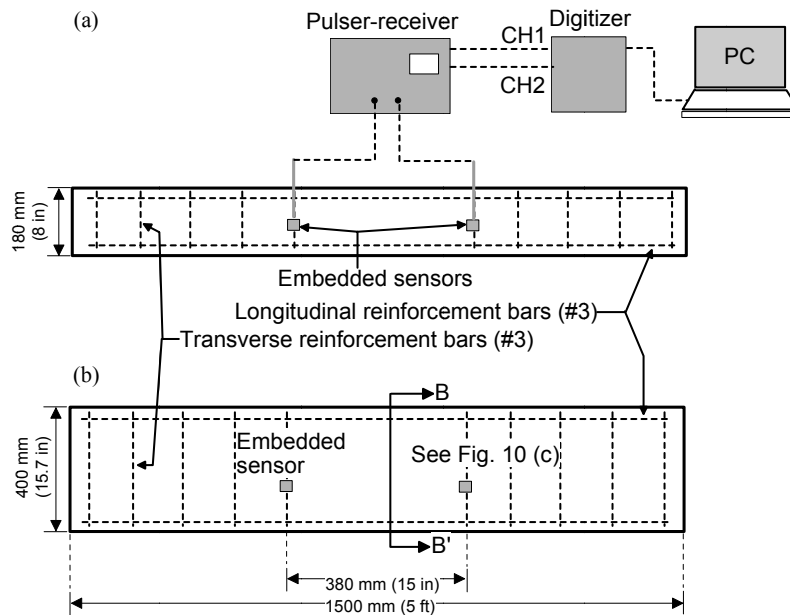
Figure 10-10: Test setup for embedded sensors and data acquisition system. (a) a side view of the concrete specimen, location of embedded sensors, and data acquisition system, (b) a top view of the concrete specimen, and location of embedded sensors.
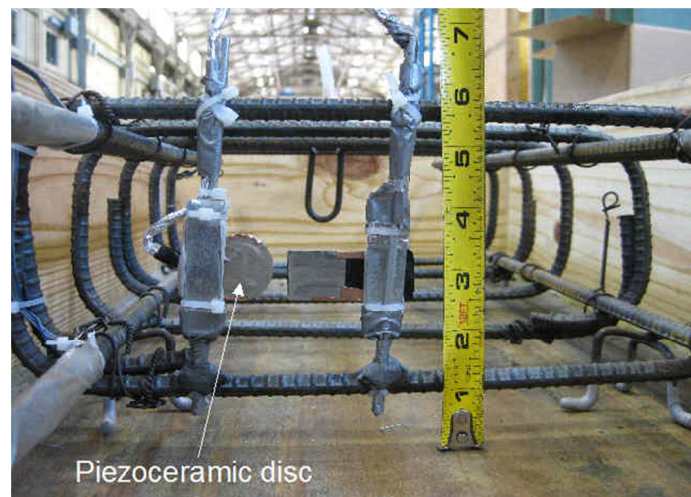
Figure 10-11: Installation of embedded piezo sensors to reinforcing bars in a concrete specimen.

10.3.3.3   *Result and discussion*

Figure 10-12 shows the typical time signals through concrete specimens measured by a set of embedded piezoceramic discs. The measurement was taken from a 6-month old hardened concrete. Ultrasonic pulse waves generated by the sensor located at A were received by the sensor at B. Raw signal data measured by the embedded sensors contained cross-talk signals, and low frequency components caused by electromagnetic interference between the generator and the receiver. This makes it difficult to determine first arrival of ultrasonic waves. In this study, the undesirable components were subtracted from the raw signal data using digital signal processing. First, the low frequency signals V_L were assumed to have an exponential function as follows,

$$V_L = ae^{bt} + ce^{dt}$$

<div align="right">Equation 10-2</div>

where t is time, and constant coefficients a, b, c, and d were determined by regression of the measured raw signal data. Then, the calibrated signals V_{cal} $(=V_{raw}-V_{ghost})$ were calculated and presented in the same figure.

The wave velocity can be calculated by dividing a wave path L over the travel time in the concrete specimen. The actual wave travel time t was obtained using Equation 10-1. In this study, the distance between the embedded sensors was 38 mm. From **Figure 10-12**, the arrival of the first and second pulses were 94.3 μs, and 162.8 μs, which give the P wave velocity of 4098 m/s, and the S wave velocity 2356 m/s in the concrete specimen. The conventional ultrasonic P wave test (UPV) was also conducted on the slab, which gives P wave velocity around 4100m/s. The embedded sensors and UPV tests agree well on P wave velocity measurement.
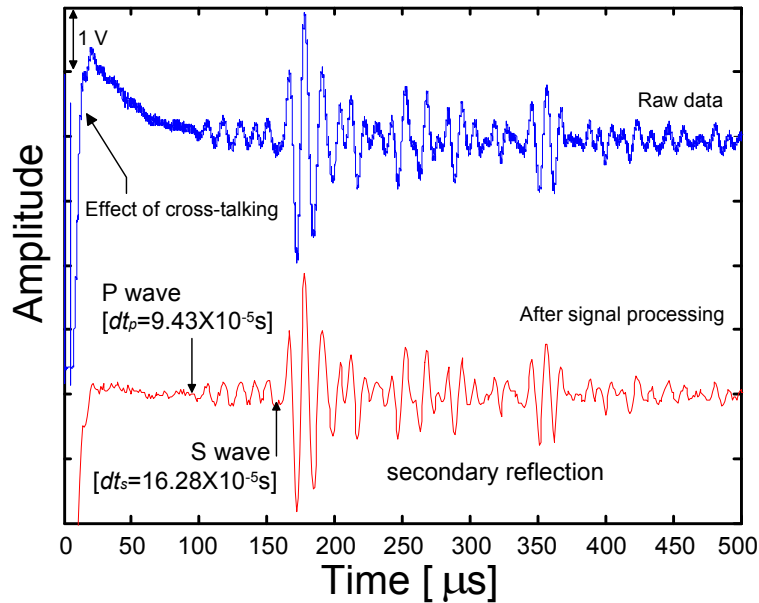
Figure 10-12: The time signals measured by the embedded sensors in the pitch-and-catch mode.

10.4 CONCLUSIONS

In this study, two types of piezoelectric sensors were proposed to be used for NDT of concrete structures. The preliminary test results in this study shows that the piezoelectric discs used in this study are very effective in generating and monitoring ultrasonic waves on concrete surface. In addition, the low cost piezoceramic discs can be embedded in concrete structures for long term health monitoring. Finally, the study presented in this chapter shows the potential to use the piezoelectric discs as low cost sensors to monitor long term performance of concrete structures. Specific findings from this study are summarized as follows:

(1) The surface mount piezoelectric discs are effective to measure surface waves on concrete. Transmission coefficient of surface waves can be used to evaluate the depth of surface-breaking crack in concrete.

(2) The surface mount piezoelectric discs are also effective to measure velocities of direct P, S, and surface waves on concrete surface.

(3) Due to the small size and low cost, the piezo sensors can be embedded in concrete during construction. The embedded piezoelectric discs are very effective in measuring UPV of P, and S waves propagating through concrete. The P wave velocity measured with embedded sensors agrees with UPV tests. The measured P wave velocity can be used for condition assessment of concrete structures.

PART IV FIELD APPLICATION

Chapter 11 Application of the Air-coupled SWT Method to in-situ Concrete Bridge Girders

The purpose of this chapter is to develop a rapid in-situ non-destructive test (NDT) method to evaluate surface-breaking cracks in concrete structures. Air-coupled sensors were used to measure surface wave transmission across surface-breaking cracks in concrete. The surface wave transmission (SWT) method was developed to determine crack depth and characterize cracking damage in concrete structures. In this chapter, the developed SWT method was used to identify and characterize cracks in three pre-stressed concrete beams with different degrees of deterioration due to Alkali Silica Reaction/Delayed Ettringite Formation (ASR/DEF). The SWT measurement results were presented as transmission maps and compared with crack patterns and severity of deterioration. The crack depths determined from the SWT test showed good agreement with direct measurements from core samples. The findings demonstrate potential of the air-coupled SWT method for in-situ evaluation of cracking damage in large concrete structures.

11.1 INTRODUCTION

The author has attempted to obtain reasonable solutions for the limitations of the SWT method categorized in Chapter 2 through theoretical studies (Chapter 3-5) and experimental studies (Chapter 6-10). However, the air-coupled SWT method should be carefully applied to actual concrete structures in field testing. Particularly, unevenly distributed cracks with higher density may increase near-field effects (refer to Chapter 3), and interaction of surface waves between multiple surface-breaking cracks (refer to Chapter 4).

The objective of this chapter is to apply the air-coupled SWT method to identify critical cracks and estimate the depth of surface-breaking cracks in the dapped end regions of three pre-stressed concrete trapezoidal box beams. Surface wave transmission

was measured on surfaces of the beams which experienced different degree of deterioration caused by Alkali-Silica Reaction/Delayed Ettringite Formation (ASR/DEF). Non-contact air-coupled sensors were used to improve the signal consistency and test speed for inspection of large concrete structures. For these purposes, the research described herein consists of two principal tasks: *(i) application of the air-coupled SWT method to in-situ concrete structures for indentifying critical cracks, and (ii) evaluation of the depth of the critical cracks using the air-coupled SWT method and verification through comparison with core samples*.

11.2 FIELD APPLICATION OF THE AIR-COUPLED SWT METHOD

11.2.1 Test specimens

The SWT method was applied to identify and characterize surface-breaking cracks in the dapped end regions of three pre-stressed concrete trapezoidal box. Typical geometry of the concrete beams is shown in **Figure 11-1**. The beams have experienced ASR/DEF damage and shown various distributed surface-breaking cracks, especially around the dapped end regions (see **Figure 11-2**). The dapped end regions of the beam have a solid end block that extends 1067 mm (42 in.) past the reentrant corner. Specific descriptions of the beams (e.g., reinforcement details, geometry, mixing properties in fabrication) are given in the reference [96-98].
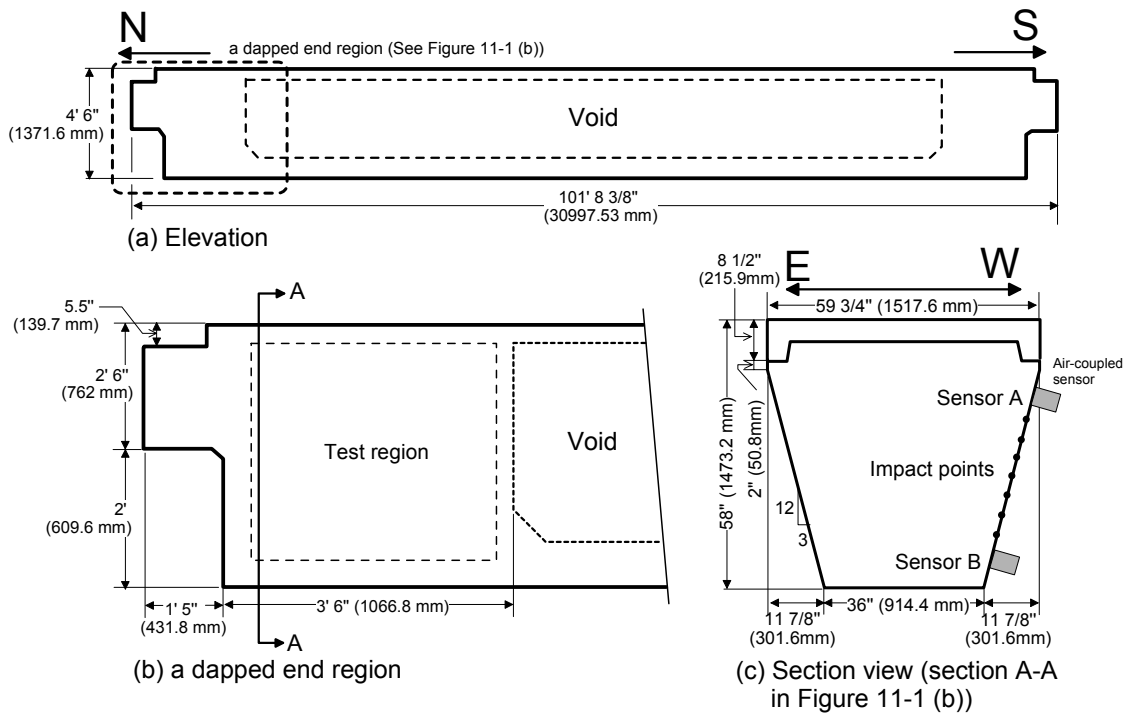
Figure 11-1: Geometry of a prestressed concrete trapezoidal box beam: (a) elevation, (b) side view of a dapped end region, and (c) sectional view (section A-A in (b)).
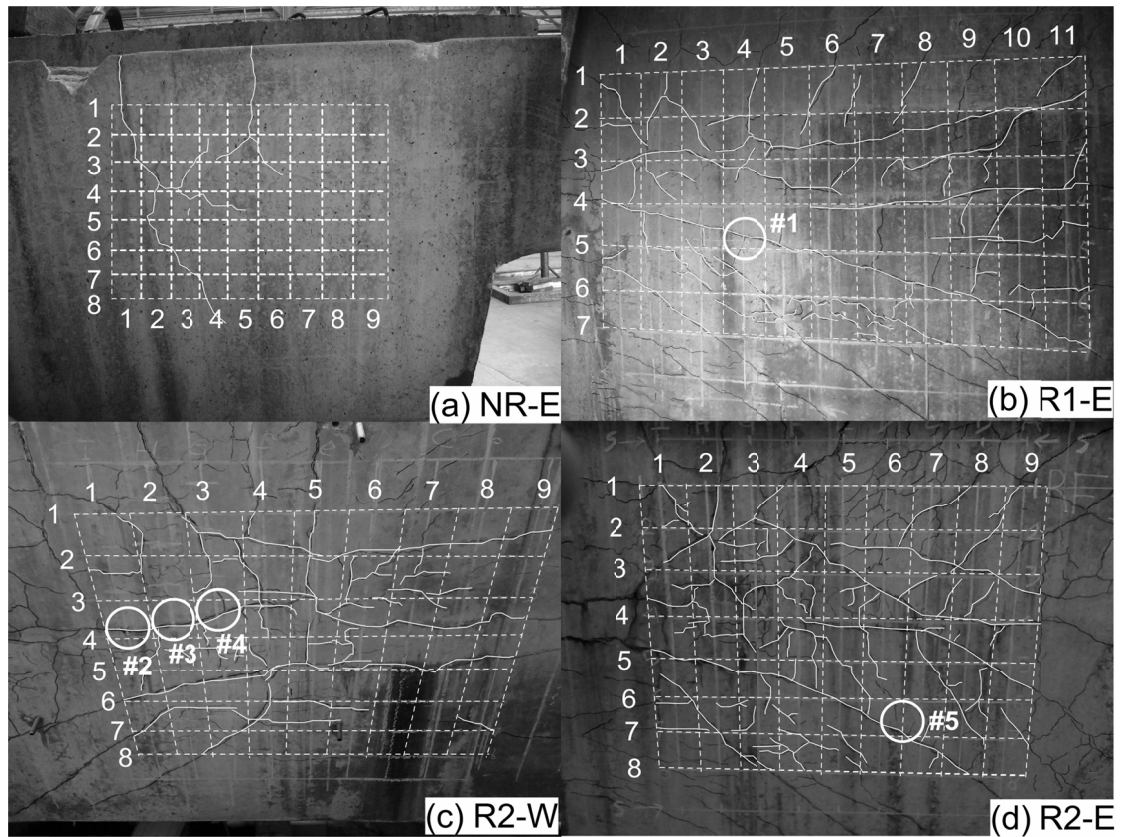
Figure 11-2: Crack patterns in the test regions of beams: (a) NR-E, (b) R1-E, (c) R2-W, and (d) R2-E.

Visual inspection of three beams revealed that the test regions in this study show different degrees of deterioration (crack patterns and crack width). **Figure 11-2** shows four dapped end sections of the three beams. Specimen NR-E, classified with mild damage, had no obvious evidence of deterioration except for several hairline cracks initiating from top of the beam. In contrast, specimens R1-E, R2-E, and R2-W, classified as moderately damaged beams, showed extensive typical ASR/DEF cracking. The specimens contained map-like hairline cracks and diagonal cracks with width ranging from hairline to 1.5 mm (0.06 in.) in the dapped end regions. The map-cracking was dominant near the corner where heavy reinforcement restrained expansions in the

209

horizontal and vertical directions. In contrast, orient-preferred cracks appear parallel to the compressive stress trajectories for pre-stressed beams. The cracks initiated from the top or bottom and continued in diagonal way towards mid-depth where the cracks turn horizontal.

11.2.2 Test setup, data acquisition system and signal processing

Two air-coupled sensors (PCB model No. 377B01) were used to acquire leaky surface wave signals. Details of the air-coupled sensing technique are described in other publications [10-13, 40] and Chapter 6. The test setup and data acquisition system for measurements of surface wave transmission were based on the previous research by author [40]. A steel ball with a diameter 14 mm was used as an impact source. It generates incident surface waves with a center frequency around 17 kHz. The acquired signals were digitized at a sampling frequency of 10 MHz using an NI-USB 5133 oscilloscope.

11.2.3 Modified self-calibrating procedure (MSC)

The modified self-calibrating (MSC) procedure was used to test large test-regions in the concrete beams. **Figure 11-3** (a) shows the test scheme to construct a 1-D B-scan image based on transmission measurement in the vertical direction. The test regions were meshed by grid lines with m columns and n rows as seen in **Figure 11-3**. For each column, two sensors A and B are located at the ends of test regions (open circles), and an impact force is applied on the grid points 1~n between two sensors. For example, **Figure 11-1** (c) shows location of sensors A and B and impact sources of the test region for column i=1. For an impact source at row j=1, the Fourier transform of signals received by sensors A and B are denoted as $\mathbf{S}^1_{(A,1)}$, and $\mathbf{S}^1_{(B,1)}$, respectively. Subsequently, a set of signal data are obtained by moving impact sources from row j=2 to n. Similarly, by moving sensors A and B, signals for other columns (i=2~m) are recorded. Finally,

(a) Measurements in the vertical direction   (b) Measurements in the horizontal direction
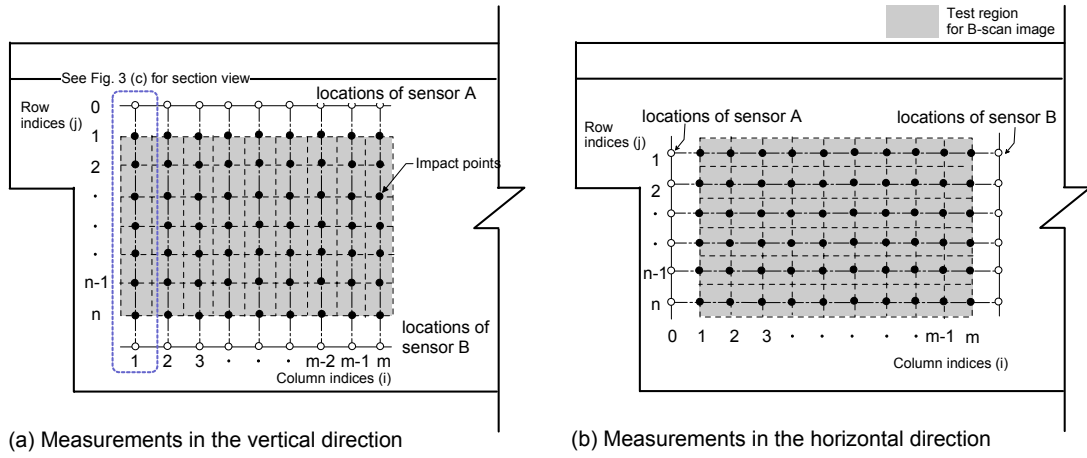
Figure 11-3: Test scheme for transmission maps of test regions based on transmission measurements: (a) in the vertical direction, and (b) in the horizontal direction. Locations of air-coupled sensors are denoted as void circles, and impact sources as solid circles.

transmission coefficients of the test regions defined by two impact sources located at the rows l and k and the column i can be calculated as

$$Tr_{lk}^{i} = \sqrt{\frac{\mathbf{S}_{(A,l)}^{i}\mathbf{S}_{(B,k)}^{i}}{\mathbf{S}_{(A,k)}^{i}\mathbf{S}_{(B,l)}^{i}}}\,, \qquad \text{Equation 11-1}$$

where $\mathbf{S}_{(A,l)}^{i}$ is the Fourier transform of the wave signal generated by an impact source at row l and measured by the sensor A in a test along column i. A Hanning window was applied to the time domain signals to extract the surface wave components [7, 8, 40] before conducting spectral analysis. Note that Equation 11-1 is equivalent to the transmission definition in the self-calibrating procedure [7, 9] according to the source-receiver reciprocity [57].

On the other hand, transmission coefficients measured in the horizontal direction can be obtained using the similar way. As seen in **Figure 11-3** (b), the transmission coefficient of the test region defined by two impact sources located at columns l and k, and row i can be calculated as

211

$$Tr_i^{lk} = \sqrt{\frac{\mathbf{S}_i^{(A,l)}\mathbf{S}_i^{(B,k)}}{\mathbf{S}_i^{(A,k)}\mathbf{S}_i^{(B,l)}}} \quad,$$

Equation 11-2

Where $\mathbf{S}_i^{(A,l)}$ is the Fourier transform of the wave signal generated by an impact source at column l and measured by sensor A in a test along row i.

In this study, five repeated signal data sets were collected at the same test location to improve signal consistency. The signal coherence function was used to evaluate repeatability of the obtained signals. Signal coherence of the signals measured by sensors A and B is given by

$$SC_{AB}(f) = \frac{\left|\sum_{m=1}^{5} G_{AB}(f)\right|^2}{\sum_{m=1}^{5} G_{AA}(f) \times \sum_{m=1}^{5} G_{BB}(f)} \quad,$$

Equation 11-3

where m is the index of five repeated signal data, and $G_{AB}(f)$, $G_{AA}(f)$ and $G_{BB}(f)$ are the cross spectrum and auto spectrum functions between two time-domain signals measured by sensors A and B, which are $\mathbf{V}_{(A,l)}^i$ and $\mathbf{V}_{(B,l)}^i$ for the vertical measurements, or $\mathbf{V}_i^{(A,l)}$ and $\mathbf{V}_i^{(B,l)}$ for the horizontal measurements. Similarly, for an impact at row k, $SC_{BA}(f)$ can also be calculated from two time-domain signals $\mathbf{V}_{(A,k)}^i$ and $\mathbf{V}_{(B,k)}^i$ (or $\mathbf{V}_i^{(A,k)}$ and $\mathbf{V}_i^{(B,k)}$).The averaged SC (f) is defined as

$$\mathbf{SC}(f) = \sqrt{\mathbf{SC}_{AB}(f)\mathbf{SC}_{BA}(f)} \quad,$$

Equation 11-4

which ranges from 0 to 1.0. A value close to 1.0 indicates good signal quality and repeatability. Finally, five transmission functions were then arithmetically averaged in the frequency domain. In addition, the measured surface wave transmission coefficients were further normalized by transmission coefficients measured from a solid region without cracks. This procedure will eliminate the geometric spreading effects caused by a point source and material damping.

11.2.4 Solid regions versus cracked regions

Figure 11-4 (a) and (b) show typical time domain signals measured from the specimen NR-E using an impact source applied at a column 8 and row 4 (i.e., I(8,4)), and from the specimen R1-E at I(4,3), respectively, using two air-coupled sensors. The raw signal data and windowed signal data were presented as dash lines and solid lines.
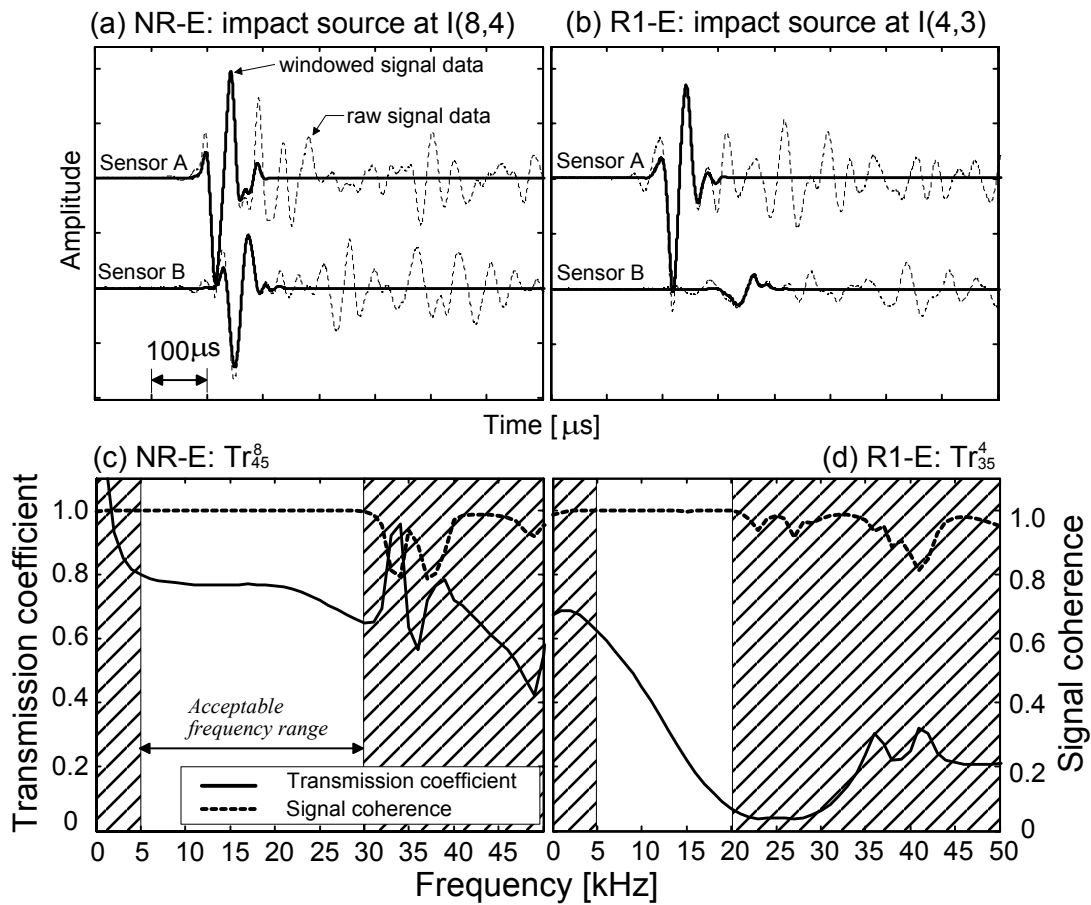
Figure 11-4: Comparison of typical signals measured from concrete beams of NR-E and R1-E measured by air-coupled sensors:(a) typical time signals measured from the concrete beam NR-E using an impact source applied at the column 8 and row 4 (i.e., I(8,4)); (b) typical time signals from R1-E at I(4,3); (c) and (d) show typical transmission coefficient and signal coherence in the frequency domain of the signals shown in Figs.8 (a) and (b), respectively.

Figure 11-4 (c) and (d) give transmission coefficients and signal coherence function of the windowed time-domain signals presented in **Figure 11-4** (a) and (b). Consistent with observations from previous researchers [7, 8, 40], in the solid region, transmission coefficient is relatively constant in the frequency range of 5 to 30 kHz, whereas in the cracked region, transmission coefficients decrease with increasing frequencies in the range of 5 to 20 kHz. This property of surface waves is useful to identify and characterize surface-breaking cracks in concrete.

11.3   EVALUATION OF SURFACE-BREAKING CRACKS

11.3.1   Identification of critical cracks using image technique

Figure 11-5 (a)-(d) show 1-D transmission maps representing transmission coefficients measured from test regions in concrete beams of NR-E, R1-E, R2-E, and R2-W, respectively. The size of transmission maps was adjusted according to the size of the end block region of the beams. The spatial resolution of the transmission maps was determined so that the grid size is comparable to the wavelength of incident surface waves (i.e., 10 cm in this study). Each pixel of the images presents the normalized transmission coefficients of surface waves at the center frequencies. Transmission coefficients corresponding to 1 and 0 were presented as white and black colors. Transmission coefficients between 0 and 1 are presented in gray scale.

Figure 11-5 (a) shows an 1-D transmission map for NR-E (the mildly damaged beam) based on transmission coefficients measured in the vertical direction. The 1-D transmission map effectively identified existence of surface-breaking cracks. The regions without surface-breaking cracks in visual inspection are presented as light colors, while the regions with surface-breaking cracks are shown as dark colors. Note that the 1-D transmission map based on transmission measurements in the vertical direction matched the horizontal cracks well. In addition, the darkness in the transmission map may be

214

interpreted to show additional information of crack depths. Characterization of the depths of surface-breaking cracks is discussed in detail in the next section.
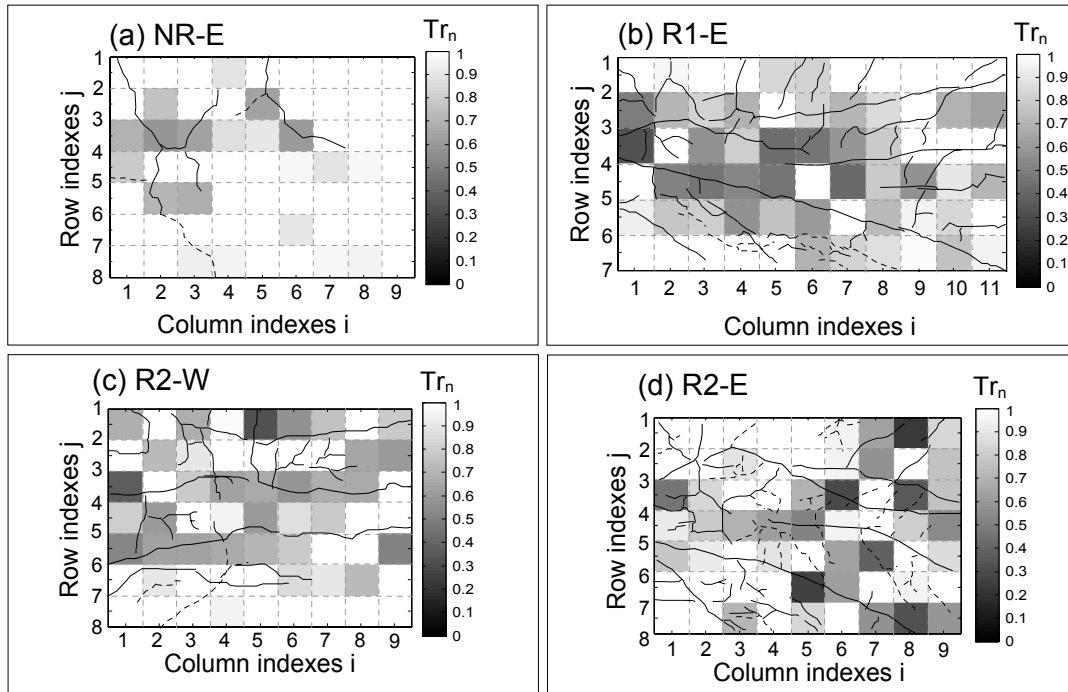
Figure 11-5: 1-D transmission maps representing transmission coefficients measured in the vertical direction from the test regions: (a)NR-E, (b) R1-E, (c) R2-W, and (d) R2-E. Both the row spacing (distance between impact points) and column spacing (horizontal sensor shift) are 10 cm.

1-D transmission maps for beams R1-E, R2-E, and R2-W based on the transmission coefficients measured in the vertical directions are shown in **Figure 11-5** (b), (c), and (d). Compared to the case of NR-E, distributed surface-breaking cracks with wider width and more complex crack patterns caused by ASR/DEF appear to raise difficulties in transmission measurements and interpretation of transmission maps. **Figure 11-5** (b) shows that the 1-D transmission map for R1-E is still effective to determine the critical damage region. However **Figure 11-5** (c) and (d) for R2-E and R2-W show that some regions with critical cracks identified by visual inspection were not properly identified in the transmission maps. Possible reasons can include *(i) near-field*

215

effects, (ii) interaction of surface waves between individual cracks, and (iii) limitation of 1-D transmission maps. The near-field effects are likely the most influential effect. Previous researchers noticed that the near-field effects [34, 40, 44, 99] cause significant enhancement in transmission measurements if sensors are too close to a surface-breaking crack in the SC procedure (see Chapter 3). For the MSC procedure, transmission coefficients are significantly enhanced if impacts are applied too close to cracks. To minimize near-field effects during acoustic scanning, it was found effective to increase spacing between impact sources. Figure 11-6 (a) and (b) are 1-D transmission maps for specimens R2-E and R2-W by increasing impact spacing from 10 to 20 cm.
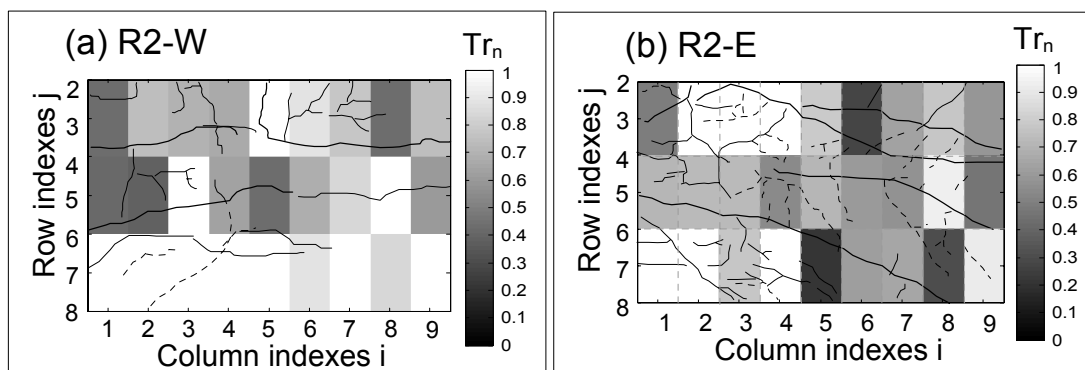
Figure 11-6: 1-D transmission maps (vertical direction) measured from (a) R2-W, and (b) R2-E with increasing a row spacing (distance between impact points) to 20 cm and with a column spacing (horizontal sensor shift) of 10 cm.

Figure 11-7 (a) and (b) show 1-D transmission maps based on the transmission coefficients measured in the vertical and horizontal directions from beam NR-W (mild damage). The transmission maps based on transmissions in the vertical direction matches crack patterns in the horizontal direction well, while the transmission in horizontal direction matches vertical cracks. Note that for 1-D transmission maps, sufficient image resolution may not be obtained in the measurement direction due to limitation of specimen size and the near-field effects. However a 2-D transmission map based on the combination of **Figure 11-7** (a) and (b) improves image resolution. Consistent

with previous findings [12], the combined 2D image shows better agreement with crack patterns observed on the surface of the beam. In addition, spatial resolution of the 2-D transmission map can be improved by using small scan line spacing in 1-D transmission map.
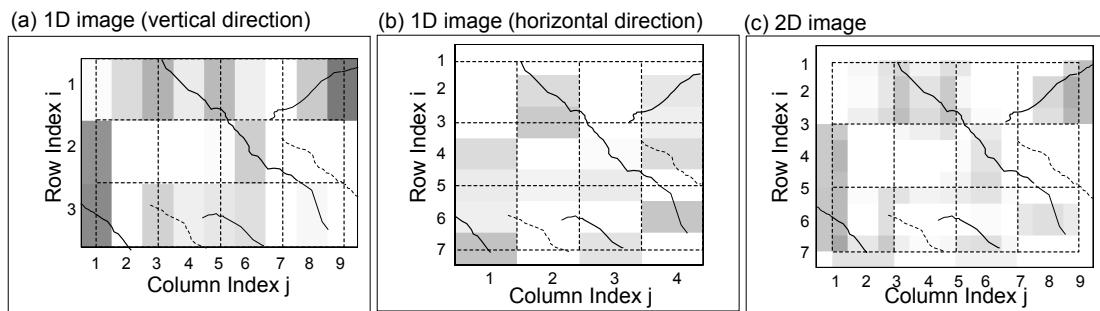
Figure 11-7: Transmission maps measured from NR-W: (a) 1-D transmission map (vertical direction) with a row spacing (distance between impact points) of 10 cm and a column spacing (horizontal sensor shift) of 5 cm; (b) 1-D transmission map (horizontal direction) with a column spacing (distance between impact points) of 10 cm and a row spacing (vertical sensor shift) of 5 cm; and (c) 2-D transmission map with combination of 1-D transmission map in the vertical and horizontal directions shown in (a) and (b).

11.3.2   Crack depth estimation using the SWT method

Depths of the critical cracks identified by 1-D transmission maps and visual inspections were characterized through inversion of transmission function shown in Figure 2-11 (b). In this study, the transmission coefficients were obtained using two ways: *(i) the MSC procedure, and (ii) the SC procedure*.

In the MSC procedure, the transmission coefficients of surface waves across the critical cracks were first calculated by Equation 8-6, and then, depths of the cracks were estimated using the simplified SWT method at the center frequencies. Multiple impact sources can provide several sets of signal data for calculating transmission coefficients of surface waves in the region between the impact sources. The predicted depths of the critical cracks (pointed out in **Figure 11-2**) are summarized in **Table 11-1**. The test regions were carefully determined to minimize the near-field effects, and to obtain

reliable and consistent transmission function for all cracks. For the critical crack #1 in R1-E (pointed out in **Figure 11-2** (b)), $Tr_{n\,45}^{4}$, $Tr_{n\,46}^{4}$, $Tr_{n\,36}^{4}$, and $Tr_{n\,35}^{4}$ were used to estimate the depth of the crack. As seen in **Table 11-1**, the transmission coefficients from various regions (4-5, 4-6, 3-6, and 3-5) provided values ranging from 0.25 to 0.52, resulting in approximate crack depths ranging from 44 to 57 mm. For other cracks, the MSC procedure provided the crack depths in ranges.

Table 11-1: Crack depth estimation using transmission coefficients measured by the MSC procedure and the SC procedure.

Specimen #	Tr_n		h/λ	f [kHz]	λ [m]	h_{ndt} [mm]
R1-E	$Tr_{n\,45}^{4}$	0.52	0.26			44
	$Tr_{n\,46}^{4}$	0.30	0.33			54
	$Tr_{n\,36}^{4}$	0.25	0.34			57
	$Tr_{n\,35}^{4}$	0.42	0.29			49
R2-W	$Tr_{n\,34}^{1}$	0.37	0.31			51
	$Tr_{n\,35}^{1}$	0.29	0.33			54
	$Tr_{n\,25}^{1}$	0.34	0.32	13	0.166	53
	$Tr_{n,sc}$	0.31	0.33			54[†]
R2-W	$Tr_{n\,25}^{2}$	0.61	0.24			40
	$Tr_{n\,35}^{4}$	0.44	0.29			48
	$Tr_{n,sc}$	0.29	0.33			54[†]
R2-W	$Tr_{n\,23}^{3}$	0.69	0.21			34
	$Tr_{n\,24}^{3}$	0.78	0.17			28
	$Tr_{n,sc}$	0.83	0.15			32[†]
R2-E	$Tr_{n\,57}^{6}$	0.46	0.28	15	0.144	41
	$Tr_{n\,58}^{6}$	0.25	0.34			49

Note: [†] results based on transmission measurement through the SC procedure.
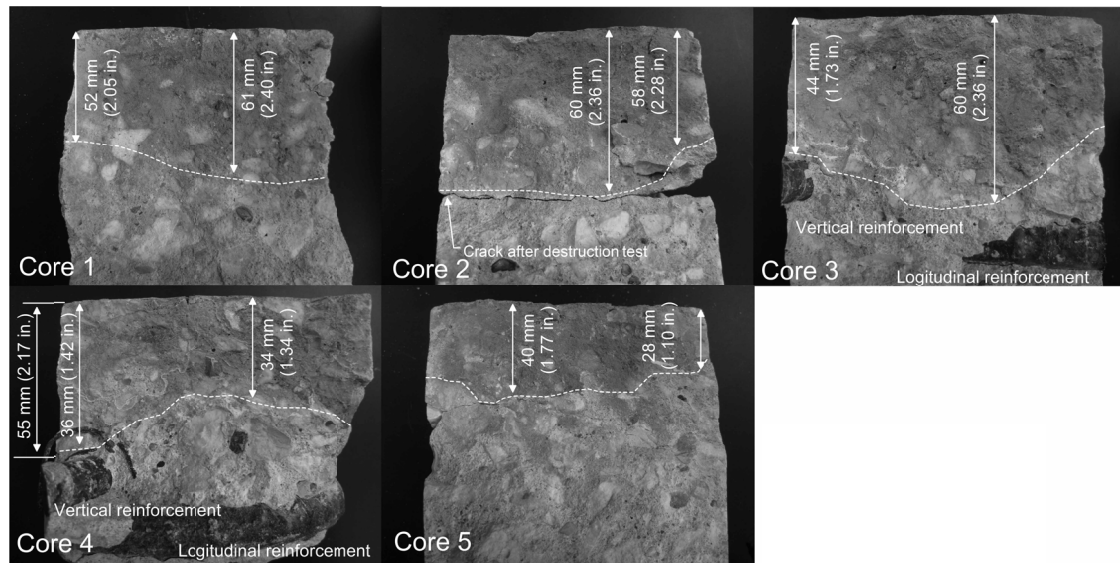
Figure 11-8: Concrete samples from core extractions.

In addition, the conventional SC procedure was also applied to measure transmission coefficients of surface waves across the critical cracks #2, 3, and 4 (see **Figure 11-2**). Transmission coefficients were calculated using Equations 11-1, and 11-2 using the test setup presented in **Figure 11-1**. The locations of sensors were adjusted to leave enough space between cracks and sensors ($x_1=x_2=15$cm). Furthermore, the impacts locations were carefully chosen in solid regions. This may be effective to further minimize the near-field effects of surface waves and interaction of surface waves between cracks. Transmission coefficients and corresponding depths of cracks are also summarized in **Table 11-1**. In three cases, the results from the SC method match with the upper limit of the MSC results. The validity of the MSC and SC procedures for the crack depth estimation will be discussed in the following section.

11.3.3   Comparison with core samples

The validity of the simplified SWT method is shown in this section by comparing with those from direct measurement from core samples. Five core samples were extracted

from the locations of the critical cracks. **Figure 11-8** shows the vertical cross sections of the core samples showing the surface of critical surface-breaking cracks. The ASR crack depth is determined by measuring the darken surface caused by dusts and carbonation. **Figure 11-8** reveals that the crack depth in concrete varies in range between 28 mm and 61 mm. The existence of reinforcements strongly affects extent of cracks. The variations of crack depths are shown on the cored samples in **Figure 11-8**.
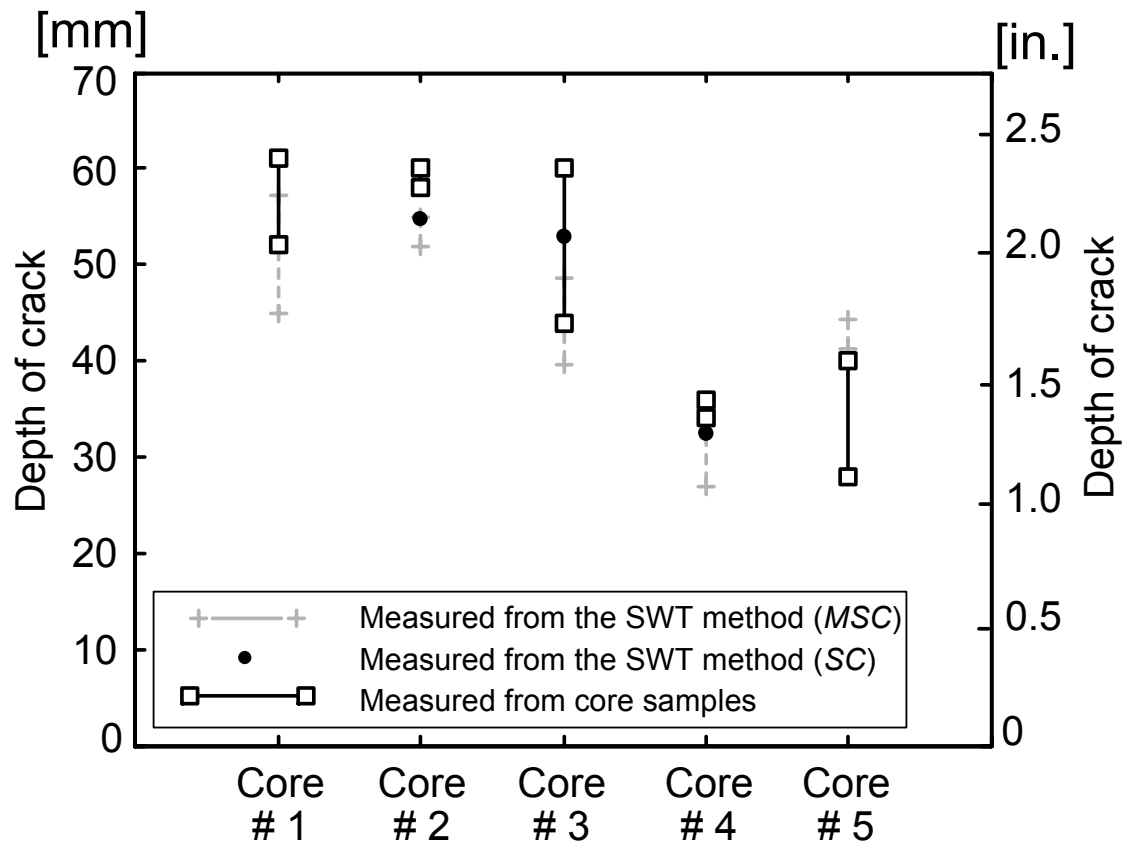
Figure 11-9: Comparison of crack depths estimated using the air-coupled SWT method by different sensor arrangement (the modified self calibrating procedure, and the self-calibrating procedure) and crack depths measured from core samples.

Figure 11-9 compares crack depth measured by the simplified SWT method, and from core samples. The results from the SWT method show fairly good agreement with the actual crack depth measurements from core samples. Particularly, depth estimation based on the original SC provides better matching to the results from core samples. Unevenly distributed cracks in test regions probably result in a certain degree of near-field effects and interaction of surface waves between individual cracks. Furthermore, the transmission function used in the simplified SWT method is only valid for the normal incident surface waves. These may cause discrepancies between the estimated crack depths from the SWT method and the results from core samples. However the errors seem to be still within reasonable ranges to provide valuable information in field practice. Therefore, we can conclude that the simplified SWT procedure is a potential method to estimate depth of a surface-breaking crack in concrete structures on sites.

11.4 CONCLUSIONS

In this study, the air-coupled SWT method was applied to evaluate surface-breaking cracks in concrete structures on sites. First, a simplified procedure of the SWT method was proposed. Next, the simplified SWT method was applied to pre-stressed concrete beams with different degrees of damages by ASR/DEF. The findings obtained in this study are shown as follows:

(1) Comparison studies showed that both the air-coupled sensors and accelerometers give good signal coherence (greater than 0.98) in frequency range of 10 kHz to 30 kHz. In this frequency range, measurement from the air-coupled sensors and from accelerometer show good agreements, especially around the center frequency (~17 kHz). This results shows that the air-coupled sensors provide the same accuracy as accelerometers in the frequency range used in this study. In addition, field application in this study demonstrated that

the air-coupled sensors substantially improved the test speed in measurements on large concrete structures compared to the contact sensors.

(2) Using air-coupled sensors, transmission coefficients of surface waves measured in the solid regions of the beams are constant in frequency range of 5 kHz to 30 kHz, whereas in the cracked region, transmission coefficients decrease with increasing frequencies in the range of 5 to 20 kHz. This property of surface waves is useful to identify and characterize surface-breaking cracks in concrete.

(3) The SWT method can be extended to the global inspection using the modified self-calibrating procedure (MSC). Using the MSC procedure, 1-D and 2-D transmission maps were obtained to identify existence of surface-breaking cracks in concrete. 1-D transmission map was demonstrated effective to identify cracks normal to the test direction. The transmission map based on transmissions in the vertical direction is well matching with crack patterns in the horizontal direction, while the transmission in horizontal direction matches vertical cracks. The regions without surface-breaking cracks in visual inspection were presented as the lighter colors, while the regions including surface-breaking cracks were clearly identified as the darker colors.

(4) 2-D transmission maps were obtained by combination of the 1-D transmission maps in the horizontal and vertical directions. The combined 2-D transmission map shows better agreement with crack patterns observed on the surface of the beam. In addition, spatial resolution of the 2-D transmission map can be improved by using small scan line spacing in 1-D transmission maps.

(5) The depths of the critical surface-breaking cracks in concrete structures were estimated by the simplified SWT method suggested in this study. Transmission coefficients were calculated based on two ways: *(i) the modified*

222

self-calibrating procedure, and (ii) the original self-calibrating procedure. The results from the SC procedure matched well with the upper limit of the results from the MSC procedure. Comparison studies showed that the estimated depth from the SC procedure and MSC procedure matched fairly well with the results measured from core samples directly extracted on the surface of concrete beams. The discrepancies between the results from the SWT method and from the core extraction seem to be within reasonable ranges to provide valuable information in the field practices. The results presented in this study showed the simplified SWT procedure is a potential method to estimate depth of a surface-breaking crack in large concrete structures.

PART V CONCLUSIONS

Chapter 12 Summary, Conclusions and Recommendations

12.1 SUMMARY

The primary purpose of this study is to develop a non-contact air-coupled NDT method to identify and characterize surface-breaking cracks in concrete structures using surface wave transmission measurements. It has been found that the surface wave transmission (SWT) across a surface-breaking crack is related to the crack depth. However, inconsistence was noticed in surface wave transmission measurement. In this dissertation, the author first summarized limitations of the current SWT method for application to concrete structures, which include inconsistent sensor coupling, near-field effect, effects of crack width, external loading effect on surface wave transmission coefficient, and lack of repeatable source.

In this dissertation, the author attempts to find solutions to the aforementioned problems. First, non-contact air-coupled sensors were applied to the SWT method to reduce experimental errors caused by inconsistent coupling condition of conventional contact sensors. Air-coupled sensing enables reliable and consistent results, and significantly improves test-speed. Results from laboratory and field tests demonstrate effectiveness of air-coupled sensors. Second, appropriate sensor-to-source configurations are proposed to reduce undesirable effects: *(i) the near-field effect of sensors around a crack*, and *(ii) contribution of multiple modes in a plate-like structure with a finite thickness*. Near-scattering of surface waves interacting with a surface-breaking crack was investigated using numerical simulations (finite element method) and experimental studies over a wide range of the normalized crack depth (h/λ: crack depth normalized by wavelength of surface waves) and the normalized frequency-thickness ratio ($f\text{-}H/C_R$: frequency-thick normalized by Rayleigh wave speed). Third, effects of external loadings on transmission coefficient of surface waves in concrete were investigated through a series of experimental studies. In the research, variation of the transmission coefficient is

presented as a function of crack mouth opening displacement (CMOD). This provides a guideline on minimum CMOD to which the SWT method can be reasonably applied. In addition, the author experimentally demonstrates that using low-cost piezoceramic sensors is effective in generating consistent stress waves in concrete. Finally, the author demonstrates that the air-coupled SWT method developed in this study is effective for in-situ estimates of a surface-breaking crack in large concrete structures.

12.2 CONCLUSIONS

The air-coupled SWT method was developed in this study to identify and characterize surface-breaking cracks in concrete structures. The important conclusions from theoretical studies and experiments in the laboratory to field applications are drawn as follows:

12.2.1 Theoretical studies

(a) Sensors should be located approximately 1.5 λ (wavelength of surface waves) from the crack to minimize the near-field effects caused by a surface-breaking crack. Strong signal enhancement and oscillation of transmission coefficient were observed when sensors are located within 0.5 λ away from the cark opening. The oscillatory behavior of transmission coefficients becomes weaker as sensors are located approximately 1.5 λ from the crack, and almost disappears when sensors are 3.0 λ away from the crack.

(b) Interaction of surface waves between individual cracks significantly impact transmission coefficients of surface waves across distributed surface breaking cracks. Interaction of surface waves between individual cracks becomes significant when the normalized crack spacing a/h is smaller than the threshold value ($a/h \sim 6$). Tr_n reaches a minimum value when a/h is between 2 and 3 for the same crack depth h. For very large

a/h, the transmission coefficient tend to converge to a constant value. In addition, the number of cracks, and the crack depth ratio h_1/h_2 is also important parameters which may affect the transmission coefficient of surface waves.

(c) Contribution of multiple Lamb wave modes may significantly affect transmission coefficients of surface waves dependent of frequency-thickness f-H (frequency of input source, and thickness of a plate). For the thick plates ($f\text{-}H/C_R > 2$), when sensors are located in $a_n < x < a_i$, the Tr_n and h/λ relation converged to the analytic solution obtained on the ideal far-field in the half-space model. For the medium thicknesses ($1.6 < f\text{-}H/C_R < 2$), Tr_n was very sensitive to the location of sensors due to contribution of multiple modes of Lamb waves. In this case the analytic solution for the thick plates cannot be used for estimation of a crack-depth. For the resonance range ($0.5 < f\text{-}H/C_R < 1.6$), considerable energies are imparted by resonance modes of higher-order lamb waves, which are not informative on the depth information of a surface-breaking crack. For the thin plates ($f\text{-}H/C_R < 0.5$), Tr_n versus h/λ based on the half-space model is also effective to estimate the depth of surface-breaking crack in solid media.

12.2.2 Experimental Studies in the Laboratory

(a) Experimental studies demonstrated that condenser microphones could be a good choice for air-coupled sensors in NDT for concrete in civil engineering. Comparison studies showed that the transmission coefficient and the phase velocity of surface waves measured by air-coupled sensors had a good agreement with those measured by accelerometers. This revealed that air-coupled sensors can provide the same accuracy as accelerometers in the useful frequency range for concrete NDT of using stress waves. The self-calibrating procedure, originally developed for contact sensors, was verified still effective to minimize effects caused by asymmetry in a test specimen and a test setup on calculation of transmission coefficient and the phase velocity of surface waves using air-coupled sensors.

(b) Using air-coupled sensors was an effective way to obtain reliable surface wave transmission measurement across a surface-breaking crack in concrete. Non-contact features of air-coupled sensors increased signal consistency, and significantly improved test speed compared to using contact sensors. Experimental studies from 'a thick concrete plate' verified the validity of a simplified algorithm for estimating the depth of a crack in concrete. If surface wave velocity is known, the crack depth can be calculated from the predetermined transmission function. For application of the air-coupled SWT method to 'a concrete plate with a medium thickness', a measurement model was proposed in this study. The measurement model includes appropriate configurations of a source-and-receiver, signal processing procedure, and a transmission function for the given configuration.

(c) The transmission coefficient of surface waves was verified the more sensitive acoustic parameter to a surface-breaking crack compared to other parameters (the phase velocity of surface waves, and time-of-flight diffraction of P waves). The phase velocity of surface waves was not sensitive acoustic parameter to estimate the crack depth in concrete when crack depth h is smaller than or comparable to wavelength of incident surface waves. Time-of-flight diffraction method was used to estimate the depth of a surface-breaking crack in concrete using two different test setups: (i) using ultrasonic transducers with a center frequency of 50 kHz, and (ii) using transient waves generated by a impact source. The test setup of using ultrasonic transducer resulted in very large errors, which was mainly due to errors in selecting the first-arrival of diffracted waves in receivers. In contrast, using transient waves provides better agreement with the designed crack depths in concrete. However, compared to the results from the air-coupled SWT method, the estimated crack depth by the TOFD method tended to overestimate the crack depth, especially for cracks with shallow depths.

228

(d) Interfacial conditions in surface-breaking cracks in concrete may affect the transmission coefficient of surface waves in concrete. For the crack-free regions, applying external loadings did not affect the transmission coefficient surface waves. After cracking, transmission coefficient gradually, however, increases with monotonically increasing compressive forces applied perpendicular to crack surface. This demonstrated that some portions of incident waves can be transmitted through the interface of the crack (i.e., the crack interfacial waves). Transmission coefficient-CMOD curve showed that transmission coefficient appears stable when CMOD was greater than 0.18 mm. Decreasing CMOD from 0.18 to 0.01 mm substantially grow up transmission coefficient, in which the SWT method may not provide the reasonable crack depth estimation in concrete.

(e) Surface mount sensors and embedded sensors, made of low cost piezoelectric elements, can be a low cost solution to develop a computer-controlled source and receiver for application to concrete NDT. Experimental studies demonstrated that the patched piezoelectric discs were effective to measure surface waves on concrete surface. The transmission coefficient surface waves were used to evaluate the depth of surface-breaking crack in concrete. The estimated crack depth using the signal data generated by the piezoelectric discs showed good agreement with the directly measured from a core sample extracted from a concrete specimen. In addition, the patched sensors were also effective to measure ultrasonic pulse velocity (UPV) of direct P, and S and surface waves on concrete surface. Moreover, due to the small size and low cost, the piezo sensors can be embedded in concrete during construction. This embedded piezoelectric disc was verified very effective to measure UPV of P, and S wave propagating through concrete. The UPV from embedded sensors agreed well with that measured from a commercial UPV unit. The measured UPV provides information on effective stiffness of concrete, which has been regarded as a good indicator of evaluating concrete in structures.

12.2.3 Field application

(a) The SWT method can be applied to global inspection using the modified self-calibrating procedure (MSC). Using the MSC procedure, 1-D and 2-D transmission maps were obtained to identify existence of surface-breaking cracks in concrete. 1-D transmission map was demonstrated effective to identify cracks normal to the test direction. Furthermore, 2-D transmission maps were obtained by combination of the 1-D transmission maps in the horizontal and vertical directions. The combined 2-D transmission map showed better agreement with crack patterns observed on the surface of the beam. In addition, spatial resolution of the 2-D transmission map can be improved by using small scan line spacing in 1-D B-scan images.

(b) The results from field applications demonstrated that the simplified air-coupled SWT procedure showed a potential for estimating depth of a surface-breaking crack in large concrete structures. Comparison studies showed that the estimated depth from the self calibrating procedure and the modified self-calibrating procedure matched fairly well with the results measured from core samples directly extracted on the surface of concrete beams. The discrepancies between the results from the SWT method and from the core extraction seem to be within reasonable ranges to provide valuable information in the field practices.

12.3   RECOMMENDATIONS FOR THE FUTURE WORK

The author has attempted to solve the limitations categorized in Chapter 2 through theoretical studies (chapters 3, 4, and 5), and experimental work (Chapters 6, 7, 8, 9, and 10), and reached reasonable answers. However, there are still unsolved problems in the Air-coupled SWT method. According to this research, following topics are proposed to further develop the air-coupled SWT method and to extend the applicability to automatic health monitoring systems for in-situ concrete structures. The future works are recommended as follows.

230

12.3.1 Effects of distributed cracks on SWT measurements in concrete

Generally, reinforced concrete structures contain distributed surface-breaking cracks. The author investigated effects of distributed cracks on surface-wave transmission measurements through numerical simulations and experimental studies in Chapter 4: however, the experimental results were only obtained from homogeneous material (Plexiglas). More work is still needed to reach a more reasonable answer on applicability of the SWT method to estimate depths of multiple distributed cracks in concrete. A future work may include theoretical works such as developing signal processing algorithm and advanced inverse techniques, and experimental work for verification.

12.3.2 Using non-linear acoustic parameters

Ultrasonic methods are one of the most powerful nondestructive ways of evaluating material degradation. Traditional ultrasonic NDT/E is based on linear theory and normally relies on measuring some particular parameter (sound velocity, attenuation, transmission and reflection coefficients) of the propagating signal to determine the elastic properties of a material or to detect defects. In this dissertation, the author also placed a heavy emphasis on using linear acoustic parameters (transmission coefficient, and phase velocity of surface waves). However, the conventional ultrasonic techniques are sensitive to gross defects or open cracks, where there is an effective barrier to transmission, whereas it is less sensitive to evenly distributed microcracks or degradation. In addition, as demonstrated in Chapter 11, linear acoustic parameters (transmission coefficient and phase velocity) do not look sensitive to various interfacial conditions of cracks.

An alternative technique to overcome this limitation is nonlinear ultrasonics. Comprehensive reviews on application of nonlinear ultrasonics to NDT/E were provided by Jhang [91]. In non-linear ultrasound NDE, the existence and characteristics of defects are often related to an acoustic signal whose frequency differs from that of the input signal. This is related to the radiation and propagation of finite amplitude (especially high

power) ultrasound and its interaction with discontinuities, such as cracks, interfaces and voids. Considerable attention has been focused on the application of nonlinear ultrasonics owing to two reasons: (i) material failure or degradation is usually preceded by some kind of nonlinear mechanical behavior before significant plastic deformation or material damage occurs, and (ii) non-linear ultrasonic parameters are very effective to investigate the interfacial conditions of cracks [100].

12.3.3   Sensor array and data analysis algorithm

The air-coupled SWT method has been developed based on a test setup that included two sensors. The author demonstrates that the two-sensor setup is still effective method for identifying and characterizing surface-breaking crack in concrete structures. However, using the two-sensor setup may not provide enough speed for global inspection of large civil infrastructure systems (concrete bridge decks, pavements in highway and air-port, etc.). In addition, higher-order modes in thin plate cannot be separated using the two-sensor setup.

The alternative choice is developing a test setup of using air-coupled sensor array. Using air-coupled sensors array will significantly improve test speed for application to large concrete structures. For these purposes, the author proposes research topics that should include (i) optimization of spacing and configuration of air-coupled sensor array, and (ii) developing an advanced signal processing algorithms for sensor array, and developing computer program to control data acquisition, data reduction, and interpretation.

232

Appendix A Near-field Scattering of Surface Waves

A.1   PROPAGATION PATHS OF DOMINANT WAVES

Backward scattering field| Forward scattering field
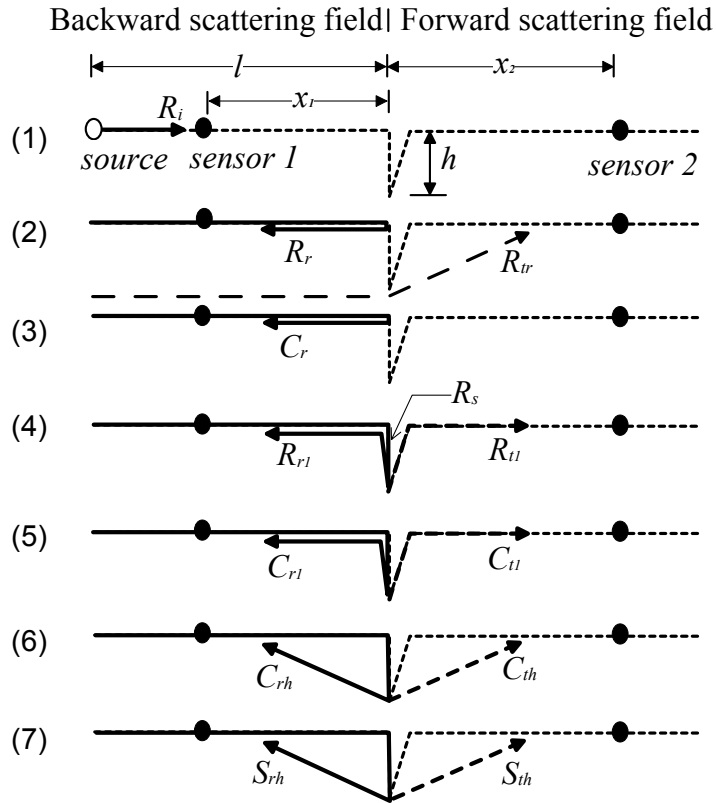
Figure A-1: Propagation paths of the scattered waves. (after Jian et al. [34]).   h is the depth of the crack. Sensors 1 and 2 are located in the backward and forward scattering field. l is the distance of a source from the crack mouth, and x_1 and x_2 are distances of sensors 1 and 2, respectively, from the crack mouth.

- R_i is incident surface wave.
- R_r is reflected surface wave at the front surface of the crack and propagates backward.
- R_{tr} is a portion of incident surface waves with wavelength larger than the crack depth through passing underneath the crack.

233

- C_r is a mode converted compression wave (R-P) reflected backward from the front surface of the crack.
- R_s is a portion of incident surface waves propagating around the top crack corner and down to the vertical crack face to the tip of the crack.
- R_{r1} and R_{t1} are a portion of R_s reflected at the tip of crack and propagating up along the vertical face of the front and rear top crack corners, respectively.
- C_{r1} and C_{t1} are a portion of R_s mode-converted longitudinal waves from the bottom tip of crack and propagating up along the vertical face of the front and rear top crack corners, respectively.
- C_{rh} and S_{rh} are mode-converted longitudinal and transverse (P, and S waves) propagating to 'the backward scattering field' by diffraction at the tip of the crack [26, 27].
- C_{th} and S_{th} are mode-converted P, and S waves propagating to 'the forward scattering field' by diffraction at the tip of the crack [26, 27].

The arrival times of possible wave modes shown in Figure A-1 can be calculated using equations as follows;

$$t_R = (l - x_1)/C_R,$$

Equation A-1

$$t_{R_r} = (l + x_1)/C_R,$$

Equation A-2

$$t_{R_{tr}} = \begin{cases} \dfrac{l}{C_R} + \dfrac{\sqrt{x_2^2 + h^2}}{C_R} & \text{when } x_2 < \dfrac{C_S}{C_P} h \\[2ex] \dfrac{l + \sqrt{x_2^2 + h^2}}{C_R} & \text{when } x_2 \geq \dfrac{C_S}{C_P} h \end{cases}$$

Equation A-3

$$t_{C_r} = l/C_R + x_1/C_p,$$

Equation A-4

$$t_{R_{r1}} = (l + x_1 + 2h)/C_R,$$

Equation A-5

234

$$t_{R_{t1}} = (l + x_2 + 2h)/C_R,$$ Equation A-6

$$t_{C_{t1}} = (l + 2h)/C_R + x_2/C_P,$$ Equation A-7

$$t_{R_{tr}} = \begin{cases} \dfrac{l+h}{C_R} + \dfrac{\sqrt{x_1^2 + h^2}}{C_P} & \text{when } x_1 < \dfrac{C_S}{C_P}h \\[2em] \dfrac{l + x_1 + (1 - C_S/C_P)h}{C_R} + \dfrac{h\sqrt{C_C^2 + C_S^2}}{C_C C_S} & \text{when } x_1 \geq \dfrac{C_S}{C_P}h \end{cases}$$

<div style="text-align:right">Equation A-8</div>

$$t_{S_{rh}} = (l + h)/C_R + \sqrt{x^2 + h^2}/C_S,$$ Equation A-9

$$t_{C_{th}} = (l + h)/C_R + \sqrt{x^2 + h^2}/C_P,$$ Equation A-1

$$t_{S_{th}} = (l + h)/C_R + \sqrt{x^2 + h^2}/C_S,$$ Equation A-11

where C_P, C_S, and C_R are velocities of P, S and surface waves in solid medium.

Appendix B Seismic Reflection Theory in A Free-Plate

B.1 ARRIVAL TIME CALCULATION OF VARIOUS REFLECTED WAVES IN A FREE PLATE

Possible modes of impact-induced waves in plate-like structures are summarized in Table C-1. First arrivals of individual mode can be calculated using the seismic reflection theory. Direct P, S and surface waves were denoted as P_i, S_i, and R_i and first arrival of the direct waves can be presented as follows,

$$t_{P_i} = \frac{x}{C_p}, \quad t_{S_i} = \frac{x}{C_S}, \quad \text{and} \quad t_{R_i} = \frac{x}{C_R}. \qquad \text{Equation B-1}$$

In addition, first several modes caused by multiple reflections of P and S waves are denoted as PP_n, and SS_n, where PP and SS are reflected P and S waves from free boundary of a plate (i.e., P-P, and S-S), and n is the number of reflections from the bottom of a free plate. The first arrival of PP_n and SS_n can be presented as follows,

$$t_{PP_n} = \frac{2n\sqrt{H^2 + (x/2n)^2}}{C_p}, \qquad \text{Equation B-2}$$

$$t_{SS_n} = \frac{2n\sqrt{H^2 + (x/2n)^2}}{C_S}. \qquad \text{Equation B-3}$$

Furthermore, arrival of the multiple reflections of coupled P and S waves (i.e., mode converted waves) can be expressed as
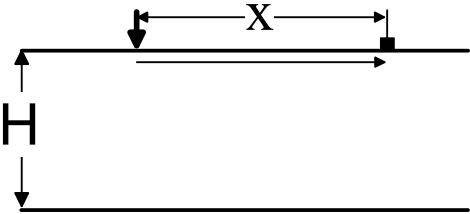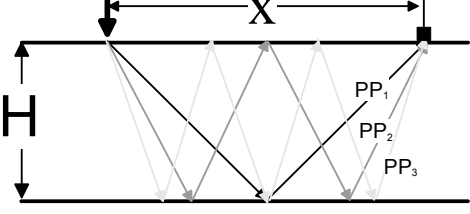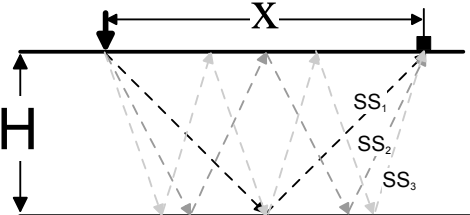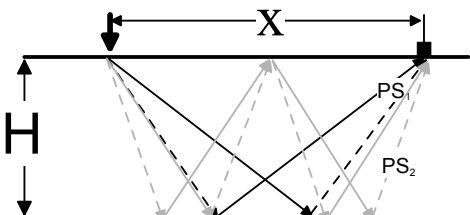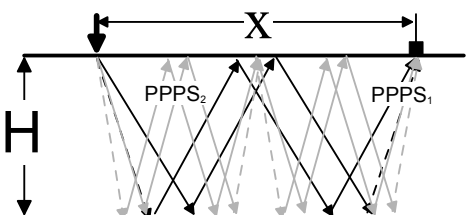
$$t_{PS_n} = n\left[\frac{l\sqrt{H^2 + (\alpha x/ln)^2}}{C_P} + \frac{m\sqrt{H^2 + [(1-\alpha)x/mn]^2}}{C_S} \right] \qquad \text{Equation B-4}$$

where l, and m are the number of P and S waves in a unit reflection, and n is total repetition of the unit reflections, and α is can be obtained by using Equation C-7,

$$\gamma = \frac{m^2}{(1-\alpha)^2(\eta-1)} - \frac{l^2\eta}{(\alpha)^2(\eta-1)} \qquad \text{Equation B-5}$$

where γ is $(x/H)^2$ and η is $(C_p/C_s)^2$.

Table B-1: Possible modes of impact-induced waves in a free-plate

	Wave paths	Symbol
Direct waves		P_i, S_i, and R_i
Multiple reflected P waves		PP_n
Multiple reflected S waves		SS_n
Multiple reflected P-S waves (symmetric mode)		PS_n
Multiple reflected P-S waves (antisymmetric mode)		$PPPS_n$

Appendix C Developing a LabVIEW-based Computer Program

C.1 INTRODUCTION

The SWT measurement system is a LabVIEW-based computer program developed by the author in this study. This program was used to measure surface waves, as well as to calculate the transmission coefficient, the signal coherence function, and the phase velocity of the surface waves. The program includes four parts of *(i) configuration setup, (ii) measurements, (iii) analyses, and (iv) reviewing saved data.* **Figure C-1** shows the introduction page of the computer program.
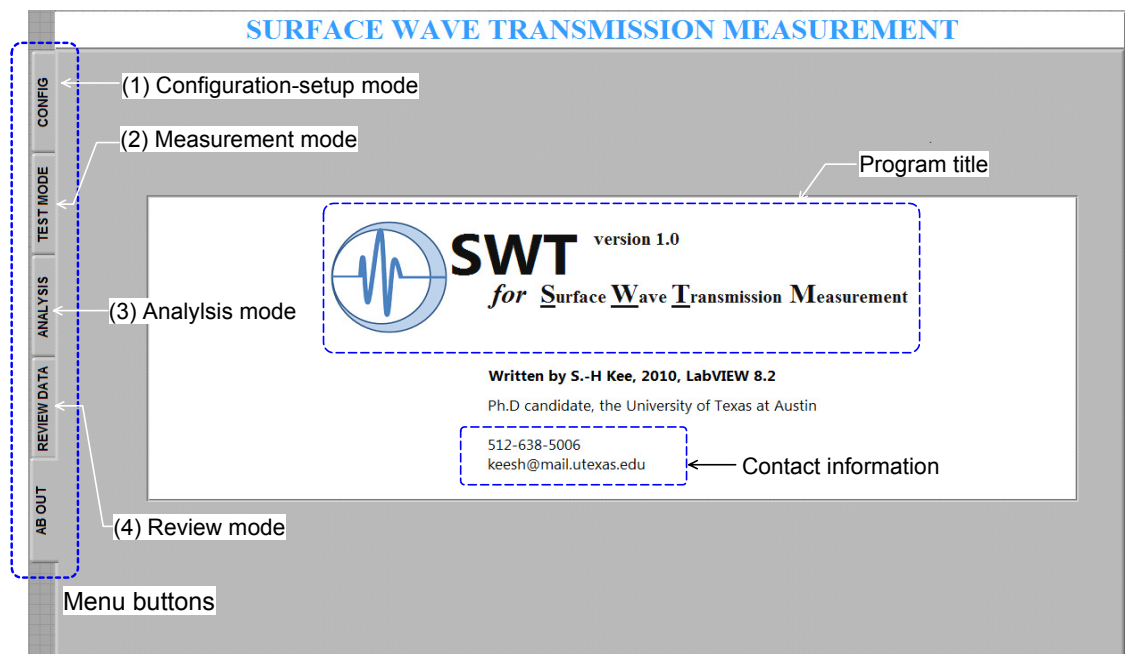
Figure C-1: The introduction page of the computer program.

C.2 CONFIGURATION SETUP FOR MEASUREMENTS

Figure C-2 shows the user interface to assign input parameters for data acquisition system to measure surface waves. Input parameters are summarized in **Table C-1**.
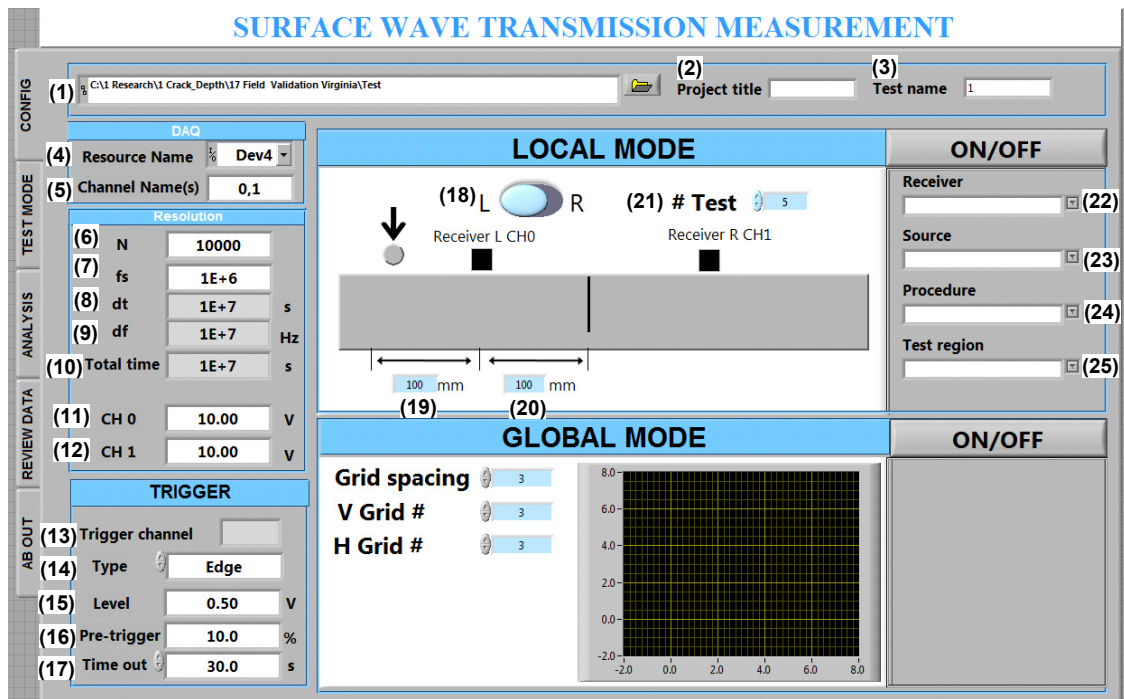
Figure C-2: The user interface to assign parameters for data acquisition, saving, and sensor-receiver configuration.

Table C-1: Summary of input parameters for measuring signal data

Creation of file name for data saving	
(1)	Control to assign a path for data files created during measurements
(2)	Control to write project title
(3)	Control to write test name
Inputs for data acquisition	
(4)	Multi-selection to choose a data acquisition system
(5)	Control to assign active channels
(6)	Control to define the total number of samples N
(7)	Control to assign a sampling frequency f_s (=the number of samples saved for a second) [Hz]
(8)	Indicator to show the time interval Δt (=$1/f_s$)
(9)	Indicator to show frequency interval Δf (=$1/N\Delta t$)
(10)	Indicator to show total time of the measured signal data (=$N\Delta t$)
(11)	Control to assign vertical amplitude limit for channel 0
(12)	Control to assign vertical amplitude limit for channel 1
(13)	Control to assign trigger channel
(14)	Multiple-selection to choose trigger type
(15)	Control to assign trigger level
(16)	Control to assign pre-trigger
(17)	Control to assign time-out
Source-to-sensor configuration	
(18)	Indicator to show location of source
(19)	Control to assign distance between a source and a receiver
(20)	Control to assign distance of receiver from a surface-breaking crack
(21)	Multiple-selection to choose distance a receiver from a surface-breaking crack
(22)	Control to assign the number of repetition in measurements at the same location to check signal consistency of the measured data n
(23)	Multiple-selection to choose receiver types
(24)	Multiple-selection to source types
(25)	Multiple-selection to choose procedures

C.3 MEASUREMENT MODE

Figure C-3 shows the user interface of the SWT measurement system for data acquisition and data saving. A flow chart of a procedure for data acquisition is also summarized in **Figure C-4**. The first step is to assign a appropriate value of a window size. Then, clicking the button of 'acquire' will make a data acquisition system ready to work. Measured time-domain signals by the channel 0 and channel 1 will appear in the time window of (3) and (4), respectively. Moving cursors in the time windows can help selecting a referent point to apply a window function to the time-domain signals. Note that a hanning window is implemented in the program by default. In real time, spectral amplitude of the windowed signals will be shown in the frequency-domain window of (7). When pushing the button of 'TR/SC', users can obtain the transmission coefficient,
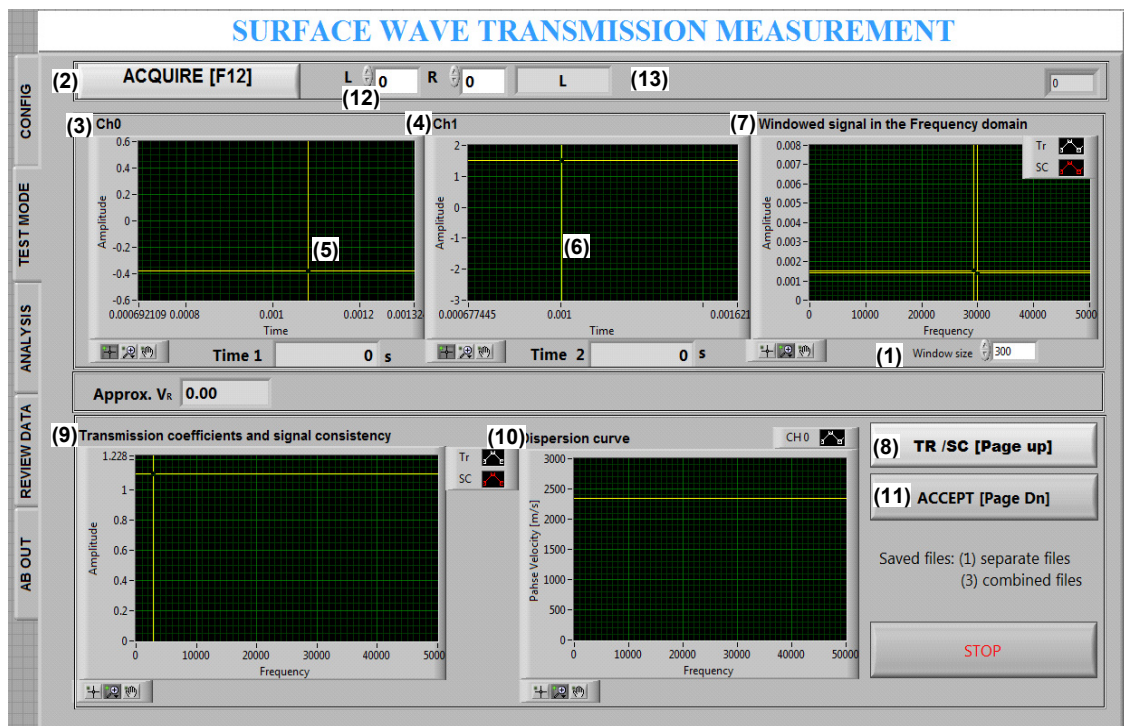
Figure C-3: The user interface to input parameters for data acquisition, saving, and sensor-receiver configuration.

241
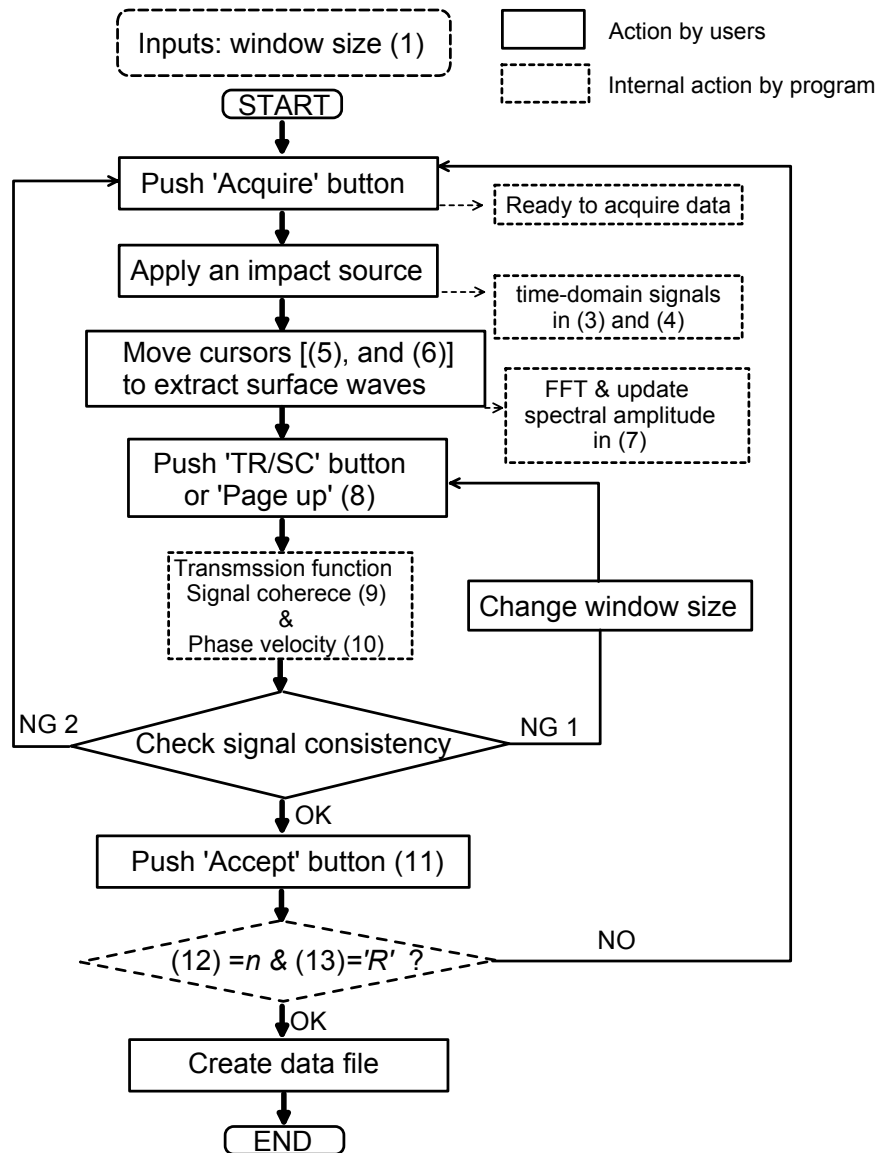
Figure C-4: Flow chart of measuring signal data using the SWT measurement system (see also Figure C-3).

the signal coherence function, and the phase velocity of the surface waves in the window of (9) and (10). If signal consistency of the measured signals will satisfies the criteria, users can accept the measured data by clicking the button of 'Accept'. If not, signal

consistency may be improved by changing window size; or users can discard the measured data by push the button of 'acquire' again. The measurement step described above can be repeated until all sets of data will be obtained from left and right sides of a surface-breaking crack.

C.4 DATA INTERPRETATION AND CRACK DEPTH ESTIMATION

Figure C-5 shows the user interface for data interpretation and crack depth estimation. The flow chart of this mode is also summarized in **Figure C-6**. The first step is to assign input parameters including *(i) window size*, *(ii) paths of saved files measured from crack-free and cracked regions*, and *(iii) distance of a sensor from a crack mouth*. After then, clicking the button of 'start analyses' will automatically generate spectral amplitude of windowed signals and the phase velocity of surface waves measured in the
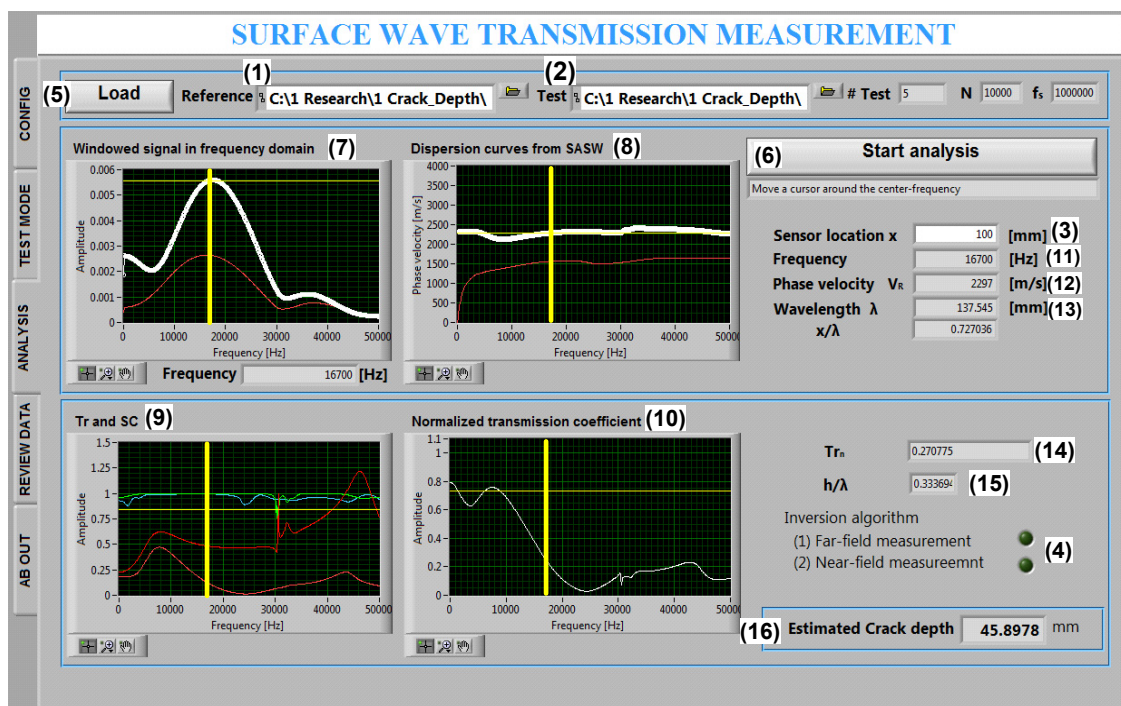
Figure C-5: The user interface to data interpretation and crack depth estimation.

243

Inputs

(i) Path of saved signal from a crack-free region (1)
(ii) Path of saved signal from a test region (2)
(iii) Distance of sensors from a crack mouth (3)
(iv) Algorithm for crack-depth estimation (4)

START

Click 'Load files' button

☐ Action by users

⌐ ¬ Internal action
    by program

Click 'Start analysis' button

Spectral amplitude of windowed signal (7)
Phase velocity (8)
Transmssion coefficient (9)
&
Normalize transmission coefficient (10)

Locate a cursor in (7) around
a center frequency

center frequency fc (11)
phase velcoity at fc (12)
wavelength of fc (13)
Normalize transmission coefficient at fc(14)
&
normalized crack depth (15)

Estimated crack depth

END

Figure C-6: Flow chart of data interpretation and crack depth estimation.

crack-free region in the frequency domain windows of (7) and (8), respectively. At the same time, the window (9) will show the transmission functions of surface waves measured from crack-free and cracked regions, and the window (10) will show the normalized transmission function. By moving the cursor in the window (7), users can choose a frequency, to which the computer program will provide corresponding acoustic

244

parameters (e.g., phase velocity, wavelength, normalized transmission coefficient, and normalized crack depth of surface waves). Finally, the estimated crack depth can be obtained by multiplying normalized crack depth over wavelength.

C.5   REVIEW OF THE SAVED DATA

Figure C-7 shows the user interface to review signal data measured by the SWT measurement system as well as prior versions of LabVIEW-based program. The flow chart of the procedure for review mode is summarized in **Figure C-8**. The first step is to assign input parameters including *(i) window size*, *(ii) file path of save data generated by a impact source located in left side (L) and right side (R)*, and *(iii) selection of appropriate algorithm to pick up a reference point for applying window function to raw time-domain signals*. Then, saved signal data can be loaded by clicking the button of
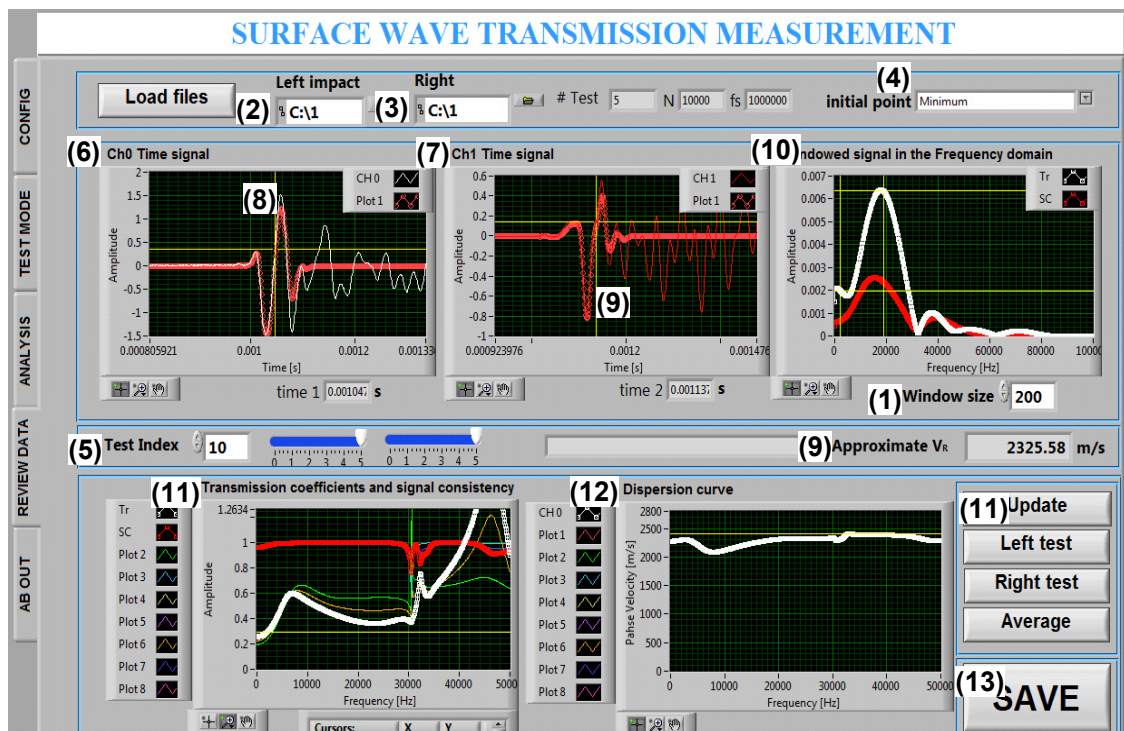
Figure C-7: The user interface to review saved signal data.

245
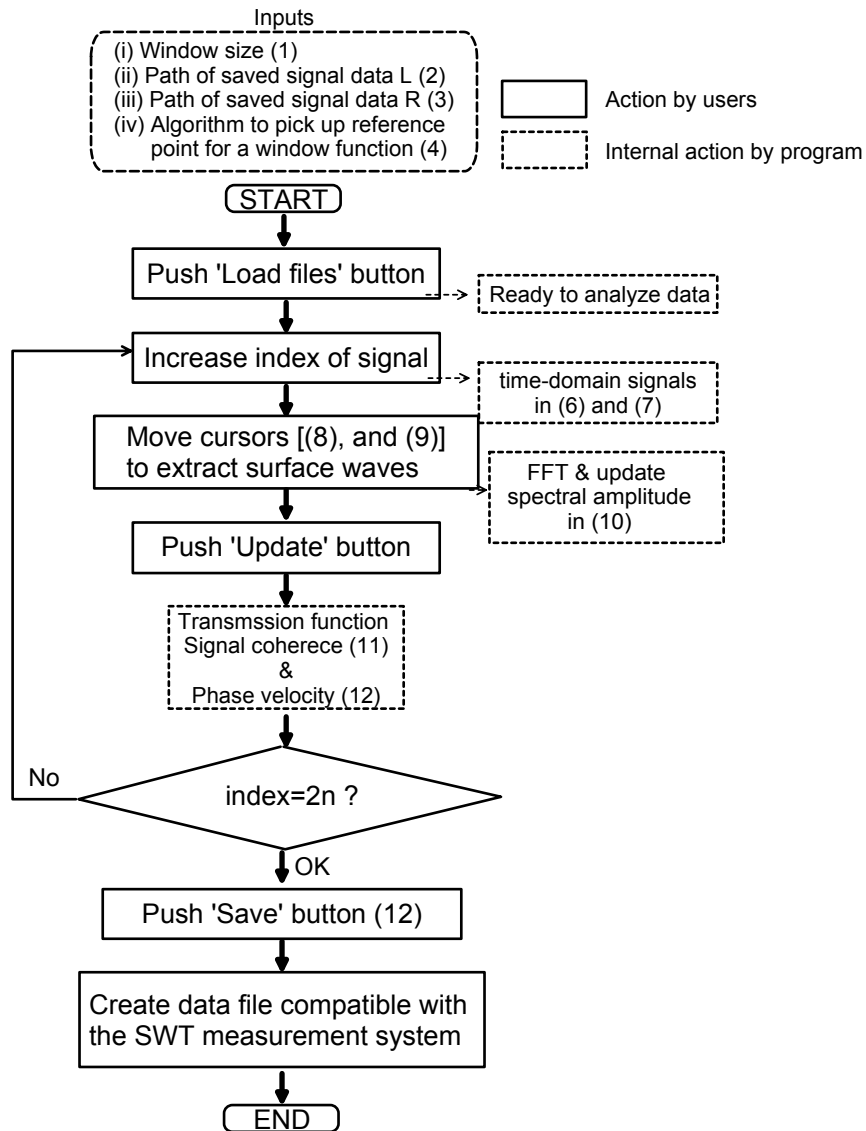
Figure C-8: Flow chart of reviewing saved signal data using the SWT measurement system (see also Figure C-6).

'Load files'. Increasing index of the save data will show the time-domain signals in the time window of (6) and (7). At the same time, windowed signals will be presented as open circles with overlapping to raw signal data. Moving cursors in the time windows

246

can help choosing a reference point for applying window function. In real time, spectral amplitude of the windowed signals will be shown in the frequency-domain window (10). Any changes in the window size (1) will result in updating the spectral amplitude. When clicking the button of 'update', frequency-domain windows (12) and (13) will show the transmission coefficient, the signal coherence function, and the phase velocity of the surface. The measurement step described above can be repeated until index of signal data reaches to 2n, where n is the number of signal data generated at the same location to calculate the signal coherence function. Clicking the button of 'Save' will result in a data file compatible with 'analysis mode' in this computer program.

Bibliography

1.   The American Society of Civil Engineers, "Report card for america's infrastructure [Online]." Available: http://www.infrastructurereportcard.org/.

2.   Lin YC, Liou TH, Tsai WH, "Determining crack depth and measurement errors using time-of-flight diffraction techniques," *ACI Materials Journal*, V. 96, No. 2, Mar-Apr. 1999, pp. 190-5.

3.   Lin YC, Su WC, "Use of stress waves for determining the depth of surface-opening cracks in concrete structures," *ACI Materials Journal*, V. 93, No. 5, Sep-Oct. 1996, pp. 494-505.

4.   Sansalone M, Lin JM, Streett WB, "Determining the depth of surface-opening cracks using impact-generated stress waves and time-of-flight technique," *ACI Materials Journal*, V. 95, No. 2, Mar-Apr. 1998, pp. 168-77.

5.   Krüger M, Grosse CU, "Crack depth determination using advanced impact-echo techniques," *ECNDT 2006, European Conference on NDT*, Berlin, 2006, p. Tu.4.2.

6.   Song W-J, Popovics JS, Achenbach JD, "Crack depth determination in concrete slabs using wave propagation measurements," *1999 FAA (Federal Aviation Administration) Airport Technology Transfer conference*, Atlantic City, NJ, 1999.

7.   Popovics JS, Song W-J, Ghandehari M, Subramaniam KV, Achenbach JD, Shah SP, "Application of surface wave transmission measurements for crack depth determination in concrete," *ACI Materials Journal*, V. 97, No. 2. 2000, pp. 127-35.

8.   Song W-J, Popovics JS, Aldrin JC, Shah SP, "Measurement of surface wave transmission coefficient across surface-breaking cracks and notches in concrete," *The Journal of the Acoustical Society of America*, V. 113, No. 2. 2003, pp. 717-25.

9.   Achenbach JD, Komsky IN, Lee YC, Angel YC, "Self-calibrating ultrasonic technique for crack depth measurement," *Journal of Nondestructive Evaluation*, V. 11, No. 2. 1992, pp. 103-8.

10.   Zhu J, Popovics JS, Schubert F, "Leaky Rayleigh and Scholte waves at the fluid-solid interface subjected to transient point loading," *The Journal of the Acoustical Society of America*, V. 116, No. 4, Oct. 2004, pp. 2101-10.

11.   Zhu J, Popovics JS, "Imaging concrete structures using air-coupled impact-echo," *Journal of Engineering Mechanics-ASCE*, V. 133, No. 6, Jun. 2007, pp. 628-40.

12.   Zhu J, Popovics JS, "Non-contact imaging for surface-opening cracks in concrete with air-coupled sensors," *Materials and Structures* V. 38, November. 2005, pp. 801-6.

13. Zhu J, "Non-contact NDT of concrete structures using air-coupled sensors," *Doctor of Philosophy*, Department of Civil, Environmental and Architectural Engineering, The University of Illinois at Urbana-Champaign, Urbana-Champaign, 2005.

14. Ryden N, Lowe MJS, Cawley P, "Non-contact surface wave scanning of pavements using a rolling microphone array," *Review of Progress in Quantitative Nondestructive Evaluation*, Vol 27a and 27b, 975, Thompson DO, Chimenti DE, eds., Amer Inst Physics, Melville, 2008, pp. 1328-32.

15. In CW, Kim JY, Kurtis KE, Jacobs LJ, "Characterization of ultrasonic Rayleigh surface waves in asphaltic concrete," *NDT & E International*, V. 42, No. 7, Oct. 2009, pp. 610-7.

16. Rayleigh L, "On Waves Propagated along the Plane Surface of an Elastic Solid " *Proceedings of the London Mathematical Society*, V. s1-17, No. 1 1885, pp. 4-11

17. Viktorov IA, "Rayleigh Waves and Lamb waves-Physical Theory and Application ". New York: Plenum; 1967.

18. Lamb H, "On the propagation of tremors over the surface of an elastic solid," *The Philosophical Transactions of the Royal Society* V. A 203. 1904, pp. 1–42.

19. Pekeris CL, "The seismic surface pulse," *Proceedings of the National Academy of Sciences*, V. 41. 1955, pp. 469–80.

20. Richart FE, Woods RD, Hall JR, "Vibration of soils and foundations." N.J.: Prentice-Hall, Englewood Cliffs; 1970.

21. Kino GS, "The application of reciprocity theory to scattering of acoustic waves by flaws," *Journal of Applied Physics*, V. 49, No. 6. 1978, pp. 3190-9.

22. Auld BA, "General electromechanical reciprocity relations applied to the calculation of elastic wave scattering coefficients," *Wave Motion*, V. 1, No. 3. 1979, pp. 3-10.

23. Achenbach JD, Gautesen AK, Mendelsohn DA, "Ray analysis of surface-wave interaction with edge crack," *IEEE Transactions on Sonics and Ultrasonics*, V. SU-27. 1980, pp. 124-9.

24. Tien JJW, Khuri-Yakub BT, Kino GS, Marshall DB, Evans AG, "Surface Acoustic Wave measurements of surface cracks in ceramics," *Journal of Nondestructive Evaluation*, V. 2, No. 3-4. 1981, pp. 219-29.

25. Jungerman RL, Khuri-Yakub BT, Kino GS, "Characterization of surface defects using a pulsed acoustic laser probe," *Applied Physics Letters*, V. 44, No. 4. 1984, pp. 392-3

26.   Cooper JA, Crosbie RA, Dewhurst RJ, Mckie ADW, Palmer SB, "Surface-acoustic wave Interactions with cracks and slots: A Noncontacting study using Lasers," *IEEE Transaction on Ultrasonics, Ferroelectrics and Frequency Control*, V. UFFC-33, No. 5. 1986, pp. 462-70.

27.   Cooper JA, Dewhurst RJ, Palmer SB, "Characterization of surface-breaking defects in metals with the use of laser-generated ultrasound," *The Philosophical Transactions of the Royal Society of London A*, V. 320. 1986, pp. 319-28.

28.   Achenbach JD, Keer LM, Mendelsohn DA, "Elastodynamic Analysis of an Edge Crack," *Journal of Applied Mechanics*, V. 47, No. 3. 1980, pp. 551-6.

29.   Mendelsohn DA, Achenbach JD, Keer LM, "Scattering of elastic waves by a surface-breaking crack," *Wave Motion*, V. 2, No. 3. 1980, pp. 277-92.

30.   Angel YC, Achenbach JD, "Reflection and transmission of obliquely incident Rayleigh waves by a surface-breaking crack," *The Journal of the Acoustical Society of America*, V. 75, No. 2. 1984, pp. 313-9.

31.   Hirao M, Fukuoka H, Miura Y, "Scattering of Rayleigh surface-saves by edge cracks: Numerical simulation and experiment," *The Journal of the Acoustical Society of America*, V. 72, No. 2. 1982, pp. 602-6.

32.   Yew CH, Chen KG, Wang DL, "An experimental study of interaction between surface waves and a surface breaking crack," *The Journal of the Acoustical Society of America*, V. 75, No. 1. 1984, pp. 189-96.

33.   Masserey B, Mazza E, "Analysis of the near-field ultrasonic scattering at a surface crack," *The Journal of the Acoustical Society of America*, V. 118, No. 6. 2005, pp. 3585-94.

34.   Jian X, Dixon S, Guo N, Edwards R, "Rayleigh wave interaction with surface-breaking cracks," *Journal of Applied Physics*, V. 101. 2007, pp. 064906.

35.   Cooke D, "Crack depth measurement with surface waves," *presented at British Acoustical Society Spring Meeting*, University of Loughborough, 1972.

36.   Morgan LL, "The spectroscopic determination of surface topography using acoustic surface waves," *Acoustica*, V. 30, No. 222-228. 1974.

37.   Jian X, Fan Y, Edwards RS, Dixon S, "Surface-breaking crack gauging with the use of laser-generated Rayleigh waves," *Journal of Applied Physics*, V. 100, No. 6, Sep. 2006.

38.   Cheng A, Achenbach JD, "A roller device to scan for surface-breaking cracks and to determine crack depth by a self-calibrating ultrasonic technique," *Research in Nondestructive Evaluation* V. 7, No. 4. 1996, pp. 185-94.

39.   Hevin G, Abraham O, Petersen HA, Campillo M, "Characterization of surface cracks with Rayleigh waves: a numerical model," *NDT & E International*, V. 31, No. 4. 1998, pp. 289–98.

40.   Kee SH, Zhu J, "Using air-coupled sensors to determine the depth of a surface-breaking crack in concrete," *The Journal of the Acoustical Society of America*, V. 127, No. 3, Mar. 2010, pp. 1279-87.

41.   Shin SW, Zhu J, Min J, Popovics JS, "Crack depth estimation in concrete using energy transmission of surface waves," *ACI Materials Journal*, V. 105, No. 5, Sep-Oct. 2008, pp. 510-6.

42.   Kim JH, Kwak H-G, Min J, "Characterization of the crack depth in concrete using self-compensating frequency response function," *NDT & E International*, V. 43, No. 5. 2010, pp. 375-84.

43.   Chai HK, Momoki S, Aggelis DG, Shiotani T, "Characterization of Deep Surface-Opening Cracks in Concrete: Feasibility of Impact-Generated Rayleigh-Waves," *ACI Materials Journal*, V. 107, No. 3. 2010, pp. 305-11.

44.   Blackshire JL, Sathish S, "Near-field ultrasonic scattering from surface-breaking cracks," *Applied Physics Letters*, V. 80, No. 18. 2002, pp. 3442-4.

45.   Edwards RS, Jian X, Fan Y, Dixon S, "Signal enhancement of the in-plane and out-of plane Rayleigh wave components," *Applied Physics Letters*, V. 87, No. 19. 2005, pp. 194104-6.

46.   Tolstoy I, Usdin E, "Dispersive properties of stratified elastic and liquid media: A ray theory," *Geophysics*, V. 18. 1953, pp. 844-69.

47.   Wilcox P, "Modeling the Excitation of Lamb and SH Waves by Point and Line Sources," *Proceedings of Review in Progress in Quantitative Nondestructive Evaluation* Melville, NY, 2004, pp. 206-13.

48.   Kee S-H, Zhu J, "Evaluation of Distributed Surface-breaking Cracks in Concrete Using Surface Wave Transmission Method," *NDTCE' 09, Non-Destructive Testing in Civil Engineering*, Nantes, France, 2009.

49.   ABAQUS, Inc., "Analysis user's manual, Version 6.7," Providence, RI, 2007.

50.   Ihlenburg F, "Finite Element Analysis of Acoustic Scattering." New York: Springer-Verlag; 1998.

51.   Alleyne DN, Cawley P, "A two-dimensional Fourier transform method for the measurement of propagating multimode signals," *The Journal of the Acoustical Society of America*, V. 89, No. 3. 1991, pp. 1159-68.

52.   Kim JH, Kwak H-G, "Nondestructive evaluation of elastic properties of concrete using simulation of surface waves," *Computer-aided Civil and Infrastructure Engineering*, V. 23, No. 8. 2008, pp. 611-24.

53.   Park CB, Miller RD, Xia J, "Multichannel analysis of surface waves," *Geophysics*, V. 64, No. 3. 1999, pp. 800-8.

54.   Ryden N, Park C, "Surface waves in inversely dispersive media," *Near Surface Geophysics*, V. 2, No. 4. 2004, pp. 187-97.

55.   Oliver J, Press F, Ewing M, "Two-Dimensional Model Seismology," *Geophysics*, V. 19, No. 2. 1953, pp. 202-19.

56.   Zerwer A, Polak MA, Santamarina JC, "Wave propagation in thin Plexiglas plates; implications for Rayleigh waves," *NDT & E International*, V. 33, No. 1. 2000, pp. 33-41.

57.   Eisner L, Clayton RW, "A reciprocity method for multiple-source simulations," *Bulletin of the Seismological Society of America*, V. 91, No. 3. 2001, pp. 553-60.

58.   Zhang C, Achenbach JD, "Dispersion and attenuation of surface waves due to distributed surface-breaking," *The Journal of the Acoustical Society of America*, V. 88, No. 4. 1990, pp. 1966-92.

59.   Pecorari C, "Rayleigh wave dispersion due to a distribution of semi-ellitical surface-breaking cracks," *The Journal of the Acoustical Society of America*, V. 103. 1998, pp. 1383-7.

60.   Pecorari C, "Attenuation and dispersion of Rayleigh waves propagating on a cracked surface : an effective field approach," *Ultrasonics* V. 38. 2000, pp. 754-60.

61.   Achenbach JD, "Wave Propagation in Elastic Solids." Amsterdam, Holanda : North-Holland 1975.

62.   Joh S-H, "Advances in the data interpretation technique for spectral-analysis-of-surface-waves (SASW) measurements," *Doctor of Philosophy*, Department of Civil, Environmental and Architectural Engineering, The University of Texas at Austin, Austin, 1996.

63.   Cho Y, Rose JL, "An elastodynamic hybrid boundary element study for elastic guided wave interaction with a surface breaking defect," *International Journal of Solids and Structures*, V. 37. 2000, pp. 4103-24.

64.   Grandia WA, Fortunko CM, "NDE applications of air-coupled ultrasonic transducers," *1995 IEEE Ultrasonics Symposium Proceedings*, Vols 1 and 2, 1995, pp. 697-709.

65.   Blomme E, Bulcaen D, Cool T, Declercq F, Lust P, "Air-coupled ultrasonic assessment of wood veneer," *Physics Procedia*, V. 3, No. 1. 2010, pp. 193-200.

66.   McIntyre CS, Hutchins DA, Billson DR, Stor-Pellinen J, "The use of air-coupled ultrasound to test paper," *Ultrasonics, Ferroelectrics and Frequency Control, IEEE Transactions on*, V. 48, No. 3. 2001, pp. 717-27.

67.   Saggin R, Coupland JN, "Non-contact ultrasonic measurements in food materials," *Food Research International*, V. 34, No. 10. 2001, pp. 865-70.

68.   Kelly SP, Farlow R, Hayward G, "Applications of through-air ultrasound for rapid NDE scanning in the aerospace industry," *IEEE Transaction on Ultrasonics, Ferroelectrics and Frequency Control*, V. 43, No. 4, Jul. 1996, pp. 581-91.

69.   PCB Piezotronics I, "Microphone Handbook: Test and Measurement Microphones [Online]." Available: www.pcb.com/Linked_Documents/Vibration/Microphone_handbook.pdf.

70.   PCB Piezotronics I, "Acoustic Measurement Products [Online]." Available: http://www.pcb.com/Linked_Documents/Vibration/Mics_1006_0607_FTS_LOWRES.pdf.

71.   Achenbach JD, "Quantitative nondestructive evaluation," *International Journal of Solids and Structures*, V. 37, No. 1-2, Jan. 2000, pp. 13-27.

72.   Watson BB, "Dynamic and Static Method of Measuring Elastic Properties of Concrete," *Master of Science in Engineering*, Department of Civil, Environmental and Architectural Engineering, The University of Texas at Austin, Austin, 1991.

73.   Kalinski ME, "Measurements of intact and cracked concrete structural elements by the SASW method," *Master of Science in Engineering*, Department of Civil, Environmental and Architectural Engineering, The University of Texas at Austin, Austin, 1994.

74.   Bowen BR, "Damage Detection in Concrete Elements with Surface wave measurements," *Doctor of Philosophy*, Department of Civil, Environmental and Architectural Engineering, The University of Texas at Austin, Austin, 1992.

75.   Dean J. Deschenes, Bayrak O, Folliard KJ, "ASR/DEF-Damaged Bent Caps: Shear tests amd Field Implications " Technical Report No 12-8XXIA006 for Texas Department of Transportation. 2009, pp. 1-271.

76.   Cho DS, Mun S, "Developement of a highway traffic noise prediction model that consider various road surface types," *Applied acoustics*, V. 69. 2008, pp. 1120-8.

77.   Cho DS, Mun S, "Determination of the sound power levels emitted by various vehicles using a novel testing method," *Applied acoustics*, V. 69. 2008, pp. 185-95.

78.   Ti BW, O'Brian WD, Harris JG, "Measurements of coupled Rayleigh wave propagation in an elastic plate," *The Journal of the Acoustical Society of America*, V. 102, No. 3. 1997.

79.   Masserey B, Fromme P, "On the reflection of coupled Rayleigh-like waves at surface defects in plates," *The Journal of the Acoustical Society of America*, V. 123 No. 1 2008, pp. 88-98.

80.   Alleyne DN, Cawley P, "The Interaction of Lamb Waves with Defects," *Ultrasonics, Ferroelectrics and Frequency Control, IEEE Transactions on*, V. 39, No. 3. 1992, pp. 381-97.

81.   ACI committee 228, "Nondestructive test methods for evaluation of concrete in structures," *Report ACI 228.2R-98*, Farmington Hills, MI.,1998.

82.   Masserey B, Mazza E, "Ultrasonic sizing of short surface cracks," *Ultrasonics*, V. 46. 2007, pp. 195-204.

83.   Kendall K, Tabor D, "An Ultrasonic Study of the Area of Contact between Stationary and Sliding Surfaces," *Proceedings of the Royal Society of London Series A*, Mathematical and Physical Sciences, V. 323, No. 1554. 1971, pp. 321-40.

84.   Baltazar A, Rokhlin SI, Pecorari C, "On the relationship between ultrasonic and micromechanical properties of contacting rough surfaces," *Journal of the Mechanics and Physics of Solids*, V. 50, No. 7. 2002, pp. 1397-416.

85.   Kim JY, Baltazar A, Rokhlin SI, "Ultrasonic assessment of rough surface contact between solids from elastoplastic loading-unloading hysteresis cycle," *Journal of the Mechanics and Physics of Solids*, V. 52, No. 8. 2004, pp. 1911-34.

86.   Pecorari C, "Scattering of a Rayleigh wave by a surface-breaking crack with faces in partial contact," *Wave Motion*, V. 33, No. 3. 2001, pp. 259-70.

87.   Na JK, Blackshire JL, "Interaction of Rayleigh surface waves with a tightly closed fatigue crack," *NDT & E International*, V. 43, No. 5. 2010, pp. 432-9.

88.   Cheng C-C, Sansalone M, "Determining the minimum crack width that can be detected using the impact-echo method Part 1: Experimental study," *Materials and Structures*, V. 28, No. 2. 1995, pp. 74-82.

89.   Cheng C-C, Sansalone M, "Determining the minimum crack width that can be detected using the impact-echo method Part 2. Numerical fracture analyses," *Materials and Structures*, V. 28, No. 3. 1995, pp. 125-32.

90.   Zhang J, Stang H, "Applications of Stress Crack Width Relationship in Predcting the Flexural behavior of Fibre-reinforced Concrete," *Cement and Cencrete Research*, V. 28, No. 3. 1998, pp. 439-52.

91.   Jhang K-Y, "Nonlinear ultrasonic techniques for nondestructive assessment of micro damage in material: A review," *International Journal of Precision Engineering and Manufacturing*, V. 10, No. 1. 2009, pp. 123-35.

92.   Kim J-Y, Jacobs LJ, Qu J, Littles JW, "Experimental characterization of fatigue damage in a nickel-base superalloy using nonlinear ultrasonic waves," *The Journal of the Acoustical Society of America*, V. 120, No. 3. 2006, pp. 1266-73.

93.   Kim J-Y, Lee J-S, "A micromechanical model for nonlinear acoustic properties of interfaces between solids," *Journal of Applied Physics*, V. 101, No. 043501. 2007, pp. 043501-1-9.

94.   Shokouhi P, Zo¨ega A, H.Wiggenhauser, "Nondestructive Investigation of Stress-Induced Damage in Concrete," *Advances in Civil Engineering*, V. 2010, No. 740189. 2010.

95.   Jung MJ, "Shear Wave Velocity Measurements of Normally Consolidated Kaolinite Using Bender Elements," *Master of Science in Engineering*, Department of Civil, Environmental and Architectural Engineering, The University of Texas at Austin, Austin, 2005.

96.   Wang T-W, "Shear Performance of ASR/DEF Damaged Prestressed Concrete Trapezoidal Box Bridge Girders," *Doctor of Philosophy*, Department of Civil, Environmental and Architectural Engineering, The University of Texas at Austin, Austin, 2010.

97.   Larson NA, "Structural Performance of ASR/DEF Damaged Prestressed Concrete Trapezoidal Box Beams with Dapped Ends," *Master of Science in Engineering*, Department of Civil, Environmental and Architectural Engineering, The University of Texas at Austin, Austin, 2010.

98.   Bindrich BV, "The Effects of Alkali-Silica Reaction and Delayed-Ettringite Formation on the Structural Performance of the Dapped End Region of Prestressed Concrete Trapezoidal Box Beams," *Master of Science in Engineering*, Department of Civil, Environmental and Architectural Engineering, The University of Texas at Austin, Austin, 2009.

99.   Kee S-H, Zhu J, "Effects of sensor locations on air-coupled surface wave transmission measurements," *Ultrasonics, Ferroelectrics and Frequency Control, IEEE Transactions on*, V. 58, No. 2. 2011, pp. 427-36.

100.   Kim JY, Yakovlev VA, Rokhlin SI, "Surface acoustic wave modulation on a partially closed fatigsue crack," *The Journal of the Acoustical Society of America*, V. 115, No. 5, May. 2004, pp. 1961-72.

Vita

Seong-Hoon Kee attended Whimoon High School, Seoul, South Korea. After high school he enrolled in Hanyang University, Seoul, South Korea and received Bachelor of Science degree at the division of architectural engineering in February 2001. He received full-tuition scholarship during four years throughout the BS program. After graduation, he was commissioned into an engineering officer in the Republic of Korea Army (ROTC #39), and discharged upon completing his military service as a first lieutenant. He entered Master's program at Hanyang University, Seoul, Korea, in August 2003 with Hanyang Scholarship for Engineering and Science Students. After completing his Master's degree, he entered the Ph.D. program at the University of Texas at Austin in August 2006 as a recipient of Overseas Scholarship sponsored by Hanyang University. He received the ACI-James instrument research award on nondestructive test of concrete, 2010-2011. After achieving Ph.D., he started to work as a postdoctoral research associate at Center for Advanced Infrastructure and Transportation (CAIT) in Rutgers University, the State University of New Jersey.

Permanent address: Buyeong Apt. 310-1102, Donong-dong, Namyangju-si, Gyeonggi-do, South Korea, 472-793

This dissertation was typed by the author.